AFAL-TR-77-74

ADA048042
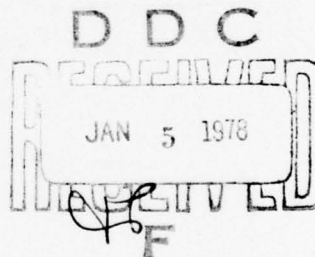
# SOLAR CELL DESIGN STUDY

①

CENTER FOR THE SYNTHESIS AND STUDY OF SEMICONDUCTING COMPOUNDS (CSSSC)
RESEARCH TRIANGLE INSTITUTE
RESEARCH TRIANGLE PARK, N.C. 27709



D D C

RECEIVED
JAN 5 1978
F

August 1977

TECHNICAL REPORT AFAL-TR-77-74

FINAL REPORT FOR PERIOD APRIL 1976 - JANUARY 1977

Approved for public release; distribution unlimited

AIR FORCE AVIONICS LABORATORY
AIR FORCE WRIGHT AERONAUTICAL LABORATORIES (AFSC)
AIR FORCE SYSTEMS COMMAND
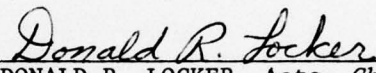Wright-Patterson Air Force Base, Ohio  45433

*NOTICE*

When Government drawings, specifications, or other data are used for any purpose other than in connection with a definitely related Government procurement operation, the United States Government thereby incurs no responsibility nor any obligation whatsoever; and the fact that the government may have formulated, furnished, or in any way supplied the said drawings, specifications, or other data, is not to be regarded by implication or otherwise as in any manner licensing the holder or any other person or corporation, or conveying any rights or permission to manufacture, use, or sell any patented invention that may in any way be related thereto.
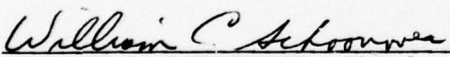
This report has been reviewed by the Information Office (OI) and is releasable to the National Technical Information Service (NTIS). At NTIS, it will be available to the general public, including foreign nations.

This technical report has been reviewed and is approved for publication.


RUSSELL W. RUNNELS, Project Engineer
Electro-Optic Detectors Group
Electro-Optics Technology Branch

DONALD R. LOCKER, Actg. Chief
Electro-Optic Detectors Group
Electro-Optics Technology Branch


FOR THE COMMANDER


WILLIAM C. SCHOONOVER, Chief
Electro-Optics Technology Branch
Electronic Technology Division


"If your address has changed, if you wish to be removed from our mailing list, or if the addressee is no longer employed by your organization please notify AFAL/DHO ,W-PAFB, OH 45433 to help us maintain a current mailing list".


Copies of this report should not be returned unless return is required by security considerations, contractual obligations, or notice on a specific document.

FOREWORD

This report was prepared by the Center for the Synthesis and Study of Semiconducting Compounds (CSSSC), Research Triangle Institute, Research Triangle Park, North Carolina, under Air Force Contract No. F33615-76-C-1283. The contract was administered under the direction of the Air Force Avionics Laboratory, Wright-Patterson Air Force Base, Ohio. Mr. Russell W. Runnels (AFAL/DHO-3) was the Air Force Project Engineer.

The study began in April 1976 and was completed in January 1977. The major contributors to this work were J. R. Hauser (Section 2.0) and M. A. Littlejohn (Section 3.0) of North Carolina State University, and M. F. Lamorte (Sections 4.0, 5.0, and 6.0) of RTI. M. Simons of RTI served as project leader. Additional support and input was furnished by R. D. Alberts, J. W. Harrison, J. J. Wortman of RTI. Programming support was provided at RTI by D. H. Abbott and at NCSU by J. E. Sutherland and C. V. Parks.

| REPORT DOCUMENTATION PAGE | | READ INSTRUCTIONS BEFORE COMPLETING FORM |
|---|---|---|
| 1. REPORT NUMBER<br>AFAL-TR-77-74 | 2. GOVT ACCESSION NO. | 3. RECIPIENT'S CATALOG NUMBER |
| 4. TITLE *(and Subtitle)*<br><br>Solar Cell Design Study | | 5. TYPE OF REPORT & PERIOD COVERED<br>Technical – Final<br>4/1/76 to 1/2/77 |
| | | 6. PERFORMING ORG. REPORT NUMBER<br>41U-1259 |
| 7. AUTHOR(s)<br><br>M. F. Lamorte, J. R. Hauser, M. A. Littlejohn<br>and M. Simons | | 8. CONTRACT OR GRANT NUMBER(s)<br><br>F33615-76-C-1283 |
| 9. PERFORMING ORGANIZATION NAME AND ADDRESS<br>Center for the Synthesis and Study of Semiconduct-<br>ing Compounds (CSSSC), Research Triangle Institute<br>Research Triangle Park, N.C. 27709 | | 10. PROGRAM ELEMENT, PROJECT, TASK AREA & WORK UNIT NUMBERS<br><br>2001-03-61 |
| 11. CONTROLLING OFFICE NAME AND ADDRESS<br>Air Force Avionics Laboratory (AFAL/DHO-3)<br>Air Force Systems Command<br>Wright-Patterson AFB, Ohio 45433 | | 12. REPORT DATE<br>August 1977 |
| | | 13. NUMBER OF PAGES |
| 14. MONITORING AGENCY NAME & ADDRESS*(if different from Controlling Office)* | | 15. SECURITY CLASS. *(of this report)*<br><br>Unclassified |
| | | 15a. DECLASSIFICATION/DOWNGRADING SCHEDULE |

16. DISTRIBUTION STATEMENT *(of this Report)*

Approved for public release; distribution unlimited

ACCESSION for
NTIS          a   ion
DDC           B   Section   ☐
UNANNOUNCED             ☐
JUSTIFICATION

BY
DISTRIBUTION/AVAILABILITY CODES
DIST.          A/or SPECIAL

*A*

17. DISTRIBUTION STATEMENT *(of the abstract entered in Block 20, if different from Report)*

18. SUPPLEMENTARY NOTES

19. KEY WORDS *(Continue on reverse side if necessary and identify by block number)*
Solar Cells, Gallium Arsenide, III-V Compound Semiconductors, High Efficiency,
Heterojunction, Two-junctions.

20. ABSTRACT *(Continue on reverse side if necessary and identify by block number)*
This report reviews the present state-of-the-art in the technology of selected
III-V compounds most applicable to solar cells. Emphasis is placed on those
areas of III-V materials technology that can be advanced most effectively in
the development of high efficiency solar cells for use in the near-earth space
environment. Solar cell configurations evaluated or modeled include homo-
junctions, heterojunctions, Schottky barriers, graded-structures, and multi-
junction or cascade designs.

DD FORM 1473 1 JAN 73    EDITION OF 1 NOV 65 IS OBSOLETE

## TABLE OF CONTENTS

TABLE OF CONTENTS (Continued)

LIST OF ILLUSTRATIONS

LIST OF ILLUSTRATIONS (Continued)

LIST OF ILLUSTRATIONS (Continued)

LIST OF ILLUSTRATIONS (Continued)

xiv

LIST OF ILLUSTRATIONS (Continued)

## LIST OF TABLES

## LIST OF SYMBOLS

$D$      minority carrier diffusion coefficient, $cm^2/sec$

$E_G$      bandgap values, volts (eV)

$E$      electric field strength, volt/cm

$F$      V-I Solar Cell Fill Factor

$g$      minority carrier generation rate, $cm^{-3} sec^{-1}$

$J_{sc}$      short circuit current density, $ma/cm^2$

$J_{max}$      terminal current density at maximum power, $ma/cm^2$

$J_o$      diode saturation current density, $ma/cm^2$

$J$      minority carrier current density, $ma/cm^2$

$J_J$      minority carrier current density to the dark current, $ma/cm^2$

$k$      Boltzman constant, $1.38 \times 10^{-23}$ joules/K

$L$      minority carrier diffusion length, cm

$n_{po}, P_{no}$      equilibrium minority carrier concentration, $cm^{-3}$

$n, p$      excess minority carrier electron or hole concentration, $cm^{-3}$

$n_i$      intrinsic carrier concentration, $cm^{-3}$

$N_D$      donor concentration in n-type material, $cm^{-3}$

$N_A$      acceptor concentration in p material, $cm^{-3}$

$N_o$      incident solar photon flux, $cm^{-2} sec^{-1} \lambda^{-1}$

$-P_{max}$      maximum power

$q$      electronic charge, $1.6 \times 10^{-19}$ coulombs

$R$      reflectivity at x=0 surface

$s$      surface recombination velocity, cm/sec

$s_c$      bottom contact recombination velocity, cm/sec

$T$      temperature, kelvin

| | |
|---|---|
| $V_{0c}$ | open circuit voltage, volts |
| $V_{max}$ | terminal voltage at maximum power, volts |
| $x_i-x_{i-x}$ | thickness of ith layer, cm |
| $\mu$ | minority carrier mobility, $cm^2$/volt sec |
| $\tau$ | minority carrier lifetime, sec |
| $\lambda$ | wavelength $\mu m$ |
| $\lambda_c$ | band gap cut-off wavelength, $\mu m$ |
| $\alpha$ | absorption coefficient, $cm^{-1}$ |
| $\Delta E$ | band edge discontinuity, volts (eV) |
| $C_{i1}, C_{i2}$ | constants of integration of ith layer, $cm^{-3}$ |

Subscripts

| | |
|---|---|
| p | associated with minority hole carrier properties in n-type material |
| n | associated with minority electron carrier properties in p-type material |
| 1,2,3,4 | refers to parameters of layer 1, 2, 3, or 4, respectively. |

## 1.0 INTRODUCTION

The purpose of this work has been 1) to review the present state-of-the-art of III-V solar cells and 2) to determine which III-V materials and solar cell designs can be advanced most effectively in the development of high efficiency solar cells for use in the near-earth space environment. This work has been accomplished through extensive literature surveys, in-house modeling and design optimization studies, and evaluation of the design tradeoffs and technical risks associated with the development and fabrication of specific material systems and device configurations.

In general, III-V compound semiconductors exhibit electrical and optical properties of considerable promise for photovoltaic conversion applications, and several of these compounds are prominent among the alternatives to silicon. The principal advantages of III-V solar cells over silicon cells are the higher theoretical efficiency values, increased radiation resistance, and improved high temperature performance. Because of these features, considerable effort has recently been directed toward the design, development, and fabrication of cells using III-V materials. Theoretical and experimental studies have resulted in a variety of proposed cell designs and III-V material combinations. Added impetus to these efforts has been provided by recent advances in III-V technology associated with the development of microwave and laser devices.

During this study consideration has been given to a number of III-V binary, ternary, and quaternary alloys having properties deemed particularly attractive to a specific solar cell configuration or fabrication process.

1

Special emphasis was placed on the following materials: GaAs, GaP, $Ga_xAl_{1-x}As$, $GaAs_xP_{1-x}$, $Ga_xIn_{1-x}As$, and $Ga_xAl_{1-x}Sb$. Typically, alloy ratios (x) were varied in order to determine the optimum bandgap for the solar spectrum or to optimize lattice match between dissimilar alloys. In general, GaAs served as a reasonably well-characterized base material for comparison with other III-V compounds. Solar cell configurations evaluated included homojunctions, heterojunctions, Schottky barriers, graded-structures, and multi-junction or cascaded devices.

Section 2.0 reviews homojunction, heterojunction and graded bandgap cells and presents the results of optimization studies on heterojunction and graded bandgap devices. Schottky barrier and MIS cells are discussed in Section 3.0, which also includes the results of optimum Schottky barrier performance calculations. Section 4.0 outlines a closed form analytical technique developed to calculate solar cell characteristics. This technique is then used in the development of optimized "potential well" and "cascade" configurations as presented in Section 5.0 and 6.0, respectively. A comparative assessment of the major III-V material and solar cell configurations is then summarized in Section 7.0.

2

## 2.0 BASIC SINGLE JUNCTION SOLAR CELL STRUCTURES

### 2.1 Homojunction Devices

A homojunction solar cell is a device consisting of a single semi-conductor material and having a single p-n junction. For many years this was the only device considered for solar cells and the silicon homojunction solar cell remains to date the most successful solar cell.

A cross sectional view of the typical homojunction solar cell is shown in Figure 2.1. The important elements of the cell are (1) the anti-reflecting layer to reduce optical losses at the surface, (2) the collecting p-n junction located near the surface and (3) ohmic contacts to both the back surface (shown) and the front surface (not shown). Because the diffusion length for electrons is longer in most materials than the diffusion length for holes, cells with an $n^+$ layer near the surface are typically of higher efficiency than $p^+$-n cells.
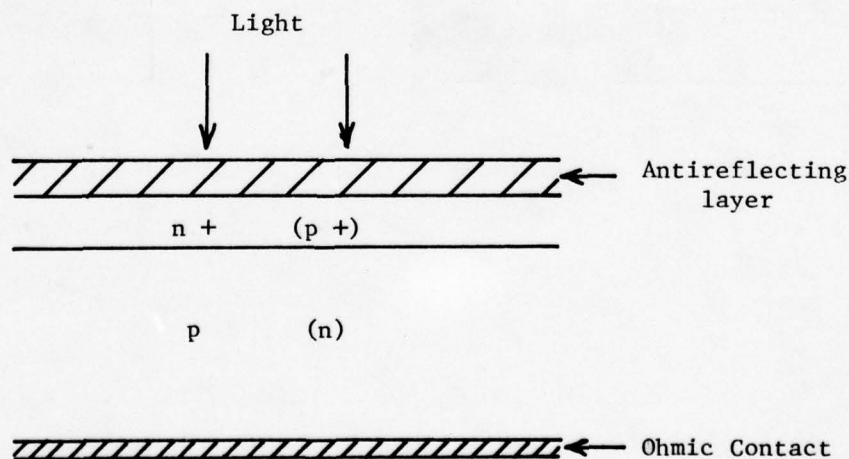


Figure 2.1. Homojunction Solar Cell

The efficiency of a solar cell is determined by the terminal parameters of short circuit current ($I_{SC}$), open circuit voltage ($V_{OC}$) and fill factor

(F) in an equation of the form

$$\eta = \frac{I_{SC} \cdot V_{OC} \cdot F}{P_o} \quad , \tag{2-1}$$

where $P_o$ is the incident optical power. In achieving maximum efficiency, the product $I_{SC} \cdot V_{OC} \cdot F$ should be maximized for a given cell design. The maximization of efficiency is not easily achieved because of the cell's internal competing process giving rise to rather complex relationships on which the terminal characteristics depend. Ideally, the maximum power point on the solar cell V-I curve should be maximized. This is equivalent to maximizing the product given in Eq. (2-1).

The internal steady-state operation of any semiconductor device is governed by the device equations given by

$$J_n = q\mu_n nE + qD_n \frac{dn}{dx} \quad , \tag{2-2}$$

$$J_p = q\mu_p pE - qD_p \frac{dp}{dx} \quad , \tag{2-3}$$

$$0 = G_e - U + \frac{1}{q} \frac{dJ_n}{dx} \quad , \tag{2-4}$$

$$0 = G_e - U - \frac{1}{q} \frac{dJ_p}{dx} \quad , \tag{2-5}$$

$$\frac{dE}{dx} = \frac{q}{\varepsilon} (n-p + N_N) \quad . \tag{2-6}$$

In these equations $N_N$ is the net impurity doping density, $U$ is the internal recombination rate which is usually modeled by the Shockley-Read-Hall theory of

$$U = \frac{pn-n_i^2}{\tau_{no}(p+p_1) + \tau_{po}(n+n_1)} \quad , \tag{2-7}$$

and $G_e$ is the external optical generation of

$$G_e = \int T\alpha N_p \exp(-\alpha x) \, d\lambda \quad , \tag{2-8}$$

4

where T is the transmission coefficient, $\alpha$ is the absorption coefficient and $N_p$ is the incident photon density per wavelength interval. The solution of this set of equations with appropriate boundary conditions give relationships between internal device parameters and the terminal characteristics.

Many of the major factors influencing steady state solar cell operation can be seen from expressing Equations (2-2) and (2-3) in integral form. Equation (2-2) is applied to the p-type side of the p-n junction while Equation (2-3) is applied to the n-type side of the p-n junction. The integrals lead to the equation for the terminal current represented by

$$J = \int_{\substack{\text{entire} \\ \text{device}}} G_e \, dx - q \int_{\text{p region}} \frac{\Delta n}{\tau_n} \, dx - q \int_{\text{n region}} \frac{\Delta p}{\tau_p} \, dx - q \int_{\substack{\text{depletion} \\ \text{region}}} U \, dx - J_{ns} - J_{ps} \, . \qquad (2-9)$$

Each term on the right can be related to specific physical processes within the solar cell. The $\int G_e dx$ term across the entire device gives the available optically generated current in the absence of any losses. The second and third terms represent the integrated electron and hole recombination losses in the p- and n-region, respectively. In these integrals the recombination rate, has been replaced by $\Delta p/\tau_p$ or $\Delta n/\tau_n$, where $\Delta n, \tau_n$ and $\Delta p, \tau_p$ are the excess carrier densities and the corresponding lifetimes in the p- and n-region, respectively. The term $\int U dx$ is the depletion region loss. The final two terms $J_{ns}$ and $J_{ps}$ represent surface recombination currents at the p- and n-type surfaces, respectively, corresponding to the back and front surfaces

5

in Figure 1. These terms are usually expressed as $q\Delta p_s S_p$ and $q\Delta n_s S_n$ where $\Delta n_s$, $S_n$ and $\Delta p_s$, $S_p$ are the surface excess carrier densities and surface recombination velocities at the p- and n-type surfaces, respectively.

In order to obtain a large external current it is obvious from Equation (2-9) that the $\int G_e dx$ should be as large as possible and all recombination losses - bulk, depletion and surface - should be minimized. Equation (2-9) explicitly shows the importance of generation rate, life-time and widths of the various regions on terminal current. However, several other important factors are not explicitly shown. Under forward bias conditions, the $\Delta p$ and $\Delta n$ terms in a solar cell can be thought of as arising from two sources. One contribution comes from the optical carrier generation rate, and a second contribution comes from the forward bias of the p-n junction. It is the forward bias contribution to $\Delta n$ and $\Delta p$ which constitutes the dark current. The dependency of this term on voltage is obtained from an approximate analytical solution or from a numerical solution of the device equations with $G_e$ equal to zero [(Equations (2-2) to (2-6)].

Consider the excess carrier densities as expressed in terms of a contribution from the incident solar flux and a contribution from the terminal voltage as[1]

$$\Delta p = \Delta p_L + \Delta p_V \qquad (2\text{-}10)$$

$$\Delta n = \Delta n_L + \Delta n_V \qquad (2\text{-}11)$$

where the subscript L indicates the solar flux contribution and V indicates

----

[1] These equations are exact representations only when superposition of solar flux and voltage effects holds for the transport equations. Linearity of the basic equations holds only at low injection levels and/or low light levels and thus these equations are not always valid. However, they can be used to illustrate the approximate dependence of solar cell properties on device parameters.

the voltage contribution. Then Equation (2-9) becomes of the form

$$J = J_{SC} - J_D(V) \, , \qquad (2-12)$$

where $J_{SC}$ is the short circuit current expressed as

$$J_{SC} = \int G_e \, dx - q \int \frac{\Delta p_L}{\tau_p} \, dx - q \int \frac{\Delta n_L}{\tau_n} \, dx - q \int U_L \, dx$$

entire      n-region      p-region      depletion region
device

$$- q \Delta p_{LS} S_p - q \, \Delta n_{LS} S_n \, , \qquad (2-13)$$

and $J_D(V)$ is the dark current expressed as

$$J_D(V) = J_n(V) + J_p(V) + J_u(V) \, , \qquad (2-14)$$

with

$J_p(V)$ = dark current contribution from n-type region

$$= q \int \frac{\Delta p_v}{\tau_p} \, dx + q \Delta p_{vs} S_p \, , \qquad (2-15)$$

n region

$J_n(V)$ = dark current contribution from p-type region

$$= q \int \frac{\Delta n_v}{\tau_n} \, dx + q \Delta n_{vs} S_n \, , \qquad (2-16)$$

p-region

7

$J_u(V)$ = dark current contribution from depletion region

$$= q \int_{\text{depletion region}} U_v \, dx \, . \tag{2-17}$$

The current contributions from the n- and p-type regions are seen to arise from two terms — bulk recombination and surface recombination.

Equations (2-13) to (2-17) aid in the identification of the important solar cell parameters for single p-n junction solar cells. In general, the short circuit current should be maximized and the dark forward current minimized. The important parameters which influence short circuit current are

1. Solar spectrum

2. Transmission efficiency

3. Absorption coefficient

4. Lifetime in n- and p-regions and in the depletion region

5. Doping density and doping gradients

6. Diffusion coefficient and mobility

7. Thicknesses of n- and p-type regions and depletion region

8. Surface recombination

Of these factors, the solar spectrum and absorption coefficient are fixed for a given cell design and semiconductor material. The diffusion coefficient and mobility are also fixed once a doping density profile is selected. Thus to maximize efficiency for a given material the device designer has at his disposal the transmission efficiency into the semiconductor, the doping densities, thicknesses of the layers and perhaps lifetime. The doping density, mobility and diffusion coefficient dependence is not

8

explicitly shown in Equation (2-13). However, it is obvious from the basic device equations [(Equations (2-2) to (2-6)] that $\Delta n$ and $\Delta p$ depend on these parameters.

The important parameters determining dark current for a given material are

1. Lifetime in the n- and p-type regions and in the depletion region

2. Doping density and doping gradients

3. Diffusion coefficients and mobility

4. Thicknesses of n- and p-type regions and depletion region

5. Surface recombination

6. Terminal voltage

These parameters are all included in the list for short circuit current parameters except for the terminal voltage.

The parameters discussed above are those which influence solar cell performance for a given semiconductor material. When the broad spectrum of available semiconductor materials is considered the bandgap of the semiconductor becomes one of the dominant factors determining efficiency. The energy bandgap is important for two reasons. First, it determines the optical absorption edge and to a large extent the absorption coefficient. This in turn determines the maximum available optical current from the $\int G_e\, dx$ term. As the bandgap is increased the available optical current decreases as less photons which are capable of producing electron-hole pairs are absorbed in the material. This is illustrated in Figure 2.2 which shows the number of photons absorbed as a function of energy gap for an AMO spectrum [2-1]. This effect alone tends to decrease efficiency as the energy band-gap is increased.

9

## THE PHOTOVOLTAIC EFFECT
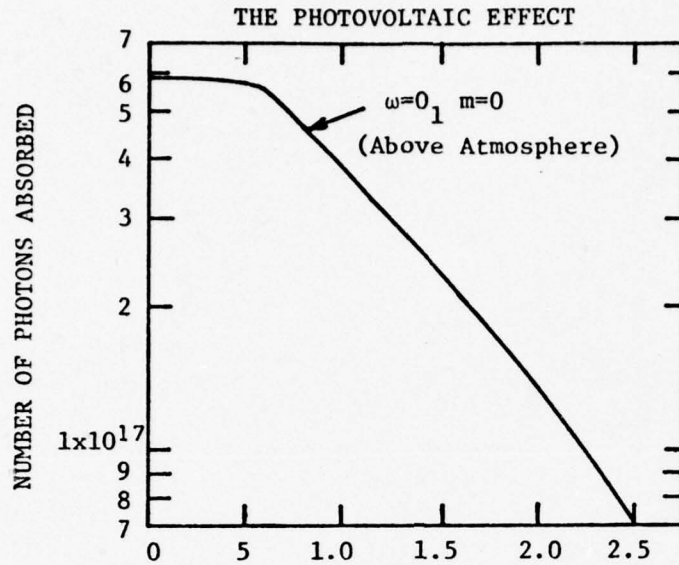


Figure 2.2.   Absorption of solar photons as a function of energy gap [2-1].

The second major effect of increasing the bandgap is a reduction in the dark current.  The ideal dark current density for a p-n junction which has regions on each side of the junction which are wide compared with a diffusion length is

$$J_D(V) = J_0 \left[\exp\left(qV/kT\right) - 1\right] ,\tag{2-18}$$

where

$$J_0 = qn_i^2 \left[\frac{1}{N_D}\sqrt{D_p/\tau_p} + \frac{1}{N_A}\sqrt{D_n/\tau_n}\right] .\tag{2-19}$$

In the above $N_D$ is the donor density on the n-side and $N_A$ is the acceptor density on the p-side.  The bandgap enters through the $n_i^2$ term as

$$n_i^2 = N_c N_v \exp\left(-E_g/kT\right) ,\tag{2-20}$$

where $N_c$ and $N_v$ are the conduction and valence bands effective density of states, respectively.

10

The open circuit voltage is determined from the dark current density, short circuit current density, and temperature as

$$V_{OC} \simeq \frac{kT}{q} \ln \left(\frac{J_{SC}}{J_0}\right) . \qquad (2\text{-}21)$$

In terms of the semiconductor bandgap this can be expressed as

$$V_{OC} = \frac{E_g}{q} - \frac{kT}{q} \ln \left(\frac{J_{OO}}{J_{SC}}\right) , \qquad (2\text{-}22)$$

where

$$J_{OO} = q N_c N_v \left[\frac{1}{N_D} \sqrt{D_p/\tau_p} + \frac{1}{N_A} \sqrt{D_n/\tau_n}\right] . \qquad (2\text{-}23)$$

This illustrates the direct dependence of open circuit voltage on bandgap (all other factors being constant). Thus, the general trend with increasing bandgap is for the short circuit current to decrease, but for the open circuit voltage to increase. These two effects cause overall cell efficiency to peak at some particular bandgap.

The above idealized discussion has to be modified somewhat for actual solar cells. First, many solar cell designs have a surface layer thickness which is less than a diffusion length. This modifies the dark current expression [(Equation (2-19)] and introduces the surface recombination velocity into the analysis as a design parameter. This however does not affect the dependence of $J_0$ on $n_i^2$ as in Equation (2-19) but does change the factor multiplying $n_i^2$ .

Another factor which has to be considered for real devices and especially for wide bandgap materials is the non-ideal components of dark current such as depletion region current as expressed in Equation (2-17). The depletion region current tends to become the dominant dark current component in wide bandgap materials. Under many conditions, the depletion region current can be approximated as

11

$$J_U \simeq \frac{q n_i W_J}{(\tau_{po} + \tau_{no})} \exp\ (qV/2kT)\ , \qquad (2\text{-}24)$$

where $W_J$ is the width of the junction depletion region. When this is the dominant component of dark current the open circuit voltage can be expressed as

$$V_{OC} \simeq \frac{E_g}{q} - \frac{2kT}{q}\, \ell n\ (\frac{J_{OO}}{J_{SC}})\ , \qquad (2\text{-}25)$$

with

$$J_{OO} = \frac{q\sqrt{N_c N_v}\ W_J}{(\tau_{po} + \tau_{no})}\ . \qquad (2\text{-}26)$$

This has a similar dependence on bandgap as for the ideal diffusion current. However the magnitude of the open circuit voltage is reduced when the depletion region current dominates the dark current. Also, the fill factor is reduced when the current exhibits the $\exp\ (qV/2kT)$ dependency.

The peak efficiency of homojunction solar cells has been studied by many investigators [2-2]. The maximum available efficiency for homojunctions as a function of the bandgap of the semiconductor has also been calculated many times. The results of five reported studies are shown in Figures 2.3 through 2.7. The major predictions of the various curves are very similar although the details vary somewhat depending on the assumptions made in the calculations. Figure 2.3 shows an early calculation by Prince [2-3] which predicts a maximum efficiency of about 22.5% at a bandgap of around 1.3 eV.* The curves shown in Figures 2.3 through 2.7 show peak efficiency

---

*The calculated power density values in Figure 2.3 can be divided by the assumed solar power density of 108 mW/cm$^2$ to obtain the corresponding efficiency values.
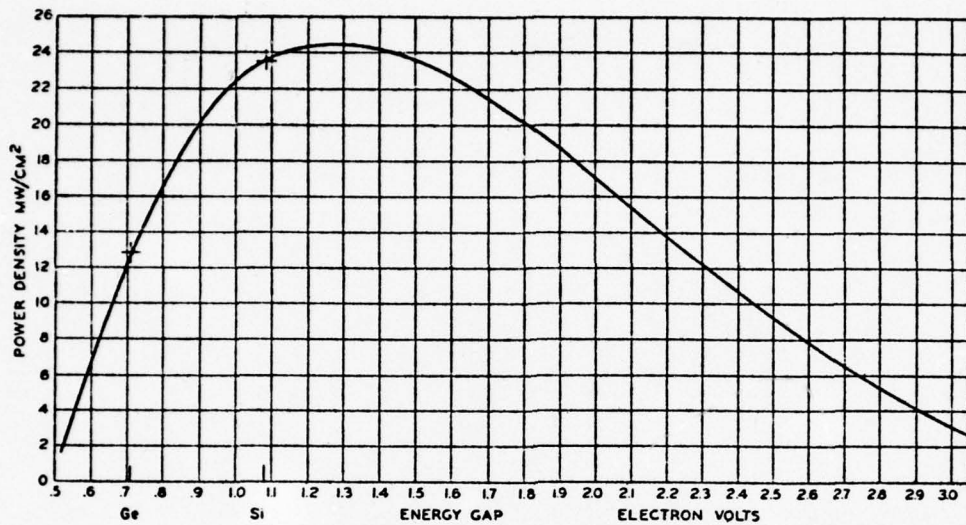
Figure 2.3. Maximum converted power density in bright sunlight as a function of energy gap of semiconductor [2-3].
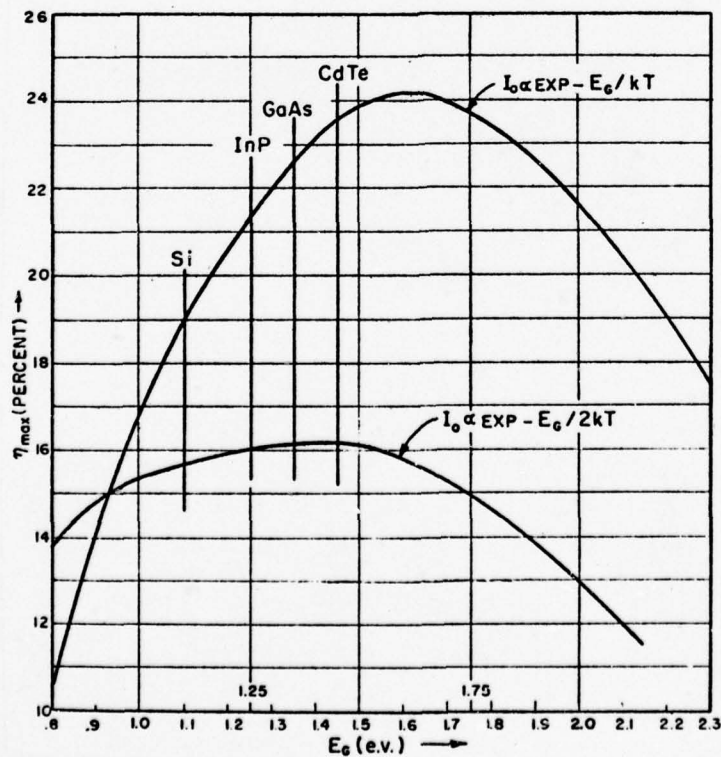


Figure 2.4. Theoretical efficiency versus semiconductor bandgap [2-1].

13
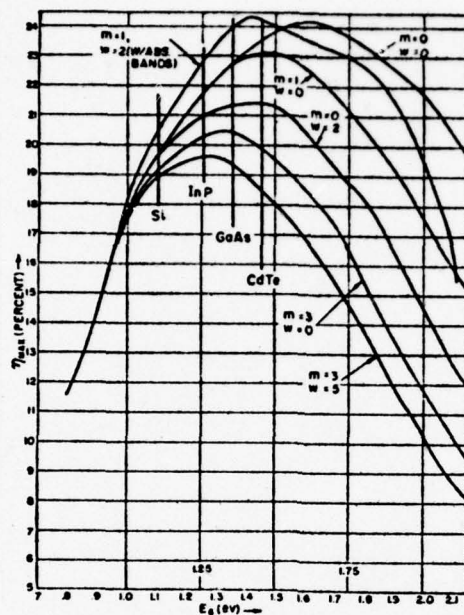
Figure 2.5.  Maximum efficiency for different optical spectra conditions [2-4].
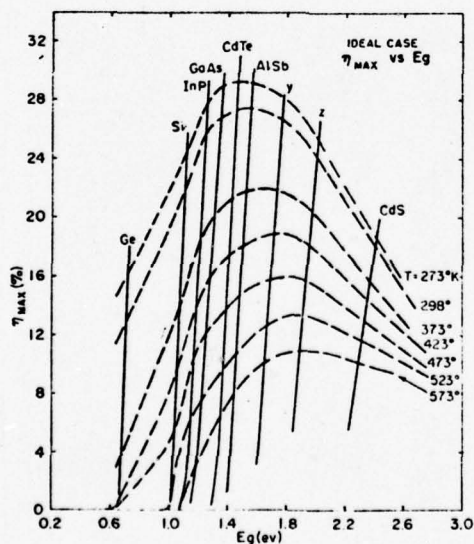


Figure 2.6.  Efficiency versus energy gap for various temperatures [2-1].

14
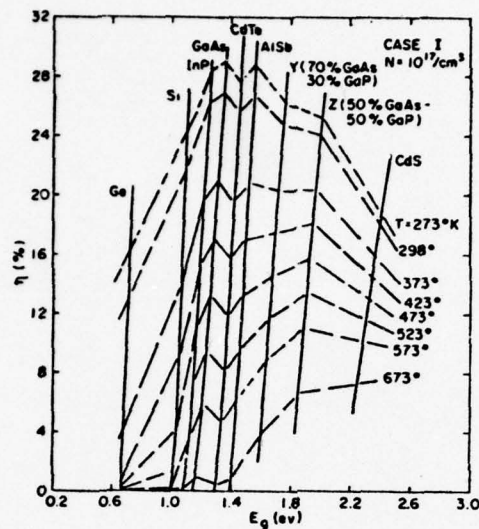
Figure 2.7.  Ideal efficiency versus energy gap [2-5].

values at room temperature of about 22% to 27% with the energy at which

the peak occurs ranging from about 1.3 eV to about 1.6 eV.  These

differences are due to different assumptions in the various models with

regard to lifetime, optimum doping densities, etc.

All of the reported studies of peak efficiency as a function of

bandgap contain certain important assumptions and approximations which

should be understood.  First, the calculations typically assume that all

of the available photons above the bandgap create electron-hole pairs

which are collected by the p-n junction.  This over-estimates the short

circuit current because of the neglect of reflection losses at the

surface and internal recombination processes.  Second, the calculations

typically assume that the dark current is an ideal diffusion current.

The lower curve in Figure 2.4 shows calculated values when the depletion

region recombination current is assumed to dominate the dark current.  This

is seen to reduce considerably the peak efficiency for wide bandgap cells

15

resulting in a peak efficiency of only about 16% at a bandgap of about
1.4 eV. Finally, in making the calculations, assumptions must be made
with respect to diffusion coefficients, lifetimes and doping densities.
The selection of lifetime values is especially difficult because it varies
greatly from one material to another and with doping density. For example,
the lifetime in direct bandgap semiconductors such as GaAs and other
III-V materials is typically much lower than in indirect bandgap
semiconductors such as Si and Ge. These differences are not taken into
account in most of the reported efficiency calculations.

Figure 2.5 includes calculated efficiency values for different solar
spectra conditions incident on a cell. The curves from m = 0, w = 0 to
m = 3, w = 5 show calculated efficiency values corresponding to increasing
losses within the atmosphere. The peak efficiency and the bandgap at
which the peak occurs is seen to both decrease with increasing absorption
in the atmosphere.

Figures 2.6 and 2.7 show the effects of temperature on predicted
efficiencies. Increasing the temperature lowers the available efficiency
and shifts the bandgap energy for peak efficiency to larger values. This
reduction in efficiency with increasing temperatures is due largely to
a decreasing open circuit voltage [(see Equation (2-22)] with temperature.

The approximations made in obtaining the peak efficiency curves of
Figures 2.3 to 2.7 are such that the predicted values tend to be considerably
larger than experimentally observed values. The various curves predict
about 19%-20% for silicon and after many years of work the peak efficiencies
are beginning to pass the 15%-16% range [2-6]. The second most extensively
studied homojunction cell is the GaAs cell. The best efficiencies which

16

have been obtained to date for GaAs homojunction cells are around 11%-12% for AMO conditions [2-6]. Thus the actual efficiencies of homojunction cells remains considerably below the ideal efficiency calculations. The major reasons for this are now briefly discussed.

In terms of the terminal properties, low short circuit current and low open circuit voltage are the two major causes of the reduced efficiency of homojunction solar cells. The short circuit current can be low because of optical losses at the surface and because of internal carrier recombination. Surface optical losses occur because of reflection from or absorption within the anti-reflecting layer. With a single layer anti-reflection film, surface optical losses are typically 10%-15% of the available photons. This loss has been reduced in silicon cells through the use of multiple layer anti-reflection films and textured surfaces. Similar techniques have not been developed for GaAs and other III-V homojunction cells.

Internal to the solar cell, short circuit current losses occur from bulk recombination, depletion region recombination, and surface recombination. These losses are all directly related to bulk lifetime and surface lifetime. Fundamental differences exist in terms of internal losses between direct bandgap and indirect bandgap semiconductors. First for indirect bandgap materials such as Si and GaP, the optical absorption coefficient increases rather slowly for photon energies above the bandedge. This causes appreciable carrier generation to occur deep within the semiconductor to depths of several hundred $\mu$m in silicon, for example. On the other hand, for direct bandgap materials the absorption coefficient increases much faster and carrier generation occurs much closer to the surface - in about 10 $\mu$m of GaAs for example.

Design considerations for maximum short circuit current are somewhat different depending on whether the semiconductor is a direct or indirect bandgap material. For the indirect bandgap designs, the diffusion length and material thickness must be much larger than for the direct bandgap designs. When using indirect materials, the base layer becomes of major importance in achieving a high short circuit current. Losses to recombination at the back contact become important and these are minimized in silicon cells by the use of a back surface field or high-low junction at the back contact. For direct bandgap cells, the region near the surface becomes of dominant importance. The lifetime and thickness of the thin surface layer (see Figure 2-1) becomes very important. Also surface recombination becomes much more important than for the indirect bandgap cells. Figure 2.8 shows calculated short circuit current for p on n GaAs cells as a function of p-n junction depth at various surface recombination velocities [2-7]. A
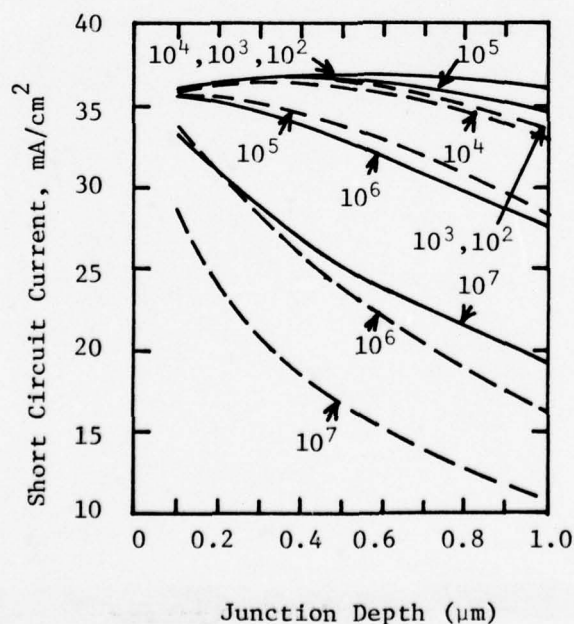


Figure 2.8. Calculated AMO short circuit current for p or n GaAs solar cells [2-7].

18

surface recombination velocity in the range of $10^6$ cm/sec, as is typical

of a GaAs surface, is seen to greatly reduce the short circuit current

unless the junction depth is below 0.1 μm.

Low open circuit voltages are caused both by low short circuit

currents and by high dark currents. The major factors determining dark

current have been presented in Equation (2-14). Low dark currents require

long bulk lifetimes and low surface recombination velocities. One of the

major factors increasing the dark current in wide bandgap semiconductors

is the junction depletion region recombination. This is typically identified

as a dark current which varies with voltage as exp (qV/2kT). Figure 2.4

shows that when this current component dominates the theoretical efficiency

is greatly reduced. This non-ideal current reduces the fill factor as

well as reducing the open circuit voltage. Figure 2.9 illustrates how the

efficiency versus bandgap might appear when account is taken of the change

from an ideal diffusion current for small bandgaps to purely depletion

region current for wide bandgap semiconductors. Silicon p-n junctions

can be readily fabricated in which the dark current is essentially the ideal

current around the open circuit voltage value. GaAs diodes typically tend

to be dominated by depletion region recombination current. However, devices

have recently been built in which it appears that the ideal current dominates

near open circuit voltage conditions [2-7]. As discussed by Hovel [2-7],

this appears to require diffusion lengths of 3 μm or more.

The major differences between the ideal and the experimentally realized

efficiencies of homojunction cells appear to be understood. The major

problems are achieving conditions sufficiently close to the ideal conditions

19
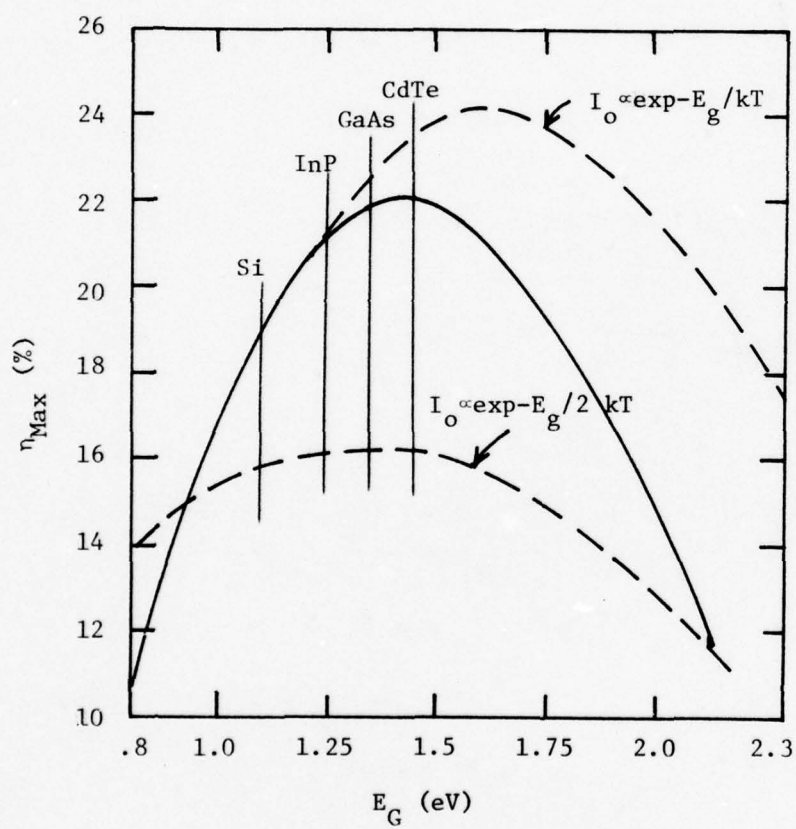
Figure 2.9.  Example of how efficiency may vary with bandgap as dark
current changes from the ideal diffusion current to
depletion region recombination.

20

to approach the theoretical values given in Figures 2.4 through 2.7. Because of the presence of depletion region current in wide bandgap devices the maximum efficiency for homojunction cells almost certainly occurs at a bandgap value below the 1.3 eV to 1.6 eV value shown in Figures 2.4 to 2.7. Thus for operation near room temperature there is probably little reason to explore III-V materials with bandgaps larger than GaAs. For high temperature operation (above 100°C) other materials may have somewhat higher efficiencies as seen from Figures 2.6 and 2.7.

Of the binary III-V semiconductors, only AlSb (1.52 eV bandgap), GaAs (1.44 eV bandgap) and InP (1.34 eV bandgap) have bandgap values close to that predicted for maximum efficiency. GaAs is the natural material because it is close to the peak efficiency and because of the advanced state of technology. Of the other two materials only InP appears to be worthy of further study because of its slightly smaller energy bandgap. As the materials technology for InP advances, it should probably be looked at more seriously as a solar cell material.

There are a large number of ternary III-V materials for possible homo-junction solar cells. Of these materials those with bandgaps slightly above or slightly below GaAs appear to have the most promise for solar cells. The most extensively studied of these are $Al_{1-x}Ga_xAs$, $GaP_{1-x}As_x$ and $Ga_{1-x}In_xAs$. The first two have similar properties and have bandgaps larger than GaAs, while the last material covers bandgap values below GaAs. The range of bandgap values covered by these materials is shown on the ideal efficiency curves of Rappaport in Figure 2.10. According to the ideal theory, the $Al_{1-x}Ga_xAs$ or $GaAs_{1-x}P_x$ cells should have slightly higher efficiencies than pure GaAs. If depletion region recombination dominates, the $Ga_{1-x}In_xAs$
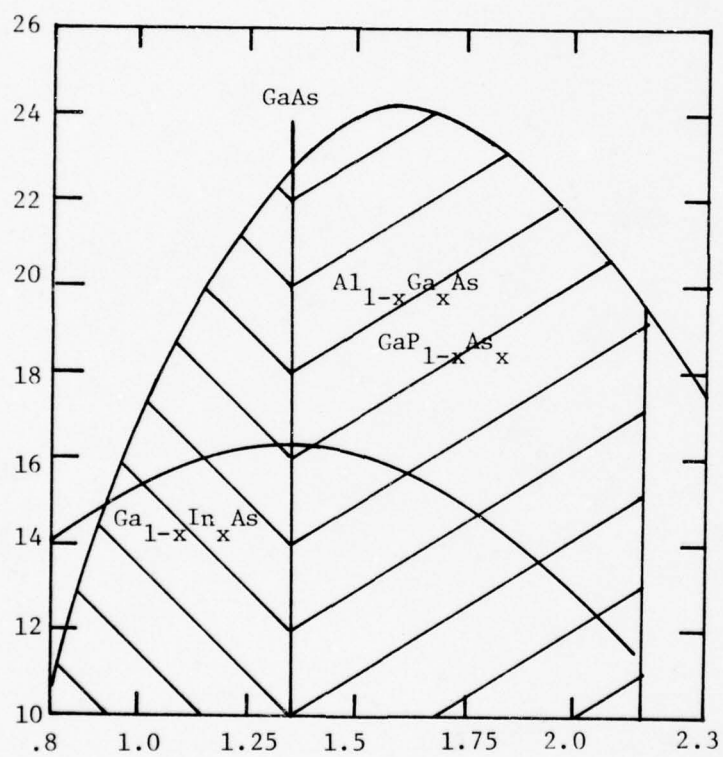
Figure 2.10.  Ideal efficiency values for some III-V ternary materials.

cell may be a better choice. Thus the ternaries offer the ability to select the truly optimum bandgaps for a particular solar cell design. However, all of this will remain speculative until means are found to achieve III-V homojunction solar cells with efficiencies exceeding that of silicon.

One of the major (if not dominant) limitations of present GaAs homojunction solar cells is the short circuit current losses to surface recombination. The dark current may also be significantly enhanced by surface recombination. The two approaches to minimizing this problem have been to reduce the junction depth or to go to a heterojunction structure. The reduction of the junction depth has the problem of increasing the sheet resistance and, therefore, the series resistance of the cells. This limits the junction depth reduction which can be achieved. At present almost all research on III-V p-n junction solar cells is directed toward the hetero-junction cell and impressive results have been achieved as discussed in the next section. Another approach which does not appear to have been extensively explored is to reduce the value of the surface recombination velocity. It may be possible to significantly reduce surface recombination by the formation of some type of native oxide at the surface, such as formed by anodic oxidation techniques. MOS devices have been constructed on GaAs through the use of such techniques and these devices generally require good surface properties. The use of a semiconductor heterojunction is simply one means of providing an improved GaAs surface interface. Improvements in surface recombination could make homojunction III-V cells competitive with heterojunction cells.

Because of the wide bandgap of GaAs, the reduction in efficiency with temperature is less than that of silicon cells. Figure 2.11 shows the terminal

23
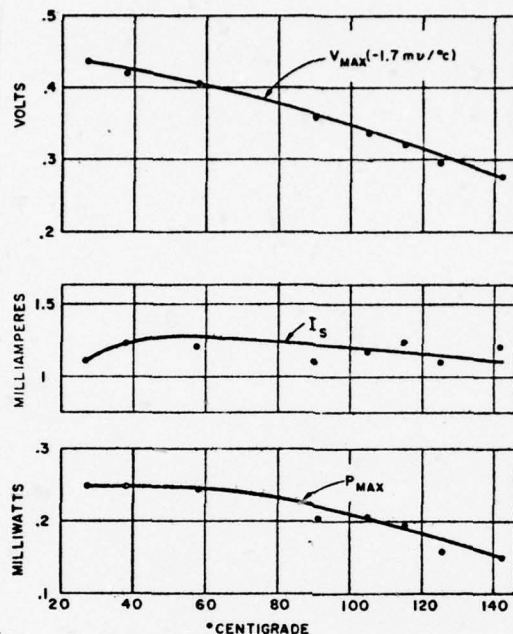
Figure 2.11. Variation of GaAs alloy-junction-solar-cell parameters with temperatures.

parameters of an early GaAs cell as a function of temperature. The short circuit current is seen to remain almost constant with the open circuit voltage changing at about -1.7 mV/°C. The improved temperature performance of III-V cells is one of the major attractive features of such cells.

Another important performance parameter is radiation resistance. Because of the short lifetime and diffusion length, GaAs homojunction cells are more resistant to penetrating radiation than silicon cells. For both high energy electrons and protons the radiation resistance of GaAs cells has been found to be about an order of magnitude larger than silicon cells [2-7, 2-8]. For low energy particles little or no improvement over silicon was observed. However low energy particles can be removed by a thin cover glass so that an overall improved radiation resistance results.

24

A summary of some of the results and potential performance of various III-V homojunctions is given in Table (2.1). As previously discussed the ideal efficiencies are much larger than can be expected in actual practice. Although GaAs is the only material extensively explored, other materials as shown have equivalent or slightly better efficiency potential. The major problem with all the homojunction III-V cells is the surface recombination. The development of a simple, practical means of greatly reducing the surface recombination velocity on any of the materials in Table 2.1 could catapult the III-V homojunction solar cell back into the picture for some solar cell applications.

The efficiency values in this section are all taken from very idealized studies of general trends of efficiency as a function of semiconductor bandgap which have appeared in the literature. These idealized studies give efficiency values which are larger than typically predicted by more complete studies of particular materials and devices. The results are useful for predicting general trends of efficiency with bandgap. However, the efficiency values reported can not be directly compared with the efficiency values reported in subsequent sections of this report because of the idealized nature of the calculations.

Table 2.1.  III-V Homojunction Solar Cells

| Material | Ideal Efficiency* | Achieved Efficiency | Remarks |
|---|---|---|---|
| GaAs | 22%-26% | 11%-12% | Limited in collection efficiency by surface recombination. Long diffusion lengths required for low dark current and for ideal dark current. |
| InP | 21%-25% | ----- | Potentially about as good as GaAs with similar problems. |
| AlSb | 23%-27% | ----- | Little development of materials technology. May be lower in practical efficiency than GaAs even if developed. |
| $Al_{1-x}Ga_xAs$ $GaP_{1-x}As_x$ | 23%-27% (large x values) | ----- | These have advanced materials technology and cover the peak in ideal efficiency. Practical efficiency may not exceed GaAs if dark current is dominated by depletion region recombination. |
| $Ga_{1-x}In_xAs$ | 21%-25% (small x values) | ----- | Small In concentrations may have slightly higher efficiencies than GaAs if depletion region recombination is important in GaAs. |

*Highly idealized values reported in literature (surface recombination neglected). These values are based upon more idealized models than the results of subsequent sections of this report and should not be compared directly with the more complete device calculations.

## 2.2  Heterojunction Devices

The heterojunction solar cell represents a practical means of
eliminating or minimizing the surface recombination loss of III-V
homojunction cells discussed in the previous section.  It was the
development of this type of cell [2-9,2-10] that generated renewed
interest in all types of III-V solar cells.  In the heterojunction
solar cell, a thin layer of a wide bandgap semiconductor is placed
at the surface on which the solar flux is incident.  Ideally the wide
bandgap material, as illustrated in Figure 2.12, acts as a window
to pass the incident light into the narrow bandgap semiconductor.

There are basically two types of heterojunction solar cells.  In
the first type the p-n junction is located at the heterojunction while
in the second type the p-n junction is located some distance below
the heterojunction.  Energy band diagrams for these two types of cells
are shown in Figure 2.13.  The diagrams show n-on-p cells, but p-on-n
cells are also possible.  In fact, cells which have been fabricated
with the junction below the interface are typically p-on-n cells.
When the p-n junction is located below the heterojunction interface,
the cell is frequently referred to as a "heteroface" cell [2-6] since
the heterojunction plays a more passive role in the operation of the
cell.  In the present study, the term heterojunction cell will be used
for both types of cells, since these can exist as a continuous variety
of cells between the cases shown in Figure 2.13.

The heterojunction cell has two major advantages over the homojunction
solar cell.  First, the optical absorption occurs strongly within the
narrow bandgap material beginning at the heterojunction interface.  The
calculated generation rate, $G_e$, for an AlAs-GaAs heterojunction of 1 $\mu$m
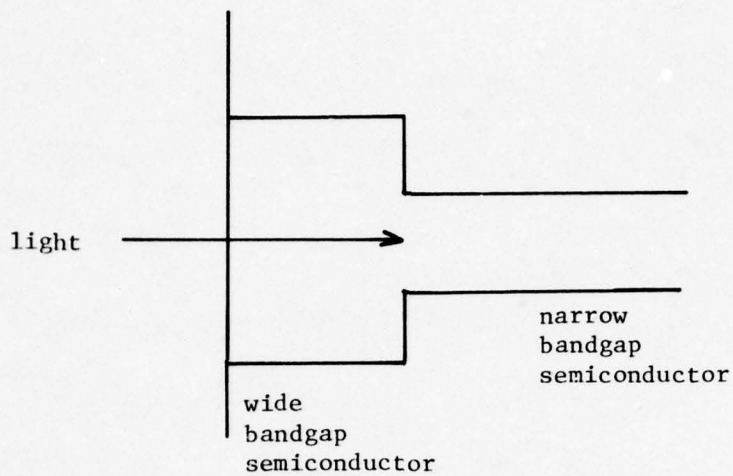
Figure 2.12. Illustration of wide bandgap window on a narrow bandgap semiconductor.
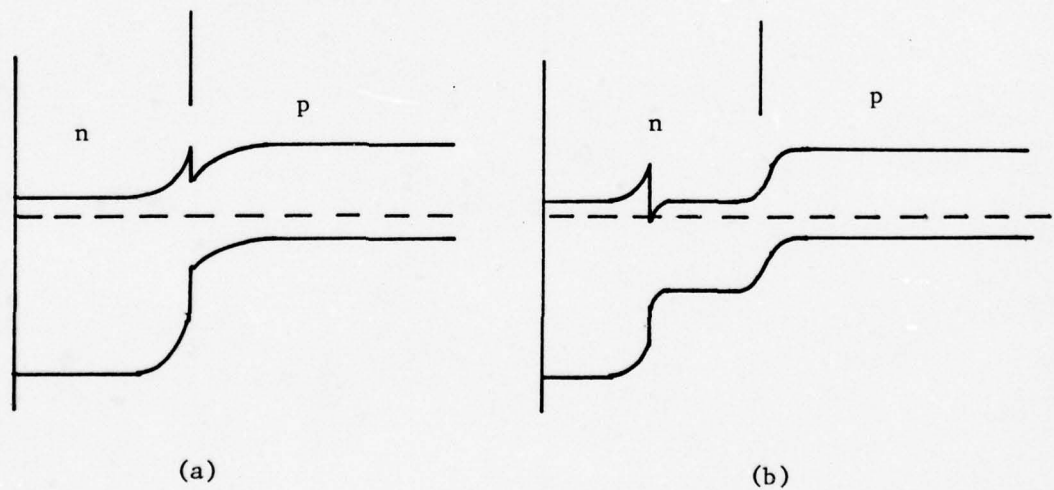


Figure 2.13. Energy band diagrams for the two types of heterojunction cells.

    (a)  p-n junction at interface.

    (b)  p-n junction below interface.

depth is shown in Figure 2.14. The generation rate shows an increase of over two orders of magnitude in value at the heterojunction interface compared to the window region. The advantage of the heterojunction cell is that the generation occurs away from the physical surface and there is an energy barrier between the generated minority carriers and the surface. Carriers are thus prevented from reaching the surface and surface recombination loss becomes relatively unimportant in the solar cell operation.

A second advantage of the heterojunction cell arises from the fact that little of the light is absorbed in the wide bandgap region. This allows the surface layer to be relatively wide compared with the surface layer of a homojunction cell. The wider region can be used to lower the sheet resistance of the surface layer and subsequently lower the series resistance of a solar cell. This, however, conflicts somewhat with high efficiency and compromises must be made between high efficiency and low series resistance.

The limitations to efficiency for a heterojunction solar cell are very similar to those of a homojunction cell of the narrower bandgap material. The dark current and short circuit considerations of Equations (2-13)to (2-17) also apply to the heterojunction cell. The short circuit current is limited by transmission into the cell, by bulk recombination, depletion region recombination and surface recombination. As previously discussed the heterojunction cell greatly reduces the front surface recombination. However, it introduces another recombination process which may be almost as severe in some heterojunction cells as surface recombination. This is the introduction of lattice mismatch recombination states at the heterojunction interface due to dangling bonds.

29
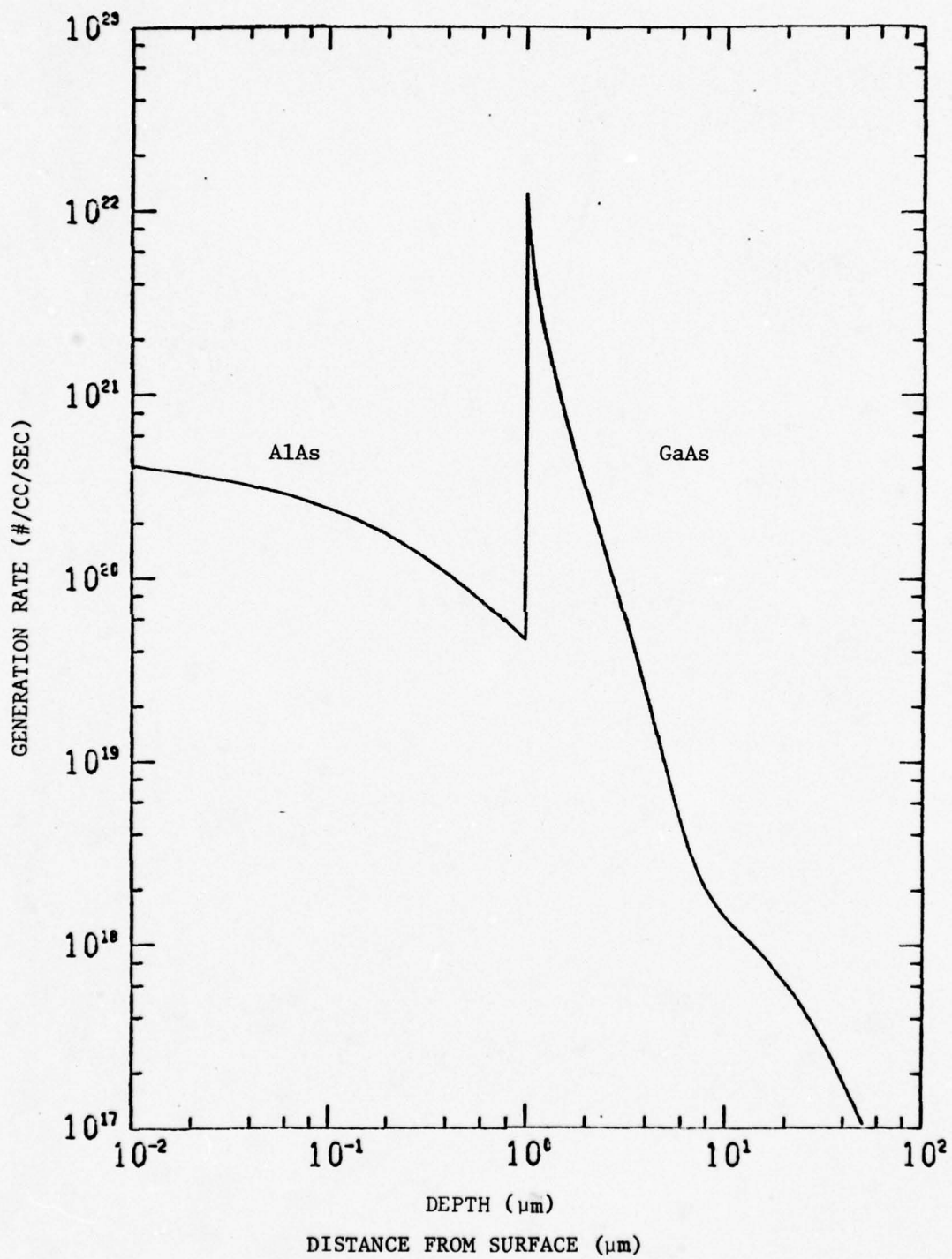
Figure 2.14. Optical generation rate for a 1 μm thick AlAs layer on GaAs.

Table 2.2. Density of Interface Dangling Bonds for Various III-V Heterojunctions [2-11].

| Heterojunction (deposit/substrate) | Lattice parameters (Å) | Plane | Dangling $\Delta N_a$ $(cm^{-2})$ |
|---|---|---|---|
| InSb/GaSb | 6.4787/6.0954 | (100) | $1 \cdot 2 \times 10^{14}$ |
|  |  | (111) | $7 \cdot 1 \times 10^{13}$ |
| InSb/GaAs | 6.4787/5.6531 | (100) | $3 \times 10^{14}$ |
|  |  | (111) | $1 \cdot 7 \times 10^{14}$ |
| InAs/GaSb | 6.0583/6.0954 | (100) | $1 \cdot 3 \times 10^{13}$ |
|  |  | (111) | $7 \cdot 4 \times 10^{12}$ |
| InAs/GaAs | 6.0583/5.6531 | (100) | $1 \cdot 6 \times 10^{14}$ |
|  |  | (111) | $9 \cdot 4 \times 10^{12}$ |
| GaSb/GaAs | 6.0954/5.6531 | (100) | $1 \cdot 7 \times 10^{14}$ |
|  |  | (111) | $1 \times 10^{14}$ |
| InP/GaAs | 5.8687/5.6531 | (100) | $9 \cdot 1 \times 10^{13}$ |
|  |  | (111) | $5 \cdot 2 \times 10^{13}$ |
| GaAs/GaP | 5.6531/5.4505 | (100) | $9 \cdot 5 \times 10^{13}$ |
|  |  | (111) | $5 \cdot 5 \times 10^{13}$ |
| AlAs/GaAs | 5.6622/5.6531 | (100) | $4 \cdot 3 \times 10^{12}$ |
|  |  | (111) | $2 \cdot 5 \times 10^{12}$ |
| AlP/GaAs | 5.451/5.6531 | (100) | $9 \cdot 4 \times 10^{13}$ |
|  |  | (111) | $5 \cdot 4 \times 10^{13}$ |
| AlP/GaP | 5.451/5.4505 | (100) | $9 \cdot 1 \times 10^{11}$ |
|  |  | (111) | $5 \cdot 2 \times 10^{11}$ |

The density of dangling bonds has been worked out for a wide range of heterojunctions [2-12] and some of the results are shown in Table (2.2). To obtain an appreciation for the magnitude of the interface recombination the following simple model can be considered. The equivalent surface recombination velocity of the interface states can be written as

$$S = N_I \sigma v_{th} , \tag{2-27}$$

where $N_I$ is the number of recombination states per unit area, $\sigma$ is the capture cross-section and $v_{th}$ is the thermal carrier velocity. For charged recombination centers $\sigma \sim 10^{-14}$ cm$^2$ [12] and taking $v_{th} \sim 10^7$ cm/sec gives

$$S \sim (10^6 \text{ cm/sec}) \ [N_I/(10^{13}/\text{cm}^2)] . \tag{2-28}$$

From this estimation, an interface density of recombination centers of $10^{13}/\text{cm}^2$ would give an equivalent interface recombination velocity of $10^6$ cm/sec or a value which is about equivalent to that of a bare GaAs surface. If every dangling bond contributes one recombination site then Table 2.2 shows that many potential heterojunction systems will have very large interface recombination and probably offer no advantage over a homojunction cell. Not all of the dangling bonds may be active as recombination centers or the capture coefficient may be smaller than that assumed in this simple calculation. The advantage of the AlAs-GaAs or $Al_{1-x}Ga_xAs$-GaAs system, as seen from Table (2.2), is the very low density of dangling bonds due to the small lattice mismatch between AlAs and GaAs.

Experimental measurements by Ettenberg and Kressel on an $Al_{0.5}Ga_{0.5}As$-GaAs heterojunction have indicated an interface recombination velocity of about $8 \times 10^3$ cm/sec for this heterojunction [2-13]. This is considerably less than would be estimated from Equation (2.28) assuming that every dangling bond acts as a recombination center. However it shows that even for this near ideal lattice match there is still a fairly large interface recombination. To show a significant improvement over a bare GaAs surface the density of dangling bonds may be limited to values no greater than about ten times the density present at the AlAs-GaAs interface. The actual influence of interface recombination on solar cell efficiency is discussed later in this section.

The dark current of a heterojunction is determined by minority carrier injection across the p-n junction and by depletion region and interface recombination. Because of the wider bandgap of the window surface layer, minority carrier injection is small into the surface layer. Neglecting interface recombination states, the dark current of a heterojunction cell should be somewhat less than that of a corresponding homojunction cell. However as shown later, interface recombination may greatly enhance the dark current if the p-n junction depletion region extends into the heterojunction.

Because the same fundamental factors limit both homojunction and heterojunction solar cells, the ideal efficiency limits discussed for homojunctions in the previous section may also be considered as upper limits to the efficiency of heterojunction cells. From these curves, the efficiency of heterojunction cells on GaAs substrates can be estimated as below the 22%-24% range. More complete calculations have given better estimates of the efficiency limits of selected heterojunction cells.

The most extensively studied heterojunction cells are the AlAs-GaAs [2-14,2-15] cell and the $Ga_{1-x}Al_xAs$-GaAs cell with x in the range of 0.8-1.0 [2-9,2-10]. Figure 2.15 [2-7] shows calculated efficiency values (x values close to unit) as a function of the depth of the p-n junction below the heterojunction. Two thicknesses (10 μm and 0.1 μm) of window material are shown as well as calculated values for AM0, AM1 and AM2 spectral conditions. The peak efficiencies for AM0 are around 14.5% for a 10 μm window and 20.5% for a 0.1 μm window. These values are lower than the ideal efficiencies of Figure 2.3-2.7 because of more realistic approximations used in the calculations. The effect of the window thickness is seen in Figure 2.16. It is seen that the window thickness must be less than 0.1 μm if the highest efficiency values are to be achieved.

The results shown in Figures 2.15 and 2.16 are based upon closed form solutions to the approximate transport equations as discussed in Appendix A. Exact numerical calculations have also been made for AlAs-GaAs heterojunction cells using the method discussed in Appendix A.[*] The peak efficiency values obtained by this exact numerical analysis are shown as a function of p-n junction depth in Figure 2.17 [2-16]. The doping densities used in the calculations were $2 \times 10^{17}/cm^3$ for the surface layer and $4 \times 10^{17}/cm^3$ for the base layer. The optimum p-n junction depth has been identified as about 0.3 μm to 0.4 μm in both calculations. The resulting efficiency values are very similar to those of Figure 2.15 obtained by the simpler analysis.

---

[*] The calculations for (Al,Ga)As heterojunction cells in this and the next section were done on a separate NASA Langley Research Grant to N. C. State University.

34
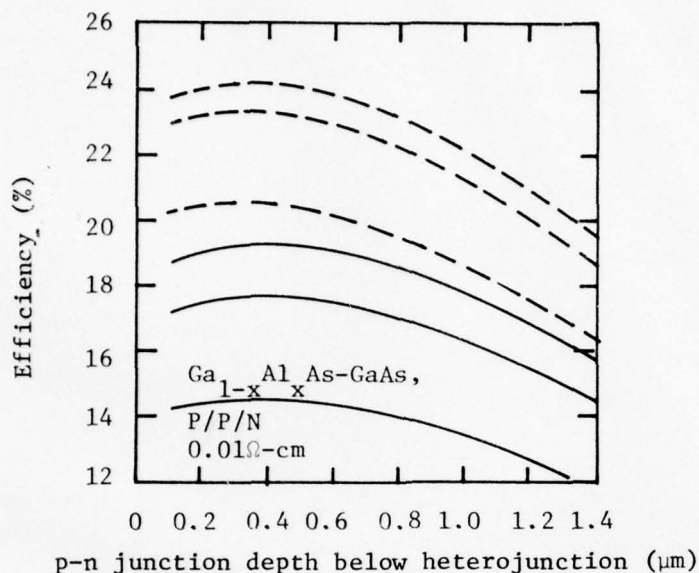
Figure 2.15. Calculated inherent efficiencies of $pGa_{1-x}Al_xAs$-pGaAs-nGaAs solar cells for 2 $Ga_{1-x}Al_xAs$ thickness. In each set of curves, the bottom represents AMO, the middle AM1, and the top AM2. No fields, $S_{back}=\infty$. —— D = 10 μm; --D = 0.1 μm [2-7].
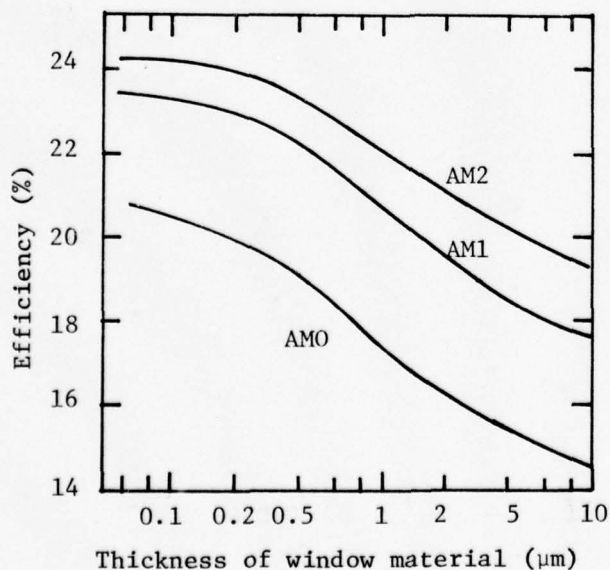


Figure 2.16. Calculated inherent efficiencies of $pGa_{1-x}Al_xAs$-pGaAs-nGaAs solar cells for 2 $Ga_{1-x}Al_xAs$ thickness. Same conditions as in Figure 2.15. No fields, $S_{back}=\infty$. —— D = 10 μm; --D = 0.1 μm. [2-7].

35
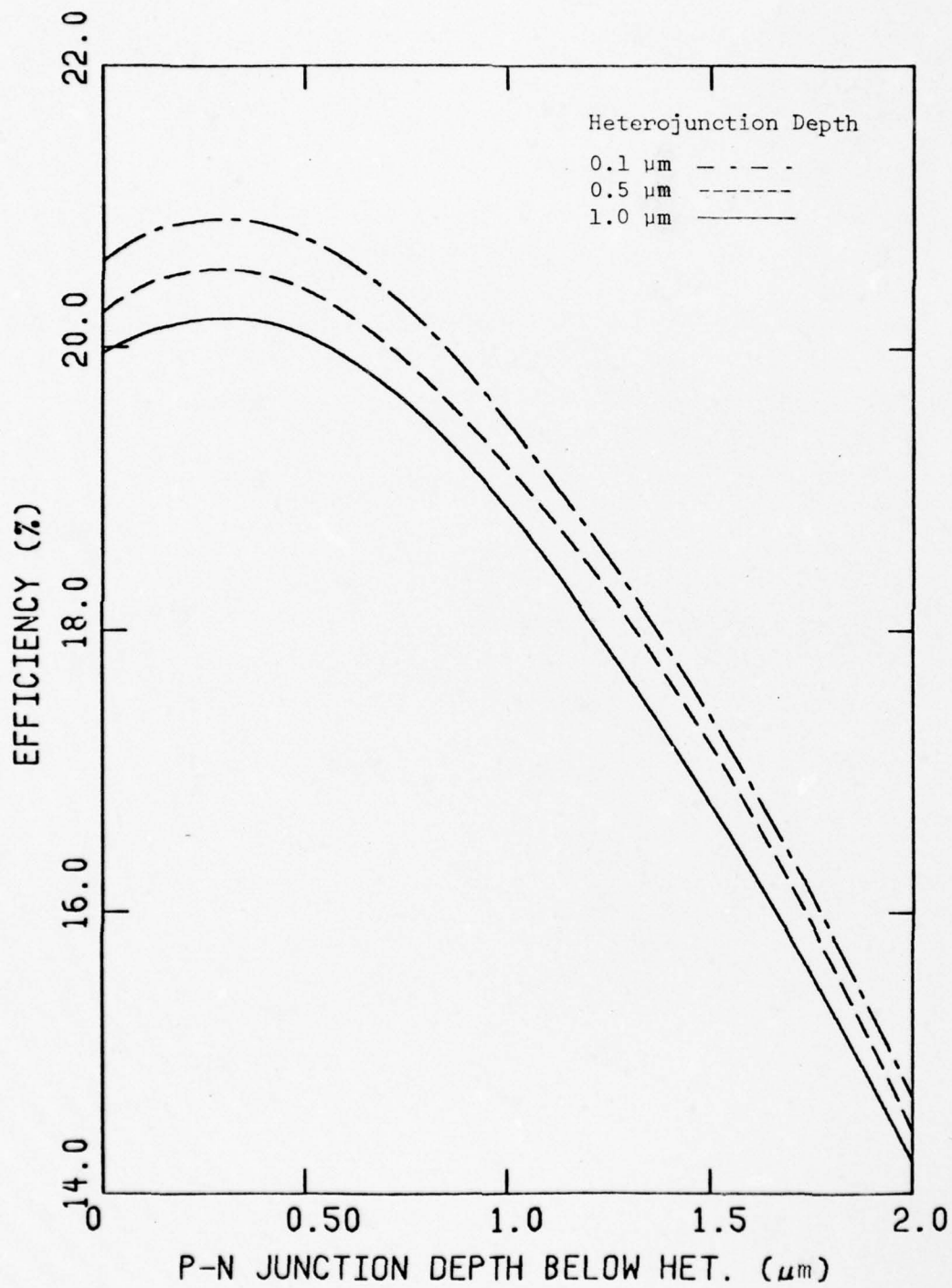
Figure 2.17. Peak efficiency of AlAs-GaAs heterojunction cells as a function of p-n junction depth below the heterojunction from numerical analysis.

This is especially interesting since the results in Figures 2.15 and 2.16 are for p-on-n cells while the results of Figures 2.17 are for n-on-p cells. These results indicate that little theoretical differences are to be expected in peak efficiency between n-on-p and p-on-n cells and the choice must be made from practical fabrication considerations.

Figure 2.18 shows the results of the detailed analysis for peak efficiency as a function of heterojunction depth. This again for the $Al_xGa_{1-x}As$ system is very similar to Figure 2.16. (The results for $GaAs_{1-x}P_x$ are discussed subsequently.) The results in general illustrate the importance of a very thin window region and indicate that the theoretical efficiency values are in the range of 20%-21%.

In addition to the (AlGa)As system, the Ga(P,As) system is probably the next most extensively explored III-V ternary system because of its applications in LEDs. GaP has similar electrical and optical properties to AlAs and should in principle behave similarly in heterojunction solar cells. This conclusion has been confirmed to a certain extent by solar cell calculations, but a problem arises with the GaP-GaAs heterojunction system which has also been identified. Calculations have been made for GaP-GaAs heterojunction cells with dimensions and doping densities identical to those used in obtaining the results of Figure 2.17. A comparison of some of the results is shown in Table (2.3). The first three lines in the table are for AlAs-GaAs heterojunctions under different conditions. Device number 1 does not include the lattice mismatch interface states while devices number 2 and 3 do include these. For the AlAs-GaAs devices, heterojunction interface states were found to reduce the efficiency only by about 0.1-0.2 percentage points.

37

A comparison of devices number 1 and 4 gives a direct comparison of the AlAs-GaAs cell and the GaP-GaAs cell before interface states are included. The GaP-GaAs cell has a slightly lower efficiency of 19.24% as compared with 19.95%, but the predicted performance is almost identical as expected. Device number 5 shows the results of including the interface states on the efficiency of the GaP-GaAs cells. The efficiency decreases from 19.24% to 15.04%. The reduced efficiency is due almost entirely to the drop in open circuit voltage from 0.985V to 0.831V. These predictions are based upon the assumption that the interface recombination velocity is directly proportional to the density of dangling bonds at the interface. This has not been experimentally verified but appears to be a reasonable assumption.

The variation in efficiency with p-n junction depth for GaP-GaAs cells is shown in Figure 2.19. As contrasted with the AlAs-GaAs cells of Figure 2.17, the efficiency was observed to increase rapidly as the p-n junction was moved to small distances below the heterojunction. Efficiencies of 19% or slightly above were calculated for junction depths of around 0.04 μm below the heterojunction. The efficiency was then observed to decrease rapidly for junction depths beyond 0.1 μm. This behavior is directly due to the large density of interface states.

Consider first the rapid increase in efficiency as the junction is moved below the heterojunction. This has the effect of moving the interface recombination states out of the center of the junction depletion region. Recombination states within a depletion region are most effective when they occur near the center of the energy bandgap. Thus moving the junction slightly below the heterojunction greatly reduces the dark
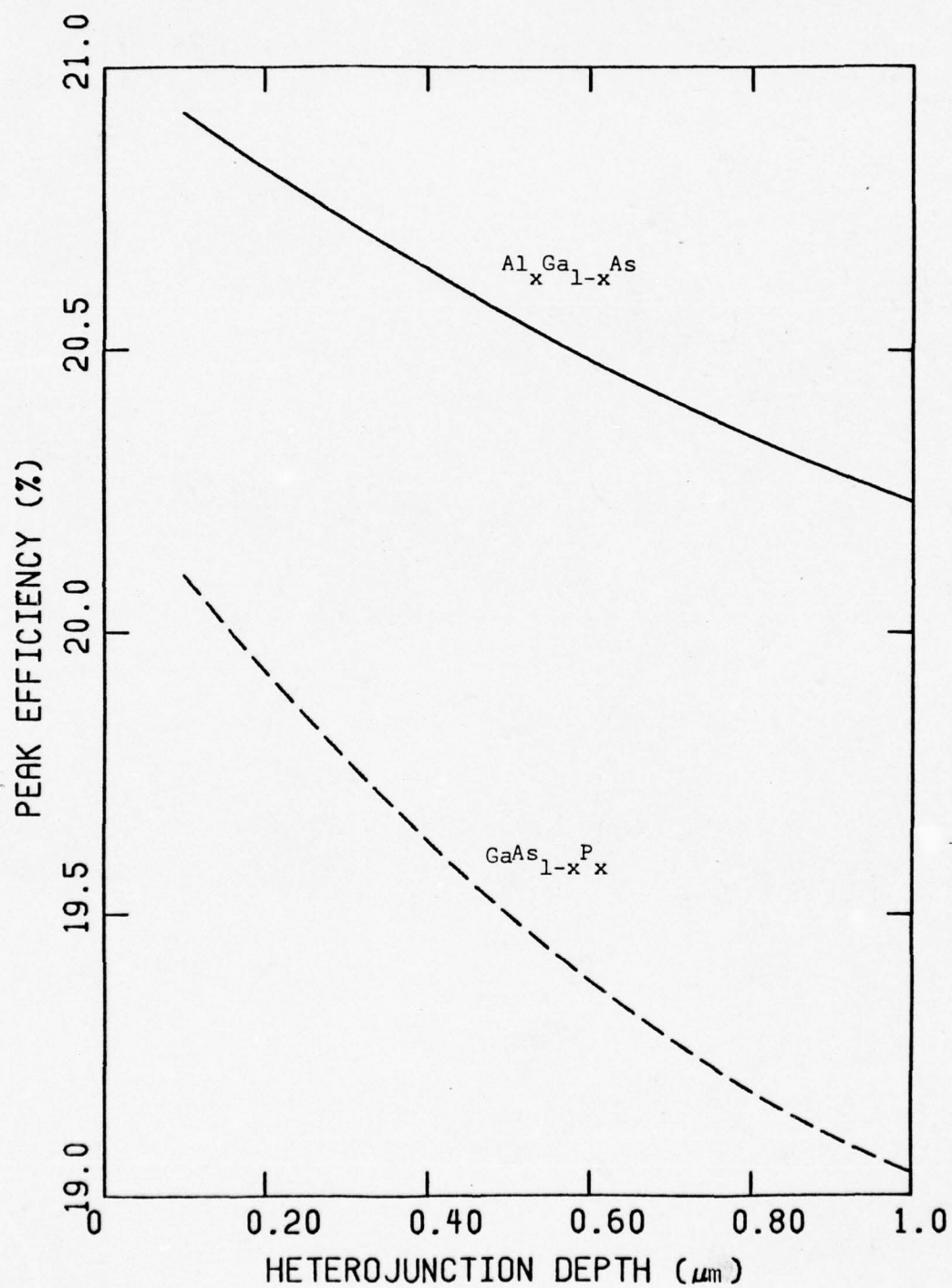
Figure 2.18. Peak efficiency as a function of heterojunction depth. The p-n junction is 0.3 μm below the heterojunction for $Al_{1-x}Ga_xAs$ and 0.04 μm below the heterojunction for $GaP_{1-x}As_x$.
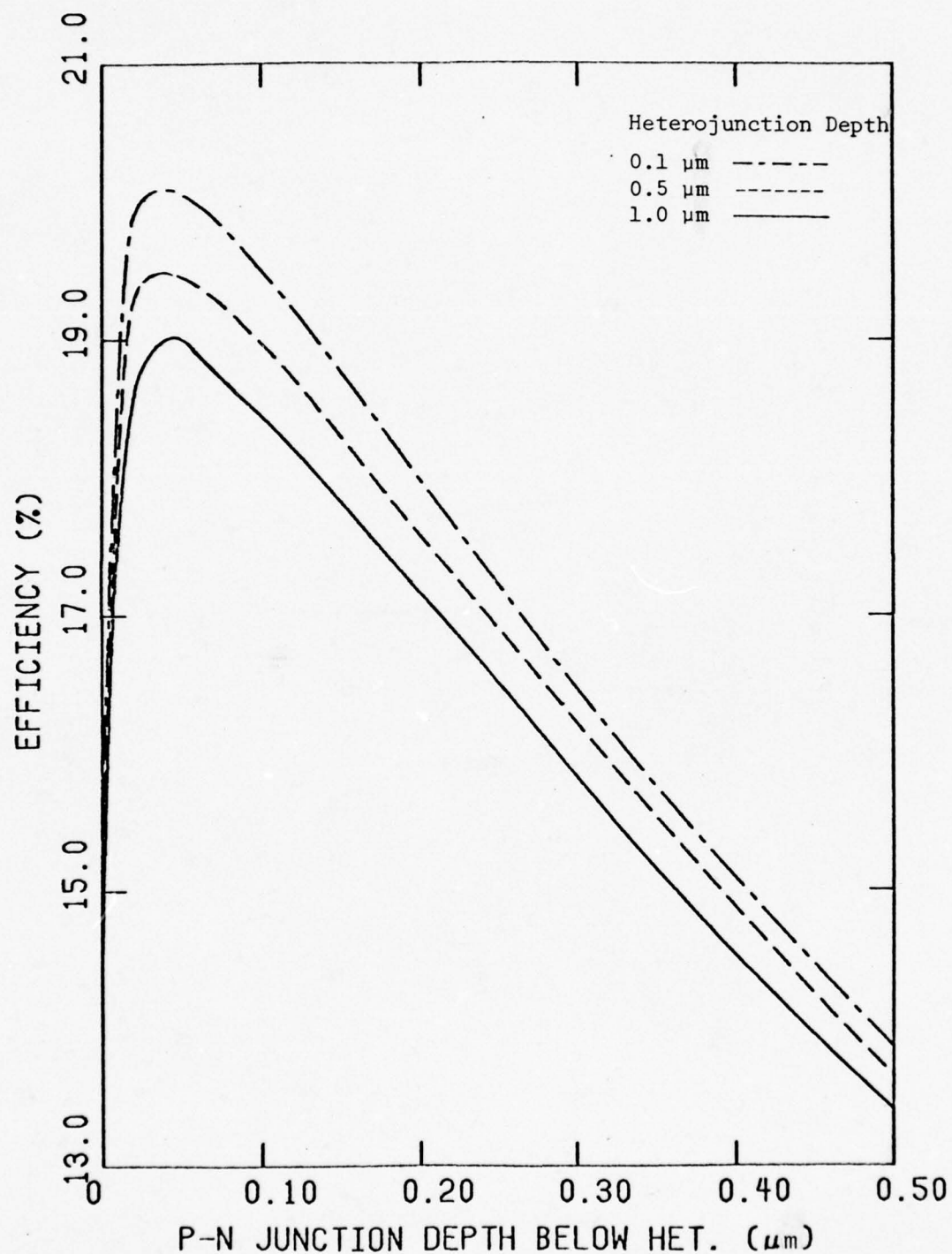
Figure 2.19. Peak efficiency for GaP-GaAs heterojunction cells as a function of p-n junction depth below the heterojunction. Analysis includes interface recombination.

current from these recombination states.  This conclusion is verified in Figure 2.20 which shows the dark current for three GaP-GaAs cells. The lowest current curve is for the p-n junction at the heterojunction but without interface states.  Keeping the junction at the interface and including the interface states results in the largest current curve ($x_J$ = 0).  The interface states result in an increase of about two order of magnitude in dark current.  This is responsible for the decrease in $V_{OC}$ shown in Table 2.3.  Moving the p-n junction only 0.04 µm below the interface is seen to reduce the dark current back almost to its original value.

The rapid decrease in efficiency for junction depths beyond the peak in Figure 2.19 is due to a second physical effect.  This is the loss of short circuit current to the interface states as the p-n junction depth increases.  The large density of interface states acts in much the same way as recombination at the surface of a homojunction solar cell.

It can be concluded from these studies that interface recombination states can severely degrade the performance of heterojunction solar cells.  For large densities of interface states, the heterojunction cell probably offers no advantages over a homojunction solar cell. High efficiency abrupt heterojunction cells can probably be made only in a few selected material combinations such as AlAs-GaAs where the lattice mismatch is small between the two semiconductor materials. The possibility may still exist in devices such as GaP-GaAs of slowly grading the material so that the lattice mismatch states can be spread

41
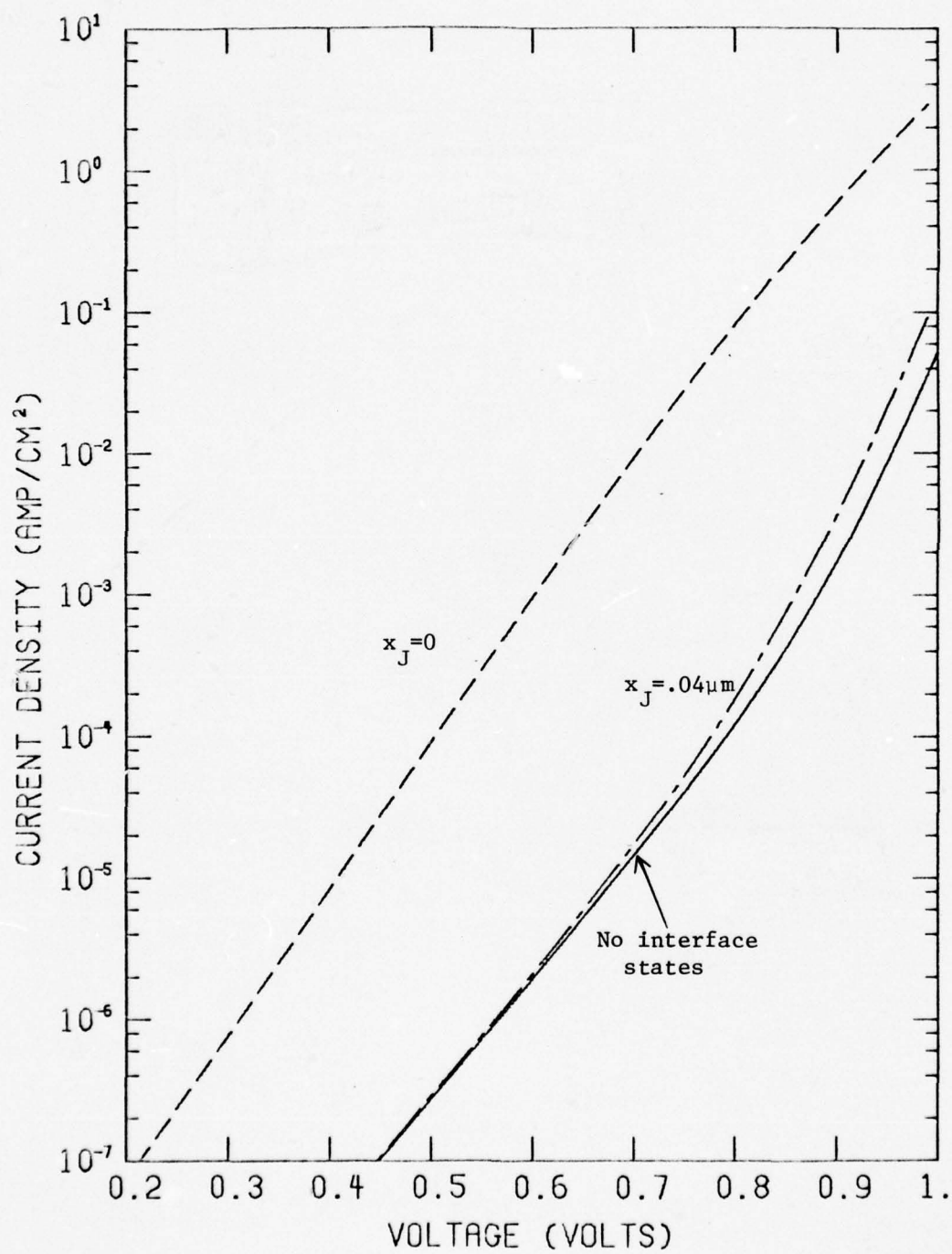
Figure 2.20. Influence of interface states and junction depth on dark current.

Table 2.3. Computer Results for Several $Al_xGa_{1-x}As$ and $GaAs_{1-x}P_x$ Solar Cells

| Device # | Alloy | Comp. Change | Het. Depth (μm) | p-n Depth (μm) | $V_{oc}$ (V) | $J_{sc}$ (mA) | Fill Factor | Peak Eff. (%) | Interface States |
|---|---|---|---|---|---|---|---|---|---|
| 1 | $Al_xGa_{1-x}As$ | abrupt | 1.0 | 1.0 | .998 | 31.40 | .861 | 19.95 | No |
| 2 | $Al_xGa_{1-x}As$ | abrupt | 1.0 | 1.3 | .998 | 31.79 | .862 | 20.21 | Yes |
| 3 | $Al_xGa_{1-x}As$ | abrupt | 0.1 | 0.4 | .999 | 32.83 | .863 | 20.91 | Yes |
| 4 | $GaAs_{1-x}P_x$ | abrupt | 1.0 | 1.0 | .985 | 30.64 | .862 | 19.24 | No |
| 5 | $GaAs_{1-x}P_x$ | abrupt | 1.0 | 1.0 | .831 | 30.64 | .799 | 15.04 | Yes |

over a larger volume and perhaps degrade less the performance. This is considered in more detail in the next section on graded bandgap solar cells.

The results of Figure 2.19 indicate that the detrimental effects of the interface states can be minimized if the p-n junction depth is selected at about 0.04 μm below the heterojunction. The peak efficiency for this junction depth is shown in Figure 2.18 as a function of the thickness of the GaP window material. The results are similar to the AlAs-GaAs cells except that the efficiency is about 1 percentage point lower in value. This solution to the interface problem may not be practical on a production basis because of the critical selection required of p-n junction depth.

In addition to the AlAs-GaAs and GaP-GaAs systems, other materials can be considered for heterojunction cells. Several other such heterojunctions have been considered by Milnes and Feucht [2-17] and by Sneedhor, $\underline{et}$ $\underline{al}$. [2-18]. Of the possible III-V materials, it appears that highest efficiency will be achieved with a base layer of GaAs or some other material with a bandgap close to GaAs such as InP, $Ga_{1-x}In_xAs$, $Al_{1-x}Ga_xAs$ or $GaP_{1-x}As_x$. The ternary III-V materials such as $Ga_{1-x}In_xAs$ and $Al_{1-x}Ga_xAs$ are especially interesting since they make possible the potential of adjusting the bandgap of the base layer for peak efficiency. Calculations for $AlAs-Al_{1-x}Ga_xAs$ heterojunctions have indicated that the efficiency decreases as the Al content of the base layer is increased. The $AlAs-Ga_{1-x}In_xAs$ heterojunction should then be more efficient than pure GaAs for the base layer. This has been verified by calculations. However the increased efficiency appears to

44

be less than 1 percentage point at an In concentration of around
10%. This small increase in efficiency probably does not justify
the development of this type of device considering the additional
fabrication problems of the ternary base layer solar cell.

The temperature performance of heterojunction solar cells has
not been extensively investigated. However the heterojunction cell
can be expected on theoretical grounds to have essentially the same
temperature performance as a homojunction cell made of the base
layer material. When the p-n junction is below the heterojunction
the wide bandgap layer acts mainly as a low surface recombination
boundary for what otherwise looks like a homojunction solar cell.
Even when the p-n junction coincides with the heterojunction, the
dark current which controls to a major extent the temperature performance
is still determined essentially by the properties of the narrow bandgap
material.

In summary the AlAs-GaAs or (Al,Ga)As-GaAs heterojunction cell
is the most highly developed III-V solar cell. The ultimate efficiency
performance does not exceed that of p-n homojunction cells. However
it has so far come much closer to achieving the theoretically predicted
performance because of problems in achieving a low surface recombination
velocity on homojunction cells. The highest efficiency heterojunction
cells require the thinnest window materials which can be partically
achieved and can be said to be approaching the homojunction solar cell
case.

It appears that lattice mismatch interface recombination will be
a real problem in any heterojunction cell which does not have close

45

lattice matching between the layers such as occurs in the AlAs-GaAs cell.
The advantage of the heterojunction cell is eliminated unless the
interface has a low surface recombination velocity (below $10^4$ cm/sec).

A summary of the most promising III-V heterojunction solar cells
is given in Table (2.4). At present none of the other possibilities
appear to offer a real challenge to the AlAs-GaAs solar cell. The
calculated efficiency values given in Table (2.4) are somewhat lower than
the ideal efficiency values of Table (2.1) for homojunction cells.
This results from the more realistic assumptions incorporated into our
calculations for heterojunction cells and is not due to an inherent limitation
in heterojunction efficiency which is not present with homojunction cells.

Table 2.4. III-V Heterojunction Solar Cells

| Material | Ideal Efficiency[*] | Achieved Efficiency | Remarks |
|---|---|---|---|
| (Al,Ga)As-GaAs | 20%-21% | 18.5% | Best cells require compositions close to pure AlAs for the surface layer. Highly developed materials technology. Thin surface layers required. |
| AlAs-GaAs | 20%-21% | ----- | Ideal case of above general cell. Pure AlAs is more difficult to achieve than (Al,Ga)As layers. |
| AlAs-(Al,Ga)As | Below above values | ----- | Theoretical efficiency decreases as band gap of base layer increases. |
| AlAs-(Ga,In)As | 21%-22% | ----- | Slightly higher theoretical efficiency than GaAs base layer for small In compositions in base layer. Difficult to achieve required base layer. |
| GaP-GaAs | 19%-20% | ----- | Interface recombination greatly reduces efficiency unless location of p-n junction is carefully selected. Difficult to achieve efficiency values as high as for AlAs-GaAs. |
| AlAs-InP or GaP-InP | ----- | ----- | Lattice mismatch is large. Similar problems to GaP-GaAs. |

*These efficiencies are theoretical values based upon active area only and including a single layer anti-reflecting film. Low loss (5% or less) antireflecting layers would increase these theoretical values for active area efficiency by 1.5 - 2.0 percentage points.

47

## 2.3  Graded Bandgap Devices

The use of a graded band gap in a solar cell gives an additional degree of freedom in solar cell design which is not present in homojunction or abrupt heterojunction solar cells.  The current density equations for a graded band-gap semiconductor are (see APPENDIX A).

$$J_n = q\mu_n nE_n + q\,D_n \frac{dn}{dp} \quad , \tag{2-29}$$

$$J_p = q\mu_p pE_p - q\,D_p \frac{dp}{dp} \quad , \tag{2-30}$$

where $E_n$ and $E_p$ are the total fields acting on electrons and holes.  Explicit expressions for these are

$$E_n = E - \frac{1}{q} \frac{d\chi_c}{dx} - \frac{kT}{q} \frac{1}{N_c} \frac{dN_c}{dx} \quad , \tag{2-31}$$

$$E_p = E - \frac{1}{q} \frac{d\chi_c}{dx} - \frac{1}{q} \frac{dEg}{dx} + \frac{kT}{q} \frac{1}{N_v} \frac{dN_v}{dx} \quad . \tag{2-32}$$

Contributions to $E_n$ arise from the electric field E, changes in electron affinity $\chi_c$ with position and changes in the condition band density of states $N_c$ with position.  Similar terms occur in $E_p$ with an additional term due to band gap $E_g$ changes with position.

There are at least three basic reasons for considering graded bandgap solar cells.  First, the built-in fields may aid in collecting the generated carriers.  Second, the built-in fields might reduce the dark current (in comparison with homojunction structures) and third, by using a graded as opposed to abrupt transition between a wide bandgap and narrow bandgap region, recombination from the interface recombination states discussed in the previous section may be minimized.  The first two reasons relate to the presence of the built-in field due to the bandgap grading.

48

The most logical use of the graded bandgap layer is in the surface layer to aid in carrier collection from this region. Figure 2.21 shows the energy band diagram near the surface of an (Al,Ga)As graded bandgap cell. This is an exact solution of the energy bands for a device which is linearly graded in composition from pure AlAs at the surface to pure GaAs at 1 $\mu$m where the p-n junction is located. Because the graded bandgap region is doped n-type, almost all of the band gap change occurs at the edge of the valence band. The change in $E_c$ at about 0.6 $\mu$m is due to the transition of (Al,Ga)As from a direct bandgap to an indirect bandgap material and the subsequent change in $N_c$. The valence band edge also shows a change in slope at this point which is also due to the transition from a direct to indirect bandgap material. The effective fields of Eqs. (2-31) and (2-32) in equilibrium are the slopes of the conduction and valence band edges in Figure 2.21. As shown in the figure, the bandgap grading gives a field acting on the minority carriers (holes) forcing them toward the collecting p-n junction. The resulting increased collection efficiency is one of the major reason for considering such graded bandgap cells.

An exact analysis of graded bandgap cells requires a numerical solution because of the nonlinear nature of the equations. However, Figure 2.21, which was obtained from such an analysis, shows that good approximations are possible for the minority carriers. For the linearly graded composition case the field acting on the minority carriers is approximately constant in both the direct and indirect bandgap regions but is much larger in magnitude in the direct bandgap region. Thus a good approximation can be made to the transport equations by assuming a constant field——$E_p$ for example in Eq. (2-30). With other simplifying approximations, as discussed in APPENDIX A, approximate

49
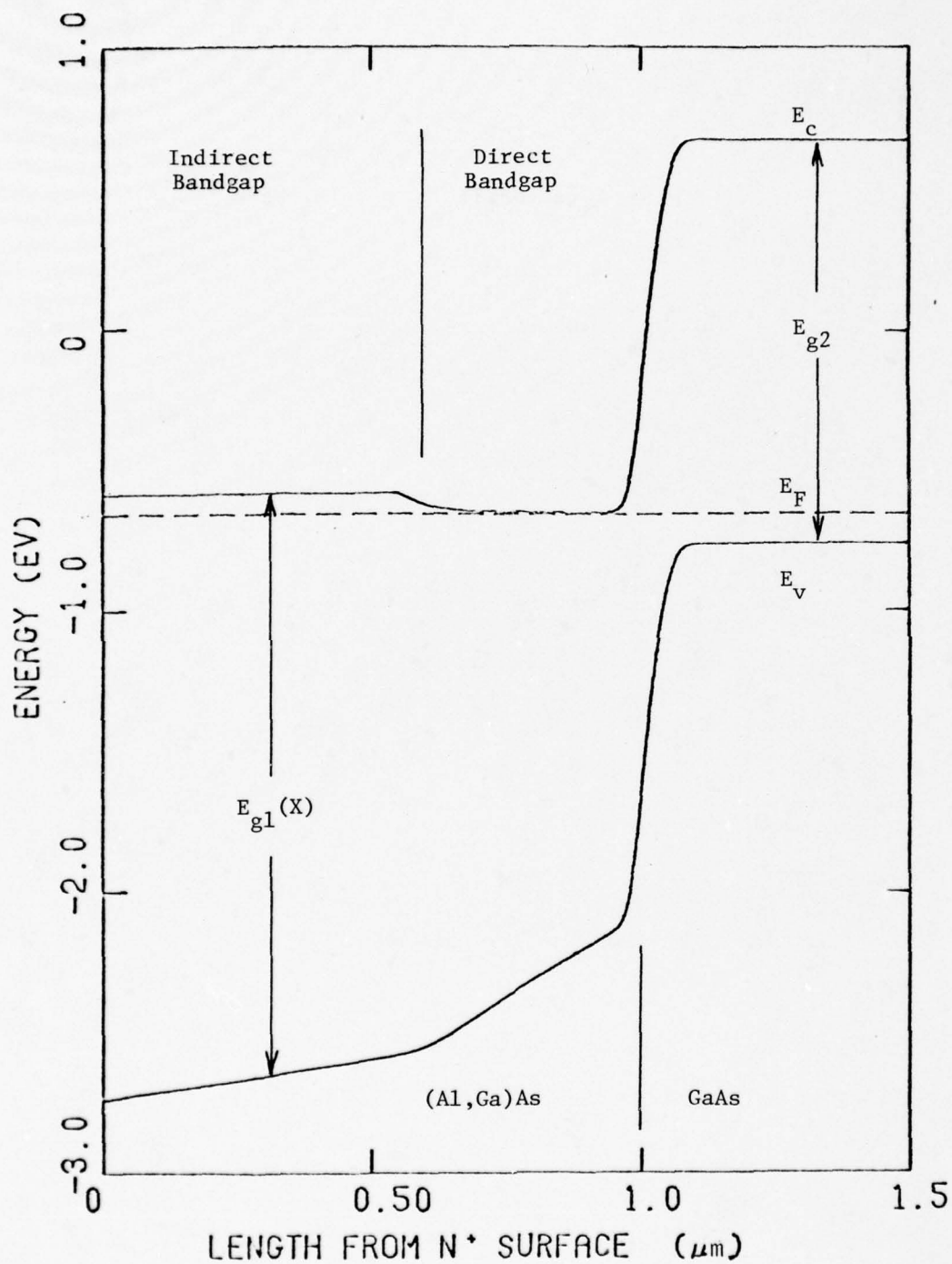
Figure 2.21. Typical energy band structure for a graded bandgap solar cell. AlAs is at the surface, and is graded linearly to GaAs for distances beyond 1 μm.

closed form solutions can be obtained. The details of the resulting
solutions are given in other parts of this report.

Using an approximate analysis as outlined above, Hutchby has studied
the design and performance of graded bandgap n-on-p (Al,Ga)As solar cells
[2-19--2-21]. Shown in Figure 2.22 is the calculated efficiency as a
function of junction depth (and also graded region depth) for various
surface concentrations $(X_{ALO})$ of Al in the (Al,Ga)As graded layer. The
efficiency is seen to be greatly increased at large junction depths by the
graded bandgap as compared with the $X_{ALO} = 0$ curve which is a homojunction
GaAs solar cell. These particular calculations are for doping densities of
$N_A = 2 \times 10^{17}/cm^3$ and $N_D = 4 \times 10^{17}/cm^3$.

The highest curve in Figure 2.22 which is for an Al composition of 35%
at the surface is just below the composition for the direct to indirect band gap
cross-over. The maximum efficiency as a function of Al composition at the
surface is seen in Figure 2.23. It is seen that the efficiency tends to
saturate at around 35% Al and in fact decreases slightly for larger compositions.
From this it can be concluded that the peak efficiency occurs at approximately
the point where the material changes from a direct band gap to an indirect band-
gap material. As previously discussed in connection with Figure 2.21 the field
acting on the minority carriers is small in the direct band gap region and
this small field is responsible for the saturation in efficiency.

The increase in efficiency of the graded band gap cell over the homojunction
cell is largely due to an increase in short circuit current. This is seen
in Figure 2.24 which shows the three terminal parameters for the same conditions
as for Figure 2.23. Very little change is seen in open circuit voltage or
fill factor. However, a very significant increase is seen in short circuit
current due to the increased collection efficiency of the surface layer.
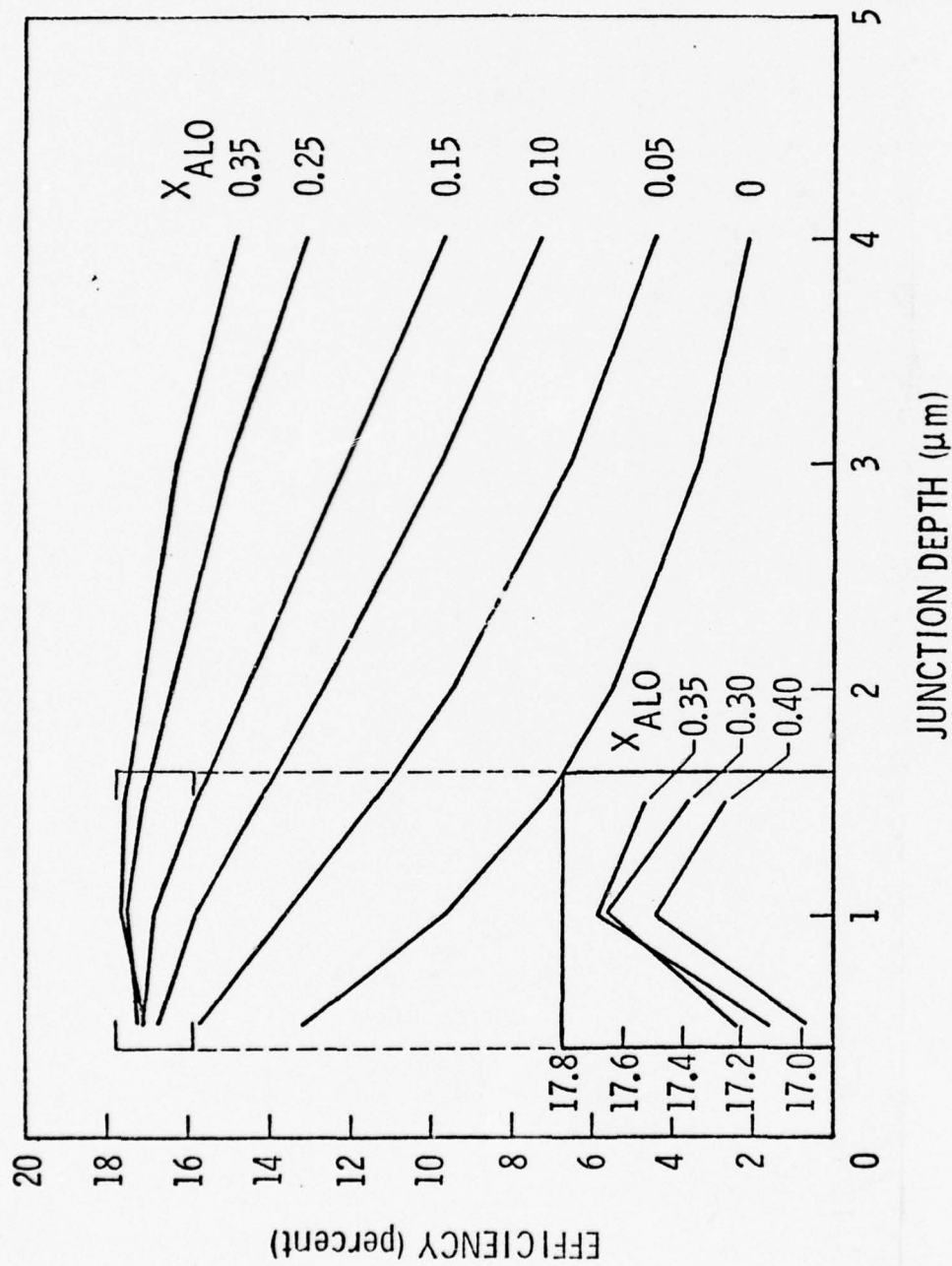
Figure 2.22. Efficiency as a function of junction depth for various surfaces concentrations ($X_{ALO}$) of Al [2-21].
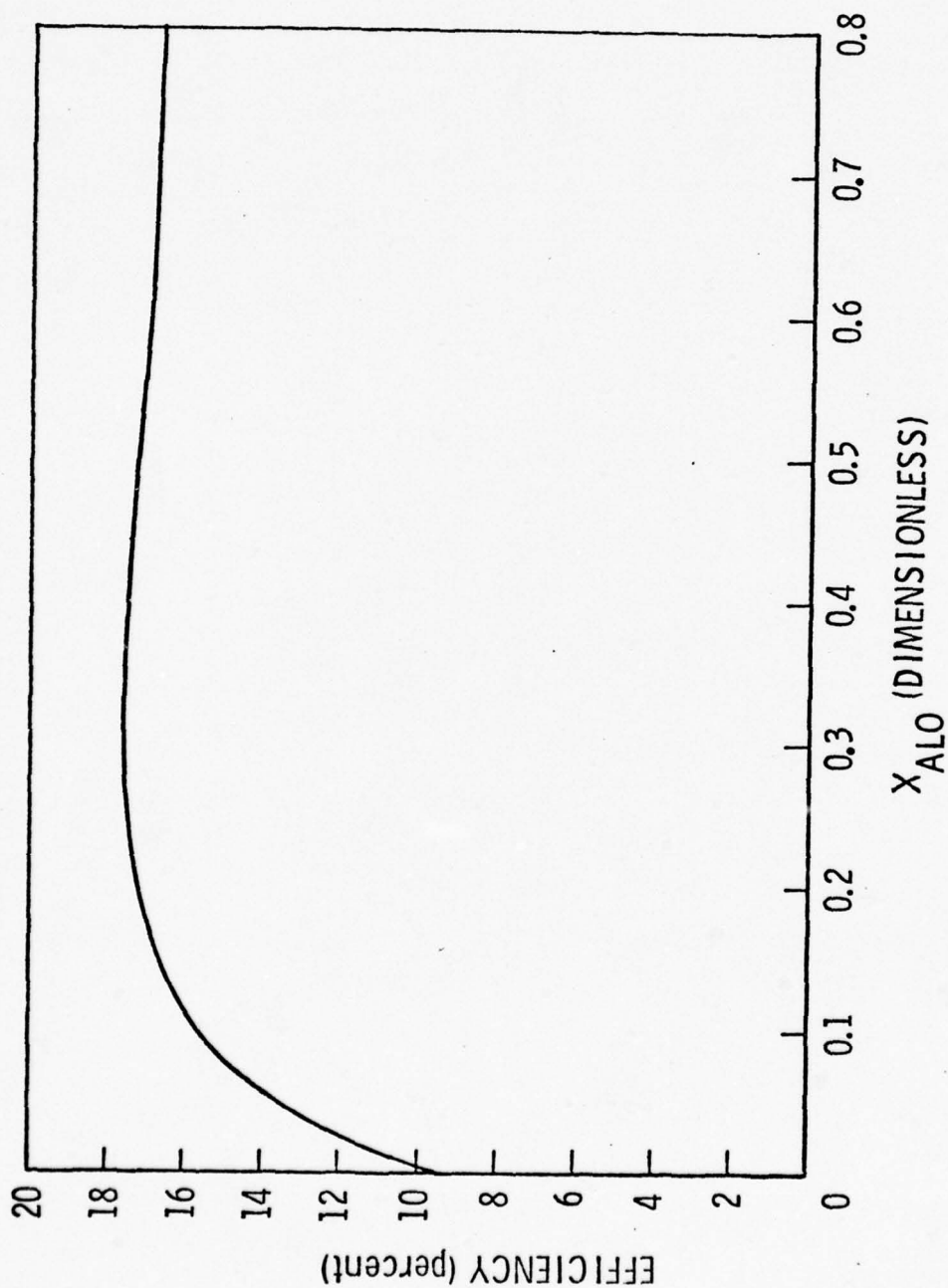
Figure 2.23. Peak calculated efficiency as a function of Al concentration at surface (1.0 equals pure AlAs) [2-20]. 1 μm junction depth (optimum value).

53
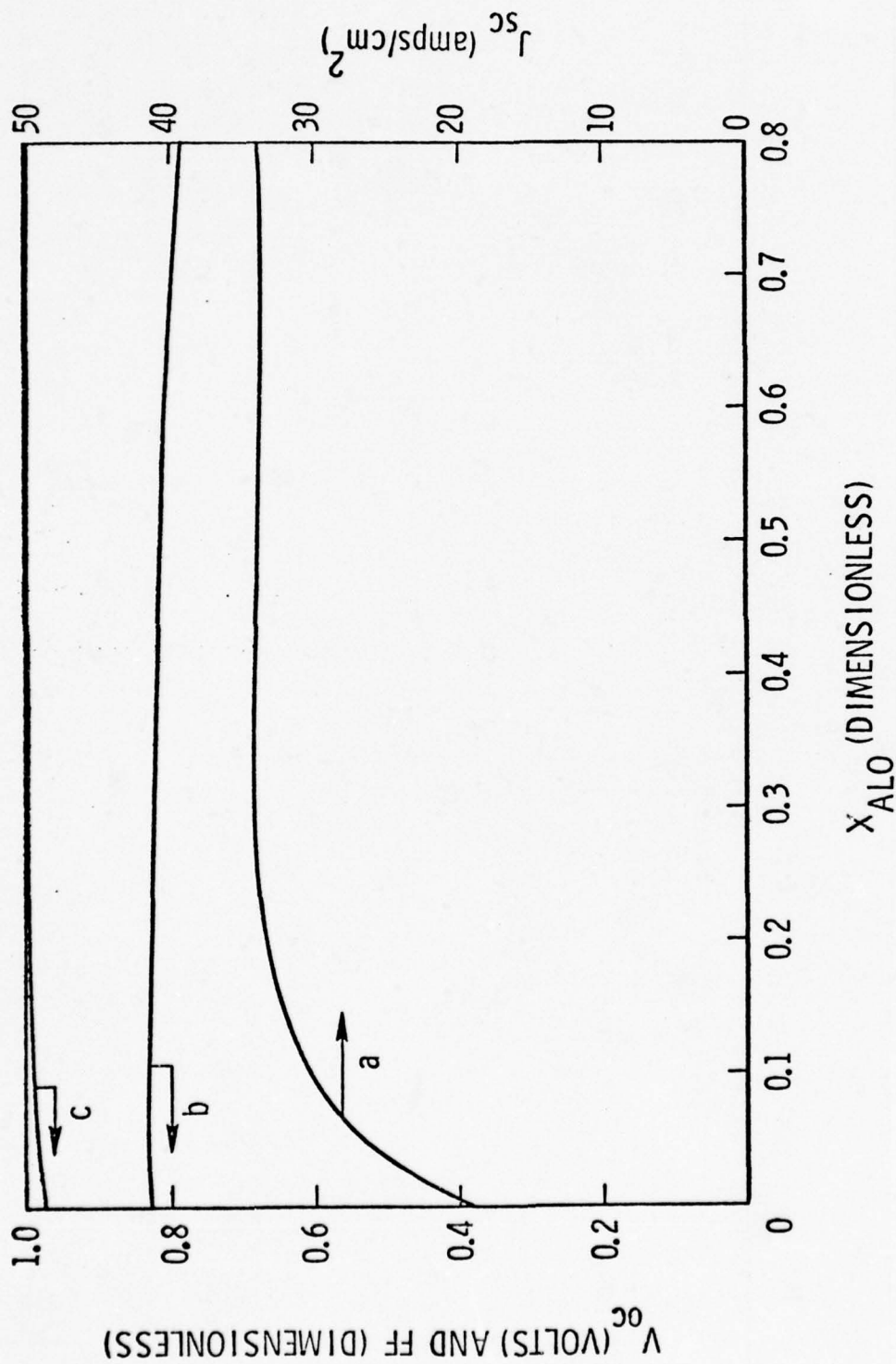
Figure 2.24. Open circuit voltage, short circuit current and fill factor as a function of Al concentration at surface (1.0 equals pure AlAs) [2-20].

54

The effect of impurity doping density on peak efficiency is shown in Figure 2.25. Over the range of $10^{17}/cm^3$ to $10^{18}/cm^3$, the efficiency is not a strong function of doping density. However, optimum doping densities were found to be $4 \times 10^{17}/cm^3$ on the n-side and $2 \times 10^{17}/cm^3$ on the p-side.

Finally the effect of surface recombination velocity on efficiency for different degrees of grading is shown in Figure 2.26. For the homojunction case ($X_{ALO} = 0$) the surface recombination velocity must be below $10^4/cm^3$ if it is not to greatly reduce the efficiency. For the optimum graded bandgap cell ($X_{ALO} > 0.3$), surface recombination velocities of even $10^7$ cm/sec reduce the efficiency only about 10%. The graded bandgap cell has the same desirable features of the abrupt heterojunction cell with regard to surface recombination velocity.

The efficiency values calculated by Hutchby and discussed above can not be directly compared with the heterojunction efficiency values given in the previous section. Hutchby's values have been corrected for series resistance and for ohmic contact stripes. The assumed contact coverage was 13% so the values must be increased by this factor to compare with the values in the previous section. Also the series resistance used by Hutchby has further reduced the efficiency. An 18% efficiency value after correcting for these, corresponds to at least a 20.5% initial efficiency. Thus the graded band-gap efficiency values are very similar in magnitude to the abrupt hetero-junction values.

An analysis of the efficiency of graded bandgap cells has also been made using the detailed numerical analysis outlined in APPENDIX A. This is a more accurate analysis than that of Hutchby but the results are very similar. Table 2.5 shows a comparison of the calculated performance of graded bandgap

55
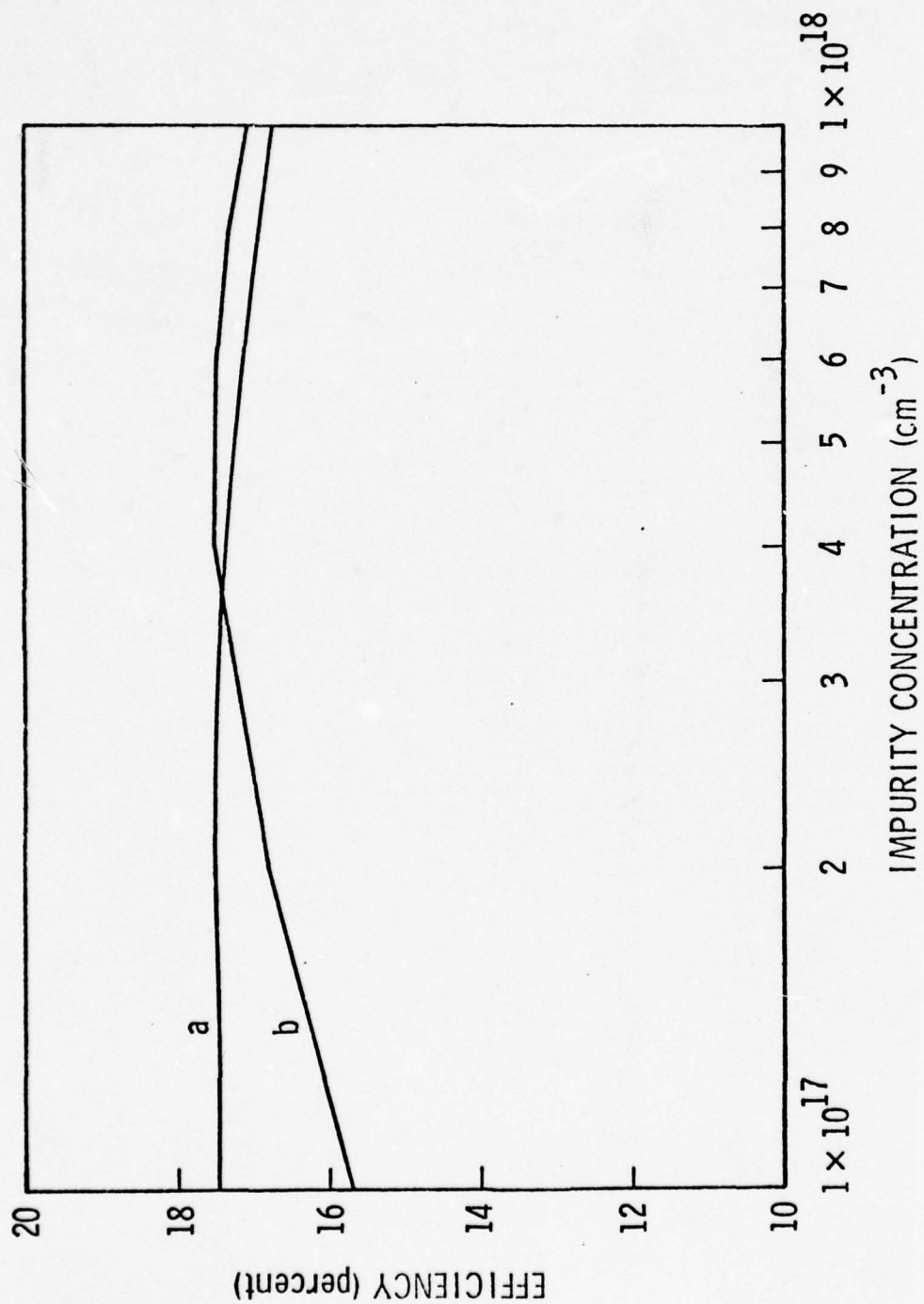
Figure 2.25. Efficiency as a function of impurity concentration. 30% Al concentration at surface and 1 µm junction depth. (a) $N_A$ variable, $N_D = 4 \times 10^{17}/cm^3$ (b) $N_D$ variable, $N_A = 2 \times 10^{17}/cm^3$ [2-21].

56
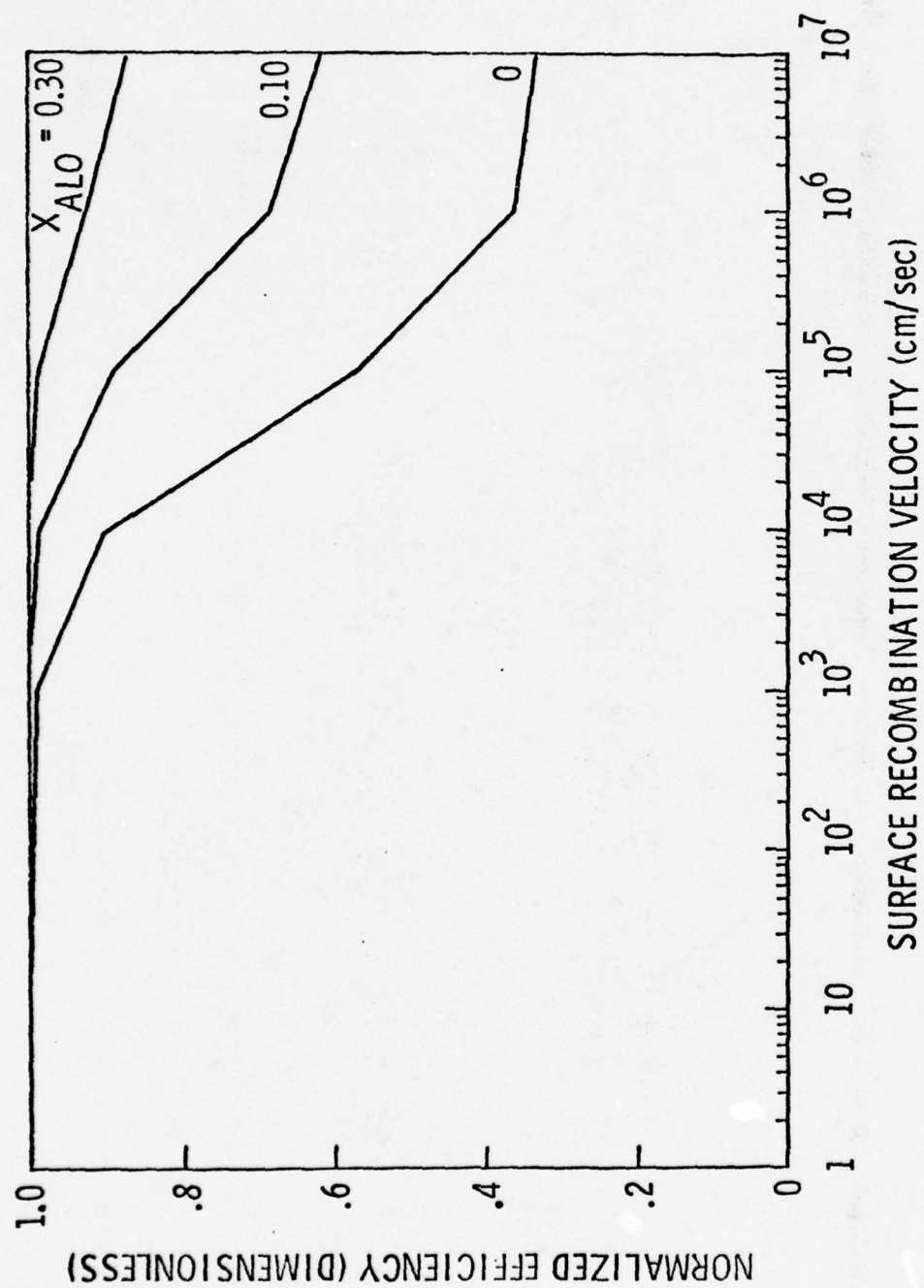
Figure 2.26. Normalized efficiency as a function of surface recombination velocity [2-21]. Junction depth at 1 μm.

(Al,Ga)As-GaAs and abrupt heterojunction solar cells. Device No. 1 is for 35% Al composition at the surface while devices No. 2 and 3 are for 100% Al composition at the surface. Devices No. 4 and 5 give results for abrupt AlAs-GaAs solar cells for comparison. First it is seen that the graded band-gap cells have slightly larger short circuit currents as expected from the built-in fields. The largest efficiency of 20.75% occurred for a grading to pure AlAs at the surface and is 0.8 of a percentage point larger in efficiency than a similar heterojunction device [(No. 4 of Table 2.5)].

These results discussed above are for (Al,Ga)As solar cells where lattice mismatch interface recombination is relatively unimportant. For other solar cells such as Ga(P,As) it may be argued that a graded bandgap region rather than an abrupt heterojunction can be used to greatly reduce the effect of the lattice mismatch states. To study this effect, a series of calculations have been made on Ga(P,As) solar cells. The devices studied have a p-n junction located at 0.1 μm from the surface and a constant GaP region near the surface. Between these constant bandgap regions is a linearly graded composition region of varying width, with the width varying from zero to the complete surface layer width of 0.1 μm. The calculations include lattice mismatch recombination states which are assumed to be uniformly distributed throughout the graded layer. The resulting efficiency values as a function of the width of the graded layer are shown in Figure 2.27. The results show that the use of a graded layer does in fact lead to an increased efficiency. However, the peak efficiency is still lower than that which could be achieved without the interface recombination series.

From the studies which have been made here and elsewhere on graded band-gap solar cells, it can be expected that such cells can have slightly larger efficiency values than abrupt heterojunction cells of similar material

58

Table 2.5. Comparison of Graded Band Gap $(Al,Ga)As-GaAs$ and $AlAs-GaAs$ Abrupt Heterojunction Solar Cells

| Device # | Alloy | Comp. Change | Het. Depth (μm) | p-n Depth (μm) | $V_{oc}$ (V) | $J_{sc}$ (mA/cm$^2$) | Fill Factor | Peak Eff. (%) | S cm/sec | Interface States |
|---|---|---|---|---|---|---|---|---|---|---|
| 1 | $Al_xGa_{1-x}As$ | linear (to 35% AlAs) | 1.0 | 1.0 | .999 | 32.07 | .864 | 20.46 | $10^5$ | No |
| 2 | $Al_xGa_{1-x}As$ | linear | 1.0 | 1.0 | .999 | 32.55 | .863 | 20.75 | $10^5$ | No |
| 3 | $Al_xGa_{1-x}As$ | linear | 1.0 | 1.5 | .998 | 32.37 | .863 | 20.60 | $10^5$ | No |
| 4 | $Al_xGa_{1-x}As$ | abrupt | 1.0 | 1.0 | .998 | 31.40 | .861 | 19.95 | $10^5$ | No |
| 5 | $Al_xGa_{1-x}As$ | abrupt | 1.0 | 1.3 | .998 | 31.79 | .862 | 20.21 | $10^5$ | No |

59
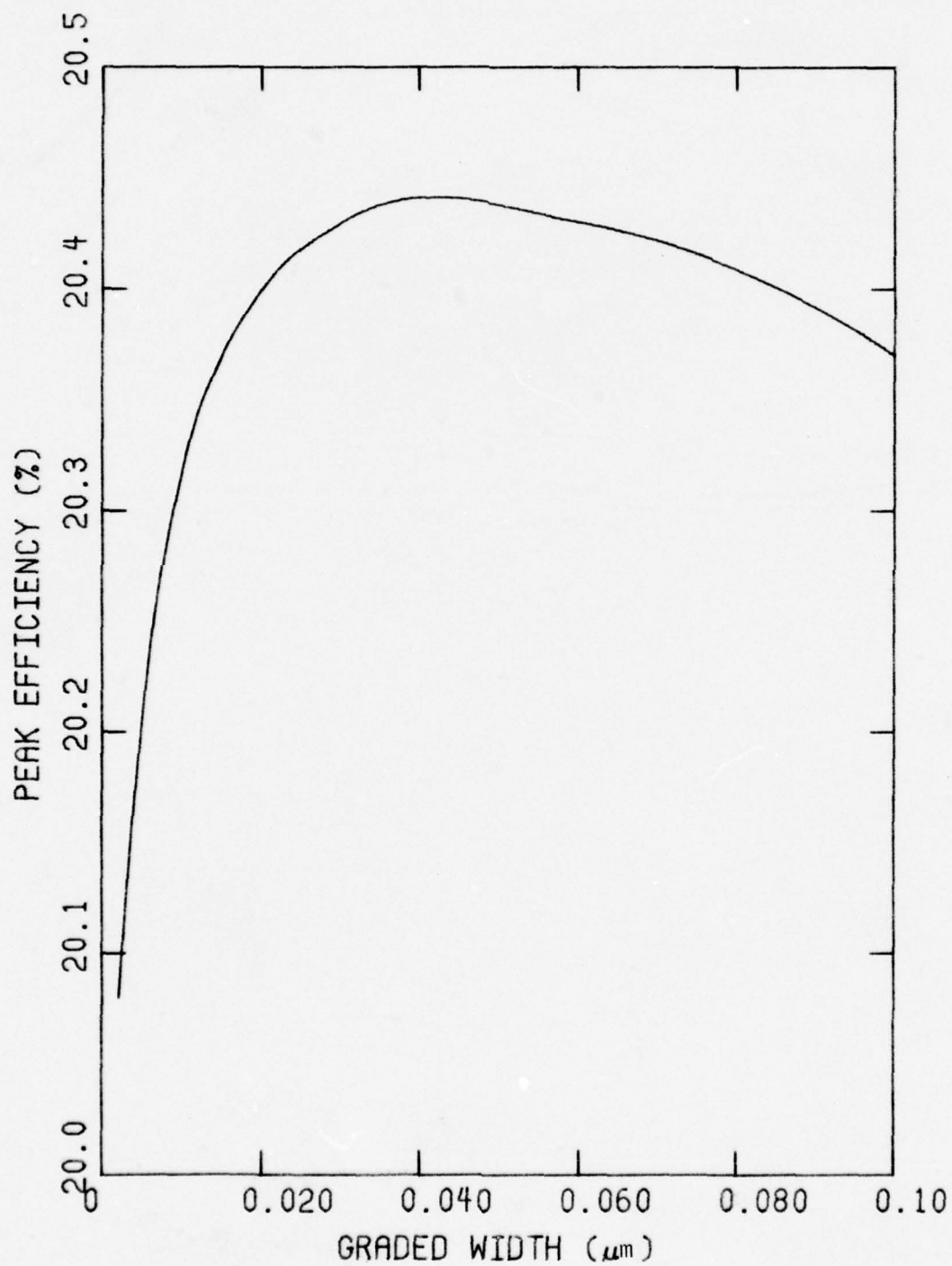
Figure 2.27. Efficiency as a function of graded region width for a GaP-GaAs solar cell. Width of window region (including graded and GaP region) is 0.1 μm.

60

compositions. These improvements result basically from an increase in carrier collection efficiency of the surface layer. However, the predicted improvements are typically less than one percentage point in overall efficiency. These improvements must be weighed against the increased difficulty of fabricating such solar cells.

REFERENCES

2-1.    P. Rappaport, "The Photovoltaic Effect and its Utilization", RCA Rev.
        20, Sept. 1959, pp. 373-397.

2-2.    A good collection of the early papers on solar cells can be found in
        Solar Cells, Edited by C. E. Backus, IEEE Press, 1976.

2-3.    M. B. Prince, "Silicon Solar Energy Converters", J. Appl. Phys. 26,
        May 1955, pp. 534-540.

2-4.    J J. Loferski, "Photovoltaic Solar Energy Conversion", J. Appl. Phys.
        27, July 1956, pp. 777-784.

2-5.    J. J. Wysocki and P. Rappaport, "Effect of Temperature on Photovoltaic
        Solar Energy Conversion", J. Appl. Phys., 31, March 1960, pp. 571-578.

2-6.    S. C. Tsaur, A. G. Milnes, R. Sahai and D. L. Feucht, "Theoretical and
        Experimental Results for GaAs Solar Cells", Gallium Arsenide and Related
        Compounds, 1972, The Institute of Physics, London, England, 1973.

2-7.    H. J. Hovel, Solar Cells, Vol. II in Semiconductors and Semimetals, Edited
        by R. K. Willardson and A. C. Beer, Academic Press, 1975.

2-8.    J. J. Wysocki, "Radiation Properties of GaAs and Si Solar Cells", J. Appl.
        Phys. 34, September 1963, pp. 2915-2917.

2-9.    J. M. Woodall and H. J. Hovel, "High-Efficiency $Ga_{1-x}Al_xAs$-GaAs Solar
        Cells", Appl. Phys. Lett. 21, October 15, 1972,
        pp. 379-381.

2-10.   H. J. Hovel and J. M. Woodall, "$Ga_{1-x}Al_xAs$-GaAs p-p-n Heterojunction
        Solar Cells", J. Electrochem. Soc. 120, September 1973, pp. 1246-1252.

2-11.   H. J. Hovel and J. M. Woodall, "Enhanced GaAs Solar Cells with Very
        Thin Junctions", 12th IEEE Photovoltaic Spec. Conf., Baton Rouge, La.,
        Nov. 15-18, 1976.

2-12.   A. G. Milnes, Deep Impurities in Semiconductors, John Wiley and Sons,
        New York, 1973.

2-13.   M. Ettenburg and H. Kressel, "Interfacial Recombination at (AlGa)As/GaAs
        Heterojunction Structures", J. Appl. Phys. 47, April 1976, pp. 1538-1544.

2-14.   W. D. Johnston, Jr. and W. M. Callahan, "VPE Growth of n-AlAs on GaAs
        for Heterojunction Devices", J. Electrochem. Soc. 123, 1976, pp. 1524-1531.

2-15.   W. D. Johnston, Jr. and W. M. Callahan, "Vapor-Phase-Epitaxial Growth,
        Processing, and Performance of AlAs-GaAs Heterojunction Solar Cells",
        12th IEEE Photovoltaic Spec. Conf., Baton Rouge, La., Nov. 15-18, 1976.

2-16.   J. E. Sutherland and J. R. Hauser, "Computer Analysis of Heterojunction
        and Graded Band Gap Solar Cells", 12th IEEE Photovoltaic Spec. Conf.,
        Baton Rouge, La., Nov. 15-18, 1976.

2-17. A. G. Milnes and D. L. Feucht, Heterojunctions and Metal - Semiconductor Junctions, Academic Press, 1972.

2-18. A. K. Sneedhor, B. L. Sharma and R. K. Purohit, "Efficiency Calculations of Heterojunction Solar Energy Converters", IEEE Trans. on ED, ED-16, March 1969, pp. 309-312.

2-19. J. A. Hutchby, "High Efficiency Graded Band Gap $Al_xGa_{1-x}As$-GaAs Solar Cell", Appl. Phys. Lett. 26, April 15, 1975, pp. 454-458.

2-20. J. A. Hutchby and R. L. Fudurich, "Theoretical Analysis of $Al_xGa_{1-x}As$-GaAs Graded Band Gap Solar Cells", J. Appl. Phys., 47, July 1976, pp. 3140-3151.

2-21. J. A. Hutchby and R. L. Fudurich, "Theoretical Optimization and Parametric Study of n- on -p $Al_xGa_{1-x}As$-GaAs Graded Band Gap Solar Cell", J. Appl. Phys., 47, July 1976, pp. 3152-3158.

3.0  SCHOTTKY BARRIER AND METAL-INSULATOR-SEMICONDUCTOR SOLAR CELL STRUCTURES

3.1  Schottky Barrier

3.1.1  Introduction

The metal-semiconductor or Schottky barrier solar cell has received attention primarily becuase of the relative simplicity of the structure compared to other fabricational techniques [3-1].  In addition, when interfacial layers are introduced between the metal and semiconductor, increased conversion efficiencies are feasible due to a variety of physical mechanisms [3-2, 3-3].

Physical modeling of the characteristics of Schottky barrier solar cells has included first order limit calculations [3-4], more detailed closed-form analytical solutions [3-1], and even more detailed computer-generated solutions of the transport equations [3-5].  Other investigators have contributed to the literature on physical modeling, treating specific physical effects and including other aspects of importance in the overall cell performance [3-6, 3-7].

In general, the approach in discussing the results of these physical models has been either to present the calculations for specific materials such as silicon or gallium arsenide, or to discuss the results in terms of general fundamental material parameters, such as energy bandgap or Schottky barrier height.  The latter approach usually assumes unity internal collection efficiency for energies above the bandgap; this eliminates the need for a knowledge of material parameters which influence the photocurrent.  These calculations have been used to establish upper limits to conversion efficiency of Schottky barrier solar cells for the general class of semiconductor materials, and to examine performance characteristics of specific materials with known energy bandgaps and barrier heights.

64

The importance of energy bandgap and barrier height in determining the performance of Schottky barrier solar cells is well known and verified [3-1 to 3-7]. The ternary alloys of the binary III-V semiconductor compounds provide the means for continuously adjusting the energy bandgap and barrier height in order to optimize this performance. For example, Yeh and Stirn [3-3] have reported a 20% improvement in cell conversion efficiency for the ternary $GaP_{.22}As_{.78}$ as compared to GaAs. At the same time, recent theoretical treatments [3-8, 3-9] provide a means whereby the important material parameters of the ternary alloys can be calculated from a knowledge of material parameters for the binary constituents. Thus, unity internal collection efficiency is not a necessary assumption. In addition, experimental data for barrier heights in ternary alloy systems of interest for Schottky barrier solar cells have been reported [3-10], and this is a subject of specific interest for many other device applications.

This section discusses Schottky barrier solar cell calculations for the $GaP_xAs_{1-x}$, $Ga_{1-x}Al_xAs$, $Ga_{1-x}In_xAs$, and $GaAs_{1-x}Sb_x$ ternary alloy systems. The device modeling approach used is similar to that discussed by Hovel [3-1], whereby an analytical transport model which takes into account important material properties is used to calculate the photocurrent. Experimental data for the energy bandgaps as a function of alloy composition x are used. Theoretical models are used to calculate the compositional dependence of other important material parameters in terms of known experimental parameters for the binary consituents, with special attention being given to the absorption coefficient. Both experimental and empirical values of the barrier height are used in the calculations. An attempt has been made to accurately

65

describe the compositional dependence of all significant material parameters
which determine cell performance, and to include these material parameter
variations in a device model which gives reasonable performance characteristics
for cells using materials with accurately known parameters (such as silicon
and gallium arsenide).

3.1.2 Device Model

A brief summary of the device equations used in the calculations
will be given [3-1]. The voltage-current characteristic for the solar cell
is given by

$$J_T (V_a) = J_o(V_a) - J_{sc} \qquad (3-1)$$

where

$J_T(V_a)$ = the terminal current density as a function of
applied voltage

$J_{sc}$ = the short circuit ($V_a=0$) photocurrent density
due to the solar spectrum

$J_D(V_a)$ = the dark current density as a function of
applied voltage

The photocurrent density $J_{sc}$ is composed of two integrated terms through the
relation

$$J_{sc} = \int_0^\infty \left[ J_{DR}(\lambda) + J_p(\lambda) \right] d\lambda \qquad (3-2)$$

where $\lambda$ = optical wavelength, and

$J_{DR}(\lambda)$ = Depletion region photocurrent density per unit
optical band width

$J_p(\lambda)$ = Minority carrier (hole) photocurrent density
per unit optical band width

66

Here an n-type semiconductor has been assumed for convenience.

The dark current density is taken to be composed of three terms as follows:

$$J_D = J_{SB} + J_R + J_{Diff} \qquad (3\text{-}3)$$

where

$J_{SB}$ = Schottky barrier current density

$J_R$ = Recombination current density integrated over the depletion region

$J_{Diff}$ = Minority carrier (hole) current density at the depletion region-quasi neutral semiconductor boundary

The only difference between the model given by Eqn. (3-1) and that used in Hovel's calculations [3-1] is the term involving $J_R$ included in the dark current. Usually $J_{SB} + J_{Dif} \gg J_R$ and this term can be neglected. However, in this work the term was included because its importance is not readily ascertainable when the complicated compositional dependence of the ternary material parameters is considered.

The dependence on material parameters of each of the terms in Eqns. (3-1) and (3-3) is presented in APPENDIX C.

These device equations are used along with the standard equation

$$\eta = \frac{P_o}{P_{in}} = \frac{V_a J_T(V_a)}{P_{in}} \qquad (3\text{-}4)$$

to calculate the cell conversion efficiency, $\eta$. The fill factor, F.F. is also calculated from

$$F.F. = \frac{P_{max}}{V_{oc} J_{sc}} \qquad (3\text{-}5)$$

67

where $P_{max}$ is the maximum output power, $V_{oc}$ is the open-circuit voltage, and $J_{sc}$ is the short-circuit current density. The input power, $P_{in}$, is based on both the AMO spectral conditions. The optical generation rate used in the device equations for calculating $J_{DR}(\lambda)$ and $J_p(\lambda)$ is based on the calculations presented by Sutherland and Hauser [3-11].

### 3.1.3 Material Parameters

The following list shows the parameters identified from the device models which are needed for the solar cell calculations.

| | |
|---|---|
| $D_p$ | minority carrier diffusion constant |
| $P_o$ | equilibrium minority carrier concentration |
| $L_p$ | minority carrier diffusion length |
| $W_n$ | depletion region width |
| $N_D$ | majority carrier doping concentration |
| $A^{**}$ | Schottky barrier effective Richardson constant |
| $\emptyset_B$ | Schottky barrier energy |
| $n_i$ | intrinsic carrier concentration |
| $\tau_p$ | minority carrier lifetime |
| $\tau_{po}, \tau_{no}$ | Shockley-Read recombination model lifetimes |
| $E_t$ | Shockley-Read recombination center energy level |
| $\alpha$ | photon absorption coefficient |
| $S$ | back surface recombination velocity |
| $W$ | total cell length |

All of these parameters are required to be known as a function of alloy composition, and the relations which describe this dependence are given in APPENDIX B.

68

The diffusion constant is calculated from the mobility by using the Einstein relation $D_p = \frac{kT}{q} \mu_p$. The diffusion length is then calculated from $L_p = \sqrt{D_p \tau_p}$. The dependence of hole mobility on doping level and alloy composition is described in APPENDIX B. The depletion layer width is calculated from the equation

$$W_n = \sqrt{\frac{2 \varepsilon_r \varepsilon_o}{q \, N_D} \left( V_D - V_a - \frac{kT}{q} \right)} , \qquad (3\text{-}6)$$

where $V_D$ is the diffusion potential, given by

$$V_D = \frac{E_G}{q} - \frac{kT}{q} \ln \left( \frac{N_c}{N_D} \right) , \qquad (3\text{-}7)$$

where $E_G$ is the band gap and $N_c$ is the conduction band density-of-states. The minority carrier density is calculated from $P_o = n_i^2 / N_D$ , where the intrinsic concentration, $n_i$, is given by

$$n_i^2 = N_c N_v \exp \left( -E_G / kT \right) . \qquad (3\text{-}8)$$

Here $N_v$ is the valence band density-of-states. Most of these parameters are used in the more detailed computer calculations described in this report, and these are discussed in more detail in these sections, and in APPENDIX B. It should also be mentioned that the absorption coefficient versus wavelength data used in these calculations was obtained by the method of Sutherland and Hauser [3-10].

3.1.4 Results

The purpose of this study was to examine the performance of Schottky barrier solar cells in ternary III-V alloys to see if improved performance could be achieved compared with the performance of GaAs. In this study,

69

four materials were examined. These materials were $GaP_xAs_{1-x}$, $Ga_{1-x}Al_xAs$, $Ga_{1-x}In_xAs$ and $GaAs_{1-x}Sb_x$. Of these four, $GaP_xAs_{1-x}$ and $Ga_{1-x}Al_xAs$ have bandgaps which are greater than that for GaAs (1.439 eV) as x increases, while $Ga_{1-x}In_xAs$ and $GaAs_{1-x}Sb_x$ have bandgaps which are smaller than that for GaAs as x increases.

In order to check the computational technique, a detailed study of the GaAs system was made so that comparison with previous calculations [3-1] could be made. The results of this study are summarized in Table 3-1.

The standard material parameters used for GaAs are listed in Table 3-2. Any deviation from these is listed as a footnote in Table 3-1. The influence of all material parameters was studied, and if no changes in the parameters are indicated in Table 3-1, then there were no changes in cell performance due to these parameters. The AMO conversion efficiencies are in good agreement with those calculated by other authors [3-1 to 3-3]. It should be noted that the transmission coefficient data used in these calculations is representation of that for thin gold films [3-6], and the barrier heights are typical of that for gold on GaAs (0.898 eV) [3-1 to 3-3].

In beginning the calculations, very little experimental data on metal-semiconductor barrier heights was found. Thus, calculations were first made using the emperical relation $\phi_B = \frac{2}{3} E_G$ [3-12]. Figure 3.1 shows the results of these calculations for $GaP_xAs_{1-x}$. It can be seen that as temperature increases the conversion efficiency decreases for a given alloy of composition x. Also, for a given cell temperature, the composition for maximum conversion efficiency increases the higher the cell temperature. At 300K, the maximum efficiency is $n_{max} = 11.92\%$ for x = 0.2, compared to the 300K conversion efficiency of 11.66% for GaAs. This is far below the 20% improvement

70

Table 3.1.  Summary of Schottky Barrier Solar Cell Performance for GaAs

| $\phi_B$(eV) | $n_{max}$(AMO) | $J_{sc}$(ma/cm$^2$) | $V_{oc}$($V_oH_s$) | F.F. |
|---|---|---|---|---|
| 0.898 | 10.0 | 36.96 | 0.463 | 0.791 |
| 0.898 | 9.96[a] | 36.94 | 0.462 | 0.792 |
| 0.898 | 9.93[b] | 36.70 | 0.462 | 0.792 |
| 0.898 | 9.57[c] | 35.47 | 0.461 | 0.792 |
| 0.898 | 10.36[d] | 35.84 | 0.463 | 0.793 |
| 0.800 | 7.51 | 36.96 | 0.364 | 0.756 |
| 1.00 | 12.63 | 39.96 | 0.565 | 0.818 |
| 1.00 | 10.24[e] | 37.06 | 0.483 | 0.774 |
| 0.898 | 7.67[f] | 37.06 | 0.381 | 0.735 |
| 0.959($\frac{2}{3}$ E$_G$) | 11.66 | 36.97 | 0.530 | 0.810 |
| 0.959 | 10.13[g] | 32.36 | 0.523 | 0.812 |
| 0.959 | 13.38[h] | 23.79 | 0.516 | 0.806 |
| 0.898 | 8.66[i] | 32.30 | 0.459 | 0.791 |
| 0.959 | 4.93[j] | 16.40 | 0.506 | 0.804 |
| 0.898 | 11.62[k] | 369.73 | 0.525 | 0.810 |
|  |  | 16.40 | 0.444 | 0.787 |

a.  W = 10 μm      e.  T = 350K      i.  $\tau_p$ = 10$^{-10}$sec

b.  W = 5 μm       f.  T = 350K      j.  $T_R$ = $T_R(\lambda)$

c.  $N_D$ = 10$^{17}$cm$^{-3}$   g.  $\tau_{no}$=$\tau_{po}$=$\tau_p$=10$^{-10}$sec   k.  Concentration Ratio = 10

d.  $N_D$ = 10$^{15}$cm$^{-3}$   h.  AM2 spectral conditions   l.  $T_R$ = $T_R(\lambda)$

$T_R(\lambda)$ is the experimentally measured transmission coefficient for thin Au films.

71

Table 3.2. Standard GaAs Material Parameters Used in Calculations

| | | |
|---|---|---|
| $A^{**}$ = 7.63 amps/cm$^2$ K$^2$ | $T$ = 300K | $\tau_{po}$ = 8.5 x 10$^{-9}$ [3-11] |
| $E_G$ = 1.439 eV | $N_D$ = 10$^{16}$ cm$^{-3}$ | $\tau_{no}$ = 5.3 x ? c [3-11] |
| $m_n^*$ = 0.0636 m$_o$ | $S$ = 10$^6$ cm/sec | $E_T - E_i$ = 0.7 eV |
| $m_p^*$ = 0.68 m$_o$ | $W$ = 100 μm | $D_p$ = 9.13 cm$^2$/sec |
| $\varepsilon_r$ = 13.2 | $\tau_p$ = 10$^{-8}$ sec | $n_i$ = 1.95 x 10$^6$ cm$^{-3}$ |

72
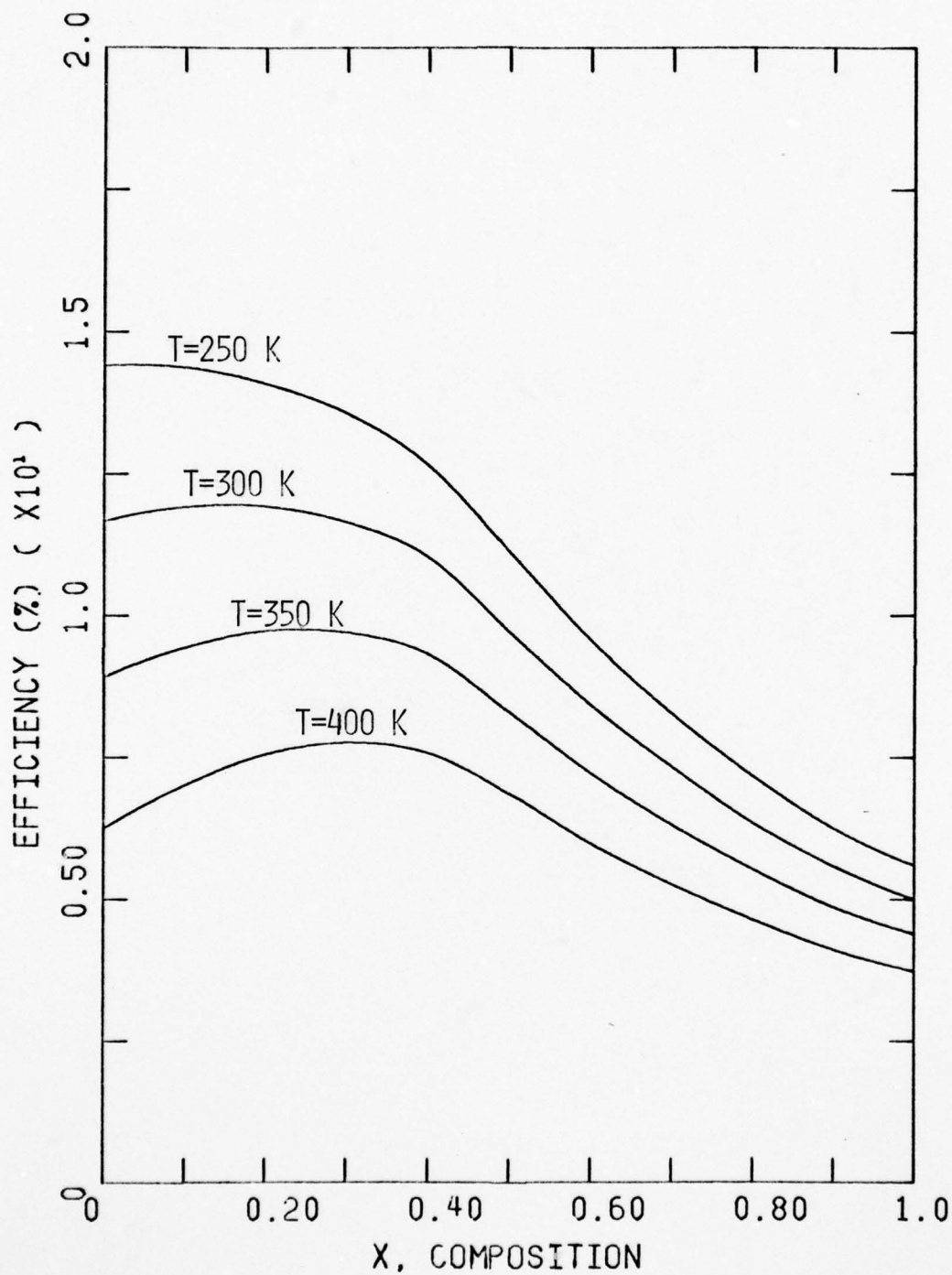
Figure 3.1. AMO conversion efficiency for $GaAs_{1-x}P_x$ Schottky Barrier solar cells as a function of alloy composition X for $\emptyset = \frac{2}{3} E_G$ and concentration ratio = 1.

73

experimentally determined for GaP$_{.22}$As$_{.78}$ [3-3]. These calculations have all assumed unity transmission coefficient.

Recent experimental measurements of barrier heights for Au Schottky barriers on GaP$_x$As$_{1-x}$ show that instead of $\phi_B = \frac{2}{3} E_G$ the data is best fit by the expression $\phi_B = E_G - 0.55$ eV [3-10]. The cell conversion efficiencies were calculated using this relation and the results are shown in Figure 3.2. In this case, the trends are still the same, although the maximum efficiency as a function of composition is much more pronounced. Here, the efficiency at room temperature for GaP$_{.22}$As$_{.78}$ is 12.16% while that for GaAs is 9.85%. Thus, the model predicts a 23% improvement in cell efficiency. The quoted experimental values of AMO conversion efficiencies given by Stern and Yeh [3-3] are 10% for GaAs and 12% for GaP$_{.22}$As$_{.78}$, or an improvement of 20%. The calculations predict a maximum conversion efficiency of 12.6% for $x \simeq 0.3$.

Figure 3.3 shows a plot of the energy bands (both direct and indirect bands) as a function of composition, along with values for the barrier heights according to the two relations used to calculate the conversion efficiencies in Figures 3.1 and 3.2. Also shown are some experimental values for the barrier height. The experimental values are not in good agreement for the P-rich ternary with $x > 0.5$.

Tables 3.3 and 3.4 summarize the results of the calculations for both GaP$_x$As$_{1-x}$ and Ga$_{1-x}$Al$_x$As ternary alloys as both temperature and solar concentration ratio is varied. As concentration ratio is increased the value of x for maximum efficiency decreases, while the converse is true when temperature increases. Thus, for concentration systems, it seems that there is an optimum value of x in these ternaries which will yield

74
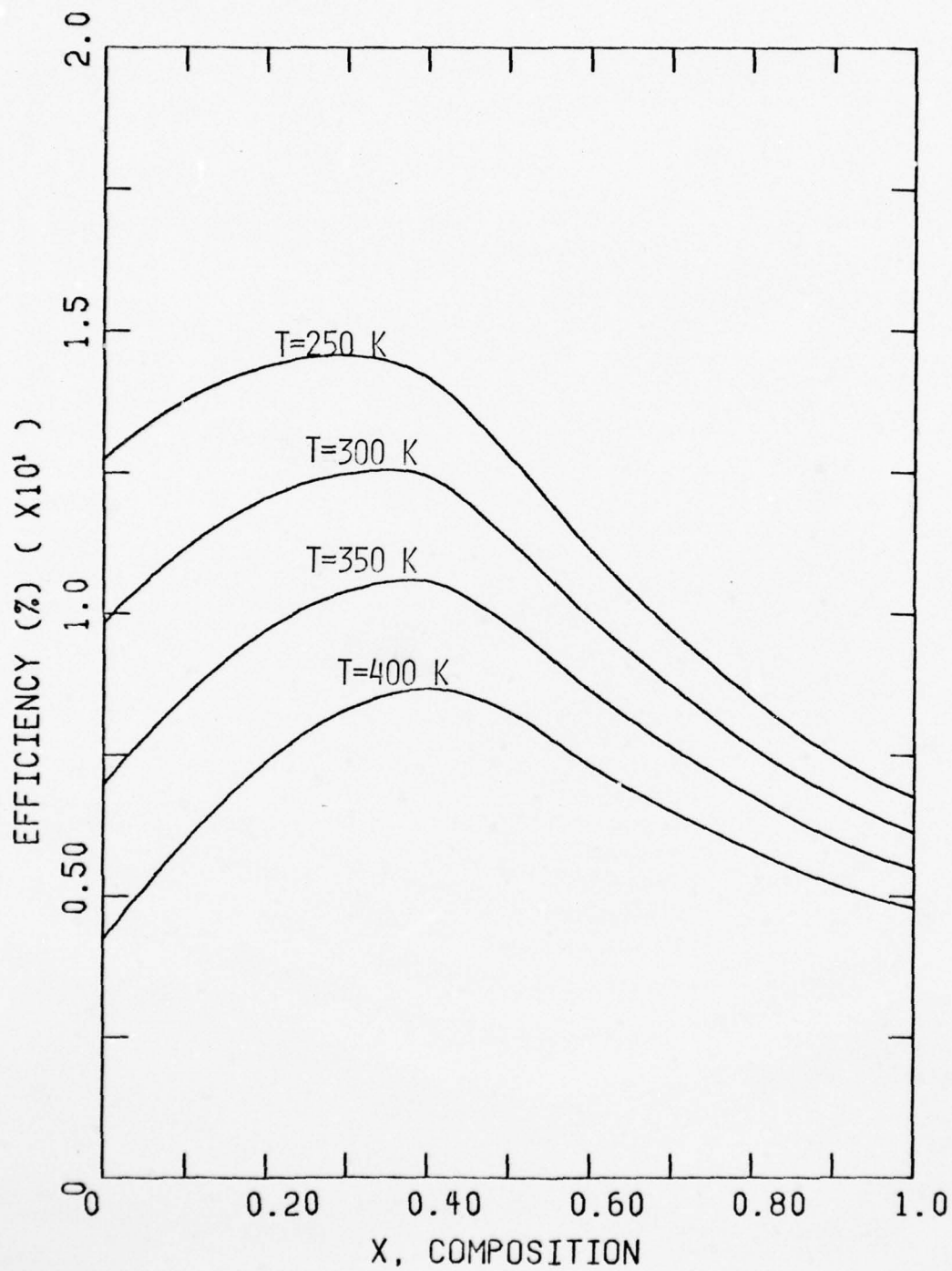
Figure 3.2. AMO conversion efficiency for $GaP_xAs_{1-x}$ as a function of alloy composition for $\phi_B = E_G - 0.55$ eV and concentration ratio = 1.

75

Table 3.3. Summary of Conversion Efficiency Calculations for $GaP_xAs_{1-x}$ and $Ga_{1-x}Al_xAs$ Schottky Barrier Solar Cells Using $\emptyset_B = \frac{2}{3} E_G$.

### A. $GaP_xAs_{1-x}$

| Temperature °K | Concentration Ratio | Maximum Efficiency, % | x, Composition at Maximum Efficiency |
|---|---|---|---|
| 250 | 1 | 14.455 | 0.06 |
| | 10 | 15.721 | 0.0 |
| | 100 | 17.028 | 0.0 |
| | 1000 | 18.337 | 0.0 |
| 300 | 1 | 11.99 | 0.160 |
| | 10 | 13.321 | 0.11 |
| | 100 | 14.772 | 0.03 |
| | 1000 | 16.319 | 0.0 |
| 350 | 1 | 9.744 | 0.2 |
| | 10 | 11.156 | 0.18 |
| | 100 | 12.651 | 0.11 |
| | 1000 | 14.294 | 0.03 |
| 400 | 1 | 7.782 | 0.3 |
| | 10 | 9.184 | 0.27 |
| | 100 | 10.716 | 0.20 |
| | 1000 | 12.40 | 0.11 |

### B. $Ga_{1-x}Al_xAs$

| Temperature °K | Concentration Ratio | Maximum Efficiency, % | x, Composition at Maximum Efficiency |
|---|---|---|---|
| 250 | 1 | 14.443 | 0.05 |
| | 10 | 15.720 | 0.0 |
| | 100 | 17.026 | 0.0 |
| | 1000 | 18.335 | 0.0 |
| 300 | 1 | 11.960 | 0.149 |
| | 10 | 13.301 | 0.08 |
| | 100 | 14.759 | 0.0 |
| | 1000 | 16.317 | 0.0 |
| 350 | 1 | 9.719 | 0.2 |
| | 10 | 11.124 | 0.18 |
| | 100 | 12.623 | 0.13 |
| | 1000 | 14.281 | 0.03 |
| 400 | 1 | 7.777 | 0.30 |
| | 10 | 9.160 | 0.23 |
| | 100 | 10.676 | 0.21 |
| | 1000 | 12.379 | 0.11 |

Table 3.4. Summary of Conversion Efficiency Calculations for $GaP_xAs_{1-x}$ and $Ga_{1-x}Al_xAs$ Schottky Barrier Solar Cells Using $\phi_B = E_G - 0.55$ eV.

### A. $GaP_xAs_{1-x}$

| Temperature °K | Concentration Ratio | Maximum Efficiency, % | x, Composition at Maximum Efficiency |
|---|---|---|---|
| 250 | 1 | 14.63 | 0.29 |
| | 10 | 15.54 | 0.25 |
| | 100 | 16.50 | 0.23 |
| | 1000 | 17.48 | 0.21 |
| 300 | 1 | 12.60 | 0.33 |
| | 10 | 13.62 | 0.31 |
| | 100 | 14.68 | 0.29 |
| | 1000 | 15.78 | 0.25 |
| 350 | 1 | 10.63 | 0.38 |
| | 10 | 11.73 | 0.33 |
| | 100 | 12.90 | 0.31 |
| | 1000 | 14.13 | 0.29 |
| 400 | 1 | 8.69 | 0.38 |
| | 10 | 9.932 | 0.36 |
| | 100 | 11.208 | 0.36 |
| | 1000 | 12.514 | 0.34 |

### B. $Ga_{1-x}Al_xAs$

| Temperature °K | Concentration Ratio | Maximum Efficiency, % | x, Composition at Maximum Efficiency |
|---|---|---|---|
| 250 | 1 | 14.561 | 0.30 |
| | 100 | 16.430 | 0.24 |
| 300 | 1 | 12.537 | 0.33 |
| | 100 | 14.595 | 0.29 |
| 350 | 1 | 10.559 | 0.35 |
| | 100 | 12.867 | 0.31 |
| 400 | 1 | 8.644 | 0.36 |
| | 100 | 11.153 | 0.34 |
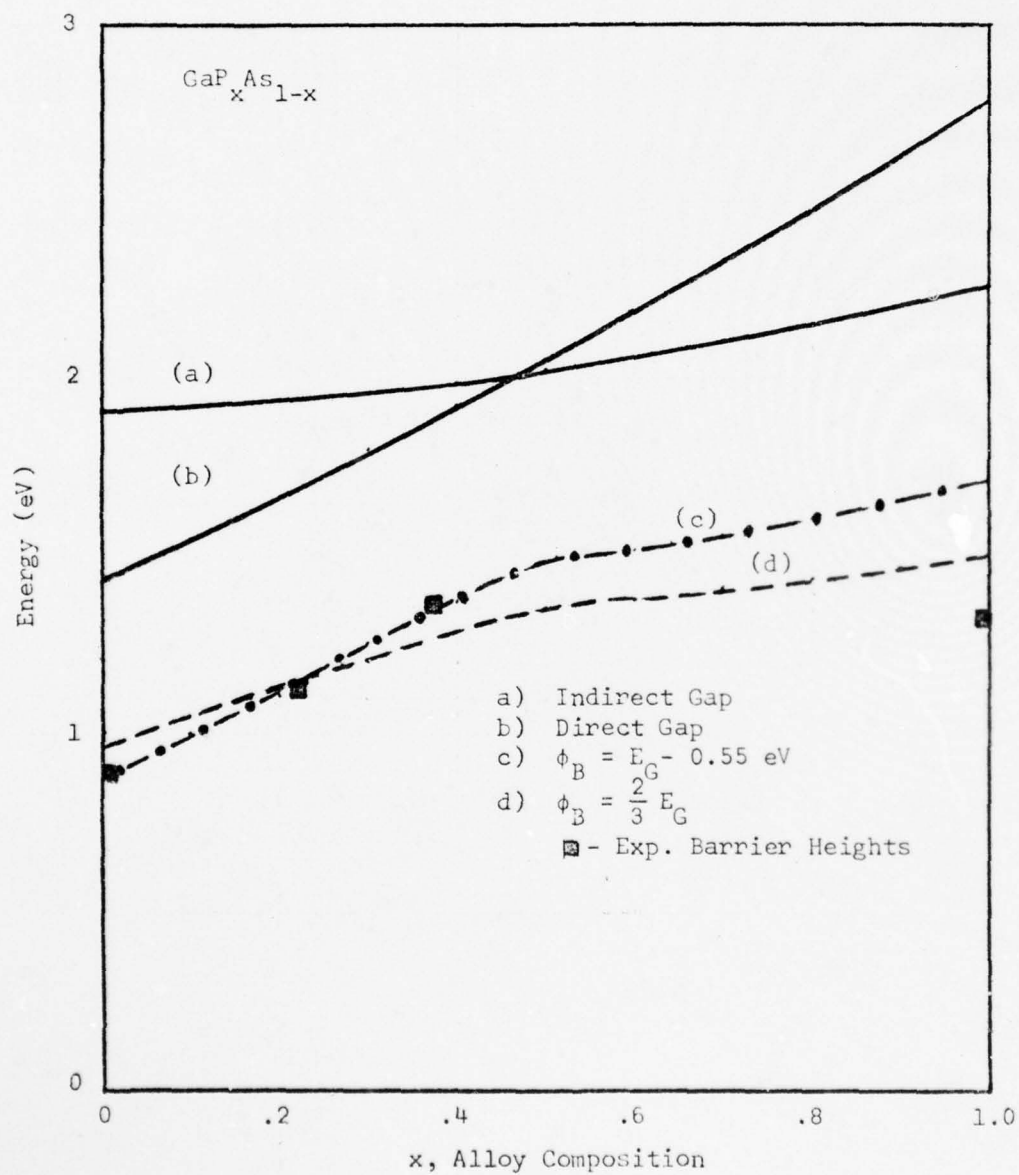
Figure 3.3.  Energy bandgaps and barrier heights as a function of alloy composition for $GaP_xAs_{1-x}$.

maximum efficiency. The ternaries which seem to offer near optimum conditions are $GaP_xAs_{1-x}$ with $x \simeq 0.3$ or $Ga_{1-x}Al_xAs$ with $x \simeq 0.27$.

The ternaries $GaAs_{1-x}Sb_x$ and $Ga_{1-x}In_xAs$ were also extensively studied. However, all of the calculations showed that GaAs was superior to either of these two alloys, and further discussion of these materials will not be presented.

### 3.2 MIS Solar Cells

The discussion in the previous section indicates that practical barrier heights for metal-semiconductor Schottky barrier solar cells are limited to a certain fraction of the energy bandgap ($\simeq \frac{2}{3} E_G$). This factor further places a lower bound on the dark current of the Schottky barrier solar cell, which in turn limits the achievable photovoltaic conversion efficiency. If barrier heights approaching the bandgap could be achieved then conversion efficiencies approaching those p-n junction cells could also be achieved.

There have been several experimental papers published in the last two years [3-13 to 3-17] which indicate that an interfacial layer (oxide layer) purposely introduced between the metal and semiconductor of a Schottky barrier solar cell structure can increase the conversion efficiency of such cells. This interfacial layer is very thin (on the order of a few atomic layers or approximately $20\overset{\circ}{A}-50\overset{\circ}{A}$ thick) and, in effect, reduces the dark current over that for the Schottky barrier while absorbing essentially none of the incident solar radiation. One can conclude that this physical effect is equivalent to an increase in the barrier height of the structure.

There have been several theoretical discussions of the physics of the MIS solar cell [3-16, 3-18 to 3-20], which elaborate the details of the transport mechanisms. In this paper, a brief discussion will be given which

79

summarizes these published results and demonstrates the basic nature of the structure.

Figure 3.4 illustrates schematically the band structure of an MIS solar cell. Here $E_{Fm}$ and $E_{Fs}$ are the quasi-Fermi levels in the metal and semiconductor, respectively. The total current flow is given by

$$J_T = J_n(0) + J_p(0) \qquad (3-9)$$
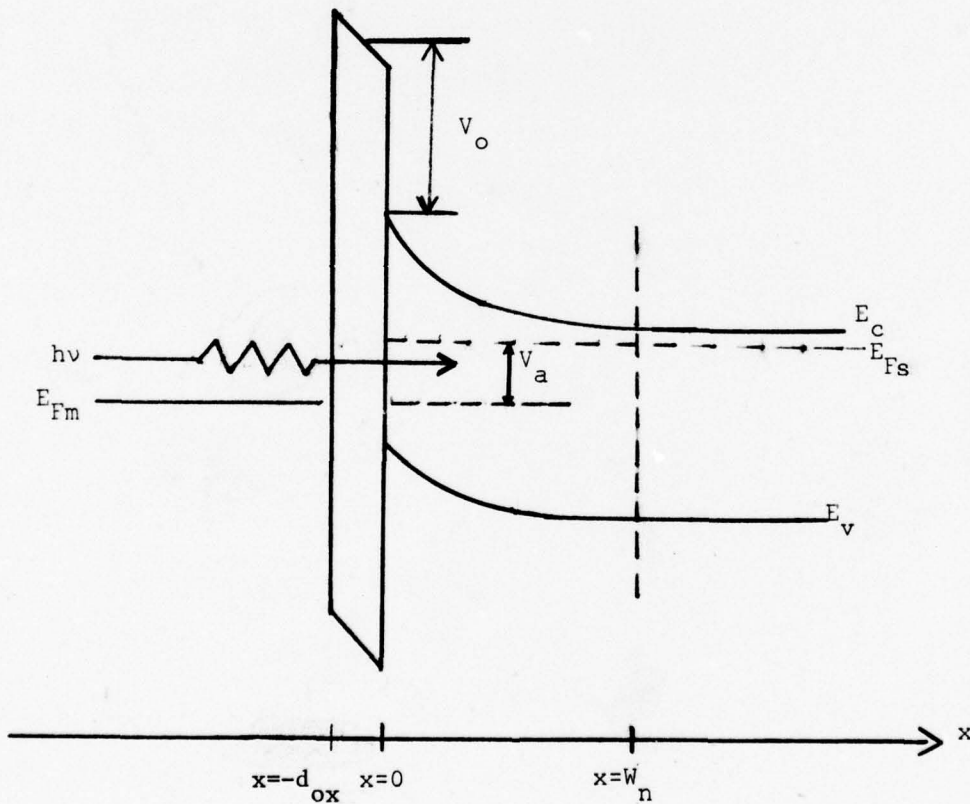


Figure 3.4. Schematic Illustration of MIS Solar Cell.

where $J_n(0)$ and $J_p(0)$ are the electron and hole currents, respectively, at $x = 0$. Now,

$$J_p(0) = J_p(W_n) + J_u . \qquad (3-10)$$

80

Here $J_u$ is the total recombination current in the depletion region, and in general will involve a term due to the optical generation in this region (i.e. $-J_{DR}$ of Eqn. 3-2), a term due to thermal generation-recombination in this region (i.e. $J_R$ of Eqn. 3-3), as well as a term due to recombination through interface states. Also, $J_p(W_n)$ would normally be calculated using a first-order diffusion model, and will be equal to the sum of the terms given by the equations in APPENDIX C, if the insulator does not influence the Boltzmann boundary condition on the minority carriers.

The most important term in establishing the major effect of the insulator on the conversion efficiency of MIS solar cells is $J_n(0)$. Here, Card and Rhoderick [3-18] show that

$$J_n(0) = J_{MIS} = A^{**}T^2 \exp\left(\frac{-\phi_B}{kT}\right) \exp\left(\frac{-2\sqrt{2m_n^* V_o}}{\hbar} d_{ox}\right)\left\{\exp\left(\frac{qV_a}{nkT}\right) - 1\right\} \quad (3-11)$$

The term $\exp(-2\sqrt{2m^* V_o}\, d_{ox}/\hbar)$ is the transmission coefficient through the oxide based on a WKB approximation to the quantum tunneling problem, and the factor n (the ideality factor) takes into account the fact that part of the applied voltage, $V_a$, is dropped across the oxide. Ponpon and Siffert [3-16] show that n obeys three different analytical expressions, depending on the nature of the interface states. It is apparent from Eqn. (3-11) that an effective barrier height can be defined as

$$\phi_{BE} = \phi_B + \left(\frac{2\sqrt{2m_n^* V_o}}{\hbar}\right)kT\, d_{ox} \quad (3-12)$$

where $V_o$ is the average surface tunneling barrier height, as shown in Figure 3.4. Also, for investigative purposes the device current can be expressed as

$$J_T = J_{MIS} - J_{sc} \quad (3-13)$$

81

where $J_{sc}$ is defined in Eqn. 3-2. However, this equation holds only as long as $J_{MIS} \gg J_R + J_{Diff}$. This may or may not be violated before $\phi_{BE} \simeq E_G$, and the importance of these terms has not been fully investigated for different materials.

If one takes $\phi_B = \frac{2}{3} E_G$ and requires $\phi_{BE} = E_G$, then

$$\frac{2\sqrt{2m_n^* V_o}}{\hbar} \, kT \, d_{ox} = \frac{E_G}{3} \tag{3-14}$$

For GaAs, this requires that

$$V_o \, d_{ox}^{\,2} \simeq 400 \text{ eV}(\overset{\circ}{A})^2$$

which for $20\overset{\circ}{A}$ oxide thickness requires $V_o$ to be 1 eV, which is a reasonable value. In general for $\phi_{BE} = E_G$, then

$$V_o \, d_{ox}^{\,2} = 157 \left[ E_G(eV) \right]^2, \text{ eV}(\overset{\circ}{A})^2 \tag{3-15}$$

for $m_n^* = m_o$. Using this model, then one can predict the limit conversion efficiencies originally given by Pulfrey and McQuart [3-4] for Schottky barrier solar cells. For example, these authors predict a maximum conversion efficiency of approximately 25% for a Schottky barrier solar cell with $\phi_B = E_G \simeq 1.4$ eV.

Figure 3.5 shows a plot of some recent calculations made by Olsen [3-20], for MIS solar cells designed for optimum oxide thickness. These calculations are discussed in detail in this reference. The results again show the prediction that large efficiencies are possible with MIS solar cells. Much experimental work needs to be done to elucidate these structures, although efficiencies of 15% for GaAs cells have already been reported [3-15].
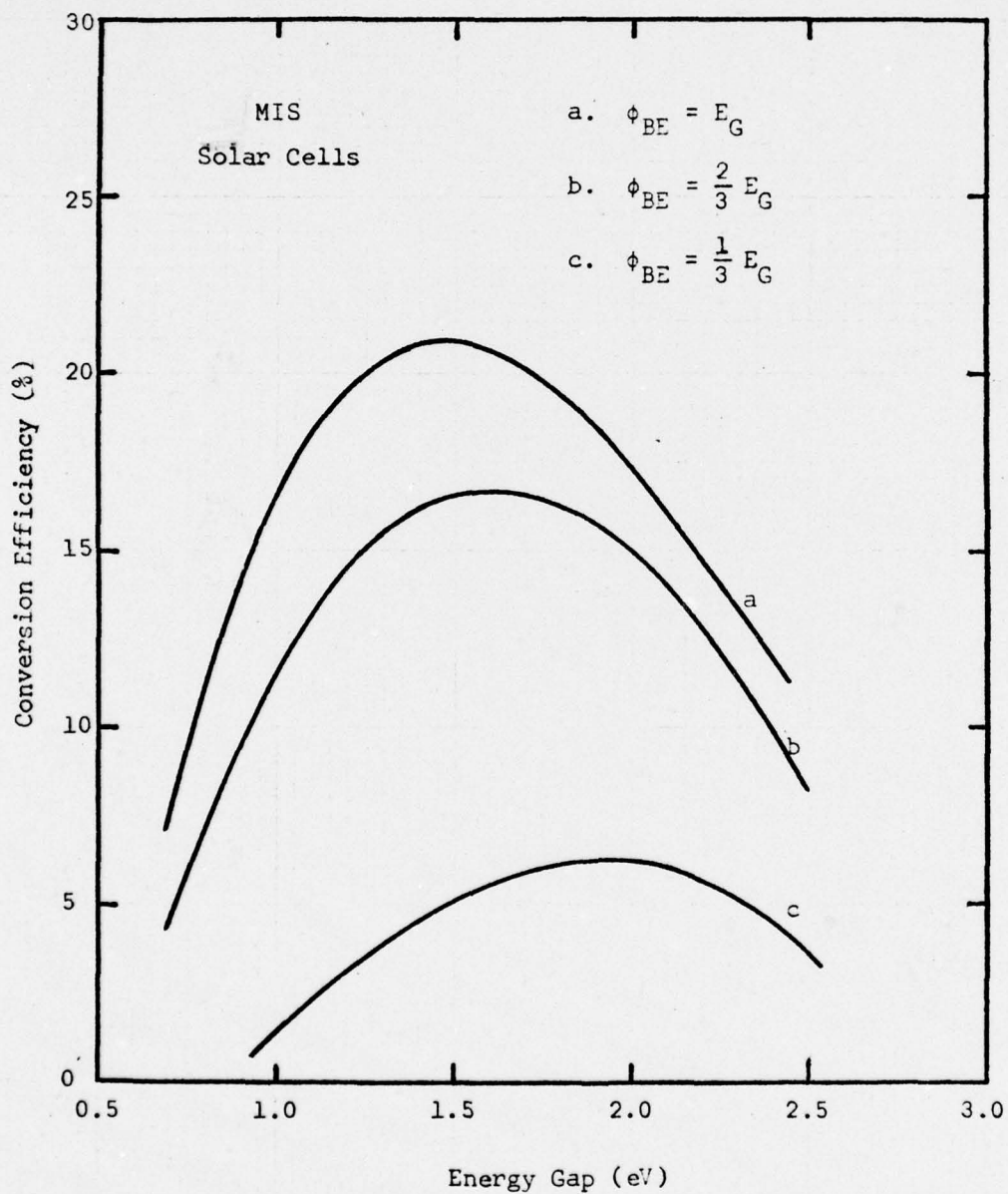
Figure 3.5. Conversion efficiency for MIS solar cells [3-20].

### 3.3 Assessment of Schottky Barrier and MIS Solar Cell Technologies

At the present time AMO conversion efficiencies of 10% for Schottky barrier cells and 15% for MIS cells have been reported in the literature. These results are for GaAs or GaAs-based ternary compounds. There is currently a significant amount of research activity, both experimental and theoretical, which is being carried out to improve the performance of these cells.

The primary consideration in discussing the utility of these cells is the relationship of total cell cost to total system cost. If cell cost is a small fraction of the total system cost then Schottky barrier solar cells probably do not deserve attention in such systems. The MIS solar cell, in principle, could receive consideration for such systems if the theoretical predictions prove feasible. However, the comparative cost of a high efficiency MIS cell to other high efficiency cells discussed in this report cannot be ascertained at this time. Although the MIS cell seems to be cost competitive with other high efficiency technologies, any discussion of this point seems to be only conjecture.

The ultimate efficiency of MIS cells is uncertain because it is not clear as to how large the energy barrier can be made by the use of various insulating layers. If the barrier height can be made to approach the values obtained with p-n junctions, then the calculated efficiencies are in the same range as those of homojunctions and heterojunctions. However, barriers this large have not so far been experimentally achieved.

When cell cost is a major part of system cost the Schottky barrier and MIS solar cells deserve much consideration. Progress in achieving both low cost silicon and GaAs make MIS cells viable alternatives in

these systems.  Although progress has been made in increasing efficiency
and solving stability problems in such low cost technologies as the
CdS cell, it is possible that silicon and GaAs Schottky barrier cells
can become cost competitive with these technologies due to higher achievable
efficiencies.

REFERENCES

3-1. H. J. Hovel, "Solar Cells", in Semiconductors and Semimetals, Vol. 11, Academic Press, New York, p. 112, 1975.

3-2. S. J. Fonash, J. Appl. Phys. 46 1286 (1975).

3-3. J. P. Ponpon and P. Siffert, J. Appl. Phys. 47 3248 (1976).

3-4. D. L. Palfrey and R. F. McQuat, Appl. Phys. Lett. 24 167 (1974).

3-5. R. F. McQuat and D. L. Pulfrey, J. Appl. Phys. 47 2113 (1976).

3-6. Y. M. Ych and R. J. Stirn, Proc. 11th Photovoltaic Specialists Conf. (I.E.E.E., New York, 1975) p. 391.

3-7. L. C. Olsen and R. C. Boharn, in Ref. 6, p. 381.

3-8. J. W. Harrison and J. R. Hauser, J. Appl. Phys. 47 292 (1976).

3-9. J. W. Harrison and J. R. Hauser, Phys. Rev. B 13 5347 (1976).

3-10. V. L. Rideout, Solid-State Elec. 17 1107 (1974).

3-11. J. E. Sutherland and J. R. Hauser, to be published in I.E.E.E. Trans. Elec. Dev., April, 1977.

3-12. S. M. Sze, Physics of Semiconductor Devices, John Wiley, New York, N.Y., p. 377, 1969.

3-13. W. A. Anderson, A. E. Delahoy, and R. A. Milano, J. Appl. Phys. 45 1913 (1974).

3-14. E. J. Charlson and J. C. Lien, J. Appl. Phys. 46 3981 (1975).

3-15. R. J. Stirn and Y. C. M. Yeh, Appl. Phys. Lett. 27 95 (1975).

3-16. J. P. Ponpon and P. Siffert, J. Appl. Phys. 47 3248 (1976).

3-17. D. R. Lillington and W. G. Townsend, Appl. Phys. Lett. 28 97 (1976).

3-18. H. C. Card and E. H. Rhoderick, J. Phys. D. 4 1589 (1971).

3-19. S. J. Fonash, J. Appl. Phys. 46 1286 (1975).

3-20. L. C. Olsen, to be published in the Proc. of 12th Photovoltaic Specialists Conference, Baton Rouge, Louisiana, 1976.

3-21. J. R. Hauser, Proc. IRE 53 743 (1965).

86

## 4.0 GENERALIZED SINGLE AND MULTI-JUNCTION SOLAR CELL CLOSED FORM ANALYSIS

### 4.1 Steady-State Integral – Differential Continuity Equations for Electro-optical Devices

In order to avoid some of the assumptions made in the conventional analysis of solar cells, an effort was made to obtain the V-I solar cell curve equation in closed form. The first step necessary to accomplish this was to derive a continuity equation (for electrons and holes) which includes the external excitation of the entire solar spectrum. This results in an integral-differential (2nd order) continuity equation. The second step requires the determination of the general solution (the homogeneous and nonhomogeneous parts) to the integral-differential equation. With the appropriate boundary conditions imposed on the general solution, the minority carrier distribution and the diffusion and drift components of electron and hole currents as a function of the photovoltage(s) are obtained. All the device characteristics may now be derived from the V-I cell equation.

In the conventional analysis the steady-state continuity equation that is employed to determine the collection efficiency is given by [4-1]

$$o = \alpha[1-R]N_o e^{-\alpha x} + D_n \frac{d^2 n}{dx^2} + \mu_n E \frac{dn}{dx} - r_n , \qquad (4-1)$$

for electrons in p-type material and

$$o = \alpha[1-R]N_o e^{-\alpha x} + D_p \frac{d^2 p}{dx^2} - \mu_p E \frac{dp}{dn} - r_p \qquad (4-2)$$

for holes in n-type material.

87

The equations appropriate for a general electric field and complete solar spectrum generation rate can be derived from the current density and continuity equations. For electrons these are

$$J_n = q\mu_n \, nE + qD_p \frac{dp}{dx} \; , \tag{4-3}$$

$$0 = G_e - r_n + \frac{1}{q} \frac{d.J_n}{dx} \; . \tag{4-4}$$

Combining these and using $r_n = \dfrac{n - n_o}{\tau_n}$ gives

$$0 = G_e - \frac{n - n_o}{\tau_n} + \mu_n \, n \frac{dE}{dx} + \mu_n \, E \frac{dn}{dx} + D_n \frac{d^2 n}{dx^2} \; . \tag{4-5}$$

Combining this with the generation rate due to the complete solar spectrum of

$$G_e = \int_0^{\lambda_c} -\frac{n - n_o}{\tau_n} \; \alpha(1-R)N_o e^{-\int_0^x \alpha dx'} \, d\lambda \; , \tag{4-6}$$

then finally gives

$$0 = \int_0^{\lambda_c} \alpha(1-R)N_o e^{-\int_0^x \alpha dx'} \, d\lambda + D_n \frac{d^2 n_p(x)}{dx^2} + \mu_n E(x) \frac{dn_p(x)}{dx} + \\ + \mu_n n_p(x) \frac{dE(x)}{dx} - \frac{n_p(x) - n_{po}}{\tau_n} \; , \tag{4-7}$$

88

where $\alpha(\lambda,x)$ and $E(x)$ are position-dependent. A similar equation exists for holes

$$o = \int_0^{\lambda_c} \alpha(1-R)N_o e^{-\int_0^x \alpha dx'} d\lambda + D_p \frac{d^2 p_n(x)}{dx^2} - \mu_p E(x) \frac{dp_n(x)}{dx} -$$

$$- \mu_p p_n(x) \frac{dE(x)}{dx} - \frac{p_n(x) - p_{no}}{\tau_p} . \tag{4-8}$$

For constant field $dE(x)/dx$ vanishes and Eqs. (4-7) and (4-8), which are the equations that will be used in the analytical work, become

$$o = \int_0^{\lambda_c} \alpha(1-R)N_o e^{-\int_0^x \alpha dx'} d\lambda + D_n \frac{d^2 n_p(x)}{dx^2} + \mu_n E_o \frac{dn_p(x)}{dx} - \frac{n_p(x) - n_{po}}{\tau_n} , \tag{4-9}$$

$$o = \int_0^{\lambda_c} \alpha(1-R)N_o e^{-\int_0^x \alpha dx'} d\lambda + D_p \frac{d^2 p_n(x)}{dx^2} - \mu_p E_o \frac{dp_n(x)}{dx} - \frac{p_n(x) - p_{no}}{\tau_p} . \tag{4-10}$$

The equations for zero field are also required in the analytical work and are obtained by setting $E_o = 0$. This results in the continuity equation for electrons

$$o = \int_0^{\lambda_c} \alpha(1-R)N_o e^{-\alpha x} d\lambda + D_n \frac{d^2 n_p(x)}{dx^2} - \frac{n_p(x) - n_{po}}{\tau_n} \tag{4-11}$$

and for holes

$$o = \int_0^{\lambda_c} \alpha(1-R)N_o e^{-\alpha x} d\lambda + D_p \frac{d^2 p_n(x)}{dx^2} - \frac{p_n(x) - p_{no}}{\tau_n} . \tag{4-12}$$

89

The absorption coefficient has been made to be position-independent
in the absence of a non-graded bandgap material in the manipulation
of Eqs. (4-9) and (4-10) to obtain Eqs. (4-11) and (4-12). However,
the position-dependent absorption coefficient could remain as such in
Eqs. (4-9) and (4-11).

## 4.2 General Solutions to the Steady-State Continuity Equations

In this discussion the general solutions to Eqs. (4-9) through
(4-12) are given. Eqs. (4-9) and (4-10) are the electron and hole
continuity equations, respectively, for which the established built-in
field is constant. The built-in field may be established by grading
the bandgap (in a ternary or quaternary) or by grading the net impurity
concentration. If the mobility and/or lifetime are position dependent,
average values are used. Eqs. (4-11) and (4-12) are obtained from the
electron and hole continuity equations, respectively, for which no built-in
field is present. The general solution for electrons will be presented
since the hole solution may be obtained by inspection.

The general solutions to Eqs. (4-9) through (4-12) contain homo-
geneous and nonhomogeneous parts. The homogeneous parts represents the
general solution to the continuity equation when the generation term
arising from the solar flux is zero. Both homogeneous and nonhomogeneous
parts, are necessary when the generation term is present.

The general solutions are required to satisfy their respective
continuity equations for all x and $\lambda$ in the range 0 to $\lambda_c$, and must satisfy
the imposed boundary conditions of the solar cell band structure model.
Not all general solutions will satisfy the continuity equation and boundary
conditions. The general solutions discussed below satisfy the continuity
equation and the imposed boundary conditions.

A general solution to Eq. (4-9) for electrons is given by

$$n_p(x) = C_1 e^{\omega_1 x} + C_2 e^{\omega_2 x} + \frac{1}{\omega_2 - \omega_1} [G_1(x) e^{\omega_1 x} + G_2(x) e^{\omega_2 x}]. \quad (4-13)$$

The functions $G_1(x)$ and $G_2(x)$ are defined by

$$G_1(x) = \frac{1}{D_n} \int_0^x e^{-\omega_1 x'} \int_0^{\lambda_c(x')} \alpha(1-R) N_o e^{-\int_0^{x'} \alpha dx''} d\lambda dx' , \quad (4-14)$$

and

$$G_2(x) = -\frac{1}{D_n} \int_0^x e^{-\omega_2 x'} \int_0^{\lambda_c(x')} \alpha(1-R) N_o e^{-\int_0^{x'} \alpha dx''} d\lambda dx' . \quad (4-15)$$

The constants $\omega$ and $\omega_2$ are given by

$$\omega_1 = \frac{\mu_n E_o}{2 D_n} + \sqrt{\left(\frac{\mu_n E_o}{2 D_n}\right)^2 + L_n^{-2}} , \quad (4-16)$$

$$\omega_2 = \frac{\mu_n E_o}{2 D_n} - \sqrt{\left(\frac{\mu_n E_o}{2 D_n}\right)^2 + L_n^{-2}} . \quad (4-17)$$

A similar set of equations exists for the general solution to Eq. (4-11) for holes.

A general solution to Eq. (4-11) for electrons is given by

$$n_p(x) = C_1 \cosh \frac{x}{L_n} + C_2 \sinh \frac{x}{L_n} - \int_0^{\lambda_c} C_3 e^{-\alpha x} d\lambda , \quad (4-18)$$

where

$$C_3 \equiv \frac{\alpha L_n^2 (1-R) N_o}{D_n (\alpha^2 L_n^2 - 1)} . \quad (4-19)$$

91

A similar set of equations exists for the general solution to Eq. (4-12) for holes.

Each of the general solutions, Eqs. (4-13) and (4-18) contain two constants of integration, $C_1$ and $C_2$. Since the continuity equations are of the second order, two boundary conditions must be imposed on each solution in order to define a physically realizable model. The two constants are therefore required to satisfy the two boundary conditions.

## 4.3 Requirements to Interchange Sequence of Integration Between Wavelength and Position in the $G_1$ and $G_2$ Integrals

To calculate the solar cell device characteristics, it is necessary to integrate the functions $G_1$ and $G_2$ numerically, because the NASA measured solar flux spectrum cannot easily be represented by a mathematical function. The forms given for $G_1$ and $G_2$ in Eqs. (4-14) and (4-15), respectively, are time consuming and costly to integrate even when performed on a computer. This may be avoided if $G_1$ and $G_2$ are represented in the following forms:

$$G_1(x) = \frac{1}{D_n} \int_0^{\lambda_c} \int_0^x e^{-\omega_1 x'} \alpha(1-R)N_o e^{-\int_0^{x'} \alpha dx''} dx'd\lambda \qquad (4-20)$$

$$G_2(x) = \frac{1}{D_n} \int_0^{\lambda_c} \int_0^x e^{-\omega_2 x'} \alpha(1-R)N_o e^{-\int_0^{x'} \alpha dx''} dx'd\lambda \ . \qquad (4-21)$$

where the integration of $x$ and $\lambda$ have been interchanged.

It is readily seen in the following manner that this interchange is possible. Since $\alpha = 0$ for wavelengths larger than the bandgap, the upper limit on $\lambda$ in Eq. (4-14) may be extended to $\infty$ without a change in value. Then

$$G_1(x) = \frac{1}{D_n} \int_0^x e^{-\omega_1 x'} \int_0^\infty \alpha(1-R)N_o e^{-\int_0^{x'} \alpha dx''} d\lambda dx' \ . \qquad (4-22)$$

Since the limits on the $\lambda$ integration are independent of x the above integrations can be interchanged to

$$G_1(x) = \frac{1}{D_n} \int_0^\infty \int_0^x e^{-\omega_1 x'} \int_0^\infty \alpha(1-R)N_o \, e^{-\int_0^{x'} \alpha dx''} dx' d\lambda \quad . \quad (4\text{-}23)$$

The upper limit on the $\lambda$ integration may now be reduced to $\lambda_c$ as in Eq. (4-20) where $\lambda_c$ is the wavelength of the smallest bandgap material in the layer under consideration. Similar considerations lead to Eq. (4-21).

REFERENCES

4-1. W. Shockley, Electrons and Holes in Semiconductors, D. Van Nostrand Co., Inc., Princeton, 1950.

93

5.0 "POTENTIAL WELL" SOLAR CELL STRUCTURE USING THE $Al_xGa_{1-x}As$-GaAs MATERIALS SYSTEM

5.1 Introduction

The potential advantages of GaAs over Si for solar cells were recognized early [5-1, 5-2]. Conversion efficiency values of 11 to 12% were reported in 1962 [5-3, 5-4], which at that time were equivalent to or greater than Si cell values. Unpublished data demonstrated GaAs efficiency values exceeding 16% [5-5]. Device parameters limiting efficiency in GaAs cells were also reported [5-6, 5-7]. The recent advances in III-V materials and device technology and their application to solar cells has resulted in significant increases in GaAs efficiency [5-8 to 5-26]. The use of these cells has been extended to concentrator systems [5-22]. These results have stimulated solar cell design in the light of recent advances in technology.

In this Section the Potential Well or PW cell structure, pAlGaAs/pGaAs/nGaAs/nAlGaAs, is analyzed and the calculation of cell characteristics are accomplished by means of a computer. In each of the 4 distinct sub-regions, the general solution of the excess minority carrier distribution is obtained from the integral form of the continuity equation. This form of the continuity equation considers the perturbation of the entire solar flux distribution in the cell. Imposing the appropriate boundary conditions gives, in addition to the usual quantities, the solar cell V-I curve from which $P_{max}$, $J_{max}$, $V_{max}$, F, $J_{Jn}$, and $J_{Jp}$ are calculated. Moreover, from $J_{Jn}$ and $J_{Jp}$ it can be determined whether charge carrier confinement for electrons and holes, respectively, occurs.

This work represents the first attempt to solve for the V-I solar cell curve, in closed form, from the integral form of the continuity

94

equation. It also represents the first attempt to solve in closed form for electron and hole concentrations in the case where both a built-in field and a barrier to minority carrier flow are both present. The analytical result of this model allows for the determination of the design conditions to optimize overall cell performance.

The absorption coefficient rises sharply at the band edge of direct transition materials, attaining values in excess of $10^5$ cm$^{-1}$ over a significant portion of the solar spectrum [5-24]. For example, 95% of the photon flux above the band edge energy is absorbed at AMO in less than 2 μm of GaAs. At the same time, however, the high surface recombination velocity (S) in conjunction with the high absorption results in a significant reduction in spectral response at short wavelengths. Several approaches have been employed to reduce surface recombination losses: a built-in aiding electric field established by an impurity gradient [5-7, 5-27]; a wide, constant bandgap surface layer serving as an optical window [5-8, 5-8a]; or bandgap grading which also establishes an aiding built-in drift field [5-28 to 5-31]. The first technique does not significantly reduce surface losses. The latter two structures have been effective in improving the spectral response of GaAs homojunction and heterojunction cells. As a result of the application of the recently developed structures. the conversion efficiencies of p-AlGaAs/p-GaAs/n-GaAs [5-30, 5-31] and nAlGaAs/pGaAs [5-31] cells have been calculated and show an improvement over earlier GaAs homojunction cells. In a concentration system of 1700 at AM1.5, similarly constructed cells have yielded 19% efficiency [5-22].

At the other extreme, the absorption coefficient in indirect transition materials rises less sharply at the band edge. In Si, for example, the absorption coefficient is less than $10^4$ cm$^{-1}$ over the portion of the solar spectrum of highest photon flux at AMO [5-23]. A Si layer of 205 μm is required to absorb 95% of the photon flux of energy above its band edge. Typically, solar cells fabricated from indirect transition materials do not exhibit high surface recombination loss. However, indirect transition materials do give rise to other losses--incomplete absorption, high base region recombination, recombination loss at the base region-base contact interface [5-27]. The latter two also affect the photovoltage. Base region recombination may be reduced by increasing the minority carrier diffusion length, while the recombination loss at the base contact is reduced by the low-high junction (LHJ) or back surface field cell (BSF) [5-32].

The Back Surface Field (BSF) $n^+pp^+$ Si solar cells result in a measurable and reproducible increase in $V_{oc}$ [5-32]. This increase typically lies in the range 30 to 50 mV. The short-circuit current (though apparently more difficult to quantify and less reproducible) and the fill factor also increase [5-33]. In $n^+p$ cells, $V_{oc}$ decreases with decreasing p-region width. In contrast, $V_{oc}$ is insensitive to the p-region width in the $n^+pp^+$ structure at least in the range 100 to 400 μm [5-33]. These improvements have been shown experimentally to be attributed directly to the barrier established by the heavily doped $p^+$ region [5-32 to 5-34].

Gunn studied the effects of a barrier such as is represented by the $pp^+$ junction [5-35]. For sufficiently long diffusion length, Gunn concluded that minority carrier accumulation may take place [5-35]. Minority carrier

96

accumulation or carrier confinement serves to reduce dark current and correspondingly increase the photovoltage and fill factor [5-32, 5-33].

Even though the minority carrier diffusion length is inherently short in direct transition materials, the high absorption coefficient allows fabrication of practical structures in which a large fraction of the photon flux generates electron-holes pairs in a region less than one diffusion length from the p-n junction. Correspondingly, the base region-contact interface recombination loss is negligible in typical solar cell structures fabricated from direct transition materials. Thin film, direct transition solar cell structures are receiving increased attention because material costs may be reduced by more than two orders of magnitude where the substrate seed can be eliminated. Technology has been developed for the III-V materials systems from which solar cells of several micrometers thickness may be fabricated. Moreover, due to the versatility and compatibility of the AlGaAs graded bandgap regions to establish aiding drift fields and junction barriers, such as the $pp^+$ barrier in Si cells, to achieve minority carrier confinement in both regions su-rounding the GaAs p-n junction to increase the photovoltage and fill factor.

## 5.2 "Potential Well" (PW) Structure

Figure 5.1 shows the band structure of the PW cell. The GaAs homojunction is sandwiched between graded bandgap layers of $Al_xGa_{1-x}As$. The ternary AlGaAs is chosen because it exhibits a bandgap range required to optimize cell performance, and it forms the best lattice match with GaAs over a wide range of alloy compositions [5-36]. Double-heterostructure $GaAs-Al_xGa_{1-x}As$ laser diodes reduced threshold current density for lasing

97
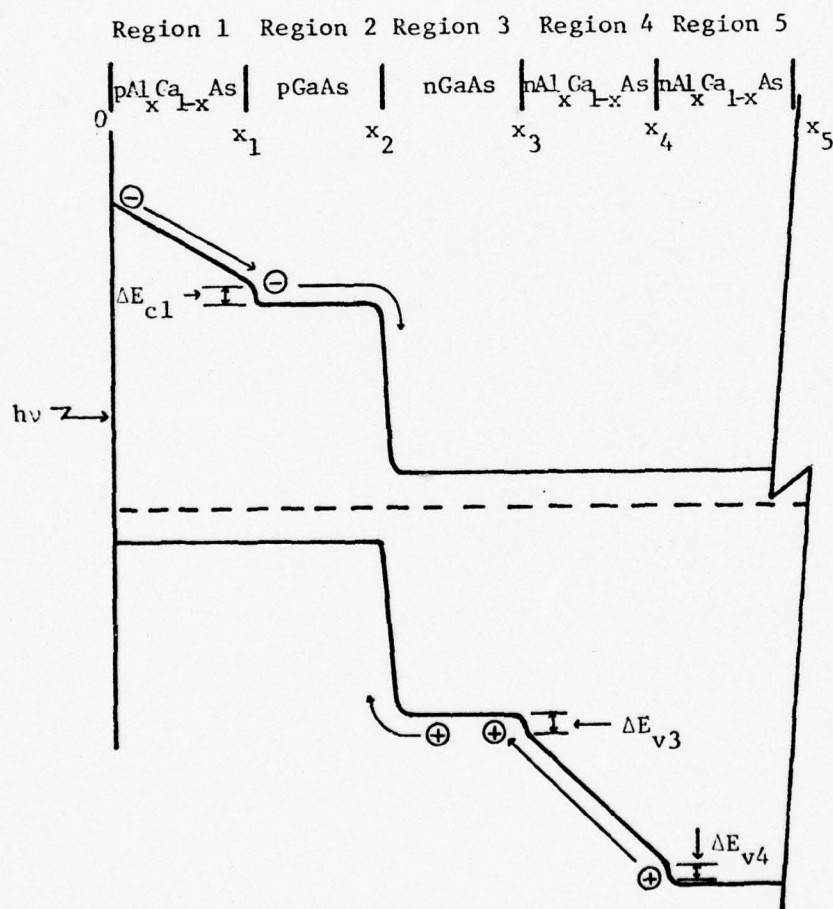
Figure 5.1. "Potential Well" Solar Cell Structure

through carrier confinements [5-37].  This behavior is further strengthened
by the low recombination rate measured at AlGaAs-GaAs interfaces [5-38].

REGION 1:  The $Al_xGa_{1-x}As$ bandgap is made to decrease linearly such
that a constant negative built-in electric field is established.  This
negative field accelerates electrons flowing toward the p-n junction,
thereby reducing bulk recombination in this region.  Surface recombination
loss is also reduced due to the drift field.  In addition, the bandgap
(being larger than for GaAs) serves as a window for the majority of the
solar flux.

The layer also serves as an additional conducting path for the
terminal load current.  By highly doping this layer, the sheet resistance
may be reduced to very low values.  The high doping level and the corres-
ponding low minority carrier diffusion length in this region is not as
critical to spectral response because of the presence of an aiding field.

REGION 2:  Due to the presence of Region 1 and its high doping level,
the design of Region 2 does not need to have imposed on it the conditions
for a low conducting path for the terminal current.  As a result, Region
2 may be more lightly doped (i.e., $10^{16}$ to $10^{17}$ $cm^{-3}$) in order to realize
higher lifetime, mobility and absorption coefficient as well as to obtain
a superior quality metallurgical and electronic p-n junction.  Typically,
solar cells without a window layer require surface concentration values
in excess of $5 \times 10^{19}$ (usually $5 \times 10^{19}$ to $10^{21}$ $cm^{-3}$) to minimize resistive
losses.  In Si this may result in a "dead layer" in which the lifetime
is estimated to be 100 psec or less [5-39].  In such cases, the efficiency
is reduced because of lower spectral response and a high dark current is
observed with a consequence that $V_{oc}$, $J_{sc}$ and F decrease.

99

In the case where the p-GaAs is lightly doped, the mobility and lifetime are higher and its absorption coefficient rises more rapidly and attains higher values than more heavily doped material. This allows for a thinner p-GaAs layer without suffering bulk recombination or incomplete absorption loss. Moreover, in conjunction with the aiding built-in field in Region 1 and the barrier, $\Delta E_{c1}$, at $x_i$ (both of which restrict electrons in Region 2 from entering Region 1 and then recombining) and a thinner Region 2, the conditions are established to obtain carrier confinement in Region 2. This reduces the dark current and increases $V_{oc}$ and F.

REGION 3: The design considerations for Region 3 are similar to those for Region 2. The doping level may also be in the same range as for Region 2 (i.e., $10^{16}$ to $10^{17}$ cm$^{-3}$) and inherently higher lifetime, mobility and absorption coefficient are realized. As in Region 2, this contributes to a superior metallurgical and electronic p-n junction. Due to the high absorption coefficient, the layer may be made thin (i.e., micron range) without incurring incomplete absorption loss. Analogous to Region 2, the excess holes in Region 3 are restrained from entering Region 4 and recombining due to the aiding built-in field in Region 4 and the barrier $\Delta E_{v3}$, formed by the discontinuity in the valence band at $x_3$. These all combine to increase the probability of making the Shockley diffusion the dominant transport mechanism. Together with hole accumulation in the n-GaAs region, the dark current is reduced with a consequent increase in $V_{oc}$ and F. This portion of the PW structure has similarities to the BSF Si solar cell, except in the PW band edge structure the barrier height, $\Delta E_{v3}$, may be made greater than the pp$^+$ barrier of the BSF Si cell and to serve as a more effective

barrier for carrier confinement. Moreover, the drift field in Region

4 may be made greater and also aid to confine holes to Region 3.

REGION 4: The bandgap increase is manifested through a negative slope

in the valence band edge. This results in a negative field which serves

to accelerate holes toward the p-n junction and to confine holes to

Region 3. This aids in reducing the dark current and increasing $V_{oc}$

and F.

## 5.3 Results and Discussion

In this section the results of the calculations are discussed.

Calculations are made on the PW structure for which each of the regions

is $10^{-4}$ cm thick and for which the bandgap of the AlGaAs at the surface

and at the base is 1.739eV (0.713 micrometers) giving a value of x = 0.258

[5-40, 5-41]. The material parameters used in the calculations are taken

from the literature. There is general agreement in the GaAs data for

electron and hole lifetime and diffusion length [5-42 to 5-51], and

mobilities [5-52 to 5-54]. The AlAs data, while not as extensive, is

also available [5-52]. To obtain alloy parameters, an interpolation

method is used [5-54], where data is not available (See APPENDIX B). The

ternary direct and indirect bandgap values are determined by well known

relationships [5-40, 5-41]. All calculations have been performed at

AMO [5-55].

## p-$Al_x Ga_{1-x}$As Layer Acceptor Concentration

In Section 5.2 we discussed the useful design functions which Region

1 (AlGaAs) serve. One of these is the conduction path for terminal current.

In this connection, a low resistance conducting path (obtained through

optimized design of doping level and thickness of Region 1) is desired.

The competing design parameters are electrons diffusion length, photon flux absorbed through the layer and sheet resistance or impurity concentration, with surface recombination velocity as a parameter. These calculations show that efficiency drops significantly when the acceptor concentration exceeds $3 \times 10^{18}$ $cm^{-3}$.

Figures 5.2 and 5.3 summarize the results of nine computer runs for which the V-I curve, maximum power, short-circuit current density, open circuit voltage, form factor, voltage at maximum power point and spectral response were calculated. These curves show that efficiency decreases markedly above $3 \times 10^{18}$ $cm^{-3}$ acceptor concentration in the $p-Al_xGa_{1-x}As$. This results because of a decrease in both electron lifetime (due to the introduction of recombination centers) and electron mobility (due to increased ionized impurity scattering) with increasing acceptor concentration. The efficiency is also reduced with increasing surface recombination velocity. These calculations are presented in Figure 5.3 in which the independent variable ($N_{Al}$) and the surface recombination velocity (S) are interchanged in order to more clearly exhibit the effect of surface recombination velocity.

For completeness the short-circuit current density vs. the acceptor concentration in the $p-Al_xGa_{1-x}As$ layer is shown in Figure 5.4. The shape of the family of curves is similar to those in Figure 5.2.

Figure 5.5 shows the reciprocal of the carrier confinement factor, $R_n$, for electrons in the p-GaAs layer and the dark current vs. $p-Al_xGa_{1-x}As$ acceptor concentration. $R_n$ is the factor by which dark current is decreased as compared with the case of pure diffusion away from the junction into an infinitely thick layer. The $R_n$ coefficient (APPENDIX

102
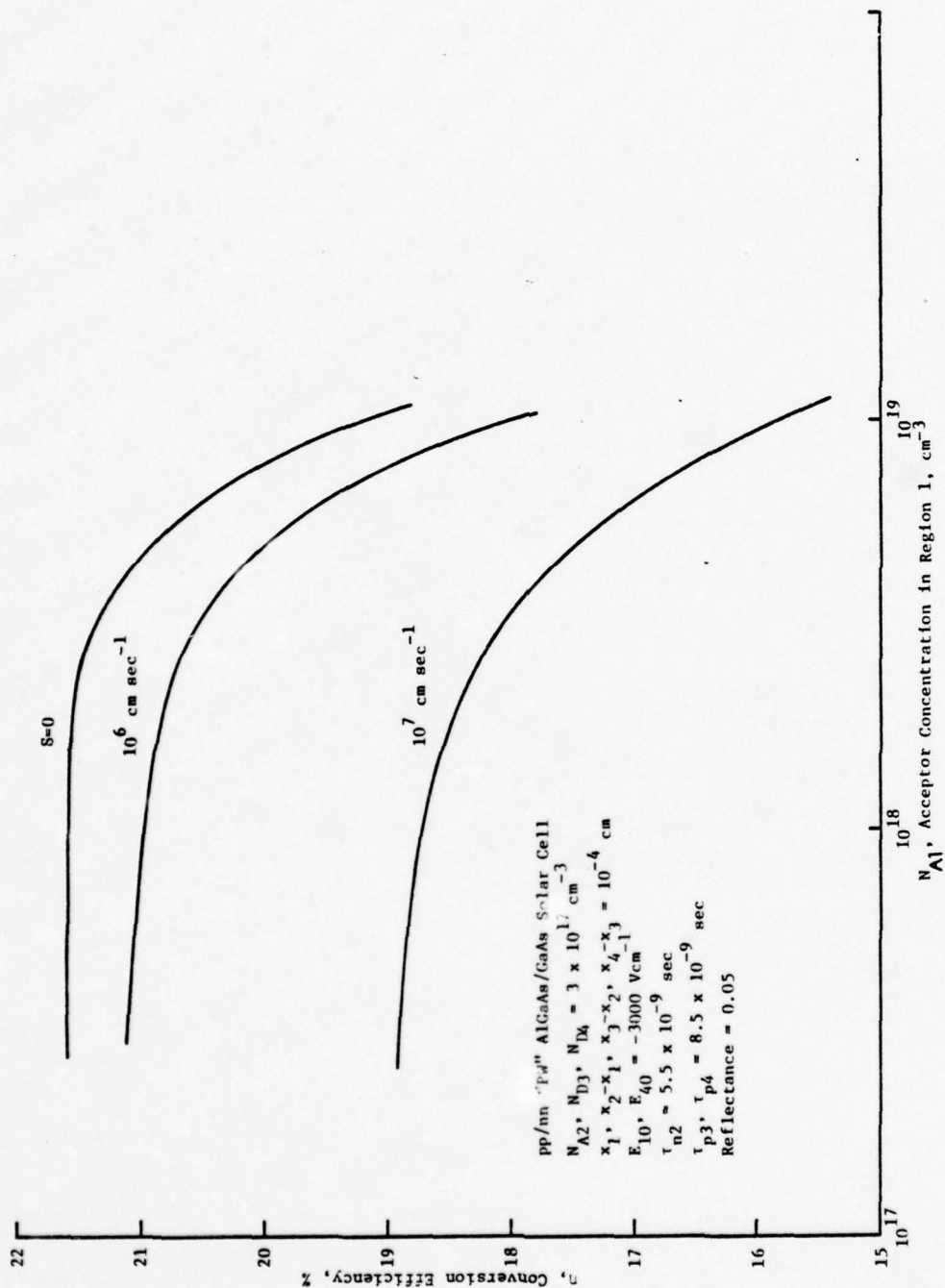
Figure 5.2. Conversion efficiency vs. p-Al$_x$Ga$_{1-x}$As acceptor concentration with surface recombination velocity as a parameter.

pp/nn "PW" AlGaAs/GaAs Solar Cell

$N_{A2}$, $N_{D3}$, $N_{D4}$ = 3 x $10^{17}$ cm$^{-3}$

$x_1$, $x_2-x_1$, $x_3-x_2$, $x_4-x_3$ = $10^{-4}$ cm

$E_{10}$, $E_{40}$ = -3000 Vcm$^{-1}$

$\tau_{n2}$ = 5.5 x $10^{-9}$ sec

$\tau_{p3}$, $\tau_{p4}$ = 8.5 x $10^{-9}$ sec

Reflectance = 0.05

$N_{A1}$=3x$10^{17}$ cm$^{-3}$

$10^{18}$

3x$10^{18}$

$10^{19}$

$\eta$, Conversion Efficiency, %

S, Surface Recombination Velocity, cm sec$^{-1}$
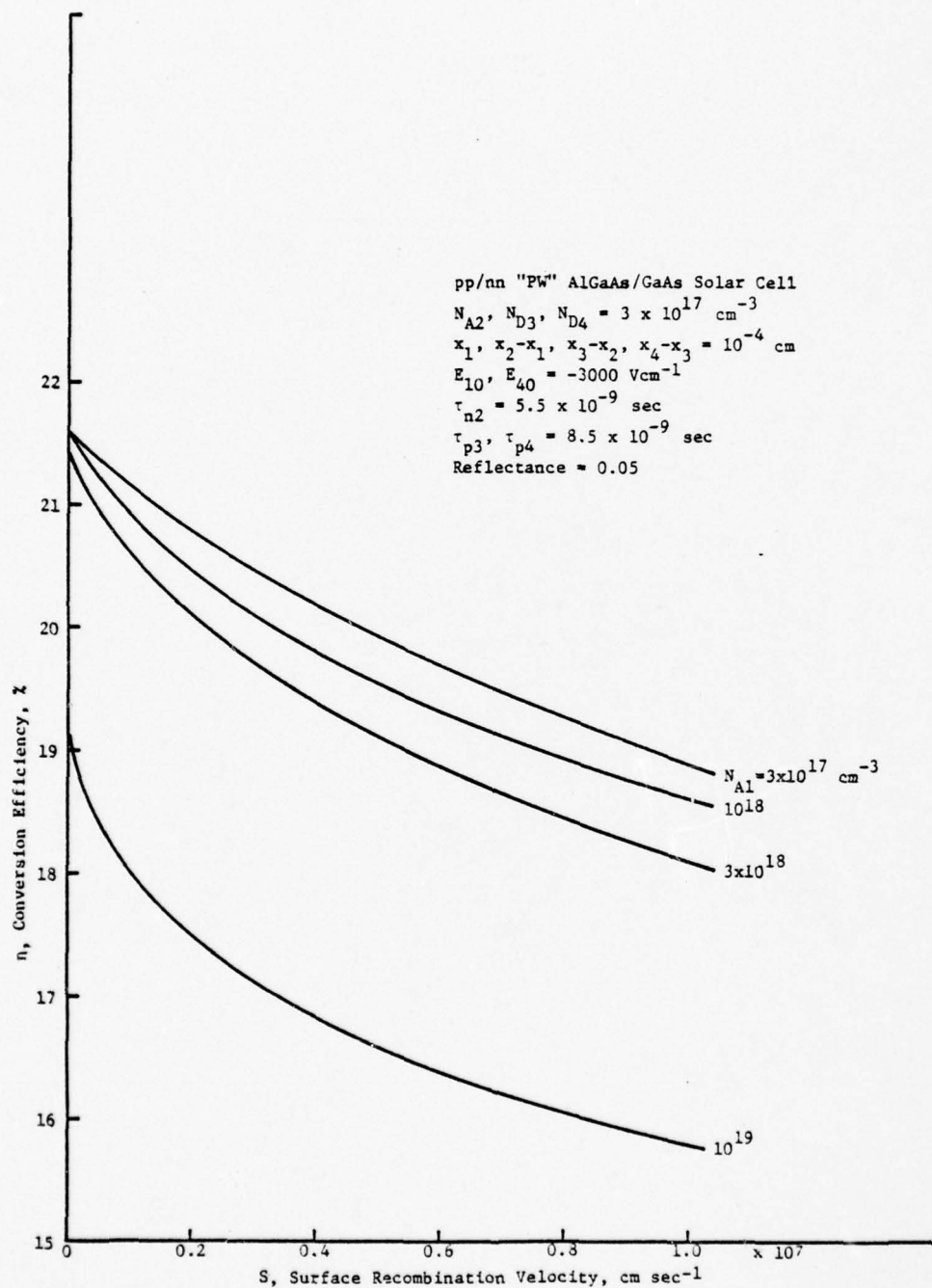
Figure 5.3. Conversion efficiency vs. surface recombination velocity with pAl$_x$Ga$_{1-x}$As acceptor concentration as a parameter.

104
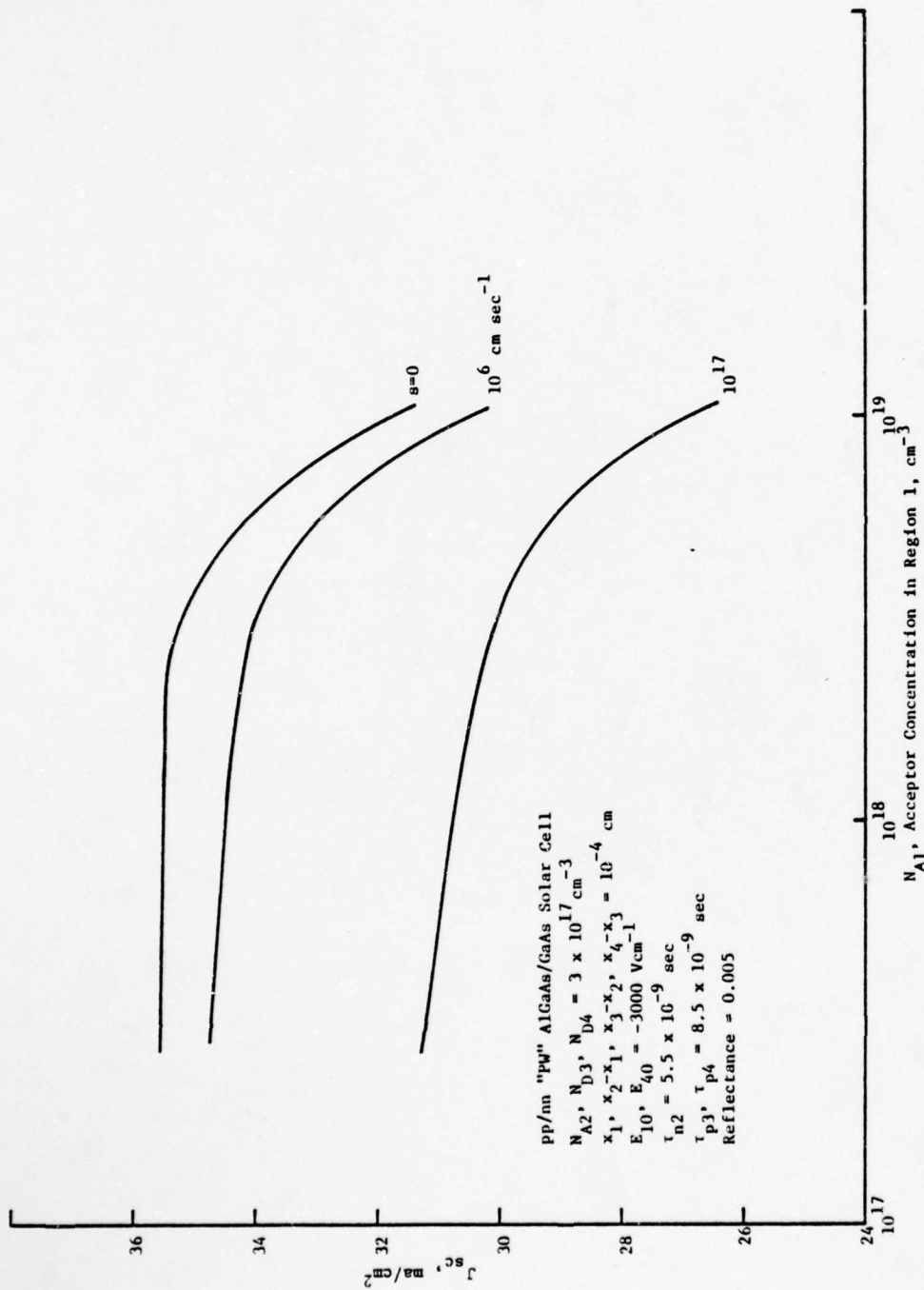
Figure 5.4. Short-circuit current density vs. p-Al$_x$Ga$_{1-x}$As acceptor concentration with surface recombination velocity as a parameter.

105
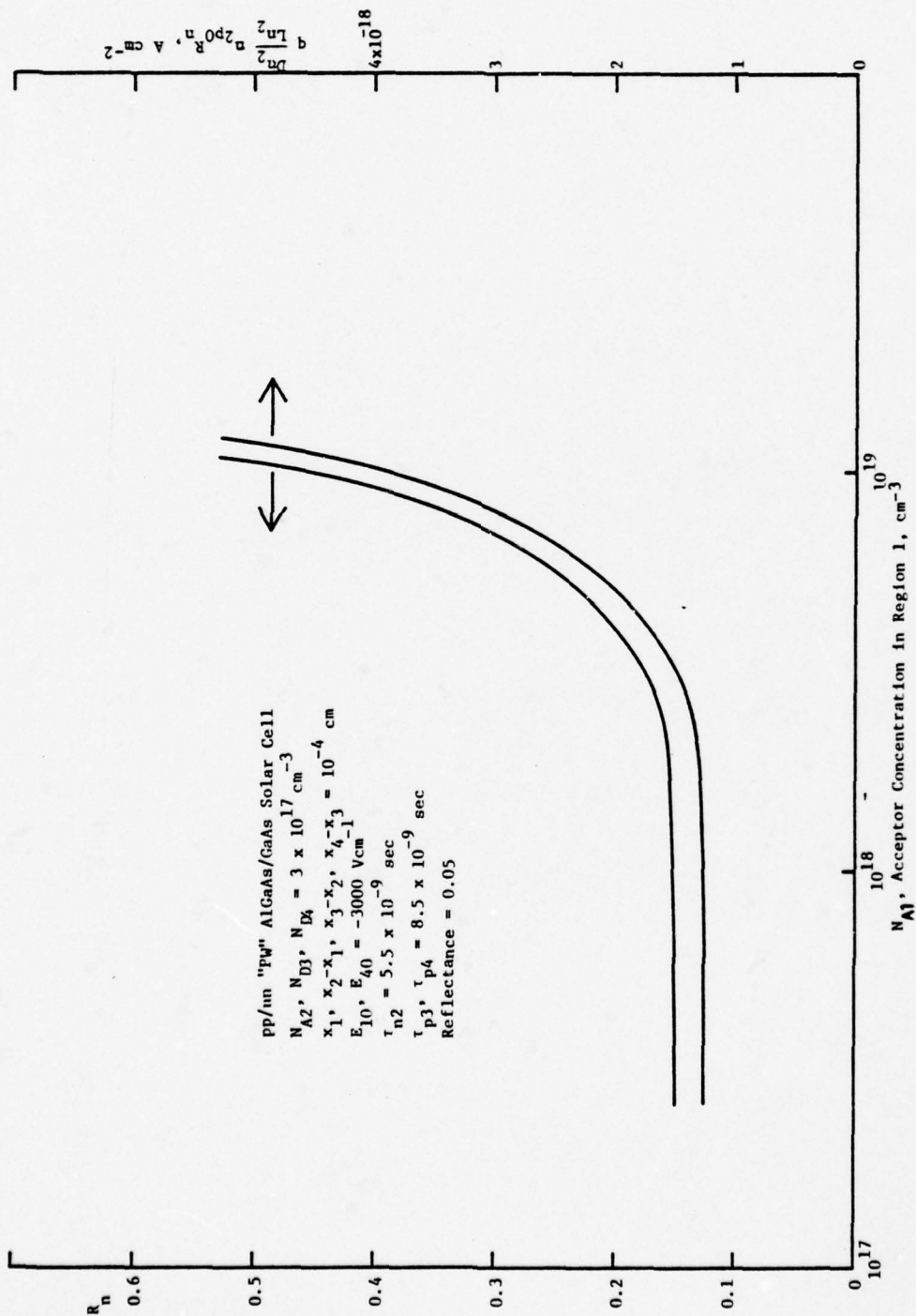
Figure 5.5. $R_n$ and dark current vs. $p$-$Al_xGa_{1-x}As$ acceptor concentration.

$pp/nn$ "pw" AlGaAs/GaAs Solar Cell

$N_{A2}$, $N_{D3}$, $N_{D4}$ = 3 x $10^{17}$ cm$^{-3}$

$x_1$, $x_2$-$x_1$, $x_3$-$x_2$, $x_4$-$x_3$ = $10^{-4}$ cm

$E_{10}$, $E_{40}$ = -3000 Vcm$^{-1}$

$\tau_{n2}$ = 5.5 x $10^{-9}$ sec

$\tau_{p3}$, $\tau_{p4}$ = 8.5 x $10^{-9}$ sec

Reflectance = 0.05

$q \frac{\Delta n_2 L n_2}{2} n_{2p0} R_n$, A cm$^{-2}$

$4x10^{18}$

$N_{Al}$, Acceptor Concentration in Region 1, cm$^{-3}$

$R_n$

F, Eqs. (F-27) and (F-28)) is unity when the minority carrier diffusion length is small compared to the semiconductor thickness. Figure 5.5 shows that below $3 \times 10^{18}$ cm$^{-3}$ the dark current and the $R_n$ coefficient are constant and that the dark current is lower by nearly an order of magnitude than that obtained when carrier confinement does not occur. For concentration levels in the p-AlGaAs layer of $3 \times 10^{18}$ cm$^{-3}$ and lower, the carrier confinement in the p-GaAs layer is high enough to significantly reduce the dark current.

With increasing acceptor concentration in the p-AlGaAs layer, the electron recombination in this layer increases. Because $\Delta E_{c1} = 0$ in this calculation, minority carriers injected into Region 2 from Region 3 (due to the photovoltage) traverse Region 2, without appreciable recombination, and enter Region 1 where they experience an increased recombination rate. This results in reducing the carrier confinement in Region 1 as is shown in Figure 5.5 and increasing the electron contribution to dark current.

As further support of the above results and the interpretation, the spectral response is shown in Figures 5.6, 5.7 and 5.8 for zero, $10^6$ and $10^7$ cm sec$^{-1}$ surface recombination velocity, respectively, with Region 1 acceptor concentration as a parameter. The three sets of curves show reduced collection efficiency for increasing S over the spectral range, except at the band edge. However, the percentage change is greatest and relatively constant in the range $\lambda < 0.38$ $\mu$m in each of the curve sets. The spectral response curves, in Figure 5.6 for zero recombination velocity, show a small change in the concentration range $3 \times 10^{17}$ to $3 \times 10^{18}$ cm$^{-3}$. This small change is due to the value of the ratio $L_{n1}/x_1$ being considerably
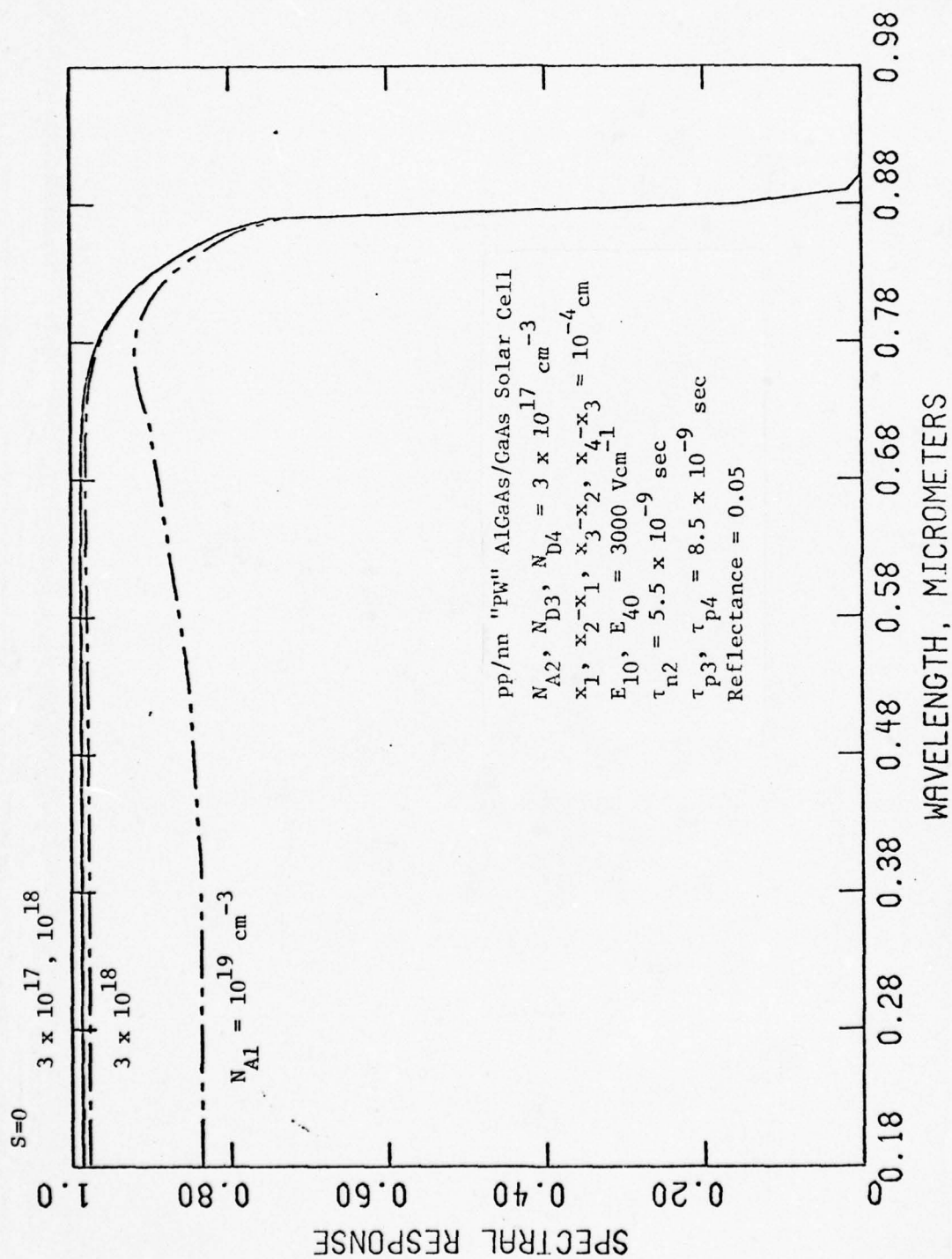
Figure 5.6. Total spectral response with Region 1 acceptor concentration a parameter and for zero recombination velocity.

The following parameters appear in the figure:

pp/nn "PW" AlGaAs/GaAs Solar Cell

$N_{A2}$, $N_{D3}$, $N_{D4} = 3 \times 10^{17}$ cm$^{-3}$

$x_1$, $x_2-x_1$, $x_3-x_2$, $x_4-x_3 = 10^{-4}$ cm

$E_{10}$, $E_{40} = 3000$ Vcm$^{-1}$

$\tau_{n2} = 5.5 \times 10^{-9}$ sec

$\tau_{p3}$, $\tau_{p4} = 8.5 \times 10^{-9}$ sec

Reflectance = 0.05

$S=0$

$3 \times 10^{17}$, $10^{18}$

$3 \times 10^{18}$

$N_{A1} = 10^{19}$ cm$^{-3}$

WAVELENGTH, MICROMETERS
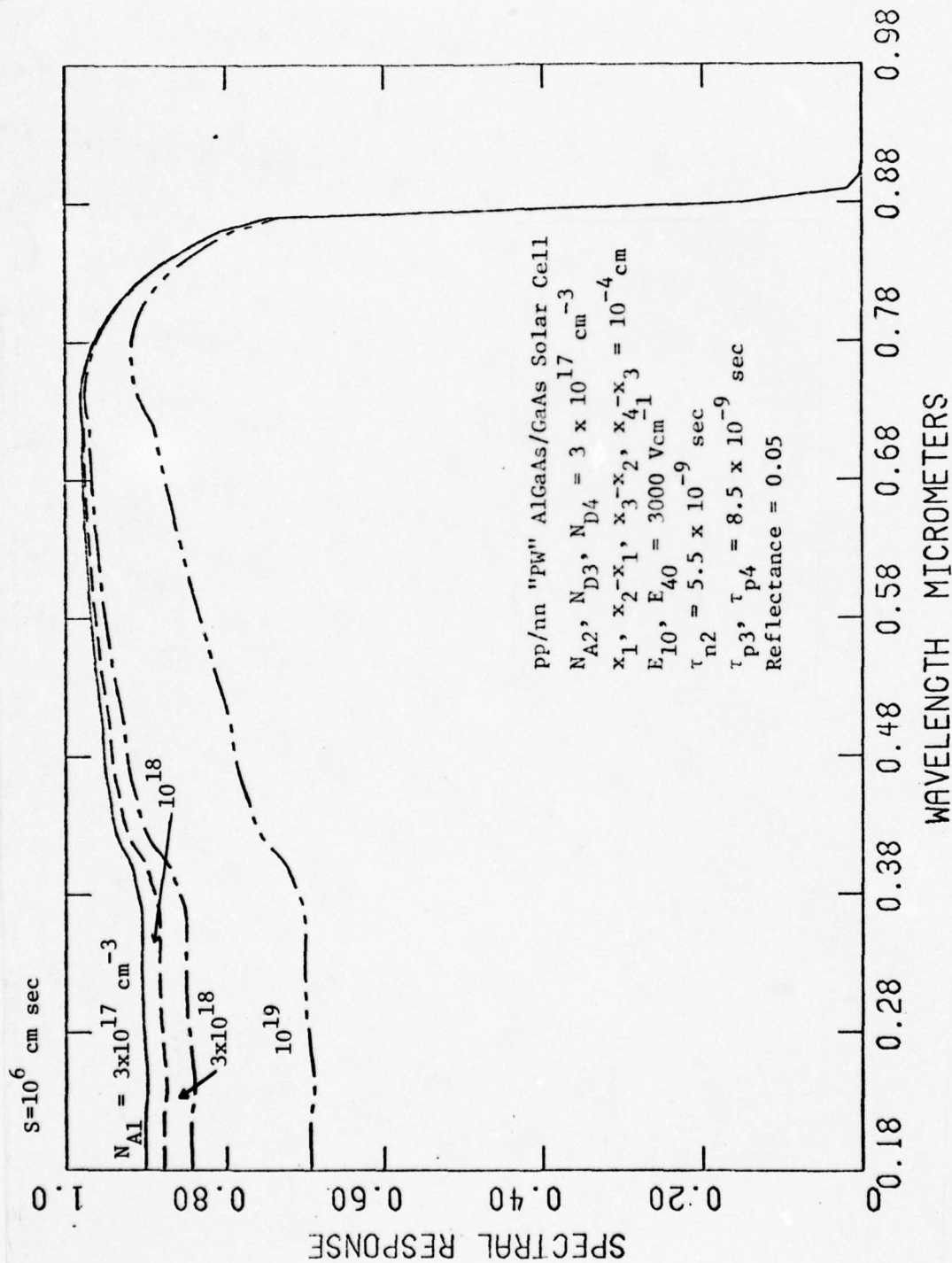
SPECTRAL RESPONSE

Figure 5.7. Total spectral response with Region 1 acceptor concentration a parameter and for $10^6$ cm sec$^{-1}$ recombination velocity.
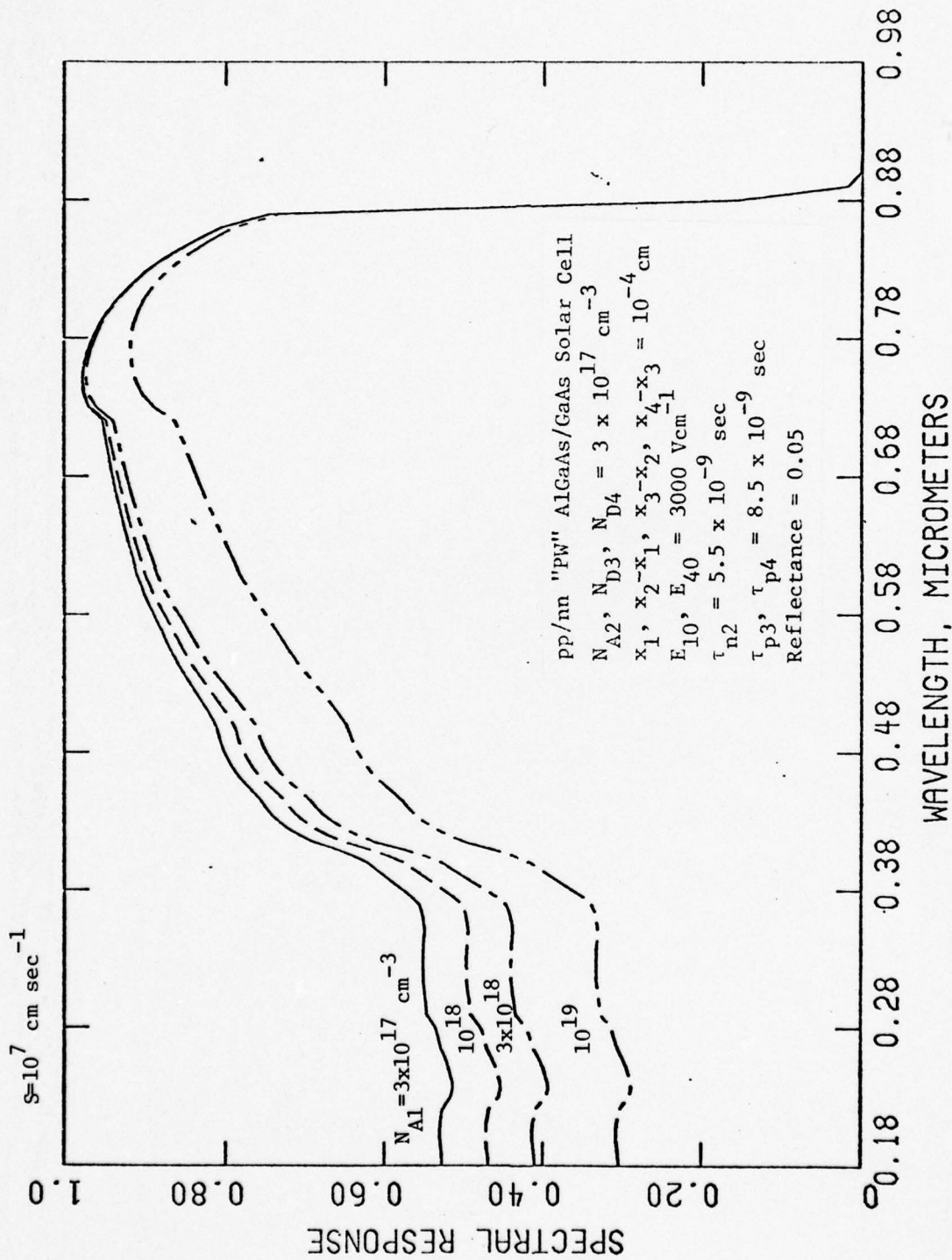
Figure 5.8. Total spectral response with Region 1 acceptor concentration a parameter and for $10^7$ cm sec$^{-1}$ recombination velocity.

greater than unity over this concentration range which results in an imperceptible change in efficiency as shown in Figure 5.2. For $10^{19}$ cm$^{-3}$ the ratio $L_{n1}/x_1$ is of the order of unity or less due to the marked decrease in electron mobility and lifetime, resulting in increased bulk recombination over the entire spectral range. However, the spectral response change is discernible over the entire concentration, $3 \times 10^{17}$ to $10^{19}$ cm$^{-3}$, for $10^6$ and $10^7$ cm sec$^{-1}$ SRV as Figures 5.7 and 5.8 show. This is reflected in a detectable change in efficiency for high surface recombination velocity and shown in Figure 5.2.

The curves in Figures 5.6, 5.7, and 5.8 generally show a drop in spectral response in the spectral range $\lambda \leq 0.38$ μm. For convenience we may define $\lambda_w = 0.38$ μm as the window wavelength over which the largest portion of the photon flux is absorbed in Region 1, and, therefore most sensitive to the electron diffusion length decrease as the acceptor concentration increases.

Table 5.1 shows the electron mobility and lifetime used in the device characteristic calculations; it also lists the calculated values of $L_{n1}$ and $L_{n1}/x_1$. The latter ratio is seen to be greater than unity for $3 \times 10^{18}$ cm$^{-3}$ and lower.

Table 5.1. Region 1 material parameters used in the calculation.

| $N_{Al}$ | $\mu_{n1}$ | $\tau_{n1}$ | $L_{n1}$ | $L_{n1}/x_1$ |
|---|---|---|---|---|
| $3 \times 10^{17}$ cm$^{-3}$ | 3150 $\frac{cm^2}{v-sec}$ | $5.5 \times 10^{-9}$ sec | $6.58 \times 10^{-4}$ cm | 6.58 |
| $10^{18}$ | 2425 | $5 \times 10^{-9}$ | $5.5 \times 10^{-4}$ | 5 |
| $3 \times 10^{18}$ | 1875 | $1.9 \times 10^{-9}$ | $3.0 \times 10^{-4}$ | 3.0 |
| $10^{19}$ | 1400 | $1.8 \times 10^{-10}$ | $7.9 \times 10^{-5}$ | 0.79 |

A concentration of $10^{18}$ cm$^{-3}$ has been selected for Region 1 as a compromise device parameter. The electron, hole and the electron plus hole collection efficiency and the corresponding V-I solar cell curve are presented in Figures 5.9, 5.10 and 5.11 for zero, $10^6$ and $10^7$ cm sec$^{-1}$ surface recombination velocity. The hole spectral response is independent of surface recombination velocity. From Figure 5.5 we see that the dark current is in the neighborhood of its minimum for $10^{18}$ cm$^{-3}$, therefore, there is an imperceptible change in $V_{oc}$ with increasing surface recombination velocity. However, the V-I curves shows $J_{sc}$ to decrease with increasing recombination velocity. This is reflected in the decrease of electron spectral response.

Window Layer, Region 1, Built-in Aiding Electric Field

In the preceding discussion the window layer acceptor concentration was optimized with a built-in field strength of -3000 V cm$^{-1}$. Accepting the optimized value of $10^{18}$ cm$^{-1}$, the influence of the electric field strength (and correspondingly, $\Delta E_{c1}$, APPENDIX F, Eq. (F-3)) on efficiency has been studied.

Figure 5.12 shows the conversion efficiency dependency on the aiding built-in drift field present in Region 1 with the recombination velocity a parameter. In this calculation the bandgap at the surface was maintained constant at 1.739 eV and $\Delta E_{c1}$ was changed from 0 to 0.3 volt to achieve the desired field strength. The efficiency is 22% and constant for zero recombination velocity. This arises because the diffusion length in Region 1 is greater than the Region 1 thickness and, in the absence of recombination velocity, the majority of the excess electrons diffuse into Region 2.

112
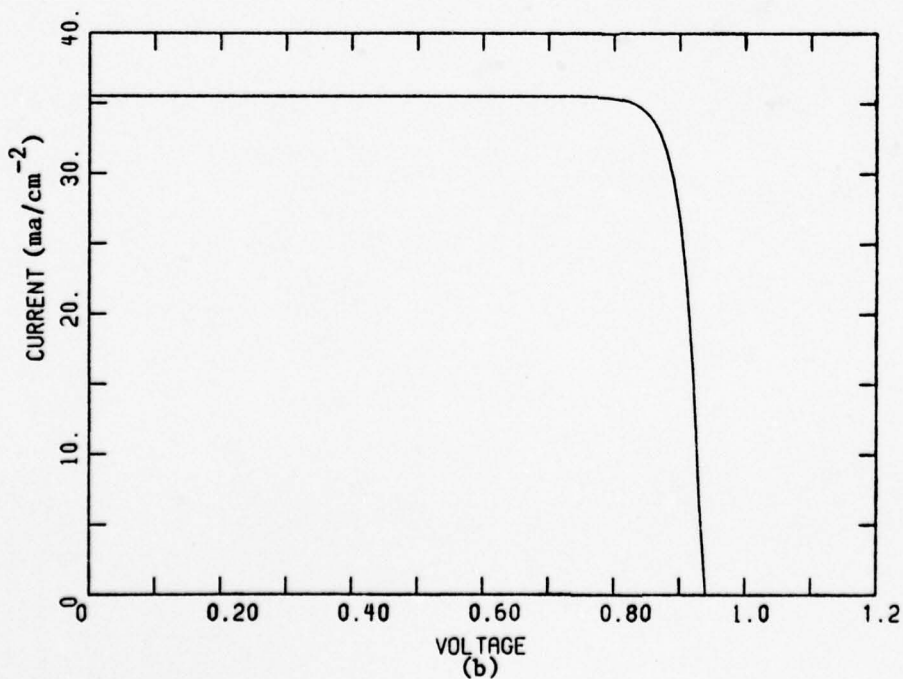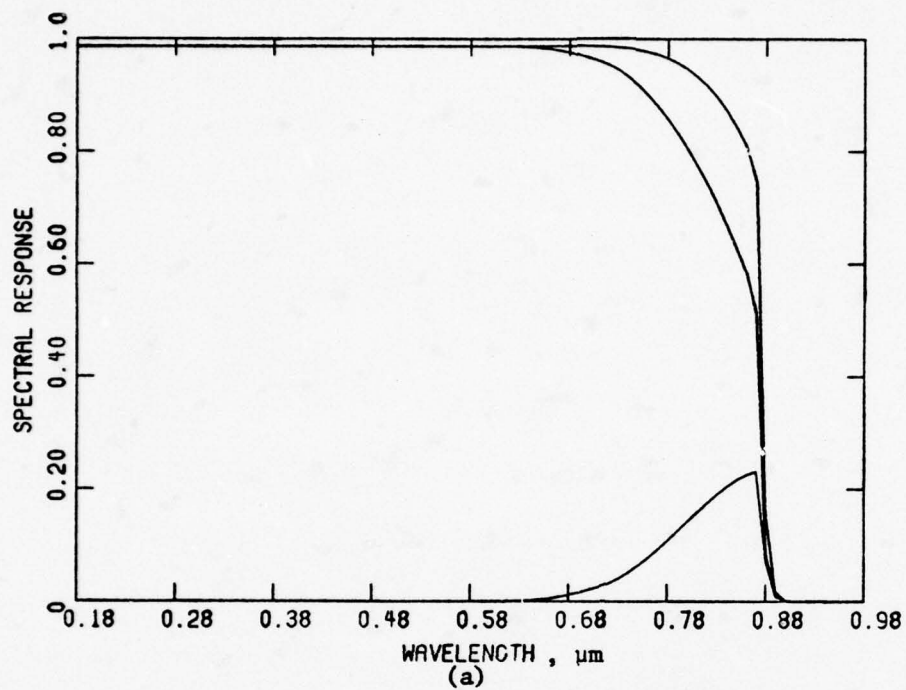
Figure 5.9. Spectral Response and V-I Solar Cell Curve for p-Al$_x$Ga$_{1-x}$As
Acceptor Concentration of $10^{18}$ cm$^{-3}$ and Zero
Surface Recombination Velocity.
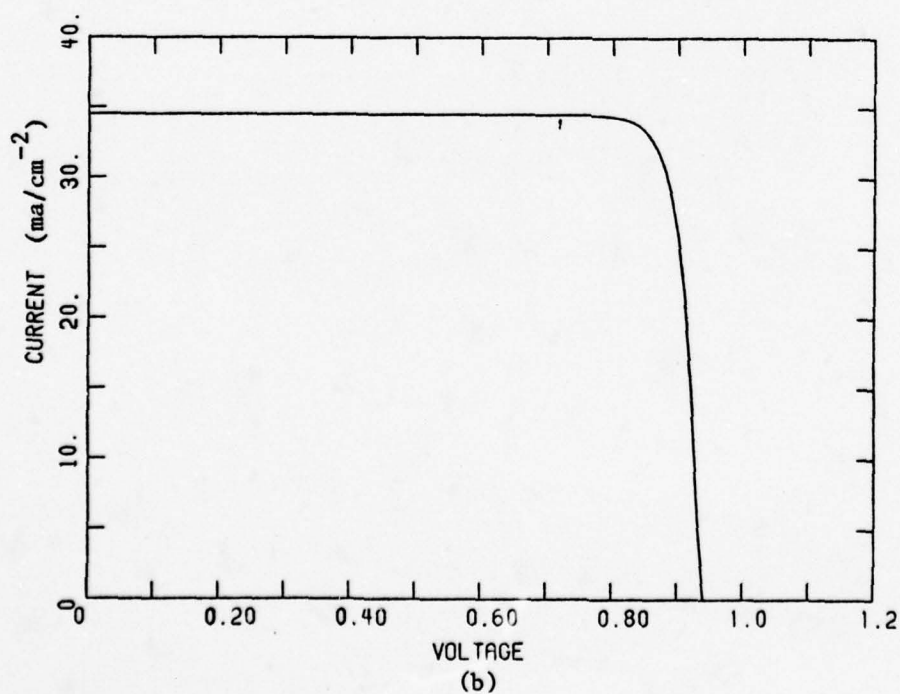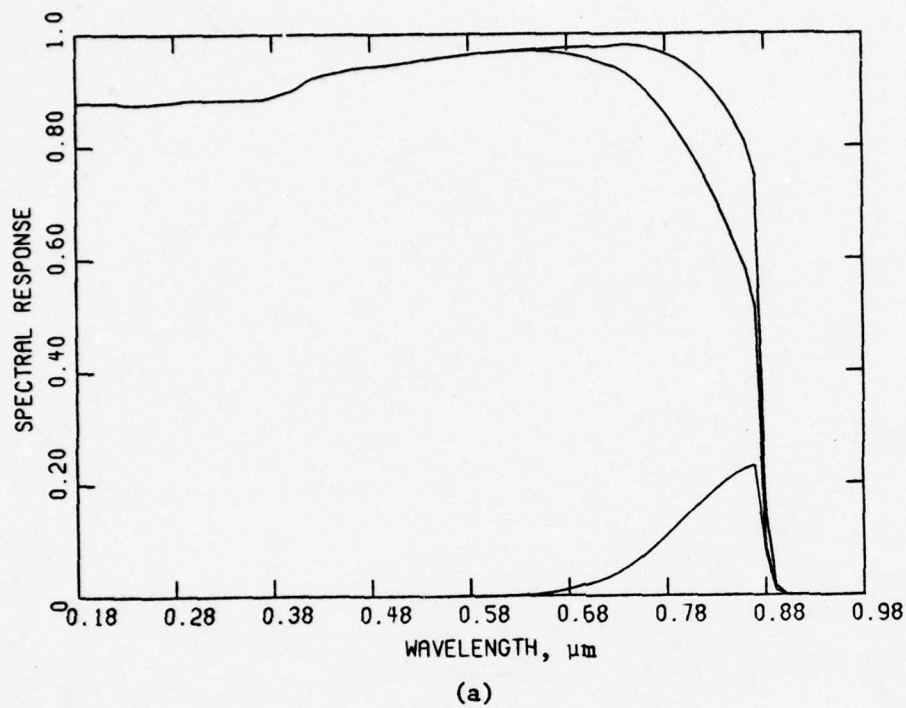
Figure 5.10. Spectral Response and V-I Solar Cell Curve for p-Al$_x$Ga$_{1-x}$As Acceptor Concentration of 10$^{18}$ cm$^{-3}$ and 10$^6$ cm sec$^{-1}$ Surface Recombination Velocity.

114
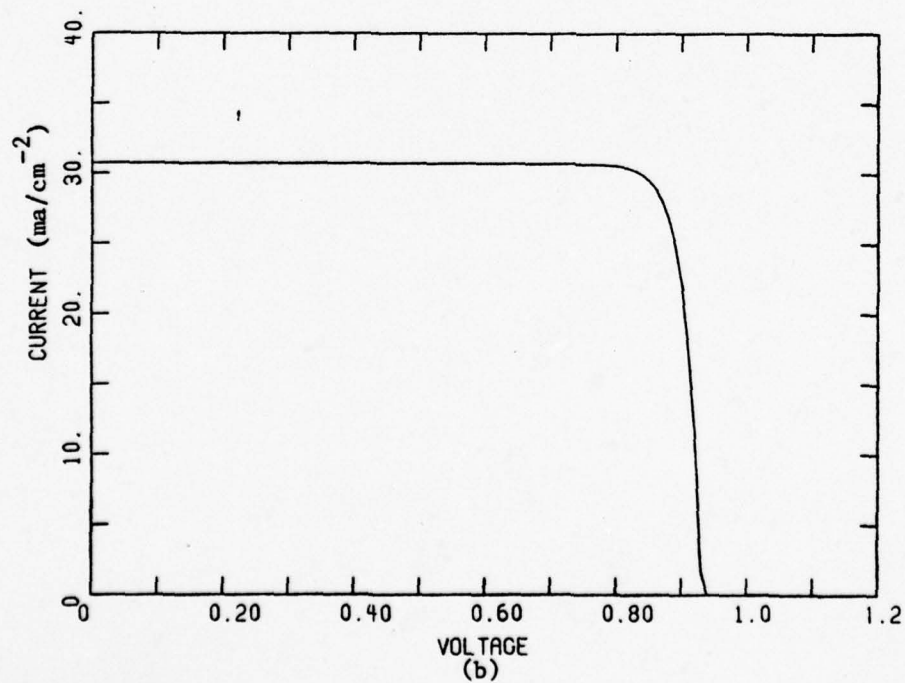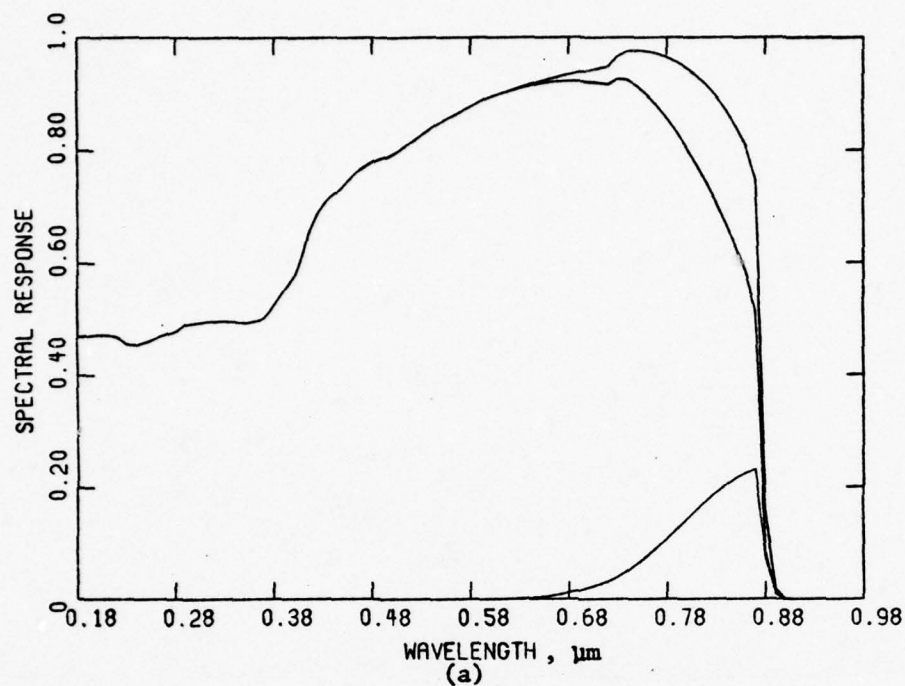
Figure 5.11. Spectral Response and V-I Solar Cell Curve for p-Al$_x$Ga$_{1-x}$As Acceptor Concentration of $10^{18}$ cm$^{-3}$ and $10^7$ cm sec$^{-1}$ Surface Recombination Velocity.
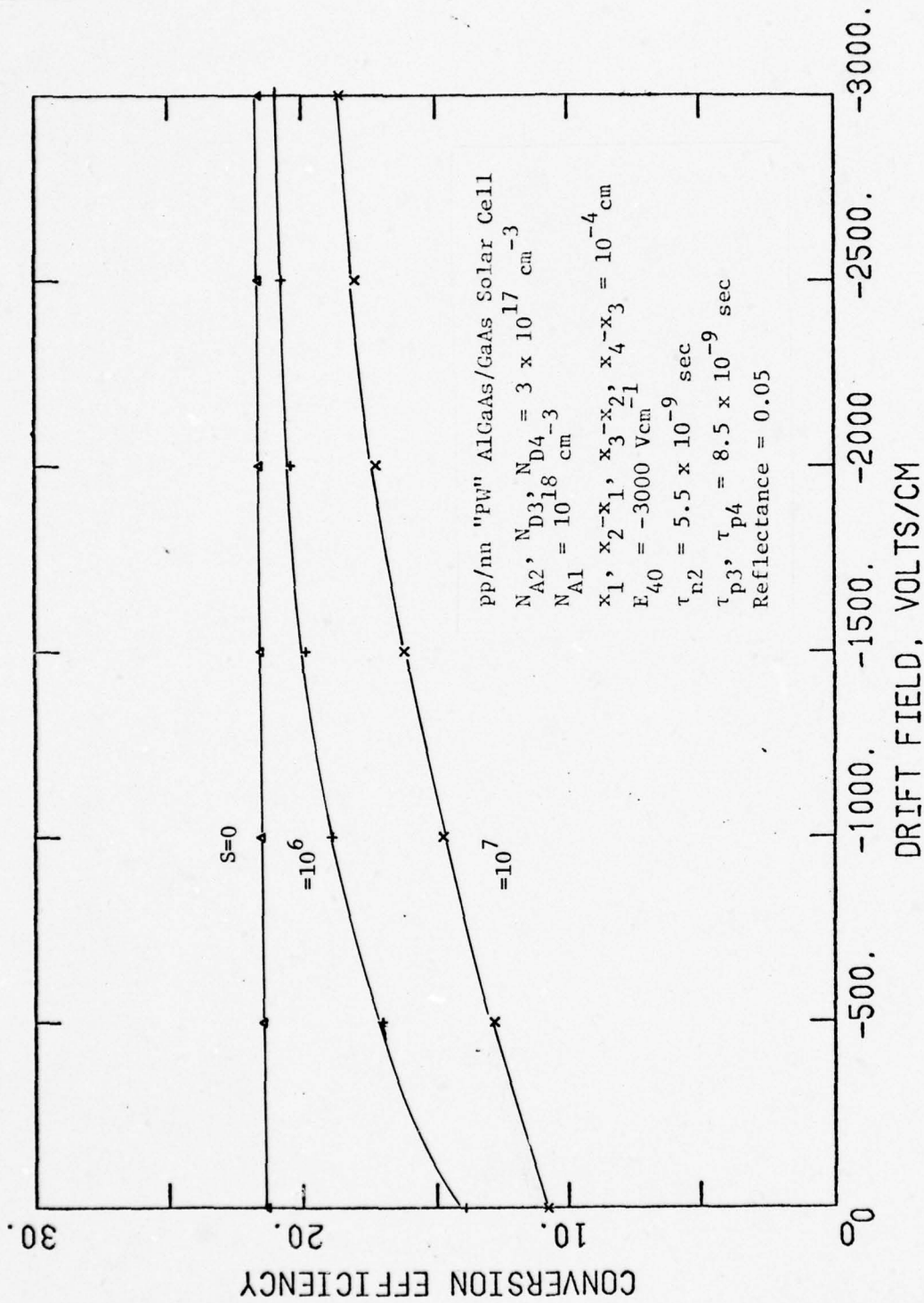
Figure 5.12. Conversion efficiency vs. drift field where the barrier height, $\Delta E_{c1}$, is changed from $0$ to $0.3$ volts and $E_{G1}(0) = 1.739$ eV.

116

The electron diffusion length in Region 2 is also greater than the Region 2 thickness and therefore, most of the electrons in Region 2 (whether produced there or not) are collected by the p-n junction.

Increasing the surface recombination velocity to $10^6$ and $10^7$ cm sec$^{-1}$ results in a significant reduction in efficiency for all field strengths, particularly at low field strengths. Efficiency increases for increasing field values. At field strengths less than 500 Vcm$^{-1}$ and $10^7$ cm sec$^{-1}$ SRV, the efficiency is reduced by 50% or more.

Figures 5.13, 5.14, and 5.15 show the total spectral response, electrons plus holes, with the field varying from 0 to -3000 Vcm$^{-1}$, for surface recombination velocity values of 0, $10^6$ and $10^7$ cm sec$^{-1}$, respectively. In the spectral region $\lambda$ < 0.73 micrometers, the field strength has only a small influence on the spectral response up to $10^7$ cm sec$^{-1}$. This is due to the window-effect of the AlGaAs Region 1. The wavelength for which the spectral response increases sharply for $E_{10} = 0$ is denoted $\lambda_w$, the window wavelength. In Figures 5.14 and 5.15, $\lambda_w$ = 0.73 micrometers. It is the shortest wavelength which is not absorbed appreciably in Region 1 allowing photons at longer wavelengths to pass through unattenuated to the pGaAs Region 2 layer. Thus, in this spectral region the recombination velocity has almost no influence.

In Figure 5.13, for which the surface recombination velocity is zero, the spectral response exhibits only small changes. However, for high recombination velocity, there is a strong field dependency in the spectral region $\lambda$ < $\lambda_w$ as indicated in Figures 5.14 and 5.15. Moreover, for a given recombination velocity the influence of the field strength on the response in the region $\lambda$ < 0.38 micrometers is very nearly uniform. In

117
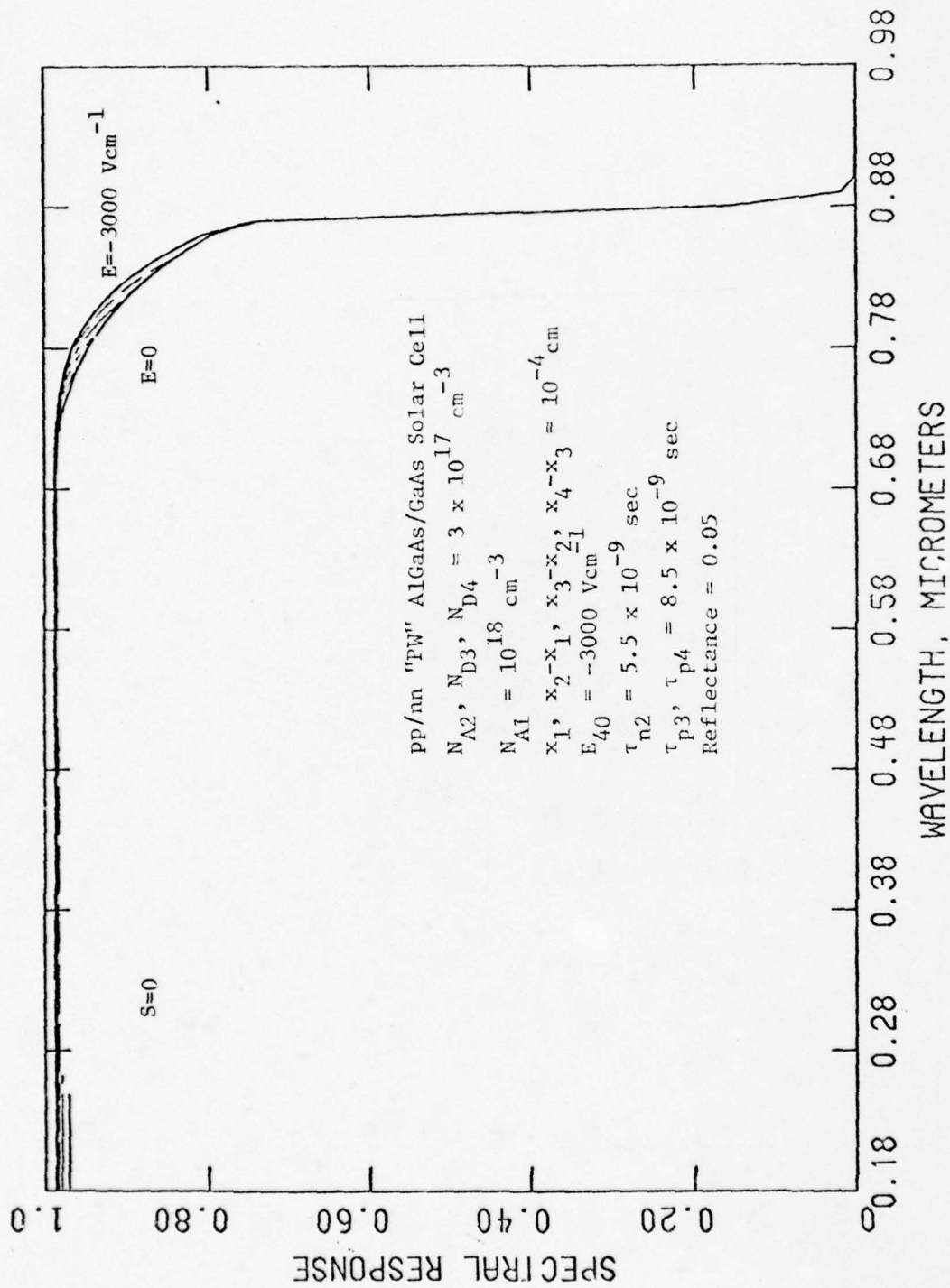
Figure 5.13. Total spectral response with the aiding built-in field a parameter for zero recombination velocity where the barrier height, $\Delta E_{c1}$, is changed from 0 to 0.3 V and $E_{G1}(0) = 1.739$ eV.

118

WAVELENGTH, MICROMETERS

SPECTRAL RESPONSE

pp/nn "PW" AlGaAs/GaAs Solar Cell

$N_{A2}$, $N_{D3}$, $N_{D4} = 3 \times 10^{17}$ $cm^{-3}$

$N_{A1} = 10^{18}$ $cm^{-3}$

$x_1$, $x_2-x_1$, $x_3-x_2$, $x_4-x_3 = 10^{-4}$ $cm$

$E_{40} = -3000$ $Vcm^{-1}$

$\tau_{n2} = 5.5 \times 10^{-9}$ sec

$\tau_{p3}$, $\tau_{p4} = 8.5 \times 10^{-9}$ sec

Reflectance = 0.05

$S = 10^6$ $cm\ sec^{-1}$

E=-3000 $Vcm^{-1}$
-2500
-2000
-1500
-1000
-500
0
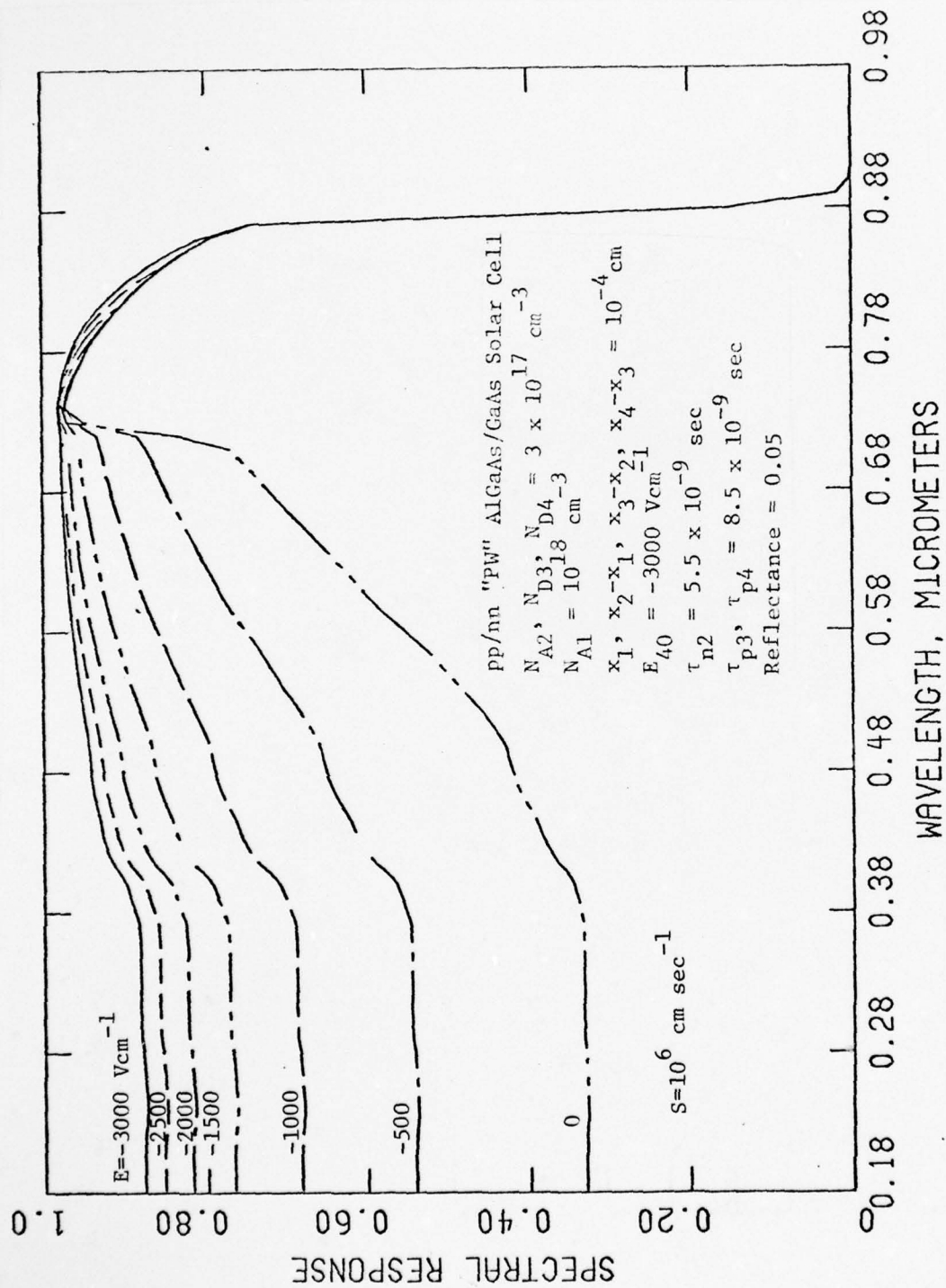
Figure 5.14. Total spectral response with the aiding built-in field a parameter for $10^6$ cm $sec^{-1}$ recombination velocity where the barrier height, $\Delta E_{c1}$, is changed from 0 to 0.3 V and $E_{G1}(0) = 1.739$ eV.

119
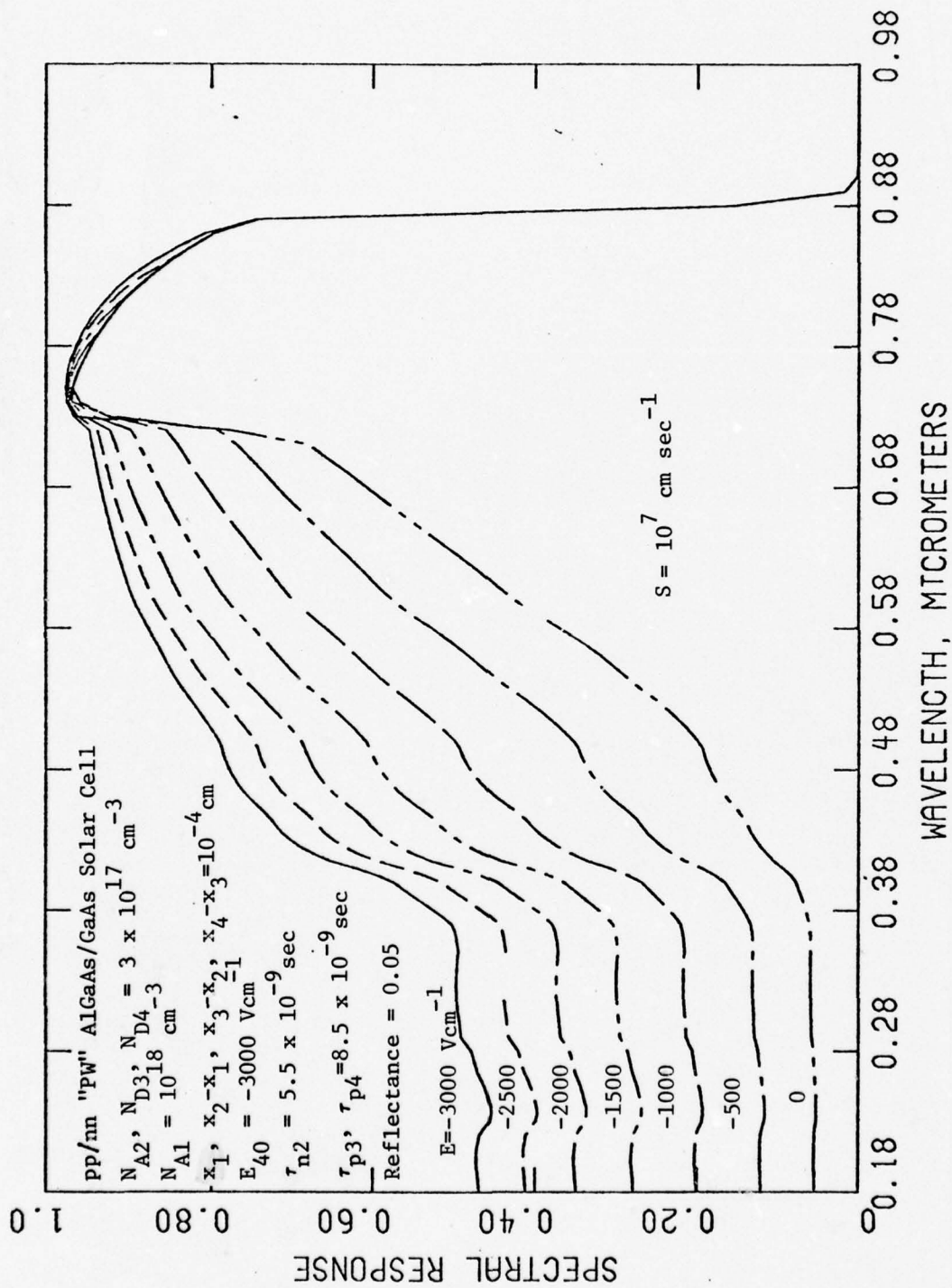
Figure 5.15. Total spectral response with the aiding built-in field a parameter for $10^7$ cm sec$^{-1}$ recombination velocity where the barrier height, $\Delta E_{c1}$, is changed from 0 to 0.3 V and $E_{G1}(0) = 1.739$ eV.

120

this spectral region of Figure 5.14 for which the recombination velocity is $10^6$ cm sec$^{-1}$, there is nearly a 300% improvement as the field strength is increased to −3000 Vcm$^{-1}$. In contrast, when the recombination velocity is increased to $10^7$ cm sec$^{-1}$, Figure 5.15 shows an order of manitude improvement in response between 0 and −3000 Vcm$^{-1}$ in this spectral region. This spectral region, $\lambda < 0.38$ micrometers, represents the region over which the absorption coefficient is greater than $10^6$ cm$^{-1}$ in Region 1. This suggests that excess electrons produced in the range 100 to 300 A° from the surface are those which are greatly affected by the surface recombination velocity and the field strength. The estimate of the thickness over which surface recombination losses occur is consistent with the discussion in APPENDIX F (Eq. (F-19)).

The influence of field on electron and hole spectral response is shown in Figure 5.16 for $10^7$ cm sec$^{-1}$ surface recombination velocity. The structure of the −3000 Vcm$^{-1}$ field case has the bandgap linearly decreasing from 1.739 eV at the surface to 1.439 eV at $x_1$. The 0.3 volt drop over one micrometer results in the −3000 Vcm$^{-1}$ field strength. For the zero field case, the bandgap in the AlGaAs Region 1 layer is constant at 1.739 eV. The latter case results in greater absorption in Region 1 in the photon energy range above 1.739 eV (0.713 micrometers), while this wavelength the photons traverse Region 1 unattenuated.

Due to the increased flux beyond $\lambda_w$ for the zero field case, the hole spectral response in the n-type Region 3 is greater than for the high field case. The difference between the hole response curves in Figure 5.16 is a measure of the higher incident flux on Region 3. At the same time, recombination losses (surface and bulk) are higher in Region 1 in the absence

121
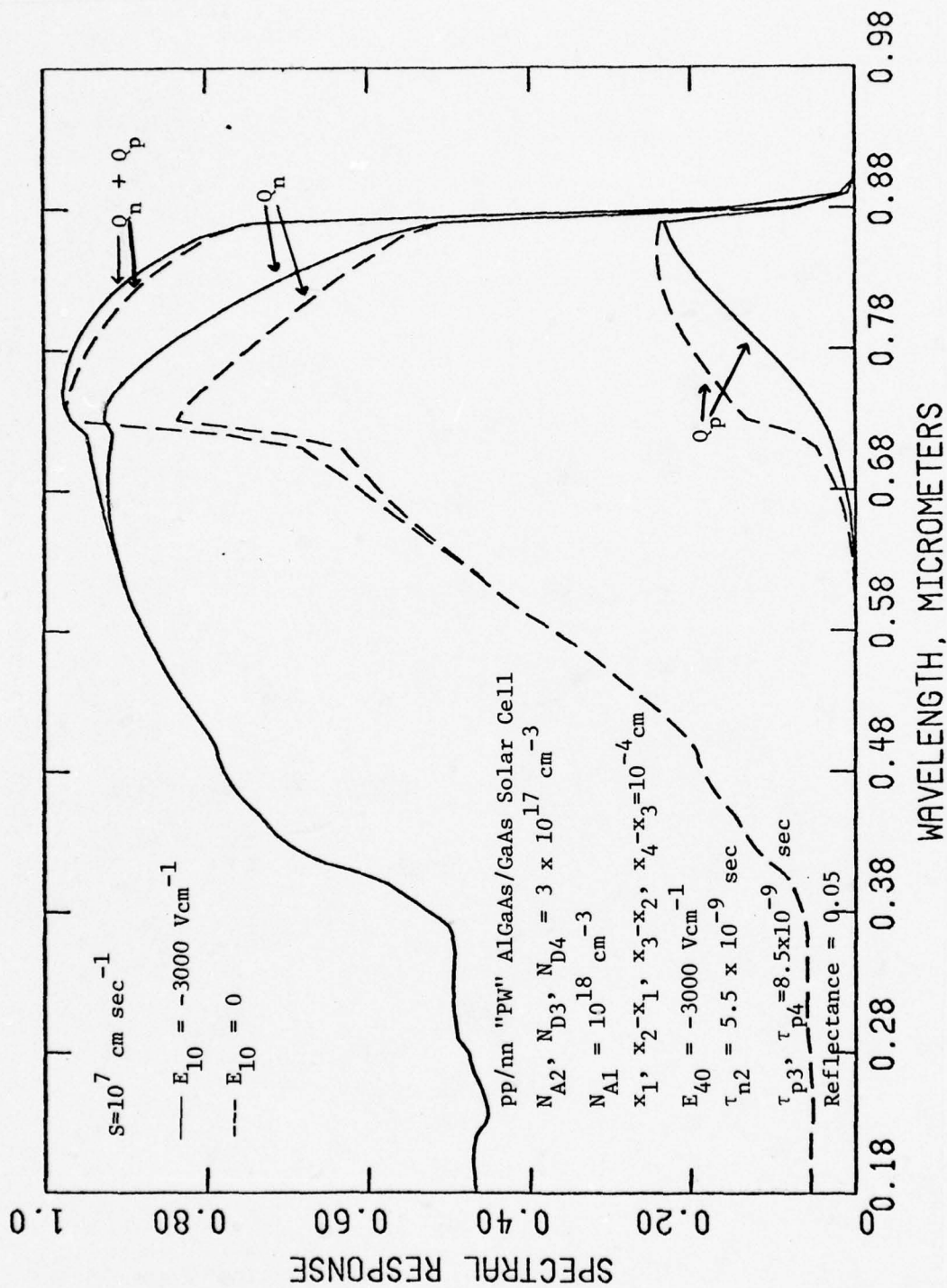
Figure 5.16. The spectral response for electrons, holes and the sum for $10^7$ cm sec$^{-1}$ recombination velocity and 0 and $-3000$ Vcm$^{-1}$ field strengths.

of an aiding field. Therefore, the difference between electron response curves in Figure 5.16 in the range $\lambda < \lambda_w$ is a measure of the increased losses. The increase in electron response for the high field case in the range $\lambda < \lambda_w$ is due to the collection of excess electrons in Region 1. In the region $\lambda < \lambda_w$ the net electron and hole responses do not compensate and result in a slightly higher response for the high field case.

In Section 2.0 we discussed the useful design functions which the Region 1 AlGaAs serve. One of these is a conduction path for terminal current. In this connection, a low resistance conducting path, obtained through optimized design of doping level and thickness in Region 1, is desired. The competing design parameters are electrons diffusion length, photon flux absorbed through the layer and sheet resistance. Figure 5.2 shows the conversion efficiency vs. Region 1 acceptor concentration, with surface recombination velocity as a parameter. These calculations show that efficiency drops significantly when the acceptor concentration, approaches $10^{19}$ cm$^{-3}$. The percentage change is approximately 10% for all values of S. At lower field strengths the percentage change is greater for a given S value.

## Temperature Behavior

High temperature operation is one of the advantages of GaAs and other wide bandgap III-V solar cells over Si cells. This is especially important in concentrator systems.

The maximum power output from a solar cell can be written as

$$P = F \, V_{oc} I_{sc} \tag{5-1}$$

123

where $V_{oc}$ and $I_{sc}$ are the open circuit voltage and short circuit current, respectively, and F is the V-I curve fill factor. The change in power output with respect to temperature may be written as [3]

$$\frac{dP}{dT} = P \left[ \frac{d\ell nF}{dT} + \frac{d\ell nV_{oc}}{dT} + \frac{d\ell nI_{sc}}{dT} \right] \tag{5-2a}$$

or in normalized form as

$$\frac{d\ell nP}{dT} = \frac{d\ell nF}{dT} + \frac{d\ell nV_{oc}}{dT} + \frac{d\ell nI_{sc}}{dT} \tag{5-2b}$$

The change in conversion efficiency at AMO is given by

$$\frac{d\eta}{dT} = \frac{1}{0.1353} \frac{dP}{dT} \tag{5-3}$$

where P is given in watts per cm $^2$. The first and second terms in Eqs. (5-2a) and (5-2b) are almost always negative while the third term tends either to increase slightly or remain constant (it is almost never negative). The typical increase in $I_{sc}$ with increasing temperature, however, is usually not sufficient to offset the decrease in $V_{oc}$ and F, leading to decreasing power output with increasing temperature. The temperature coefficients for power output, Eq. (5-2a), and for conversion efficiency, Eq. (5-3), are convenient and practical figure-of-merits for solar cells. From Eqs. (5-2a) and (5-3) we note that both temperature coefficients are linearly proportional to the power. Therefore, higher efficiency cells and/or cells subjected to concentrated incident solar energy will exhibit higher temperature coefficients. Thus, in comparing cells the normalized form, Eq. (5-2b) may be enlightening.

Table 5.2 shows the temperature coefficients for GaAs and Si
cells [5-3, 5-4]. The efficiency of these cells at ambient temperature
is comparable ($\simeq$ 11%) so that the terms in Eq. (5-2a) are listed. These
data show that the temperature coefficient for output power of the GaAs
cell is only one-half of the Si cell value. The logarithmic changes
of $V_{oc}$ and F are of a smaller magnitude for GaAs than for Si. On the
other hand the short circuit current increase is greater for Si than
it is for GaAs.

Table 5.2.   Temperature changes in power output [5-3, 5-4].

|  | $P \dfrac{d\ln(I_{sc})}{dT}$ | $P \dfrac{d\ln(V_{oc})}{dT}$ | $P \dfrac{d\ln(F)}{dT}$ | $\left(\dfrac{dP}{dT}\right)$ Meas. |
|---|---|---|---|---|
| GaAs | + 0.018 | − 0.044 | − 0.030 | − 0.050 mw/°C |
| Si | + 0.024 | − 0.091 | − 0.046 | − 0.095 mw/°C |

Figure 5.17 shows the PW calculated cell efficiency as a function of
temperature where the initial efficiency at 290°K is approximately 20%.
The slope of the S = 0 curve is constant at 0.0544%/°C or 0.074 mw/°C.
This calculated value is approximately 50% higher than the measured GaAs
value in Table 5.2. However, if the temperature coefficient is normalized
with respect to power output, the measured normalized coefficient is
0.0034/°C while the PW cell calculated value is 0.0027/°C which is in
fair agreement considering that the cells are of different structure. While
the curves for $10^6$ and $10^7$ cm sec$^{-1}$ surface recombination velocity show
a slight bowing, they are represented to  a fair approximation by the same

125
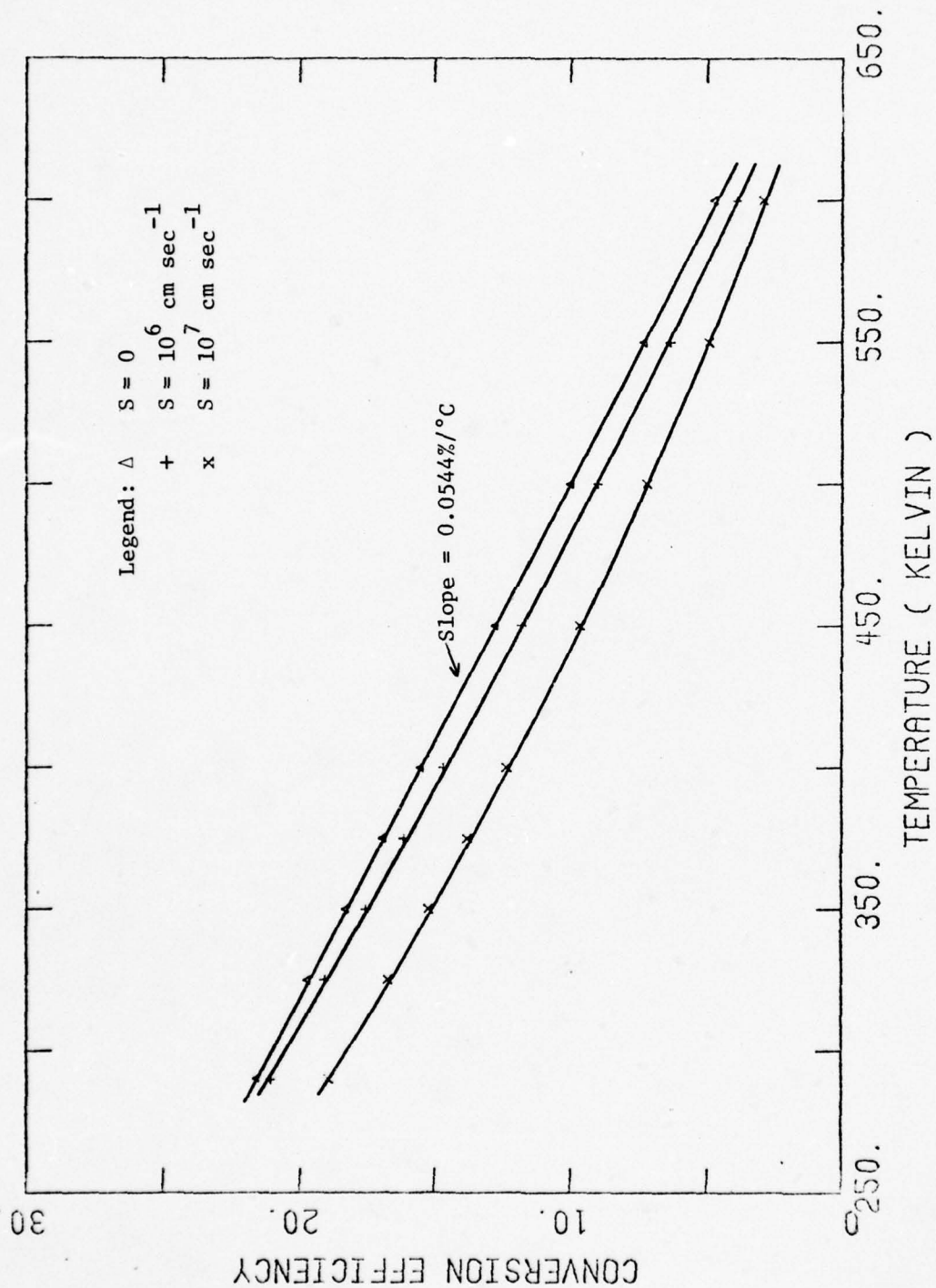
Figure 5.17. Efficiency vs. Temperature. The structure parameters are: $x_1$, $x_2-x_1$, $x_4-x_1$, $x_4-x_3 = 10^{-4} \mu m$; $E_{G1}(0) = 1.739$ eV, doping levels in Regions 1, 2, 3 and 4 are $3 \times 10^{17}$ cm$^{-3}$.

126

slope as for the zero recombination velocity. The slopes of the $10^6$ and $10^7$ compared to zero recombination velocity are slightly higher in the region < 450°K but smaller in the region > 450°K.

The major material and structural parameters which give rise to the efficiency decrease have also been studied. As shown in the analysis of APPENDIX E, temperature affects the V-I curve. The effect of temperature is observed through $I_{sc}$, $V_{oc}$ and F in the power relationship, Eq. (5-1). The V-I curve, $I_{sc}$, $V_{oc}$ and F are all greatly influenced by the diffusion length. Diffusion length almost always decreases with increasing temperature above ambient. The decrease in diffusion length arises directly from the mobility dependence on temperature, since in general the diffusion length is given by

$$L = \sqrt{\frac{kT}{q} \mu \tau} \qquad (5-4)$$

In the calculation of temperature behavior, the electron mobility temperature dependency was taken to be $T^{-2.3}$ for electrons and $T^{-2}$ for holes [5-52]. While the lifetime usually increases with increasing temperature above ambient, in these calculations the lifetime value reported at 290°K was used throughout the range 290 to 600°K. To the degree that this occurs, the temperature calculations are conservative. Therefore, in Eq. (5-4) the diffusion length for electrons is proportional to $T^{-1.15}$ and for holes at $T^{-1}$. This functional dependence is shown in Figure 5.18 for electron and hole diffusion length in their respective regions, denoted by the subscripts 1, 2, 3 and 4.

127
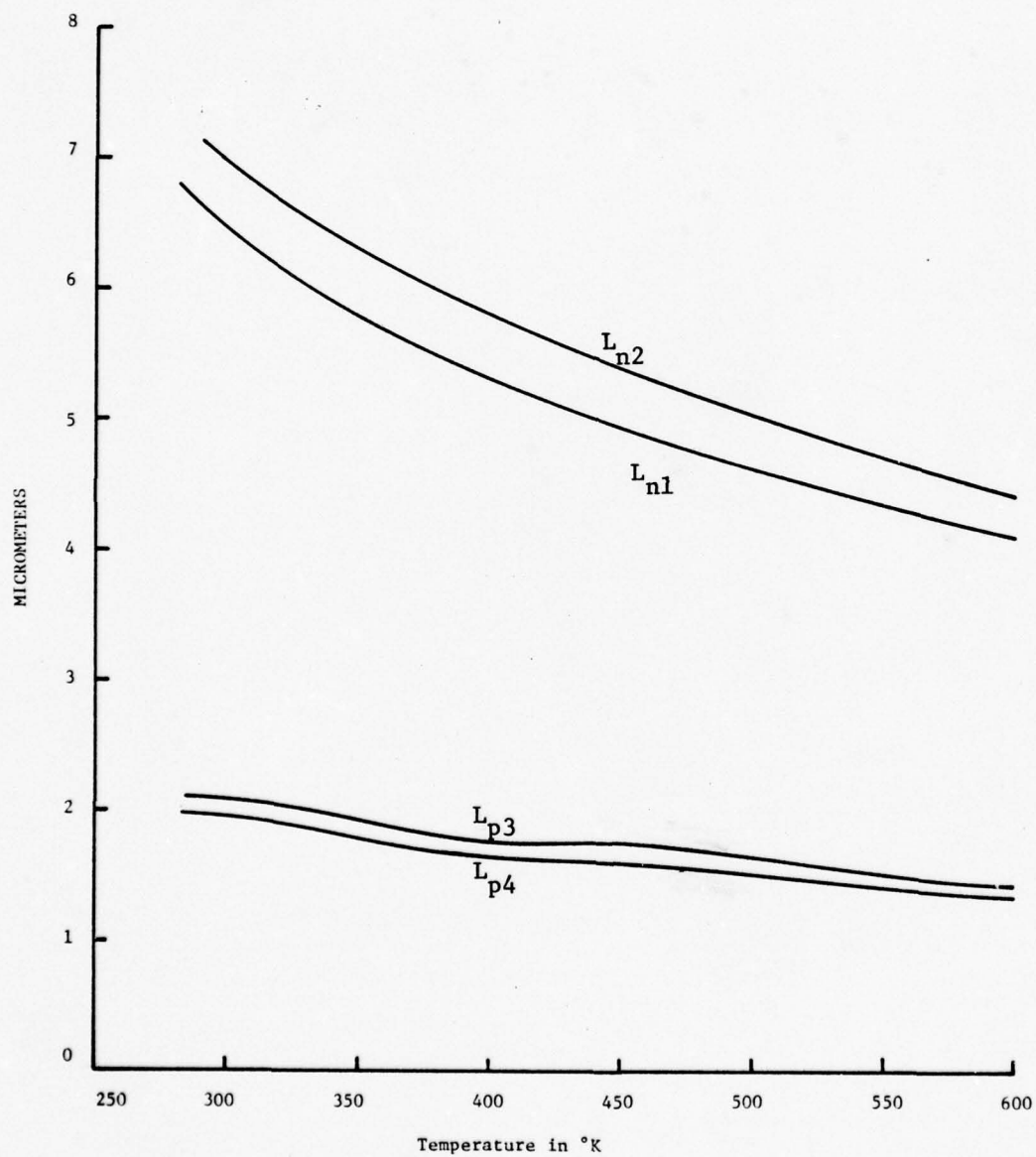
Figure 5.18.  Minority Electron and Hole Diffusion Length vs.
Temperature in each of the Regions of the PW Cell
Structure.

128

The short circuit current may be sensitive to temperature through the minority carrier diffusion length and bandgap narrowing. Figure 5.19 shows the short circuit current vs. temperature for 0, $10^6$ and $10^7$ cm sec$^{-1}$ surface recombination velocity. In the absence of surface recombination loss, the short circuit current increases due to bandgap narrowing, and is the dominant mechanism with increasing temperature. As the surface recombination loss increases, SRV increasingly compensates for the current increase due to bandgap narrowing. For $10^6$ cm sec$^{-1}$ recombination velocity the short circuit current is shown to decrease slightly with increasing temperature while at $10^7$ cm sec$^{-1}$ the current decrease is greater than for $10^6$ cm sec$^{-1}$.

The assumed general expression for the direct bandgap temperature dependency is

$$E_{Gd} (x,T) = E_{Gd} (x,0°K) - \left( \frac{dE_{Gd}}{dT} \right)_x T \qquad (5-5)$$

where x is the alloy composition, $E_{Gd} (x,0°K)$ the extrapolated direct bandgap value at 0°K and of composition x and $\left( \frac{dE_{Gd}}{dT} \right)_x$ is the direct band-gap temperature coefficient in the region 250 to 600°K. The bandgap of the alloy at 0°K is given by [5-41].

$$E_{Gd} = 0.468 \ x^2 + 1.042 \ x + 1.544 \ . \qquad (5-6)$$

This expression is similar to the relationship used at elevated temperature in which the constant term, 1.544, has been determined to give consistent results over the temperature range of interest. The temperature coefficient
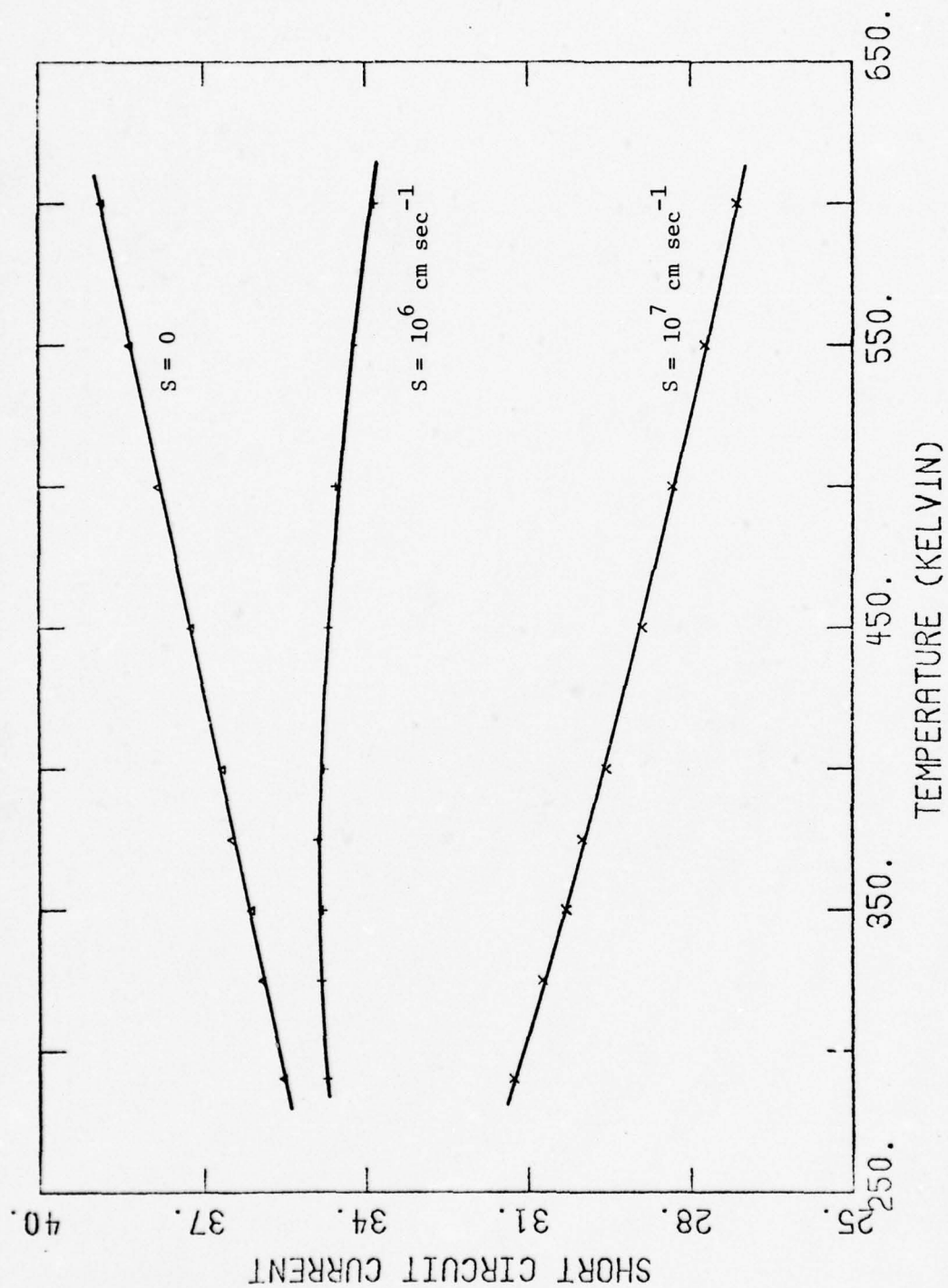
Figure 5.19. Short-circuit current vs. temperature with surface recombination a parameter.

130

for GaAs is $3.6 \times 10^{-4}$ eV/°K [5-48] and for AlAs, it is $4 \times 10^{-4}$ eV/°K [5-48]. The coefficient for the alloy $Al_xGa_{1-x}As$ is assumed to be a linear extrapolation given by

$$\left(\frac{dE_{Gd}}{dT}\right)_x = \left(\frac{dE_{Gd}}{dT}\right)_{AlAs} - \left[\left(\frac{dE_{Gd}}{dT}\right)_{AlAs} - \left(\frac{dE_{Gd}}{dT}\right)_{GaAs}\right](1-x). \quad (5-7)$$

The bandgap relationship for GaAs becomes

$$E_{Gd}(T) = 1.544 - 3.63 \times 10^{-4} T. \quad (5-8)$$

For the alloy, $E_{Gd}$ is calculated from Eq. (5-6) and $\left(\frac{dE_{Gd}}{dT}\right)_x$ from Eq. (5-7) and substituted into Eq. (5-5). The bandgap values at a given temperature, T, are then entered as input parameters into the computer program. Moreover, the bandgap changes are also required in the calculation of the intrinsic carrier concentration given by

$$n_i(x,T) = n_i(x,T_1) e^{-\frac{1}{2}\left[E_{Gd}(x,T)/kT - E_{Gd}(x,T_1)/kT_1\right]}. \quad (5-9)$$

Due to the different rates of bandgap narrowing with temperature, the built-in field values in Regions 1 and 4 may decrease slightly to -2900 from -3000 $Vcm^{-1}$.

The total spectral response (electrons plus holes) of the solar cell is shown in Figure (5.20) with temperature as a parameter. This family of curves shows that while the response decreases in the spectral region $\lambda < 0.8$ μm it increases in the region $\lambda > 0.8$ μm. The wavelength point at which this crossover occurs increases with increasing temperature. In the region $\lambda < 0.38$ μm the response decreases by 30% from 325 to 600°K.

131
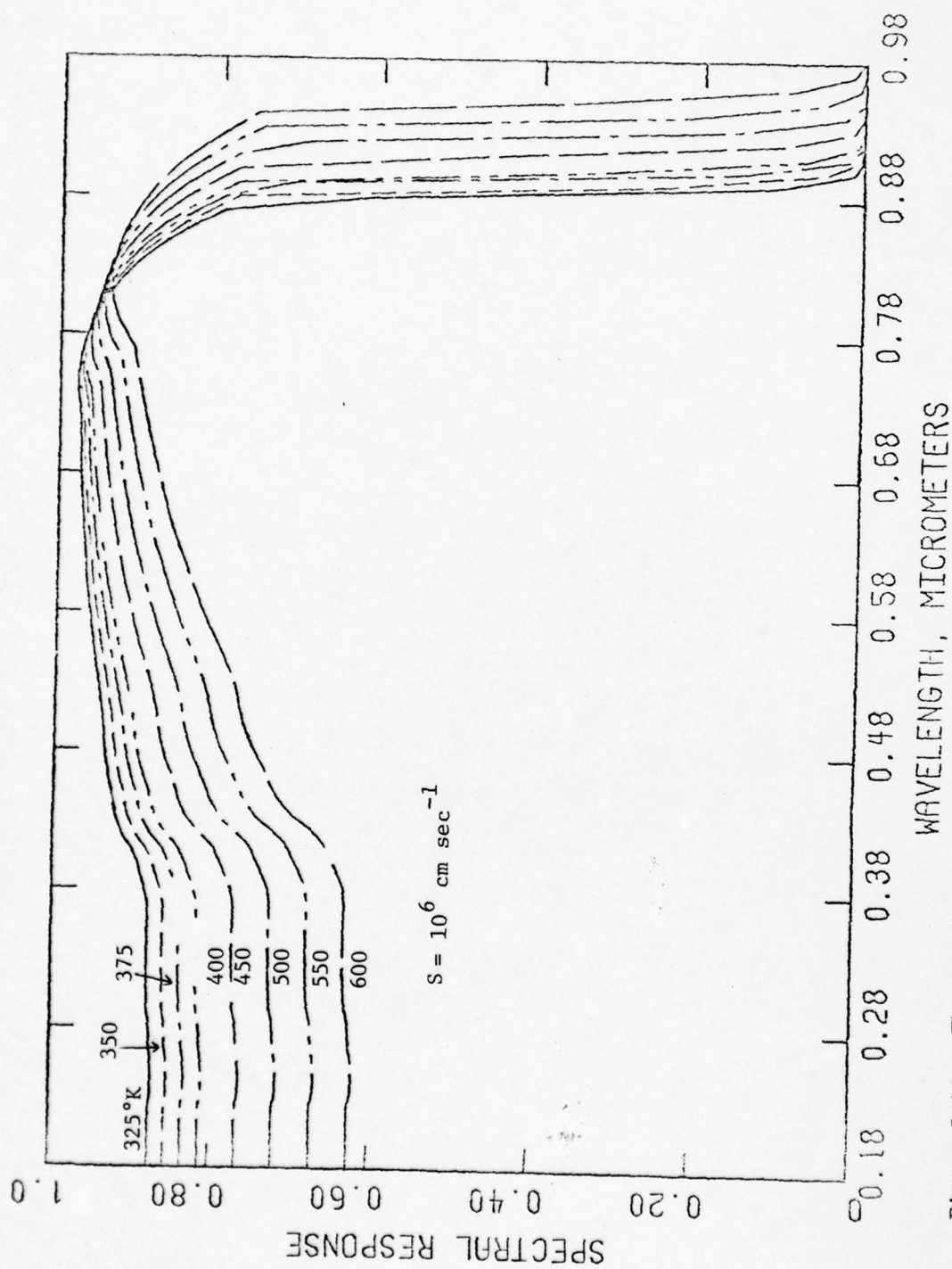
Figure 5.20. The total spectral response (electrons plus holes) in the temperature range 325 to 600°K.

Similarly, it is seen in Figure (5.18) that each of the diffusion lengths also decrease, approximately, 30% in this temperature range. Thus, we can attribute the decrease in response in the region $\lambda < 0.8$ μm to the decrease in diffusion length. On the other hand, the increase in the range $\lambda < 0.8$ μm is due entirely to bandgap narrowing and the increased photon absorption. This is clearly seen in Figure (5.20) by the cut-off wavelength increasing to higher values with increasing temperature, from 0.90 to 0.98 μm. The response for 290°K is only slightly better than the 325°K and was not shown for that reason.

Figures (5.21(a)), (5.21(b)), and (5.21(c)) show the electron, hole and total response for 325, 400 and 600°K and surface recombination velocities of 0, $10^6$, and $10^7$ cm sec, respectively. In general for $\lambda < 0.38$ μm, the change from 290 to 325°K is only of the order of 1 to 3%.

The voltage at the maximum power point on the V-I curve, $V_{max}$, and $V_{oc}$ are plotted as a function of temperature in Figure (5.22) for $10^6$ cm sec$^{-1}$ recombination velocity. These calculations show the rapid drop off in photovoltage with increasing temperature. Since the short circuit current for $10^6$ cm sec$^{-1}$ is not very sensitive to temperature, the dark current is the device parameter with is responsible for the decrease in voltage. This is seen in Figures (5.23) where the sum of the saturation currents multiplied by the appropriate R- factors, $R_n$ or $R_p$, for electrons and holes are calculated as a function of temperature. (Referring to the analysis in APPENDIX E, the ordinate is the sum of Eqs. (E-27) and (E-63) divided by $(e^{qV_2/kT}-1)$ where $V_2$ is the photovoltage at the homojunction.) The sum increases by many orders of magnitude which serves to greatly reduce the photovoltage.

133

WAVELENGTH, MICROMETERS
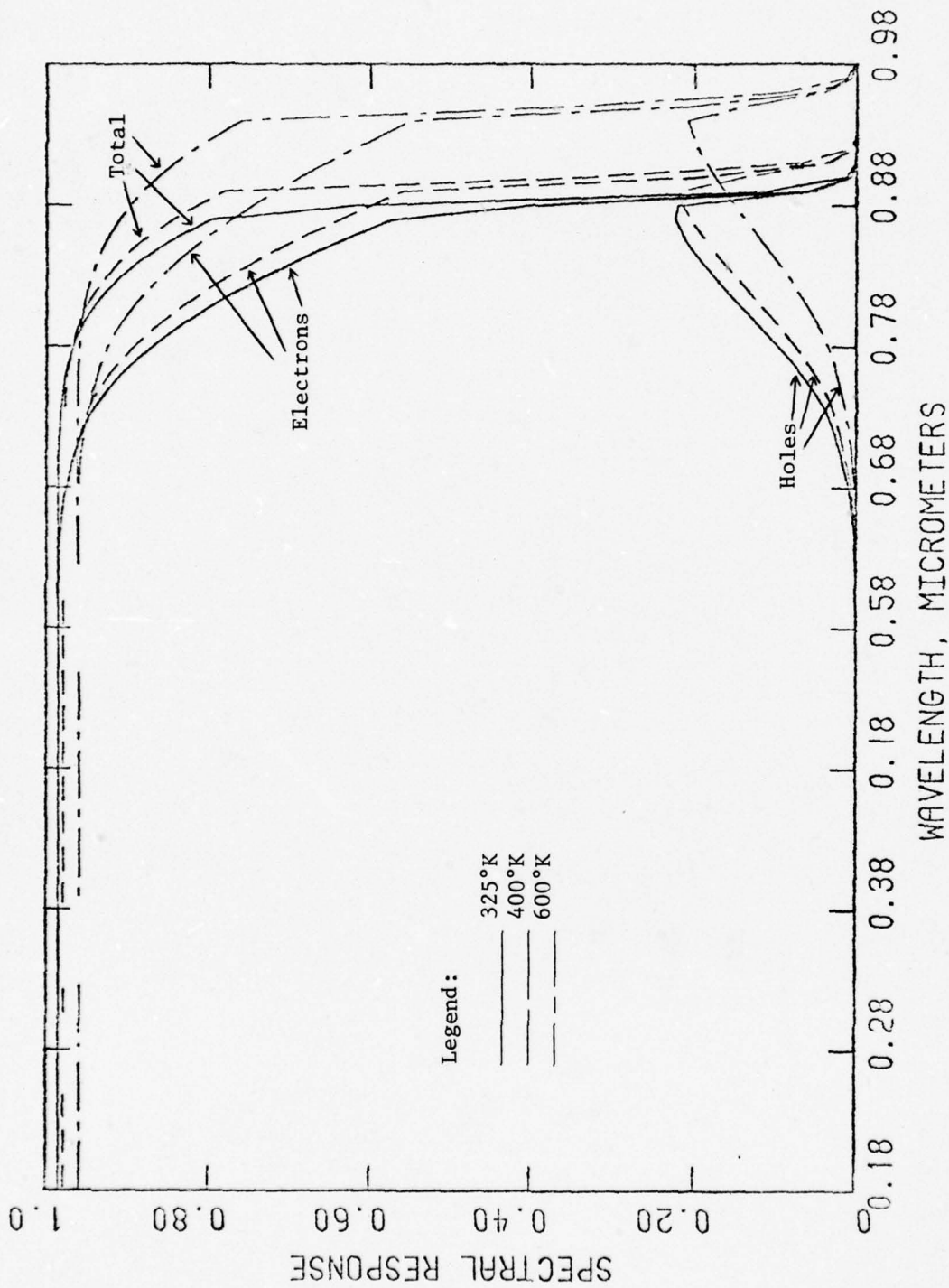
Figure 5.21(a).   The electron, hole and total spectral response for 325, 400, 600°K and S = 0.

134
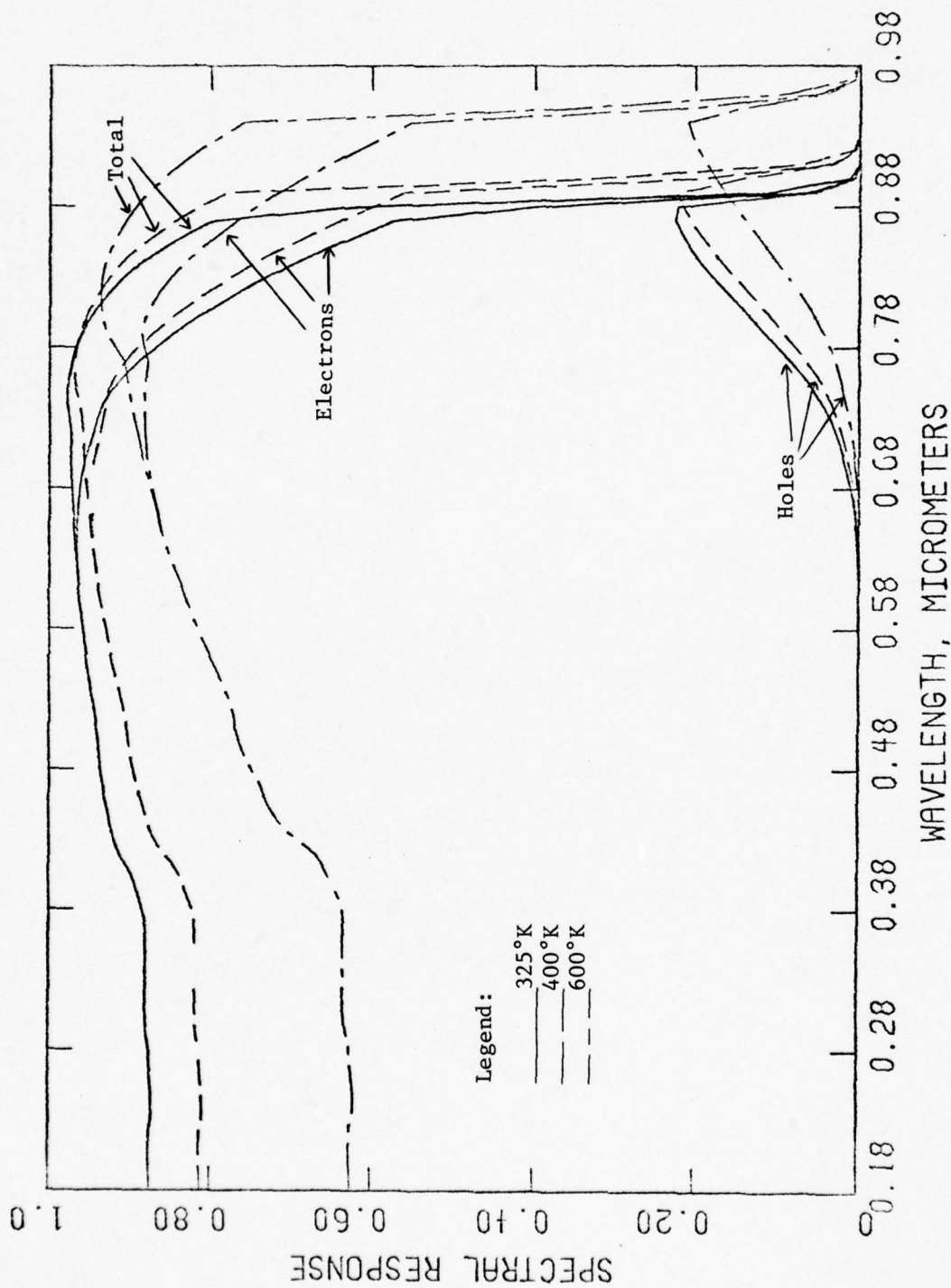
Figure 5.21(b). The electron, hole and total spectral response for 325, 400, 600°K and
S = $10^6$ cm sec$^{-1}$.

135
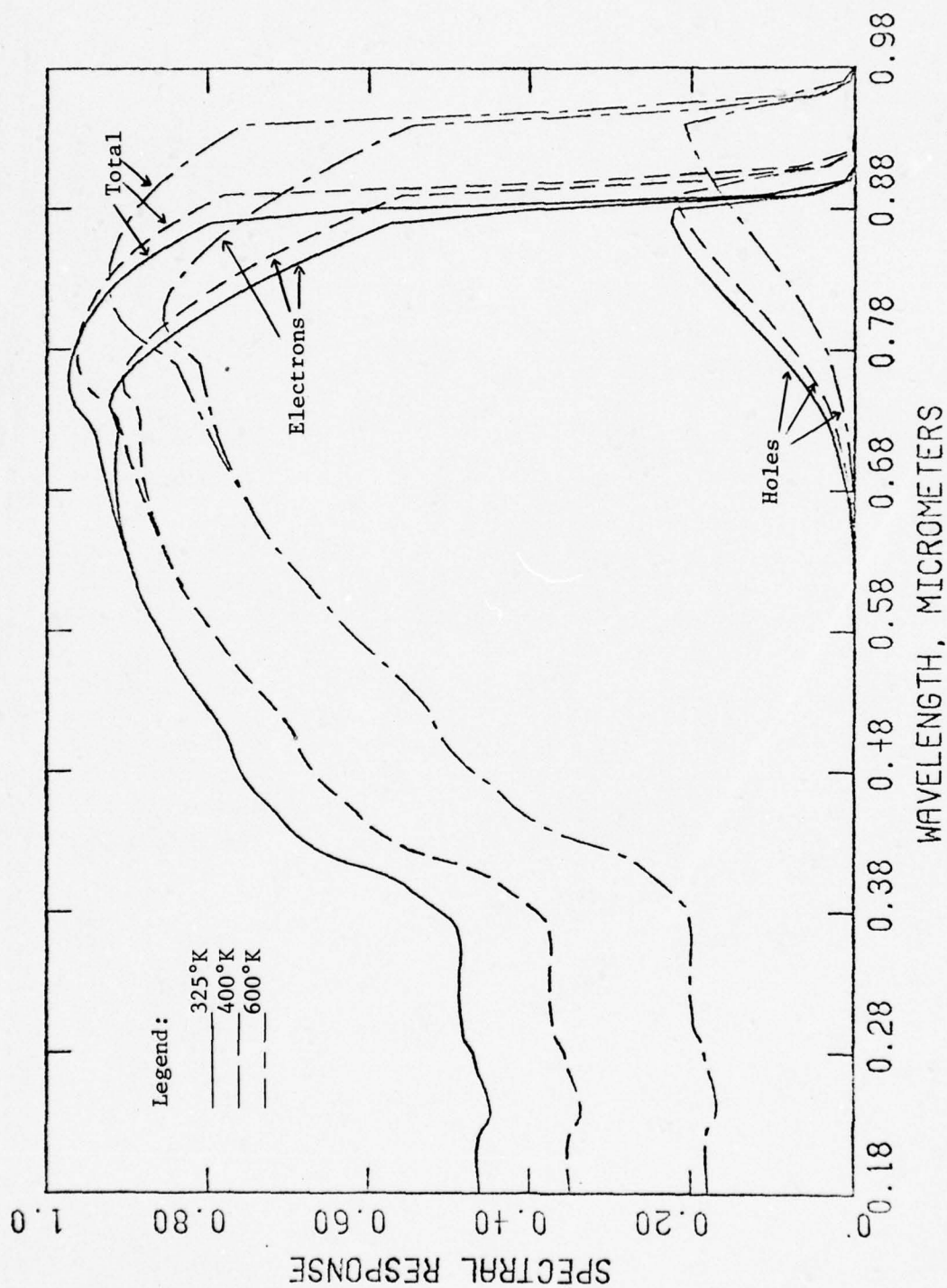
Figure 5.21(c)   The electron, hole and total spectral response for 325, 400, 600°K and S = $10^7$ cm sec$^{-1}$.

136
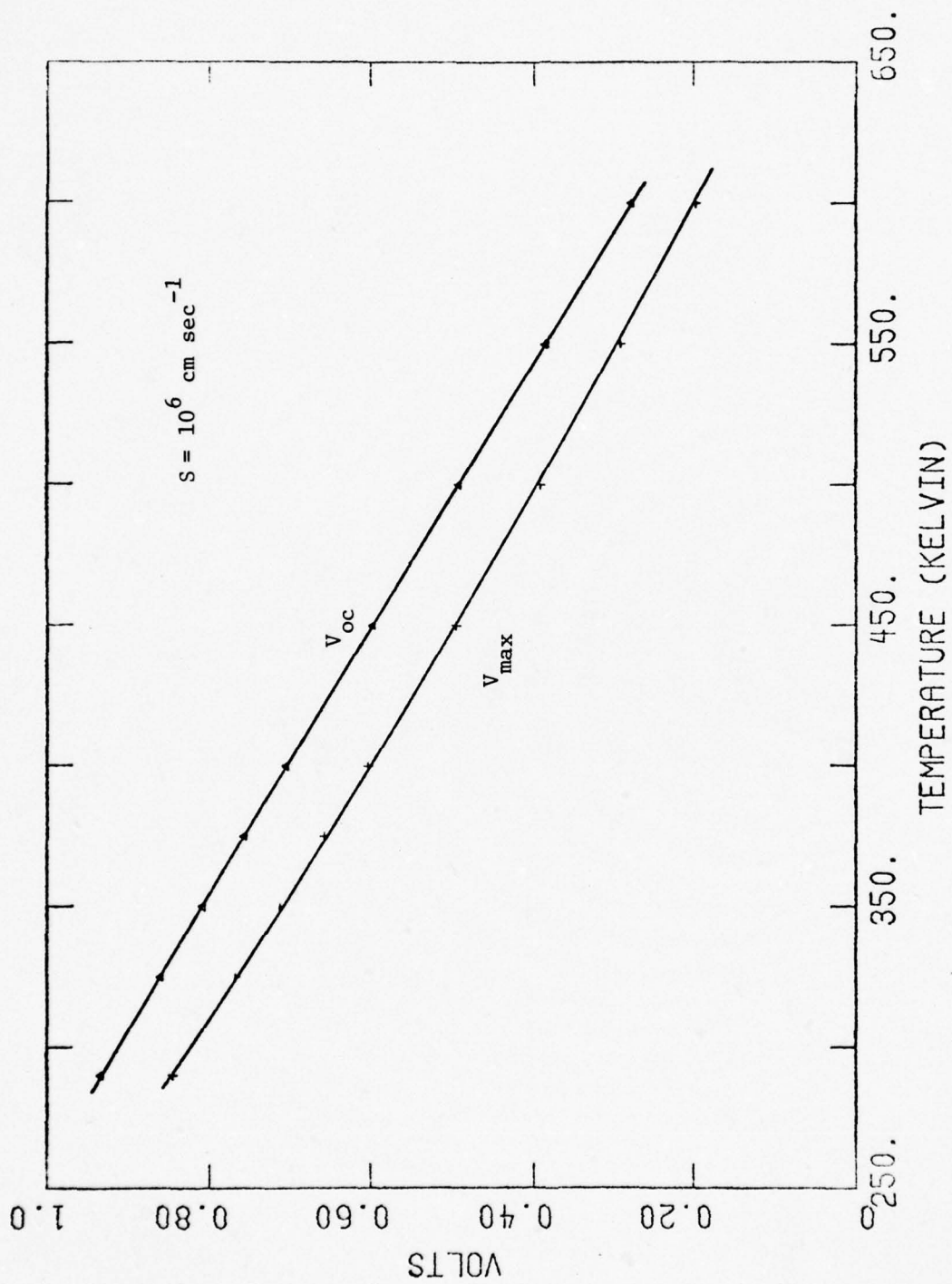
Figure 5.22. $V_{oc}$ and $V_{max}$ vs. Temperature.

137
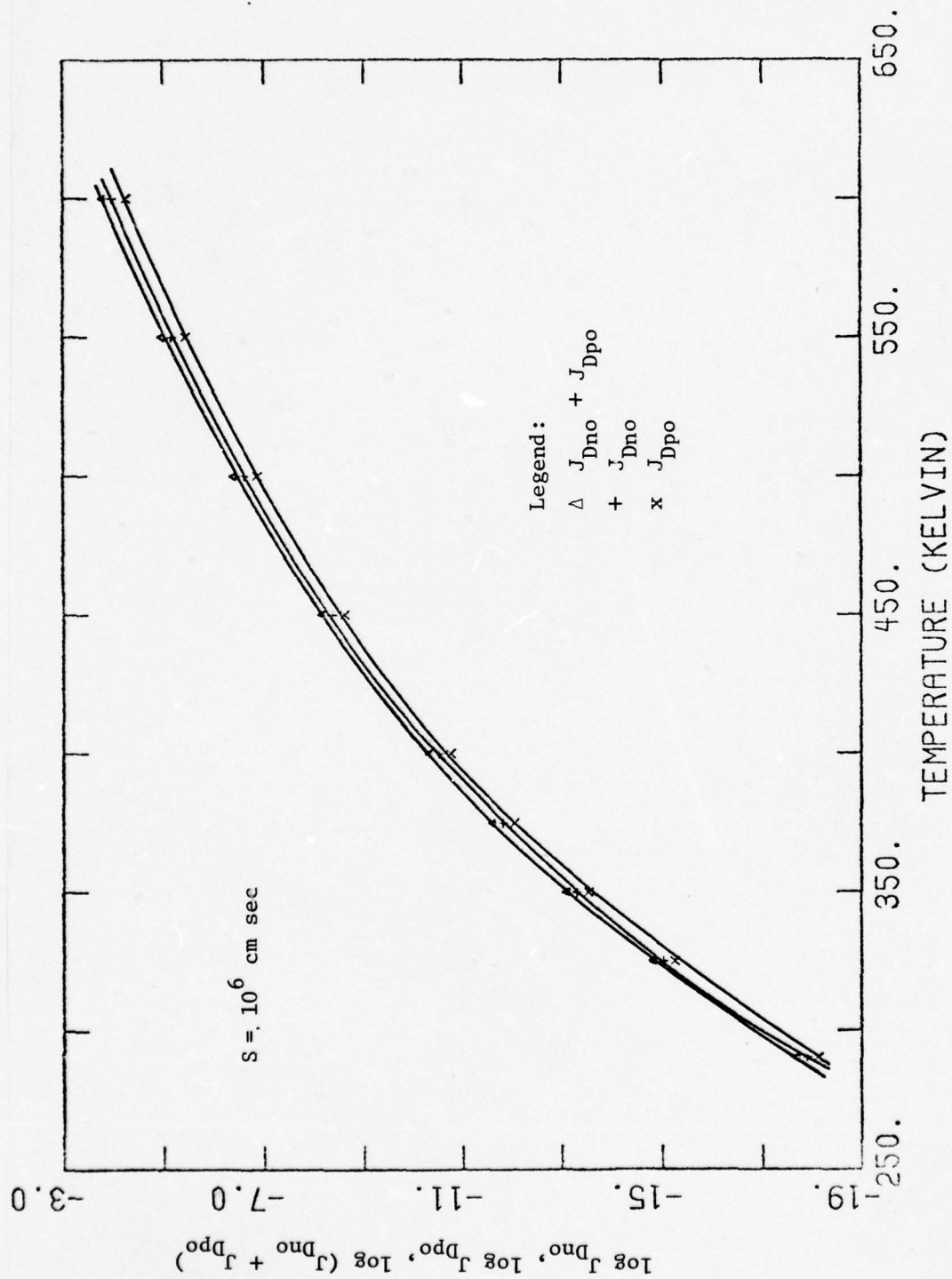
Figure 5.23. The electron, hole and the sum of the electron and hole saturation current multiplied by the appropriate R factors vs. temperature for $10^6$ cm sec$^{-1}$ recombination velocity.

138

Finally, we have calculated the curve fill factor as a function of temperature for $10^6$ cm sec$^{-1}$ recombination velocity and as shown in Figure (5.24). These calculations show that F changes from 0.87 at 290°K to 0.56 at 600°K, a 36% decrease which further reduces conversion efficiency.

Figure (5.25) illustrates PW solar cell I-V curves with temperature as a parameter. These calculations show that the combination of decreased $V_{max}$ and F results in a decrease in conversion efficiency.
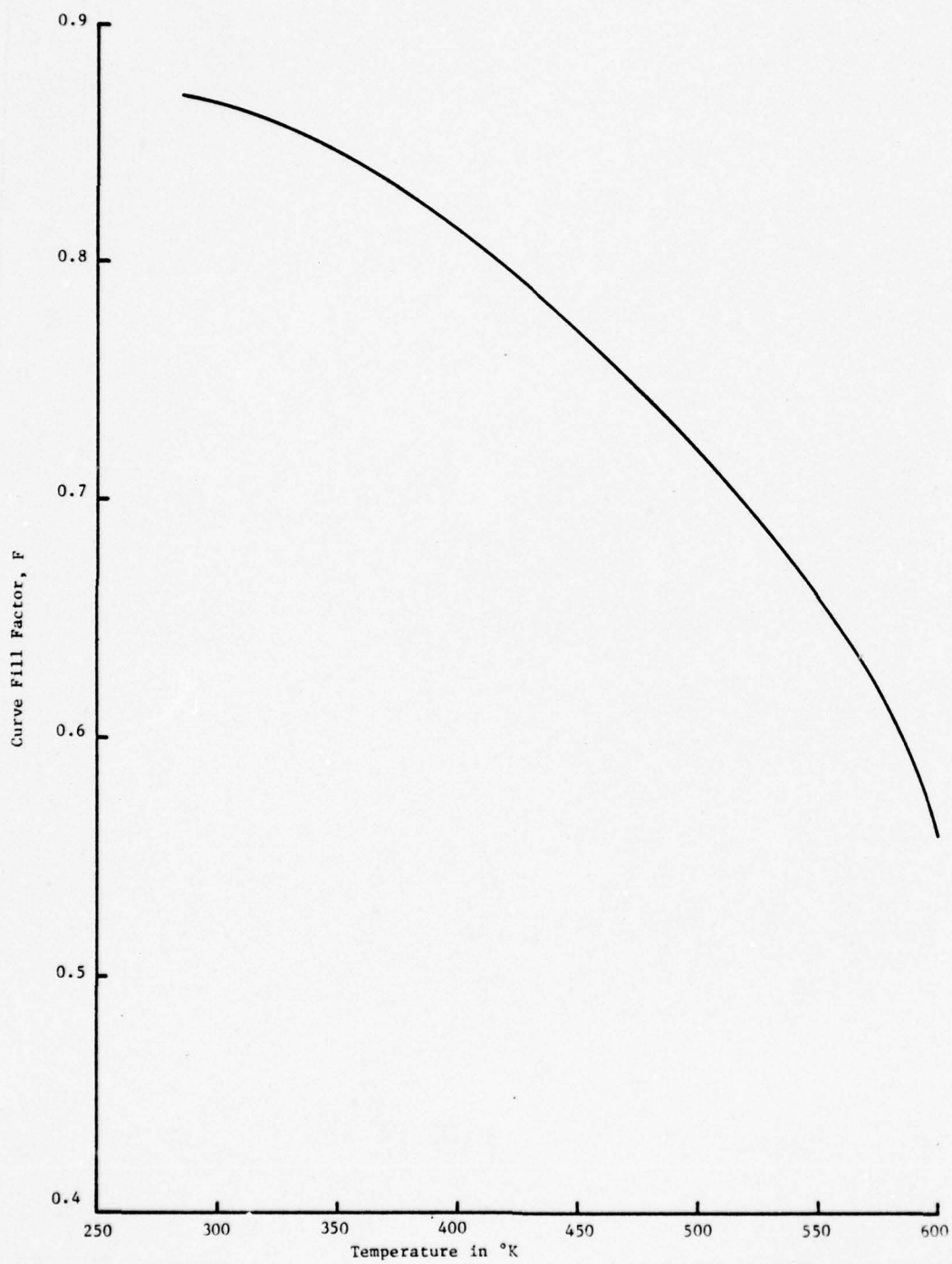
Figure 5.24. The Curve Fill Factor, F vs. Temperature for $10^6$ cm sec$^{-1}$ recombination velocity.
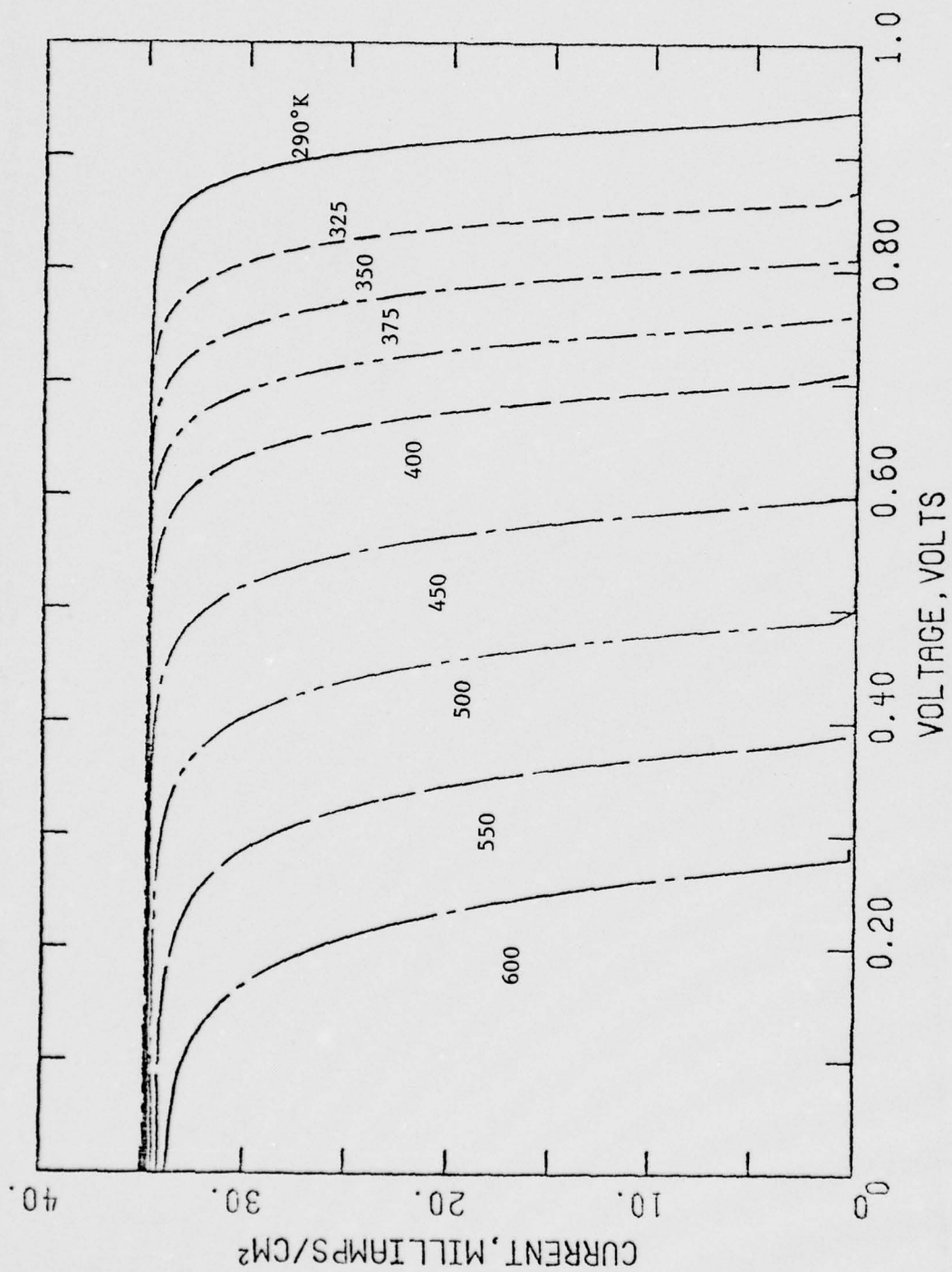
Figure 5.25. The PW solar cell I-V curves as a function of temperature.

141

REFERENCES

5-1. J. J. Loferski, "Theoretical Considerations Governing the Choice of the Optimum Semiconductor for Photovoltaic Solar Energy Conversion," Journal of Appl. Phys., vol. 27, July 1956, pp. 777-784.

5-2. J. J. Wysocki and P. Rappaport, "Effects of Temperature on Photo-voltaic Solar Energy Conversion," Journal of Appl. Phys., vol. 31, 1960, pp. 571-578.

5-3. A. R. Gobat, M. F. Lamorte and G. W. McIver, "Characteristics of High-Conversion Efficiency GaAs Solar Cells," IRE Trans. on Mil. Elect., January 1962.

5-4. M. F. Lamorte, "High Efficiency GaAs Solar Cells," Proc. of 16th Annual Power Sources Conference, 1962.

5-5. M. F. Lamorte, "Development of Improved Solar Energy Converters from GaAs," ASD-TDR-62-639 (USAF).

5-6. M. F. Lamorte, "Internal Power Dissipation in Gallium Arsenide Solar Cells," Advanced Energy Conversion, vol. 3, 1963, pp. 551-563.

5-7. B. Ellis and T. S. Moss, "Calculated Efficiencies of Practical GaAs and Si Solar Cells Including the Effects of Built-in Electric Fields," Solid-State Elec., vol. 13, 1970, pp. 1-24.

5-8. J. M. Woodall and H. J. Hovel, "High-Efficiency $Ga_{1-x}Al_xAs$-GaAs Solar Cells," Appl. Phys. Letters, vol. 21, 15 October 1972, pp. 379-381.

5-8a. H. J. Hovel and J. M. Woodall, "$Ga_{1-x}Al_xAs$ P-P-N Heterojunction Solar Cells," Journal of Electrochem. Soc., vol. 120, 1973, pp. 1246-1252.

5-9. I. Hayashi, M. B. Panish, P. W. Foy and S. Sumski, "Junction Lasers Which Operate Continuously at Room Temperature," Appl. Phys. Lett., vol. 17, 1970, p. 109.

5-10. I. Hayashi, M. B. Panish, P. W. Foy and S. Sumski, Proc. Int. Conf. Semicond. Devices, Tokyo, Sept. 1970.

5-11. M. R. Lorenz and M. Pilkuhn, J. Appl. Phys., vol. 37, 1966, p. 4094.

5-12. F. A. Trumbore, M. Kowalchik and H. G. White, J. Appl. Phys., vol. 38, 1967, p. 1987.

5-13. R. H. Saul, J. Appl. Phys., vol. 40, 1969, p. 3273.

5-14. R. H. Saul, J. Armstrong, W. H. Hackett, Jr., Appl. Phys. Lett., vol. 15, 1969, p. 229

REFERENCES (continued)

5-15.   C. S. Kang and P. E. Greene,
        Appl. Phys. Lett., vol. 11, 1967, p. 171.

5-16.   J. S. Harris and W. L. Snyder,
        Solid-State Electron, vol. 12, 1969, p. 337.

5-17.   J. S. Harris, Y. Nannicki, G. L. Pearson and G. F. Day,
        J. Appl. Phys. vol. 40, 1969, p. 4575.

5-18.   J. S. Barrera and R. J. Archer,
        IEEE Trans, vol. ED-22, 1975, p. 1023.

5-19.   K. J. Linden,
        IEEE Trans, vol. ED-23, 1976, p. 363.

5-20.   H. Kressel and H. Nelson,
        Physics of Thin Films, vol. 7, Academic Press, Inc., New York, 1973.

5-21.   L. W. James, "III-V Compound Heterojunction Solar Cells," 1975 IEEE
        Electron Devices Meetings, Washington, D.C., December 1-3, 1975.

5-22.   L. W. James and R. L. Moon, "GaAs Concentrator Solar Cells," Appl.
        Phys. Letters, vol. 26, 15 April 1975, pp. 476-470.

5-23.   R. K. Willardson and A. C. Beer, Ed., Semiconductors and Semimetals:
        H. J. Hovel, vol. 11, Solar Cells; Academic Press, New York, 1975.

5-24.   R. K. Willardson and A. C. Beer, Ed., Semiconductors and Semimetals;
        Vol. 3, Optical Properties of III-V Compounds; Academic Press,
        New York, 1967

5-25.   W. D. Johnston, Jr. and W. M. Callahan, "High-Performance Solar Cell
        Material:  n-AlAs/p-GaAs Prepared by Vapor Phase Epitaxy," Appl. Phys.
        Lett., vol. 28, 1976, pp. 150-152.

5-26.   V. M. Andreev, T. M. Golovner, M. B. Kagan, N. S. Koroleva, T. L.
        Lyubashevskaya, T. A. Nuller and D. N. Tret'yakov, "Investigation of
        the Photoelectric Characteristics of High-Efficiency $Al_uGa_{1-u}As$ Solar
        Cells," Sov. Phys. Semicond., vol. 7, 1974, pp. 1525-1529.

5-27.   M. Wolf, "Drift Fields in Photovoltaic Solar Energy Converter Cells,"
        Proc. of IEEE, vol. 51, May 1963, pp. 674-693.

5-28.   J. Tauc, "Generation of an EMF in Semiconductors with Nonequilibrium
        Current Carrier Concentrations," Rev. Mod. Phys., vol. 29, 1957,
        pp. 308

5-29.   Y. Marfaring and J. Chevallier, "Photovoltaic Effects in Graded Band-
        gap Structures," IEEE Trans. E.D., vol. ED-18, 1971, pp. 465-477.

REFERENCES (continued)

5-30. M. Konagai and K. Takahashi, "High Efficient Graded-Bandgap pGa$_{1-x}$Al$_x$As-PGaAs-nGaAs Solar Cells," IEEE Int. E.D. Mtg., Washington, D.C., 1975; Theoretical Analysis of Graded-Bandgap Gallium-Aluminum Arsenide/ Gallium Arsenide p-Ga$_{1-x}$Al$_x$As/p-GaAs/n-GaAs Solar Cells," Solid-State Electronics, vol. 19, 1976, pp. 259-264; Journal of Appl. Phys., vol. 46, 1975, pp. 3542.

5-31. J. A. Hutchby, "
       Appl. Phys. Lett., vol. 26, 1975, pp. 457.

5-32. J. Mandelkorn and J. H. Lamneck, Jr., "Simplified Fabrication of Back Surface Field Silicon Cells and Novel Characteristics of Such Cells," Proc. of 9th Photovoltaic Specialist Conf., May 2-3, 1972.

5-33. M. P. Godlewski, C. R. Baraona and H. W. Brandhorst, Jr., Proc. of 10th Photovoltaic Specialists Conf., Nov. 13-15, 1973.

5-34. M. Wolf, "Research for the Improvement of Silicon Solar Cell Efficiency, NASA Contract Rept., NASA Grant NGL39-010-001, Jan. 1971.

5-35. J. B. Gunn, "On Carrier Accumulation and Properties of Certain Semi-conductor Junctions," Journal Electron Control, vol. 4, 1958, pp. 17-50.

5-36. W. Shockley, Electrons and Holes in Semiconductors, Van Nostrand, New York, 1950.

5-37. C. T. Sah, R. N. Noyce and W. Shockley, "Carries Generation and Recombi-nation in P-N Junctions and P-N Junction Characteristics," Proc. IRE, vol. 45, 1957, pp. 1228-1243.

5-38. M. E. Ettenberg and H. Kressel, "Interfacial Recombination at (AlGa)As/ GaAs Heterojunction Structures," Journal Appl. Phys., vol. 47, 1976, pp. 1538-1544.

5-39. H. Kressel and H. Nelson, Physics of Thin Films, vol. 7, Academic Press, Inc., New York, 1973.

5-40. I. Hayashi, M. B. Parrish, P. W. Foy and S. Sumski, "Junction Lasers Which Operate Continuously at Room Temperature," Appl. Phys. Lett., vol. 17, 1970, pp. 109-111.

5-41. J. Lindmayer and J. F. Allison, "The Violet Cell: An Improved Silicon Solar Cell", Comsat Tech. Rev. 3, pp. 1-21, 1973.

5-42. A. A. Immorlica and G. L. Pearson, Appl. Phys. Lett., vol. 25, 570, 1974.

5-43. T. Kawakami and K. Sugiyama, "Electron Diffusion Lengths in Ge-Doped GaAlAs", Jpn. J. Appl. Phys. 12, 151-152, 1973.

5-44. H. Namizaki, M. Nagano and S. Nakahara, IEEE Trans. E.D. Ed-21, 688, 1974.

144

REFERENCES (continued)

5-45. C. T. Hwang, "Doping Dependency of Hole lifetime in n-type GaAs",
      J. Appl. Phys. 42, 4408-13, 1971.

5-46. H. C. Casey, Jr. B. I. Miller and E. Pinkas, "Variation of
      Minority-Carrier Diffusion Length with Carrier Concentration in
      GaAs Liquid-Phase Epitaxial Layers", J. Appl. Phys. 44, 1281-87, 1973.

5-47. R. J. Carbone and P. R. Longaker,
      Appl. Phys. Lett. 4, 32, 1964.

5-48. M. Neuberger, Handbook of Electronic Materials, Vol. 2, III-V Semi-
      conducting Compounds, Plenum Press, New York, 1971.

5-49. J. W. Harrison, "Gallium Arsenide Technology", Vol. 1, Research
      Triangle Institute, Technical Report AFAL-TR-72-312, January 1973.

5-50. J. W. Harrison and J. R. Hauser, Theoretical Calculations of Electron
      Mobility in Ternary III-V Compounds", J. Appl. Phys. 47, 292-300, 1976.

5-51. J. Tucker, R. B. Lauer and J. Schlafter, "Response Time of Ge-Doped
      (Al,Ga) As-GaAs Double - Heterostructure LED's", J. Apply. Phys. 47,
      2082-84, 1976.

5-52. T. Kawakami and K, Sugiyama, "Electron Diffusion Lengths in Ge-Doped
      GaAlAs, Jpn J. Appl. Phys. 12, 151-52, 1973.

5-53. H. Namizaki, M. Nagano and S. Nakahara, Frequency Response of $Ga_{1-x}Al_xAs$
      Height - Emitting Diodes", IEEE Trans. E.D. ED-21, 688-691,
      1974.

5-54. A. Onton, Advances in Solid State Physics, Vol. 13, Perganion, N.Y.,
      1973, p. 59.

5-55. NASA, 1971, Solar Electromagnetic Radiation, NASA Documents, NASA
      SP 8005.

## 6.0 MONOLITHIC, CASCADE SOLAR CELL

### 6.1 Introduction

The maximum theoretical energy conversion efficiency which may be obtained from a single junction photovoltaic solar cell is determined by the semiconductor bandgap. The bandgap determines the lower photon energy limit of the solar spectrum flux which may produce electron-hole pairs and, as a consequence, the maximum photon flux which may affect energy conversion. The maximum theoretical efficiency calculated from the bandgap model assumes that each solar photon possessing an energy equal to or greater than the bandgap energy produces an electron-hole pair and therefore contributes to energy conversion. This calculated efficiency is independent of material parameters because they do not enter the calculation of this simple model. The bandgap model assumes unity collection efficiency; i.e., that all electron-hole pairs produced are separated and collected by the p-n junction. Thus, the model assumes that all the photons having an energy greater than the bandgap are absorbed in a layer thickness, surrounding the p-n junction, smaller than either the electron and hole diffusion lengths. However, when a more detailed model is employed which includes the cell structure parameters with a specific semiconductor and its material parameters, the calculated collection and conversion efficiencies are usually lower than the maximum theoretical values. The material parameters which may affect efficiency values are: lifetime, minority carrier mobility, direct/indirect optical transition characteristics, and junction transport mechanisms.

By its very simplicity, the bandgap model is not encumbered by the details of device structure and material parameters. While the calculated

146

efficiency gives a higher value than can be attained in a practical case, from an overall point of view, the bandgap model does consider the more fundamental loss factors. It is, therefore, convenient to use the model as a crutch in order to explore new and fundamental methods to increase efficiency beyond the values attainable with single p-n junction solar cells.

There are three major losses incorporated in the bandgap model: dark current - forward bias current or dark current which subtracts from the photocurrent; excess photon energy - the energy difference between the individual photon energy and the bandgap energy of the material; long wavelength - that portion of the solar flux whose photon energy is lower than the bandgap and is not capable of producing electron-hole pairs. The dark current loss is largely dependent on technology and a lower limit exists due to the Shockley ideal forward current diffusion transport mechanism and to any associated carrier confinement. The excess photon energy loss cannot be reduced in conventional single junction cells. The long wave-length loss may be reduced, provided the long wavelength portion of the spectrum may be made to produce electron-hole pairs and take part in the energy process. We conclude that to obtain higher efficiency from photovoltaic devices, a cell structure is required which incorporates two or more p-n junctions in a monolithic, cascade arrangement. The structure consists of the widest bandgap junction at the surface with progressively smaller bandgap junctions into the material away from the surface. In this way, progressively larger and larger portions of the solar spectrum may be made to take part in an energy conversion process. Consequently, efficiency is increased substantially beyond the maximum theoretical value predicted by the bandgap model for a single p-n junction solar cell.

In properly designed cascade structures, the material for the first cell possesses the largest bandgap and the materials for succeeding cells deeper into the structure have progressively smaller bandgaps. Photons of energy equal to or greater than the first cell's bandgap energy are absorbed mostly in the first cell, while the free carrier absorption for photons of lower energy is small and this photon flux passes almost unattenuated onto the second cell. Photons of energy equal to or greater than the second cell's bandgap energy but less than the first cell's bandgap are absorbed mostly in the second cell, while the free carrier absorption for photons of lower energy is small and this photon flux passes almost unattenuated on to the third cell. This is repeated for as many cells as are in the structure. In this manner, the cascade structure presents a greatly improved spectral match to the solar spectrum.

Efficiency calculations using the simple bandgap model have been made for cascade cell structures. One result gives 31% efficiency at AM2 for a two terminal, two junction structure in which the top cell bandgap is 1.65 eV and the other is approximately 1.2 eV [6-1]. Calculations by other workers have reported similar results.

By the very nature of the bandgap model, structure design and material parameters are not provided. Moreover, the conventional closed form analytical method as well as the computer modeling technique involve approximations which do not give significantly improved design information for cascade cells, with respect to structure design and material parameters. In addition, development of improved efficiency calculations for practical use requires an analytical method from which the V-I curve equation is obtained. Therefore, it seemed appropriate to develop an analytical

148

method which derives the V-I solar cell curve which can be applied to the cascade structure in the case of a two-terminal device and the V-I curves of each cell in the cascade structure of a three-terminal device.

Section 4.0 outlines an improved analytical method to calculate solar cell device characteristics. This is particularly useful for cascade structures where design optimization studies of structure design and material parameters are to be made. This analysis obtains a solution for minority carrier concentration for the steady-state integral-differential continuity equation in each distinct region of the structure. Once the minority carrier solutions satisfy the imposed boundary conditions in each distinct layer, all solar cell phenomena may be recovered, consistent with the approximations used (APPENDIX D).

There are two generic types of cascade structures with respect to construction. The first is where two separately fabricated cells are mechanically attached one behind the other in a stacked manner. The second is where the cells are fabricated monolithically by sequentially fabricating on a substrate the bottom p-n junction followed by the top p-n junction. Obviously the monolithic construction may be most conveniently fabricated by a sequential epitaxial growth process, ideally by the LPE process. In each of these types, the p-n junctions may be connected so that the voltages aid or oppose each other. The most convenient way to operate the former is as a two-terminal device which requires that the same terminal current flows through each p-n junction. However, it may also be operated as a three-terminal device in which each cell delivers power to its own load. The latter configuration, in which the voltages oppose each other, is a three-terminal device (See APPENDIX H).

149

The optimized two-terminal voltage aiding cell may exhibit a lower efficiency than the three-terminal voltage opposing cell. This results because of the imposition on the former that the same terminal current flows through each junction. For most applications the two-terminal cell may be preferred and, in addition, it will be simpler to fabricate. The three-terminal cell is more difficult to fabricate because of the placement of the common contact between the two cells. Moreover, power conditioning of voltage opposing cells will be less efficient since additional cells must be stacked in parallel (rather than series) and the resultant low voltages converted externally to useable levels (See APPENDIX J). The two-terminal, voltage aiding solar cell structure appears to have a number of compelling advantages over the three-terminal, voltage opposing structure.

Since the efficiency of such stacked layers is less than doubled when comparing conventional single junction cells to a two-junction cascade cell, the cascade cell will only be economical when the cost of the second cell is small. It may be possible to construct the monolithic, two-junction cascade junction solar cell with a small incremental cost over single junction, homojunction and heterojunction cells. This results because multi-layered III-V devices are fabricated by means of the multiple well LPE technique and all layer thicknesses are of the order of 1 μm.

Over the last 25 years, little has been done to fabricate cascade solar cells. A two-terminal GaAs/Si cascade solar cell was fabricated in 1961 [M. F. Lamorte, unpublished]. The GaAs cell was mechanically thinned to 25 μm and attached with epoxy to the Si cell surface. The

150

combined efficiency of the cell was lower than the efficiency of either cell operated separately. The poor results were shown to be due to free carrier absorption in the spectral range 1.1 to 1.4 μm and to reflection losses at the GaAs/epoxy and to the epoxy/Si interfaces. Recently, a stacked junction Si solar cell composed of eight layers was reported [6-2]. This yielded an efficiency of 13.5% at a concentration of 20 suns, which is not overly impressive. Moreover, apart from the efficiency calculations made using the bandgap model, cascade cell design optimization studies have not been conducted. In Section 6.0 the analytical method presented in Section 4.0 and expanded in APPENDIX G is applied to a two p-n junction monolithic, cascade solar cell.

## 6.2 Two-junction Cascade Cell Structure - Voltage Aiding Configuration

Figure 6.1 shows an idealized cascade cell structure which is to be optimized for maximum efficiency. The cell contains three substructures: the top and bottom cells, and the tunnel junction separating the cells. The tunnel junction also serves as the electrical contact between the cells. There are a total of 10 distinct layers in this structure. Each cell is effectively a "Potential Well" (PW) cell. (For PW cell structure details see Section 5.2).

The optimum acceptor concentration of the "Window" layer is taken to be $10^{18}$ cm$^{-3}$ as was determined from the PW cell optimization studies (Section 5.3). The bandgap values of the top cell (1.590 eV) and the bottom cell (1.030 eV) were determined from calculations based on the bandgap model.

The $Al_xGa_{1-x}As$ "Window" bandgap is made to decrease linearly such that a constant negative built-in electric field is established. This

151

negative field accelerates electrons flowing toward the p-n junction, thereby reducing bulk recombination in this region. Surface recombination loss is also reduced due to the drift field which is present at the surface.

The "Window" layer also serves as an additional conducting path for the terminal load current. By highly doping this layer, the sheet resistance may be reduced to very low values. The high doping level and the correspondingly low minority carrier diffusion length in this region is not as critical to spectral response because of the presence of an aiding field.

## 6.3 Results and Discussion - Voltage Aiding Configuration

The analytical method used in Section 4.0 and APPENDIX G allows for a definitive design optimization, within the bounds of the approximations employed. As a result of the preliminary first and second iterative optimization studies, which are not presented here, a number of structural parameters were nearly optimized and are included in the band structure of Figure 6.1. They are: the impurity concentration in the p- and n-regions surrounding the homojunctions is taken at $10^{17}$ cm$^{-3}$ for no other reason than to insure that depletion region space charge recombination is minimized; the sum of the p- and n-region thickness surrounding each homojunction[*] was selected at the minimum thickness for which the normalized spectral response[**] exceeded 98%, so that incomplete absorption loss is not a major factor; the p- and n-region thickness should be nearly equal; in graded regions an assumed alloy composition gradient

---

[*] A p-n junction residing in a material of uniform alloy composition and uniform bandgap.

[**] The contribution to short circuit arising in a layer produced from the absorbed flux in that layer.

152

is imposed to establish a constant 3,000 V cm$^{-1}$ field strength at 290°K

which accelerates minority carriers toward the nearest homojunction cell;

the barrier height in the minority carrier band edge is always equal to

or greater than 4 kT to 5 kT volts for the purpose of achieving effective

carrier confinement to reduce dark current; the top cell bandgap value

was taken at the value, 1.590 eV, which on average, appears to give maximum

efficiency for a conventional single junction cell; the p- and n-region

thickness values were selected and shown in Figure 6.1.

The general optimization procedure found to be most suitable in a

multiple layer device is to begin the optimization in the bottom cell

followed by that of the top cell. The tunnel junction is made to be

optically inactive because its bandgap value is greater than the value

of the top cell. In the work described below, the study begins by optimiz-

ing the bottom cell bandgap. Having established the optimum bandgap for

the bottom cell, this value is then imposed in all subsequent calculations.

This is then followed by optimizing the n- and p-layer thickness of the

bottom cell and these two parameters are imposed in all subsequent

calculations. Finally, the n- and p-layer thicknesses of the top cell

are optimized. The temperature characteristics of the cascade structure

is then determined.

The optimization study presented here by no means exhausts the

optimization. There remains to optimize the bandgap of the top cell,

impurity concentration of the optically active and inactive portions

of the structure, and the layer thickness of the inactive regions as well

as of the "window" layer.
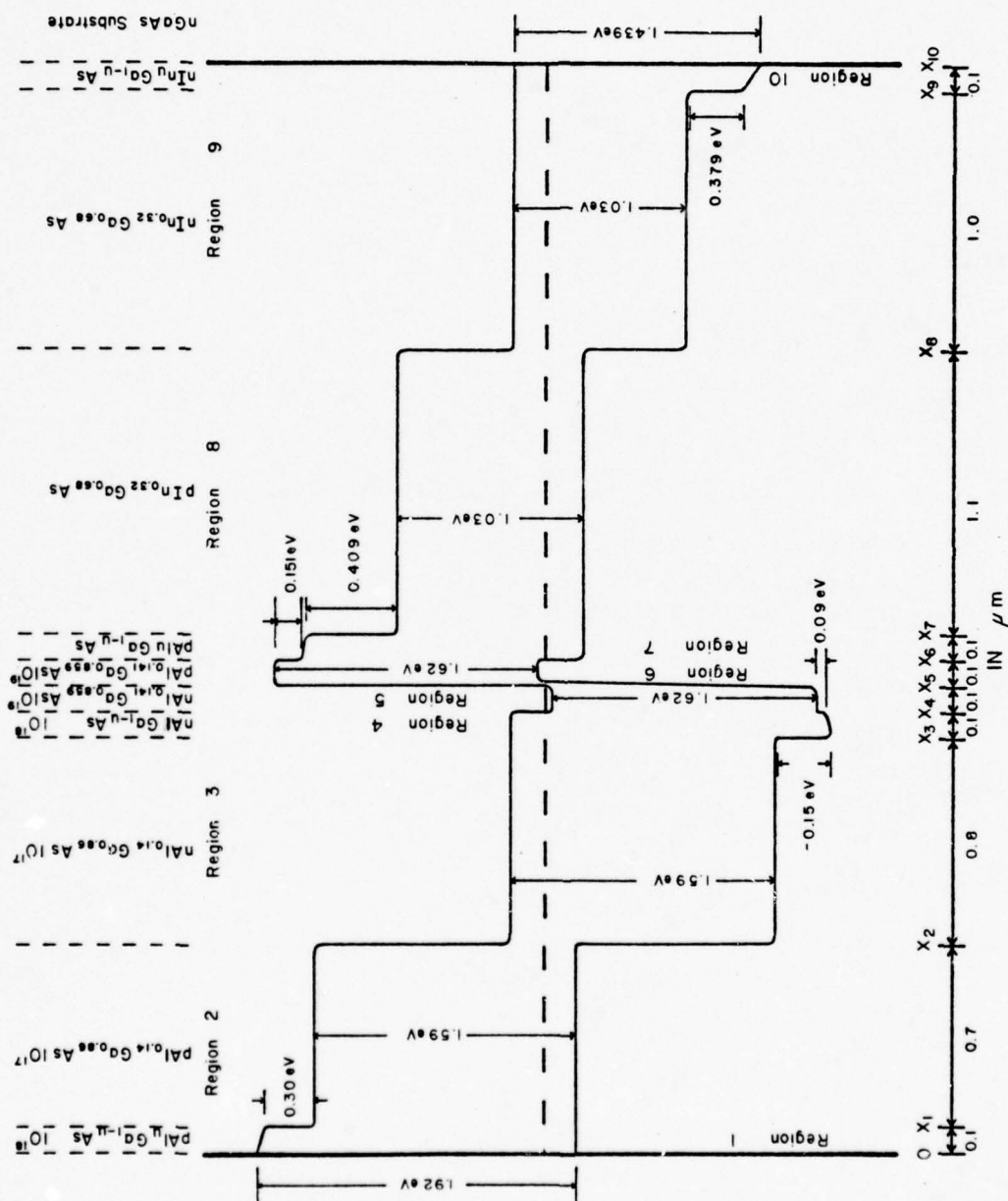
Figure 6.1. A cascade, idealized, 2-junction, voltage aiding solar cell structure.

154

The design optimization study discussed below is a third iterative calculation. The first and second iterations are not presented here since the third calculation exhibits all the features of interest to a design engineer. The design optimization sequence to be described is as follows:

1. bottom cell bandgap,

2. ratio of the n- to p-region thickness of the bottom cell,

3. sum of the p-region plus the n-region thickness of the bottom cell,

4. ratio of the n- to p-region thickness of the top cell,

5. sum of the p-region plus the n-region thickness of the top cell.

The optimization is conducted on the basis that the sum of the efficiencies of the top and bottom cells is maximized.

6.3.1  Bottom Cell

To calculate the bottom bandgap value to maximize the cascade efficiency, four bandgap values of the ternary $In_x Ga_{1-x} As$ were used. The bandgap values are:  1.030 (1.2 μm), 0.954 (1.3 μm), 0.886 (1.4 μm) and 0.827 (1.5 μm) eV.

Figure 6.2 shows the results of computer calculations of the AMO total efficiency to determine the bottom cell optimum bandgap. The calculations were performed using 0, $10^6$ and $10^7$ cm sec$^{-1}$ surface recombination velocity (SRV) at the window-air interface. The total efficiency was calculated by obtaining the V-I curve at the terminals of the cascade structure of both cells operating as a unit. The tunnel diode voltage drop was taken to be 0.050 volts and this was subtracted from the V-I curve.

155
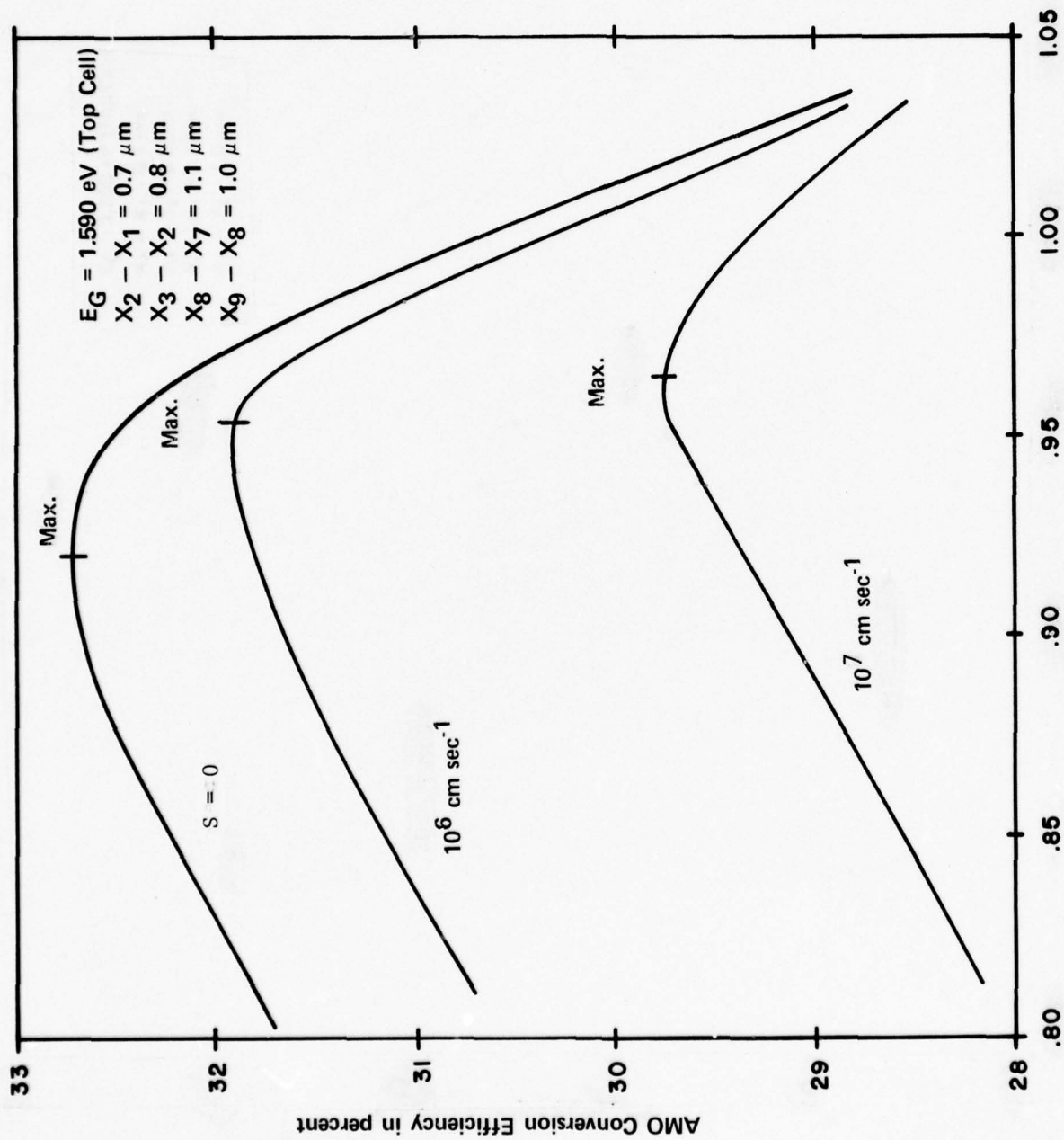
Figure 6.2. Conversion efficiency vs. bandgap of bottom cell with recombination velocity of a parameter.

There are a number of interesting observations to be made from this set of curves. The first observation is that the total efficiency is markedly sensitive to the bottom cell bandgap. The initial bandgap, 1.030 eV, gives an efficiency less than 29% for all three SRV values. For example, the efficiency increases to nearly 32% for $10^6$ cm sec$^{-1}$ and 0.954 eV. Similar increases are obtained for 0 and $10^7$ cm sec$^{-1}$ SRV.

The second is that the rate of decrease of efficiency on the high energy side is approximately three times faster than on the low energy side. A 10% increase in the bandgap energy above the optimum bandgap value results in approximately a 10% decrease in total efficiency, while a 10% decrease in bandgap below the optimum results in less than a 3% drop in efficiency.

The third observation is that while the bottom cell junction is physically remote from the cell surface, the bottom cell optimum bandgap is sensitive to SRV. Table 6.1 lists the bottom cell optimum bandgap and the corresponding calculated efficiency for each of the SRV values used. The optimum bandgap increases with increasing SRV.

Table 6.1. Optimum bandgap and the corresponding and surface recombination velocity for maxima efficiency of the cascade structure in Figure 6.1.

| Surface Recombination Velocity | Optimum Band Gap | Efficiency |
|---|---|---|
| 0 cm sec$^{-1}$ | 0.920 eV | 32.7% |
| $10^6$ | 0.954 | 32.0 |
| $10^7$ | 0.965 | 29.9 |

With increasing surface recombination velocity the terminal current and voltage at the maximum efficiency on the V-I curve of the top cell shift to lower values. Due to the imposition that the terminal current must be the net current passing through each cell, the current in the lower cell is shifted by the same amount. Therefore, the bandgap of the bottom cell may be increased to allow the terminal voltage of this cell to increase along its V-I curve to the point where the terminal current is equal to the current at the maximum power point on the V-I curve. This results in a higher photovoltage in the bottom cell.

The calculations show that even though the bottom cell is located away from the surface and from direct coupling phenomena, the design parameters of the bottom cell are very sensitive to the surface recombination velocity.

In Figure 6.2 the efficiency decreases at low bandgap values because the dark current in the bottom cell increases; at high bandgap, the efficiency decreases because the terminal current of the bottom cell decreases.

From Figure 6.2 we observe that the optimum bandgap for $10^6$ cm sec$^{-1}$ recombination velocity is 0.954 eV. Therefore, in the further optimization studies we impose these two parameters on the band structures in Figure 6.2 for all further calculations. The 0.954 eV results in the alloy $In_{0.388}Ga_{0.612}As$.

The efficiency, short circuit current, and dark current are calculated and plotted in Figures 6.3, 6.4, and 6.5, respectively, for six thickness values of the bottom cell p-region. The thickness of the p-region plus

158
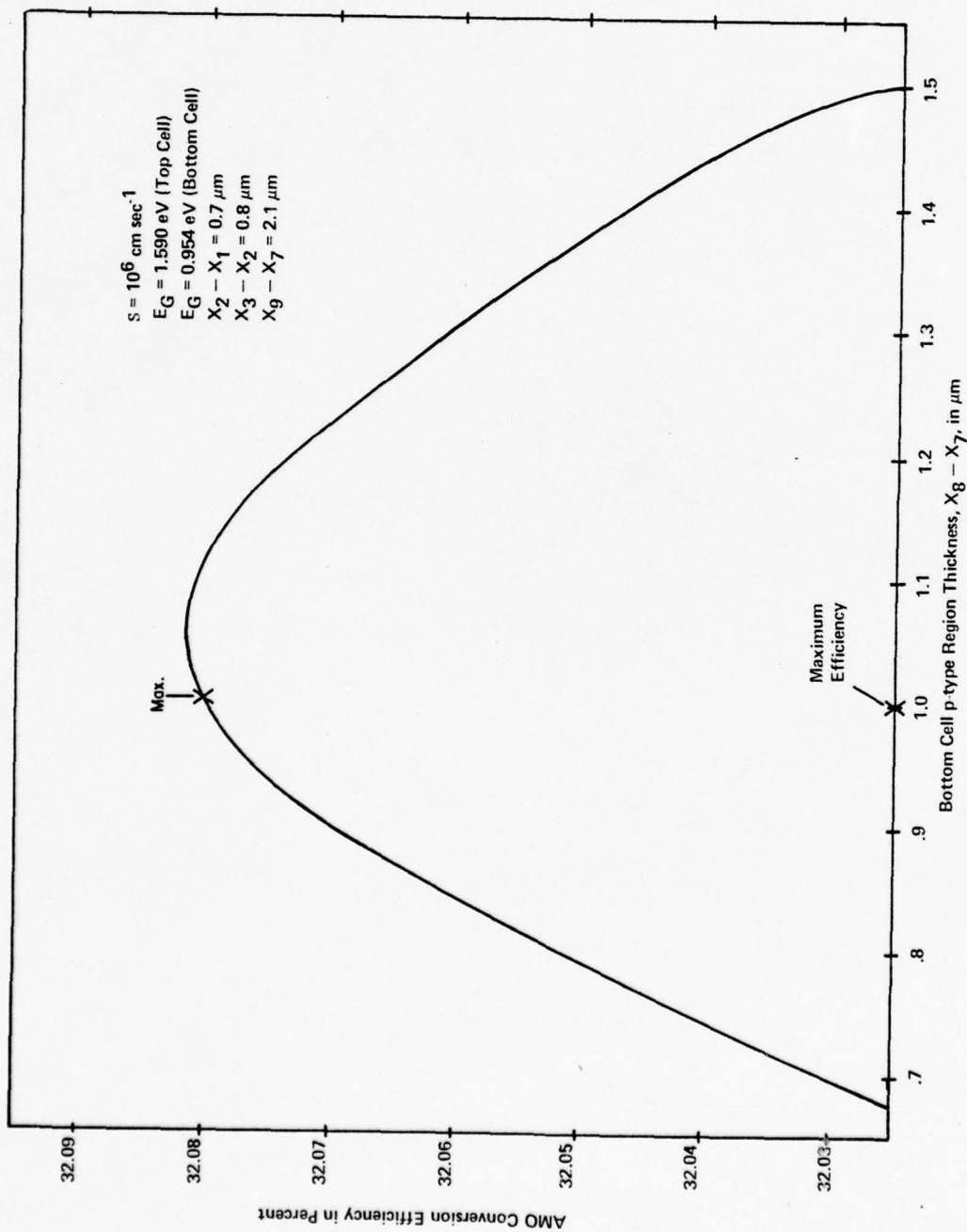
Figure 6.3. Conversion efficiency vs. bottom cell p-type thickness.

159
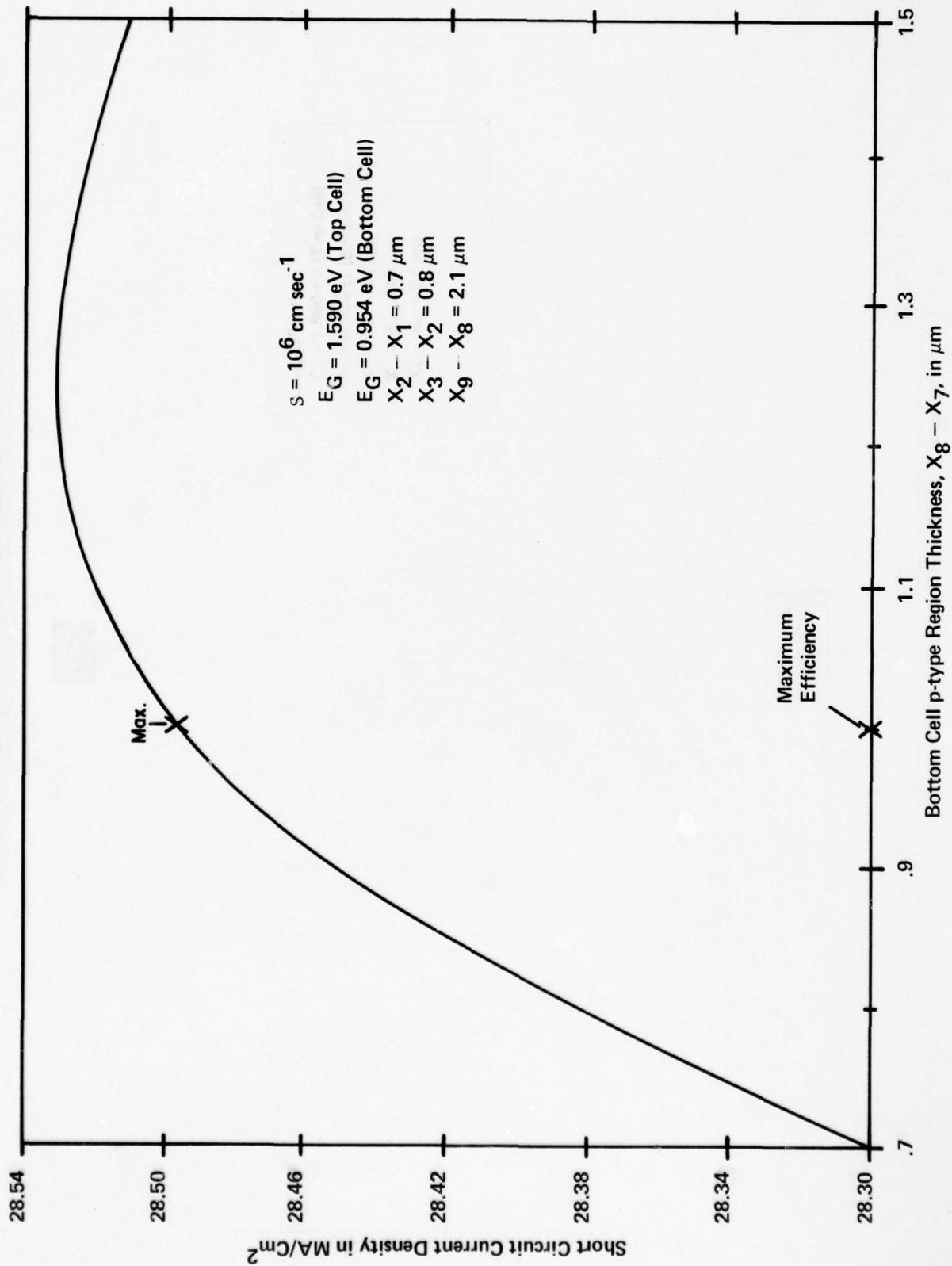
Figure 6.4. Short circuit current density vs. bottom p-type thickness.
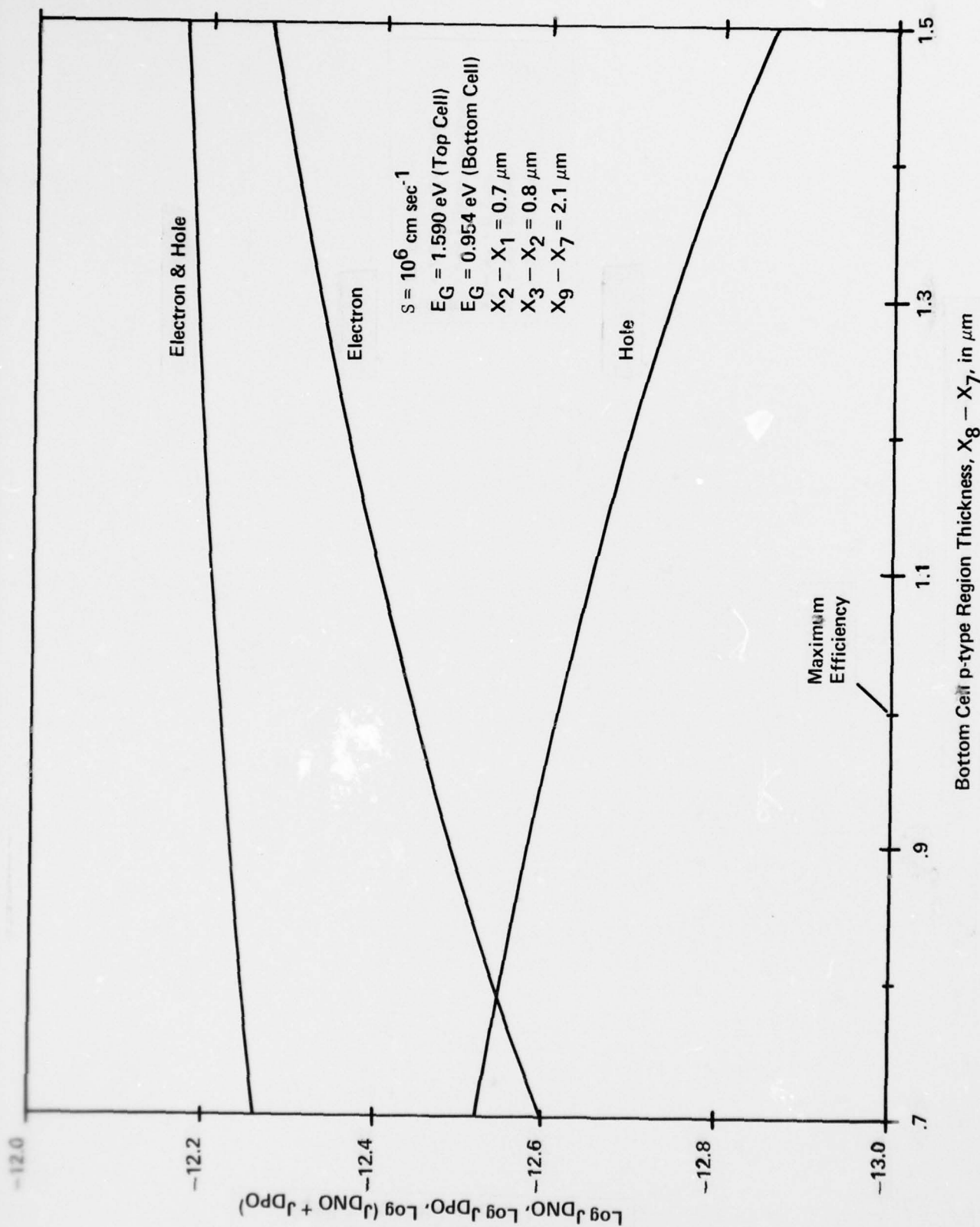
Figure 6.5. Logarithm of the electron, hole and the sum of the hole and electron dark current vs. bottom p-type thickness.

161

the n-region is maintained constant at 2.1 μm. From previous studies
we are assured that this results in a small incomplete absorption loss
in the bottom cell. The cascade efficiency peaks at 32.08% for the p-
region thickness range 1.0 μm.

In Figure 6.4 the maximum short circuit current occurs in the
region of 1.3 μm where the efficiency has decreased to 32.06% from its
maximum of 32.08% at 1.0 μm. It is seen that the maximum efficiency
does not occur at the maximum short circuit current, as is sometimes
assumed.

The total dark current and its components are shown in Figure 6.5.
Due to the completeness of the model analyzed, the influence of carrier
confinement on dark current is also manifested in Figure 6.5. With
increasing p-region thickness, electron carrier charge confinement
is reduced, thereby, increasing the electron contribution to dark current.
Contrarywise, the n-region thickness decreases with increasing p-region
thickness resulting in an increase in hole carrier charge confinment in
the n-region, thereby, reducing the hole contribution to dark current.
As seen in Figure 6.5, the total dark current increases only slightly
with increasing p-region thickness attesting to the compensating electron
and hole contributions to dark current.

We now add to the band structure in Figure 6.1 that the ratio of
the n- to the p-region thickness is to be maintained at 1.1 in all further
design optimization calculations.

In a similar way, the efficiency, short circuit current and the dark
current are calculated and plotted in Figure 6.6, 6.7, and 6.8, respectively,
for six values of p-region thickness. But, in this calculation the n-region

162
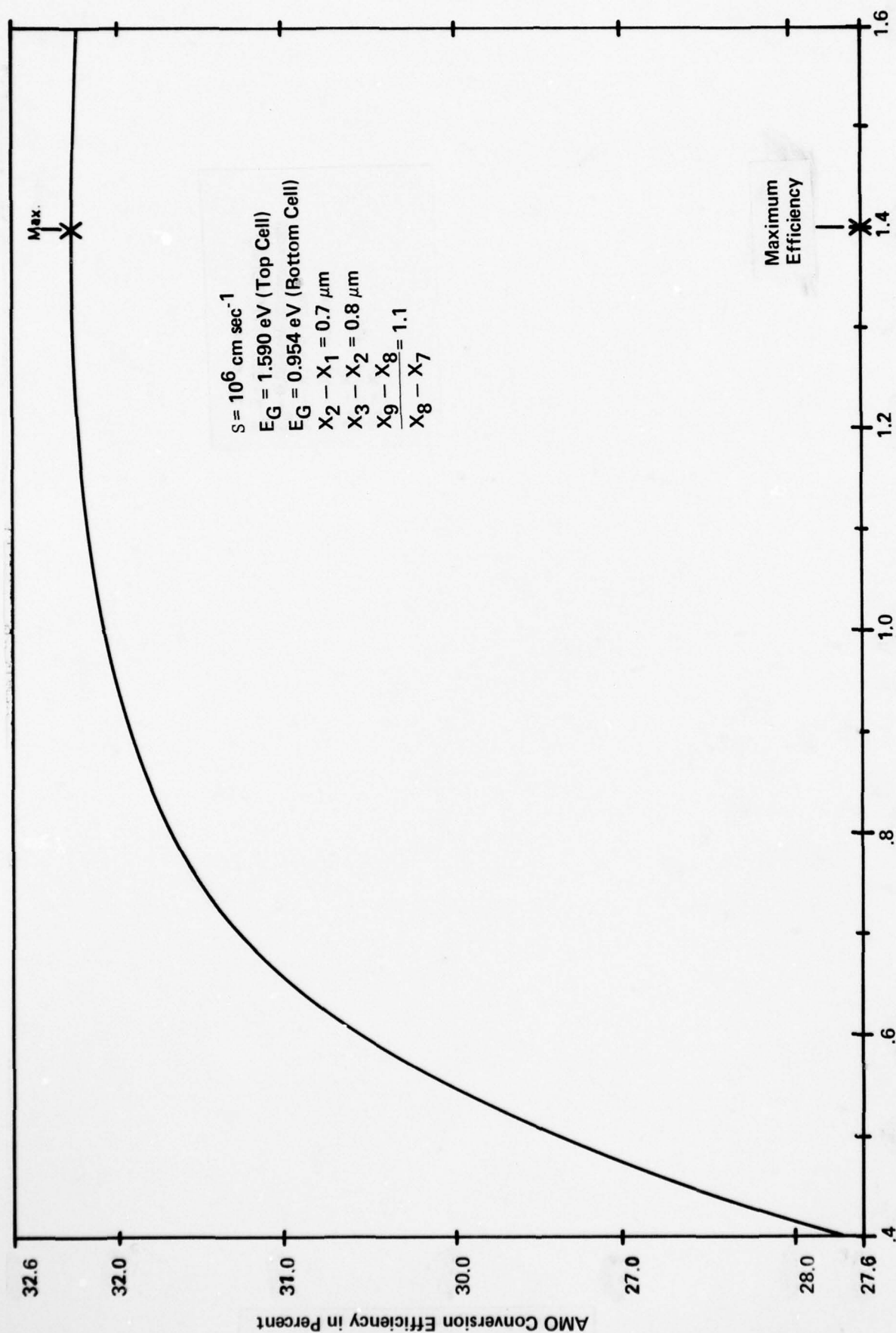
Figure 6.6. Conversion efficiency vs. bottom cell p-type region thickness with a proportional change in the n-type thickness by holding the n-type to p-type thickness ratio constant at 1.1.

163
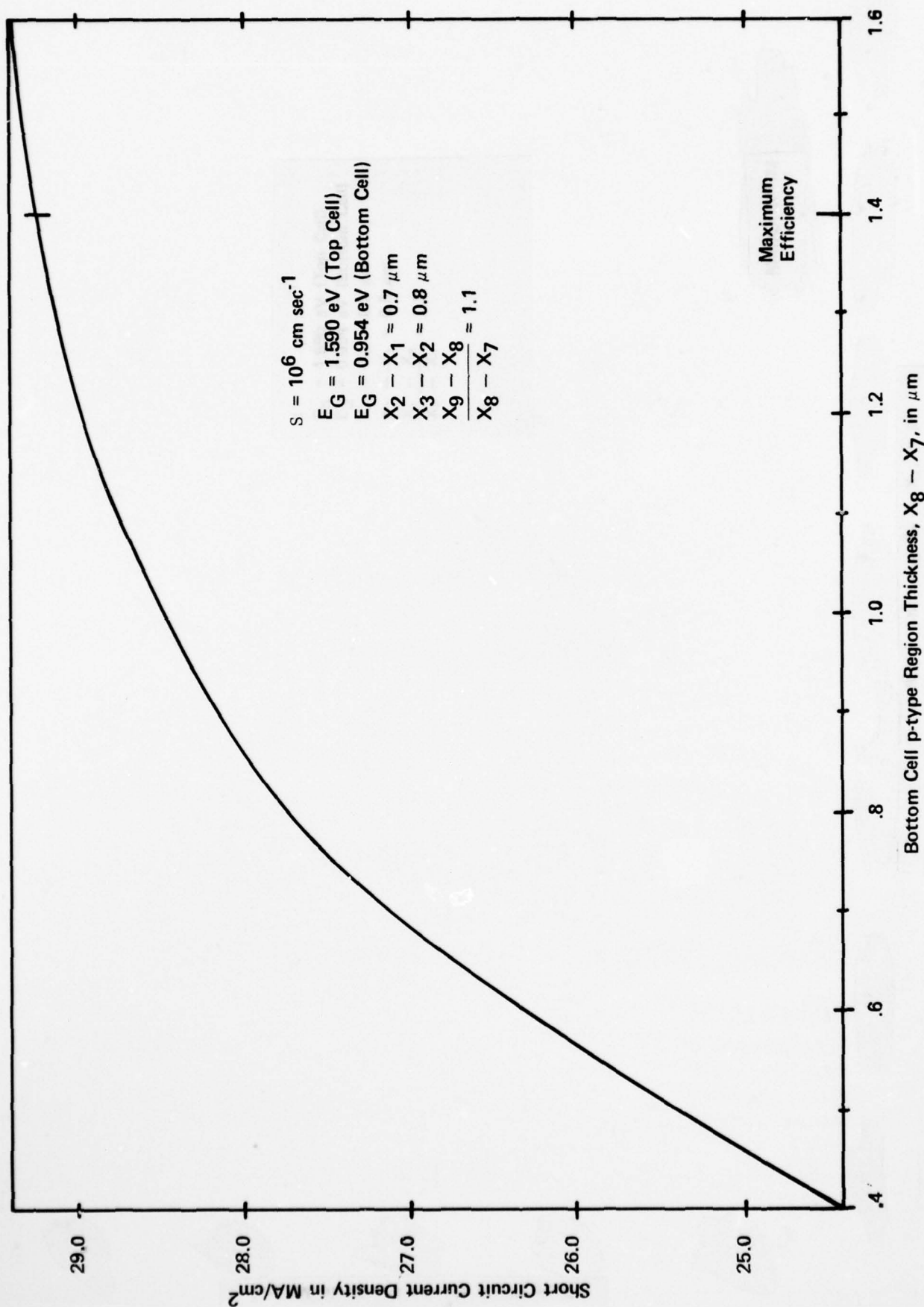
Figure 6.7. Short circuit current density vs. bottom cell p-type thickness with a proportional change in the n-type thickness by holding the n-type to p-type thickness ratio constant at 1.1.

164
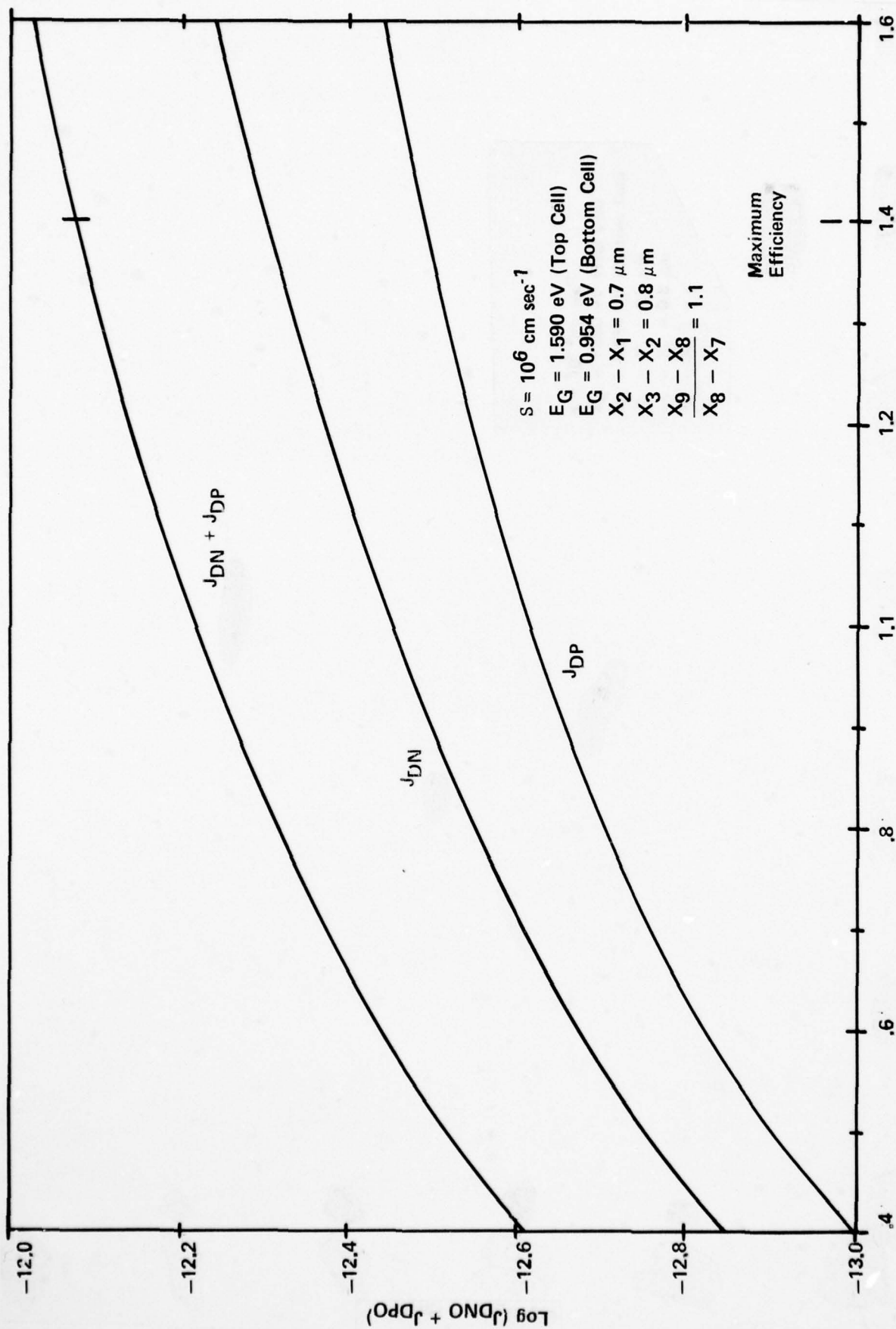
Figure 6.8. Logarithm of dark current vs. bottom cell p-type thickness with a proportional change in the n-type thickness by holding the n-type to p-type thickness ratio constant at 1.1.

thickness is changed proportionally with respect to the p-region thickness, thereby, maintaining a ratio for the n- to p-region thickness at 1.1. In Figure 6.6 maximum efficiency occurs at a value of 1.40 μm for $x_8-x_7$. This results in the optimum n-region thickness, $x_9-x_8 = 1.54$ μm.

Again we observe that the short circuit current and dark current continue to increase beyond 1.40 μm, the value of the p-region thickness for maximum efficiency. Below the 1.40 μm thickness, terminal current increases more rapidly than the terminal voltage decreases resulting in efficiency increasing at a greater rate than the terminal current increases; therefore, the efficiency shows a decreasing trend.

Having determined the optimum p- and n-region thickness of the $In_{0.388}Ga_{0.612}As$ homojunction, these values for $x_8-x_7 = 1.40$ μm and $x_9-x_8 = 1.54$ μm are now imposed on the band structure in Figure 6.1 for all subsequent calculations.

6.3.2 Top Cell

We now turn our attention to the ternary $Al_{0.14}Ga_{0.86}As$ homojunction which makes up the top solar cell. The optimization details are identical to those which are presented for the lower junction.

Figures 6.9, 6.10, and 6.11 show the efficiency, short circuit current and dark current for the $Al_{0.14}Ga_{0.86}As$ homojunction as a function of the p-region thickness, $x_2-x_1$. The sum of the p- and n-region thickness is held constant at 1.5 μm in this calculations. Efficiency peaks at 32.21% for $x_2-x_1 = 0.7$ μm and $x_3-x_2 = 0.8$ μm. This results in the optimum ratio of 1.1 μm of n- to p-region thickness, which was also obtained for the $In_{0.388}Ga_{0.612}As$ homojunction.
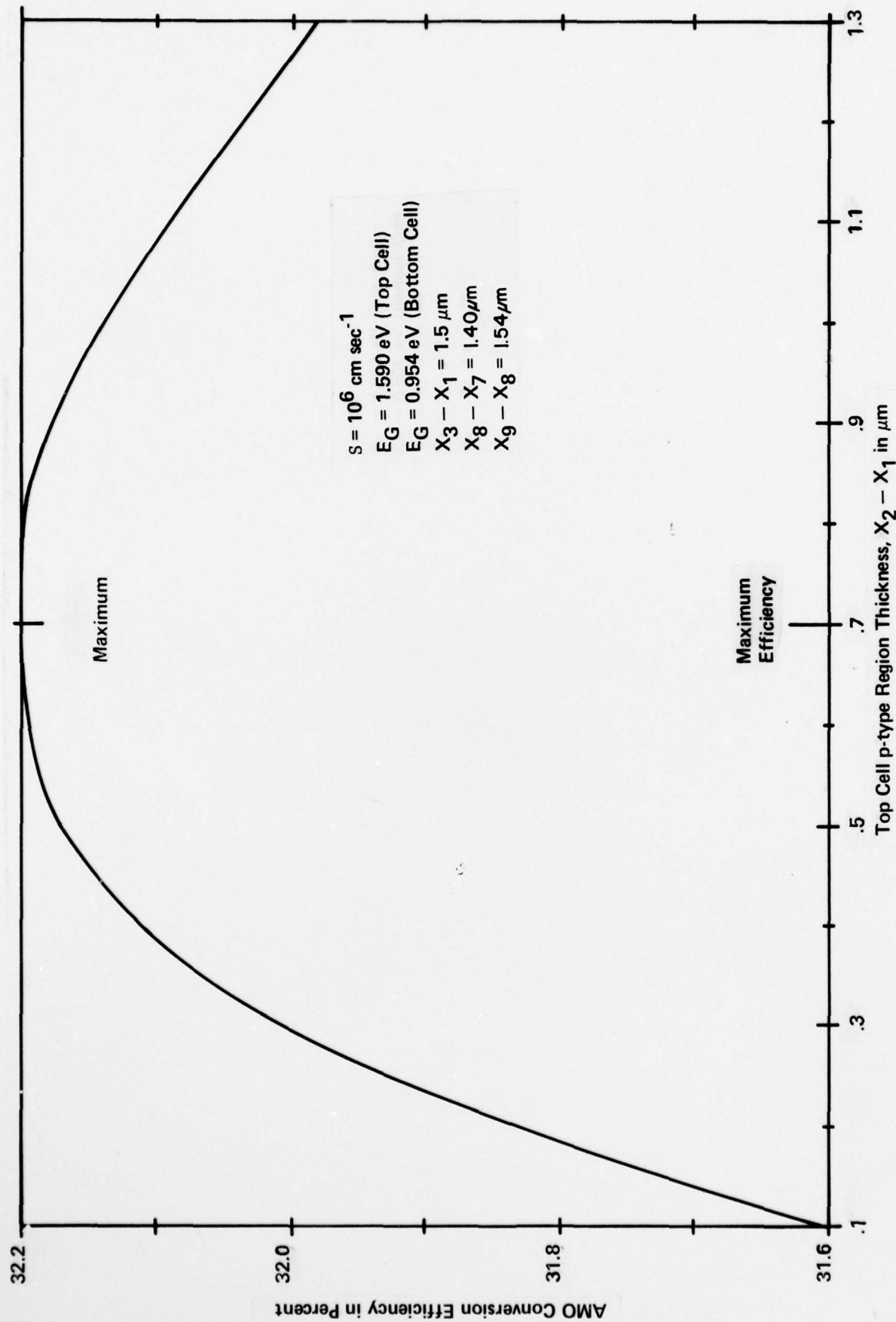
Figure 6.9. Conversion efficiency vs. top cell p-type thickness.

The figure shows AMO Conversion Efficiency in Percent (y-axis, from 31.6 to 32.2) versus Top Cell p-type Region Thickness, $X_2 - X_1$ in $\mu$m (x-axis, from .1 to 1.3).

$S = 10^6$ cm sec$^{-1}$
$E_G = 1.590$ eV (Top Cell)
$E_G = 0.954$ eV (Bottom Cell)
$X_3 - X_1 = 1.5$ $\mu$m
$X_8 - X_7 = 1.40 \mu$m
$X_9 - X_8 = 1.54 \mu$m

Maximum

Maximum Efficiency
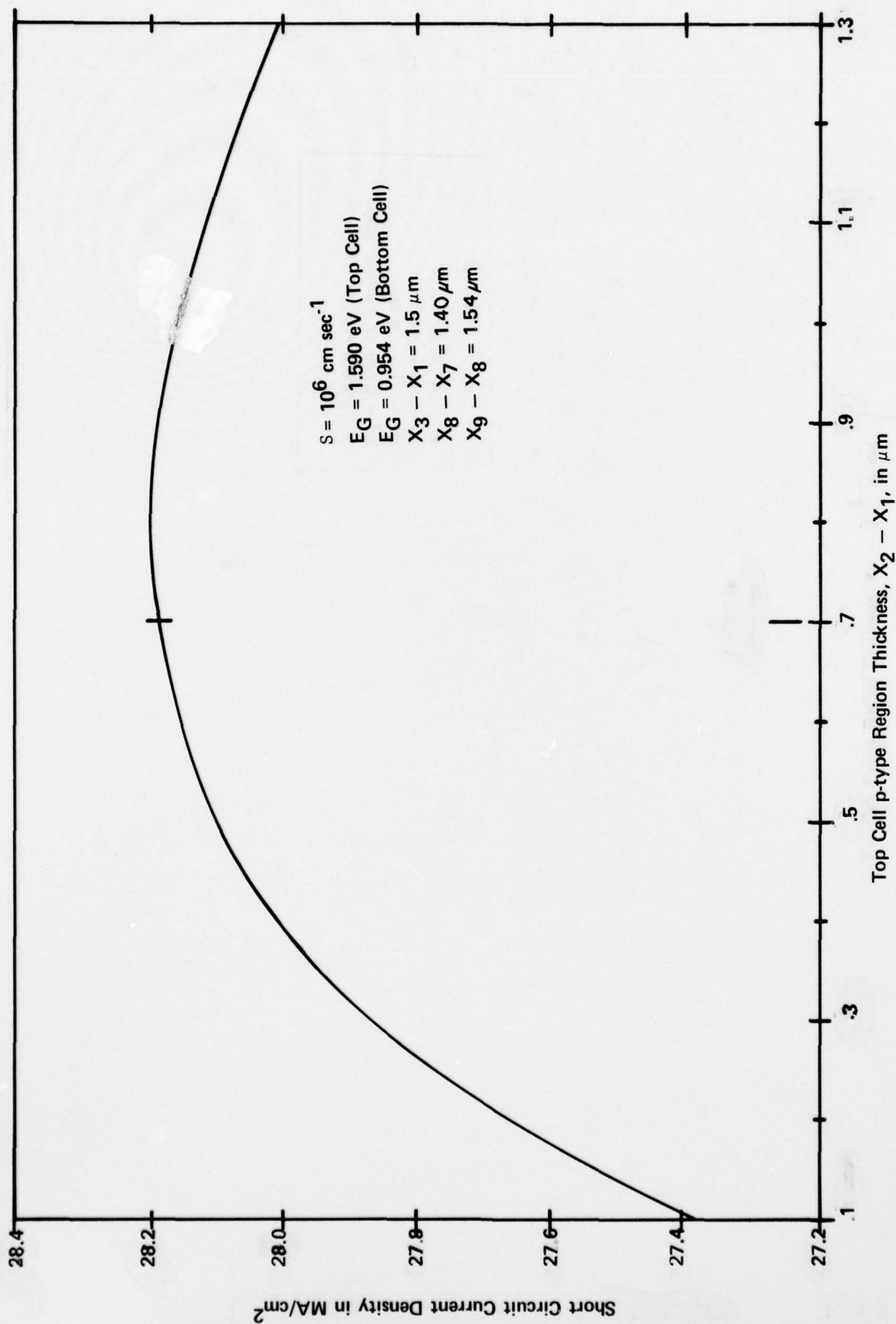
Figure 6.10. Short circuit current density vs. top cell p-type thickness.
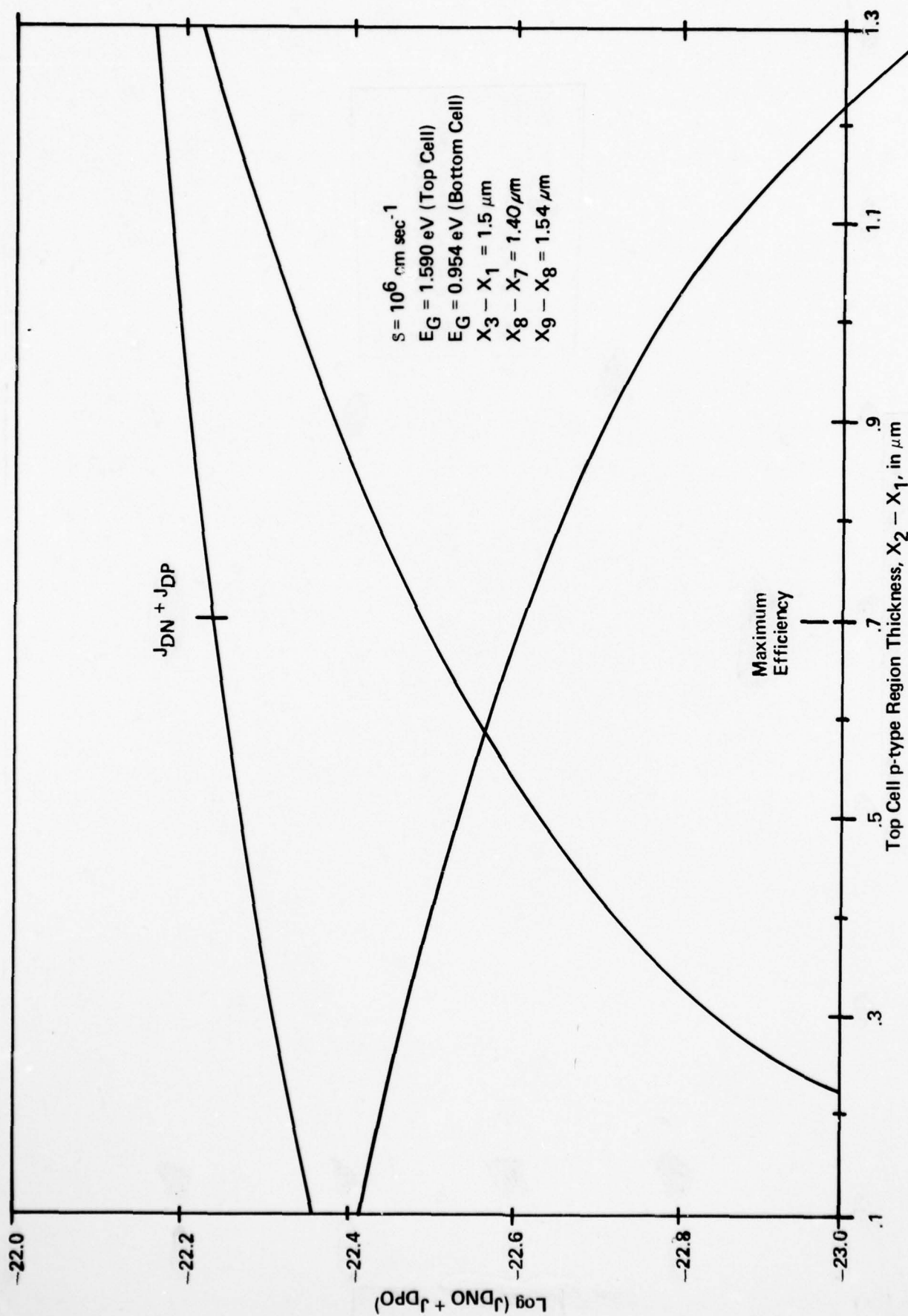
Figure 6.11. Logarithm of dark current vs. top cell p-type thickness.

169

The short circuit current in Figure 6.10 is seen to peak at 0.8 μm, while the dark current in Figure 6.11 is seen to increase monotonically with increasing $x_2-x_1$. The general shapes of these curves are strikingly similar to the corresponding curves represented in Figures 6.4 and 6.5 for short circuit current and dark current, respectively, for the $In_{0.388}Ga_{0.612}As$ homojunction. We now impose the additional design constraint on the band structure in Figure 6.1 that the ratio $(x_3-x_2)/(x_2-x_1)$ is to be held at 1.1.

Efficiency is finally calculated for seven values of $x_2-x_1$ maintaining the ratio of the n- to p-region thickness at 1.1. The curve drawn through the seven points is shown in Figure 6.12 where the efficiency peaks at 32.31% at $x_2-x_1 = 0.84$ μm and $x_3-x_2 = 0.92$ μm. The short circuit current is shown in Figure 6.13 to increase and appears to have a broad maximum beyond 1.05 μm. The dark current is also shown to increase with increasing $x_2-x_1$. All three curves show strikingly similar shapes with their corresponding curves in Figures 6.6, 6.7, and 6.8 for $In_{0.388}Ga_{0.612}As$ homojunction.

The last of the parameters to be imposed on the structure in Figure 6.1 are $x_2-x_1 = 0.84$ μm and $x_3-x_2 = 0.92$ μm, giving a total thickness of 1.76 μm for the p- and n-regions of the ternary $Al_{0.14}Ga_{0.86}As$. The resultant cascade structure of the third iterative process is shown in Figure 6.15. The efficiency of the cascade structure represented in Figure 6.15 is 32.31%, while the efficiency represented by the structure in Figure 6.1 is 29%. This represents more than an 11% increase. A further optimization with respect to the bandgap of the top cell has not been completed.
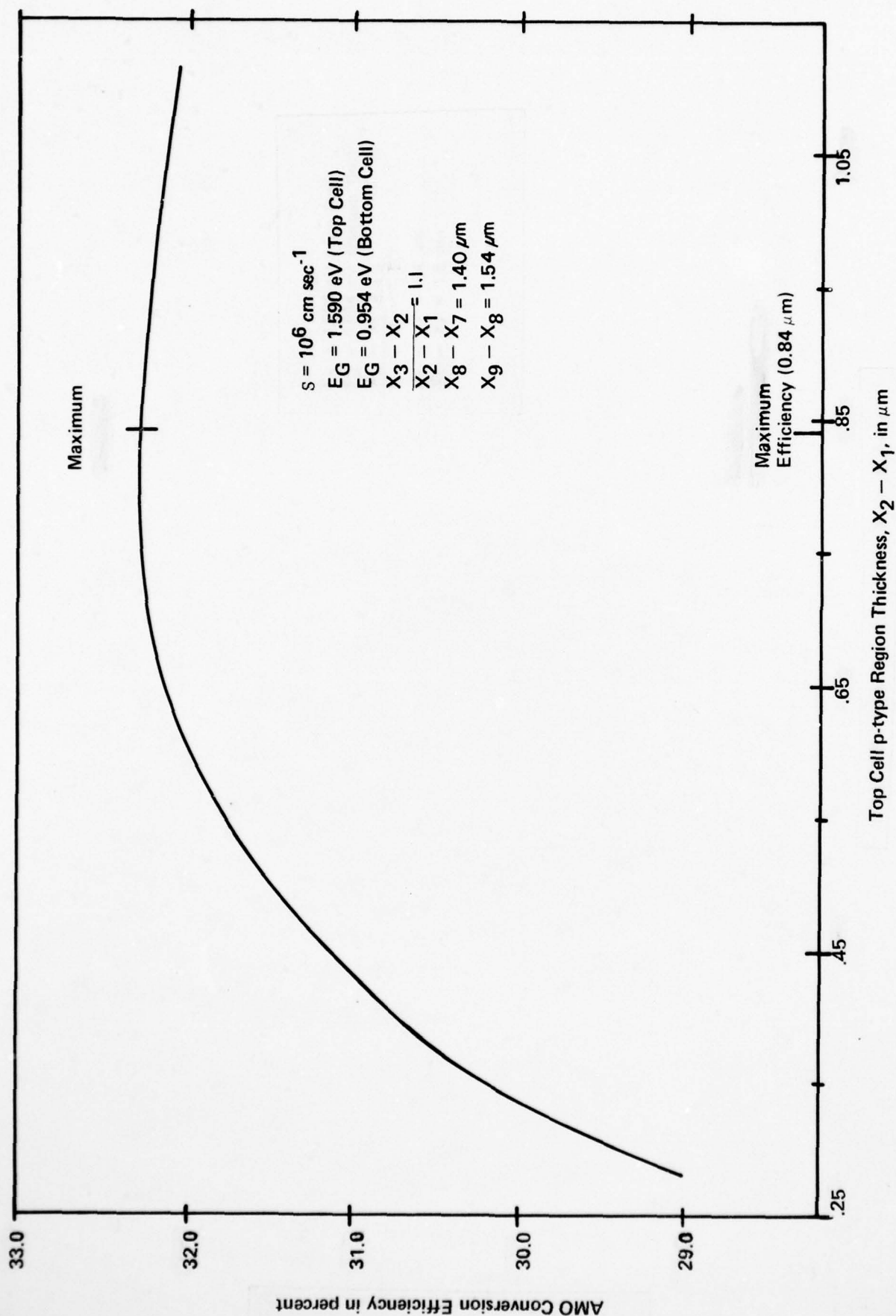
Figure 6.12. Conversion efficiency vs. top cell p-type thickness with a proportional change in the n-type thickness by holding the n-type to p-type thickness ratio constant at 1.1.

171
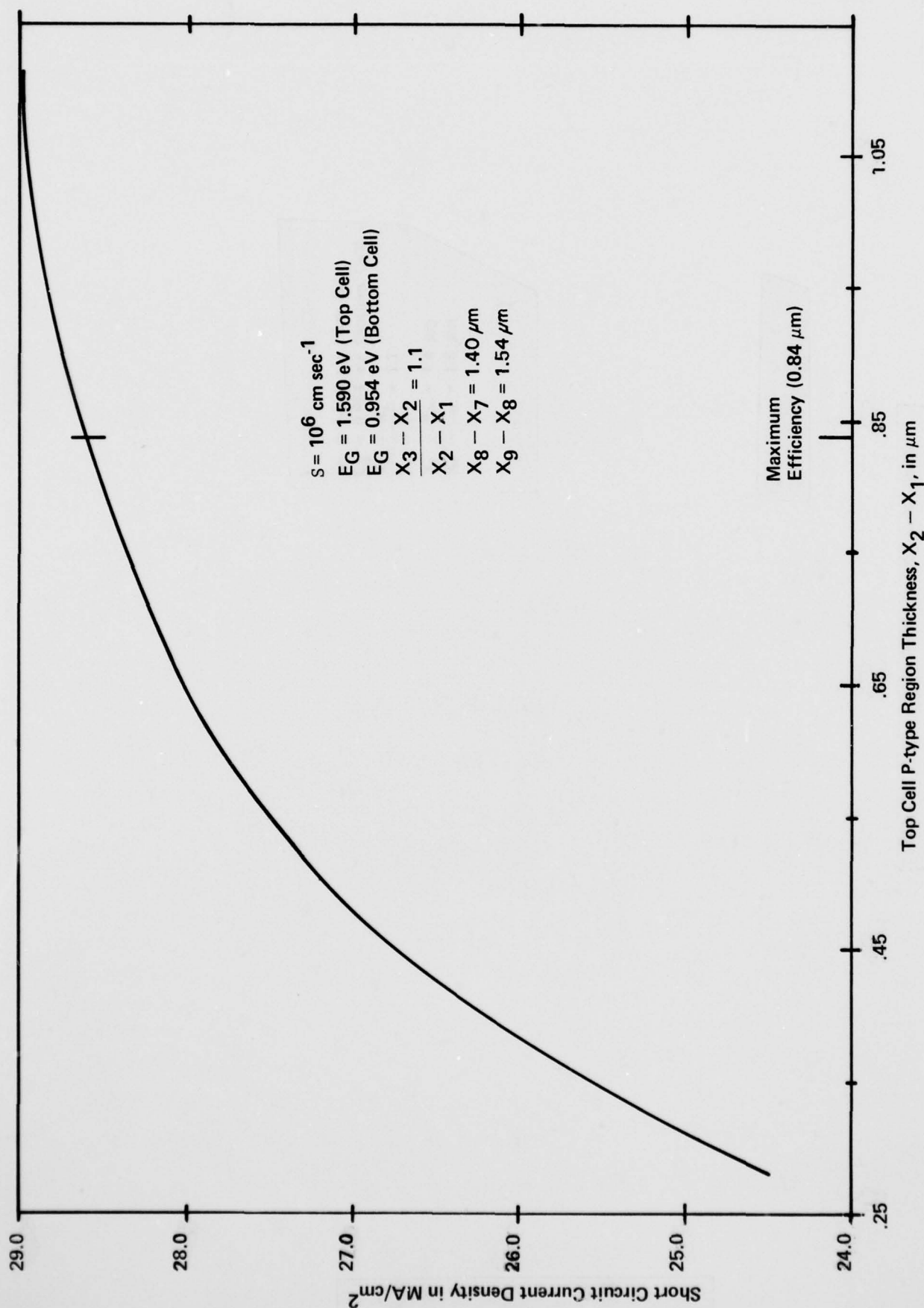
Figure 6.13. Short circuit current density vs. top cell p-type thickness short circuit with a proportional change in the thickness by holding the n-type to p-type thickness ratio constant at 1.1.
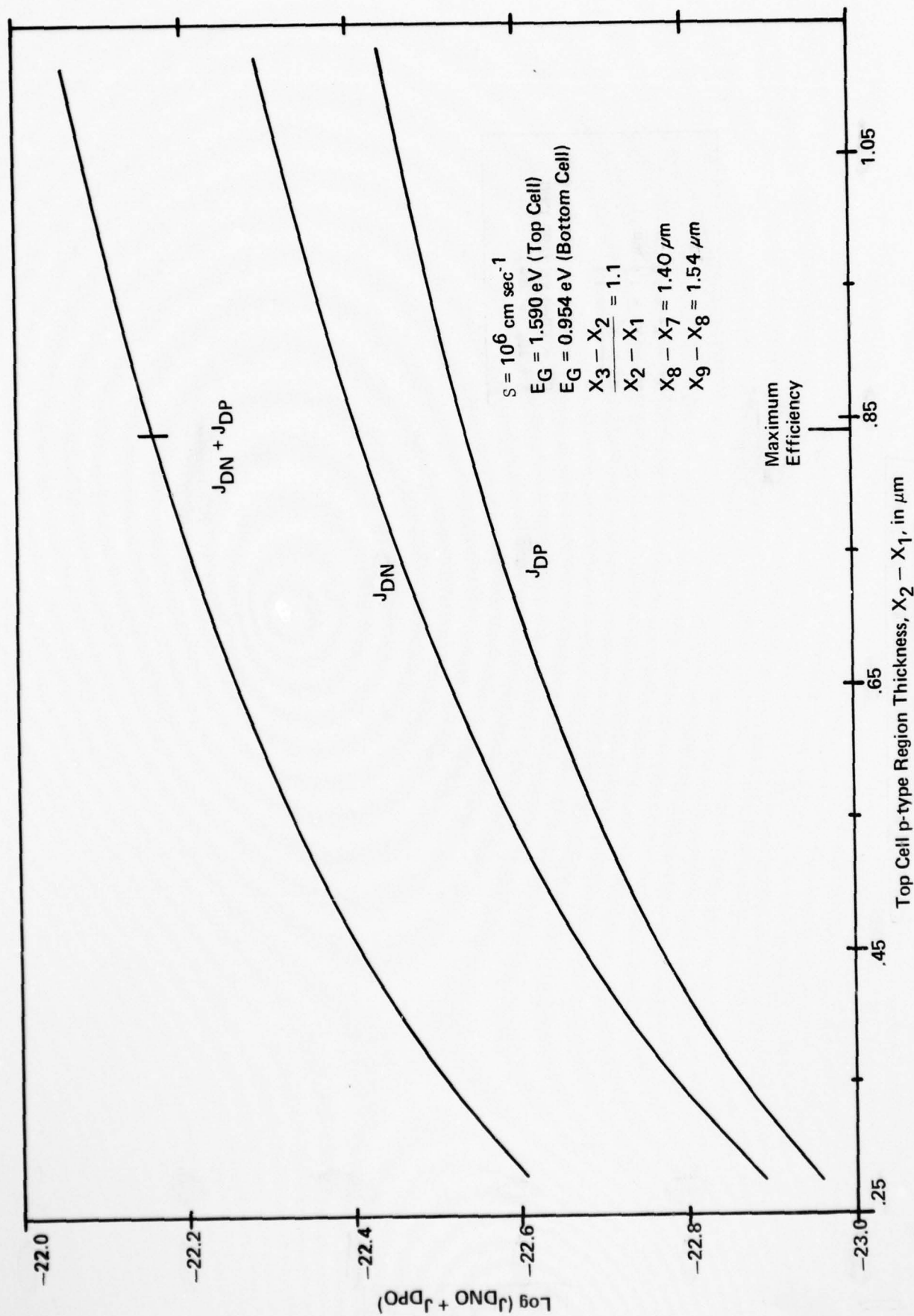
Figure 6.14. Conversion efficiency vs. top cell p-type thickness with a proportional change in the n-type thickness by holding the n-type to p-type thickness ratio constant at 1.1.

173
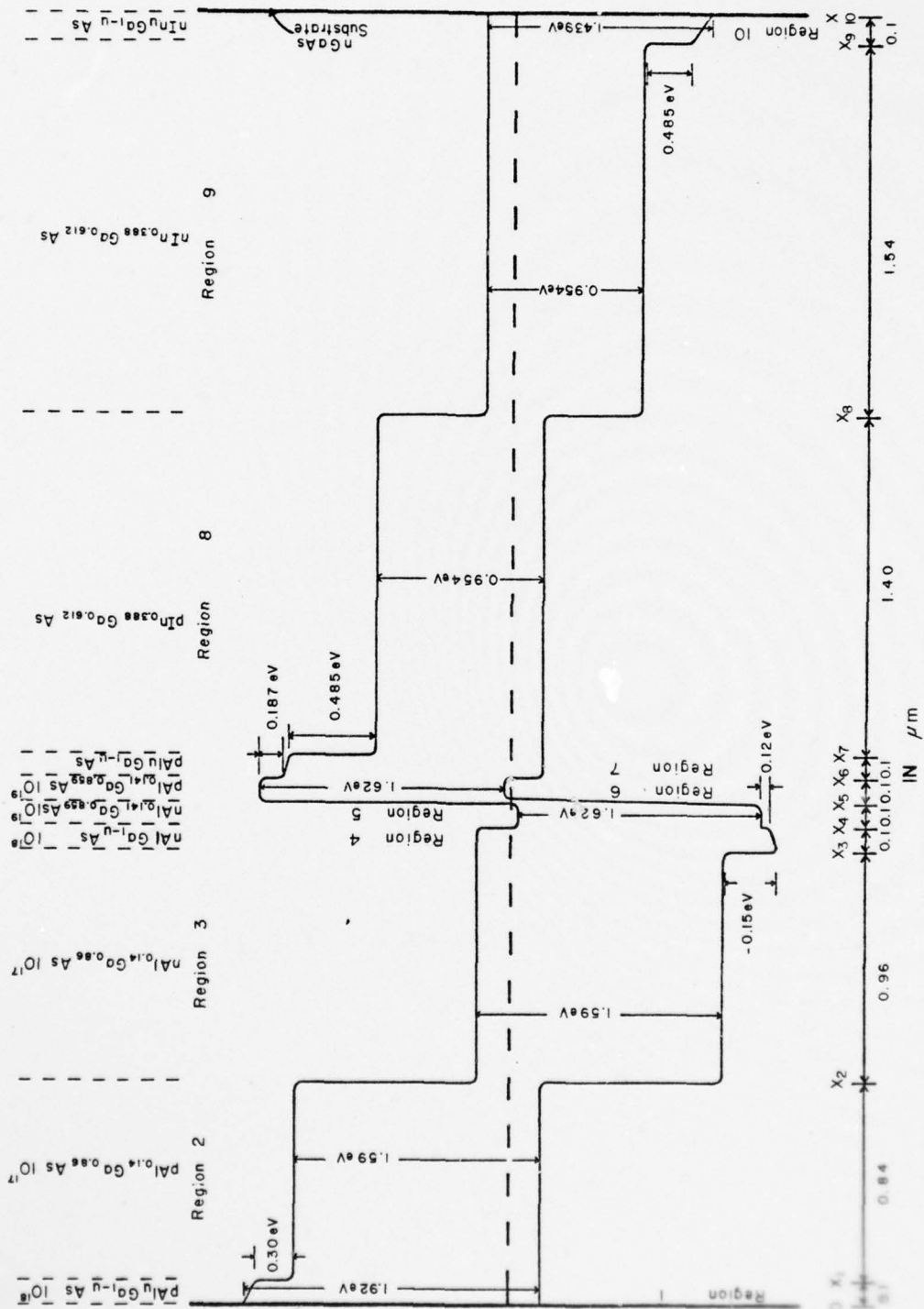
Figure 6.15. A cascade, idealized, 2-junction, voltage aiding solar cell structure resulting from the third iterative design optimization.
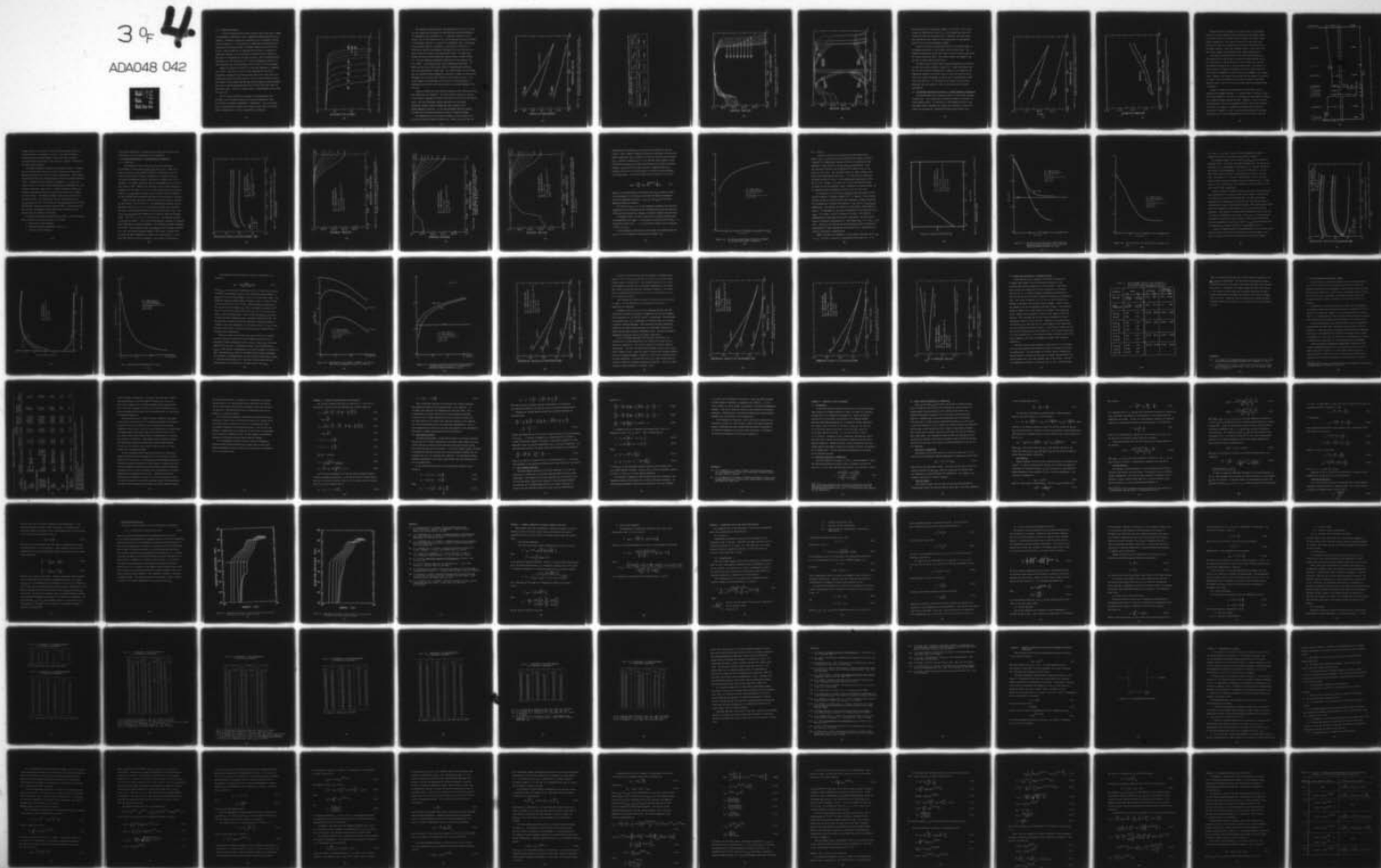
6.3.3  Temperature Behavior

To fully characterize the cascade structure under study and to compare
its performance to GaAs and Si cells, temperature characteristics must be
obtained.  Temperature studies were conducted on the "optimized" structure
given in Figure 6.15.  The calculation of temperature characteristics was
done using the identical Fortran IV computer program as was used for the
PW cell.  This provides for an excellent basis on which to compare the
temperature behavior of the PW cell and the cascade cell of Figure 6.15.
The latter is essentially two PW cells in series.  While calculations have
been done for 0, $10^6$ and $10^7$ cm sec$^{-1}$ surface recombination velocity, in
this discussion only the calculations for $10^6$ cm sec$^{-1}$ will be presented.

Figure 6.16 shows the cascade V-I curves with temperature a parameter
up to 600°K.  Each point on the V-I curve represents the sum of the
photovoltaic voltages (top and bottom cells) minus 0.050 volts due to the
voltage drop across the tunnel junction, all for a given terminal current.
This family of curves shows that the open circuit voltage at 325°K is nearly
twice that of the PW GaAs homojunction cell and more than three times the
value of Si cells.  The short circuit current is approximately equal to that
of the PW cell.

The V-I curves show that the voltage at the maximum power point
and open circuit voltage decrease with increasing temperature, while
the current is relatively independent of temperature.  Thus, the cascade
cell V-I characteristics behave like a single junction solar cell except
that the magnitudes of the device parameters are different.

175
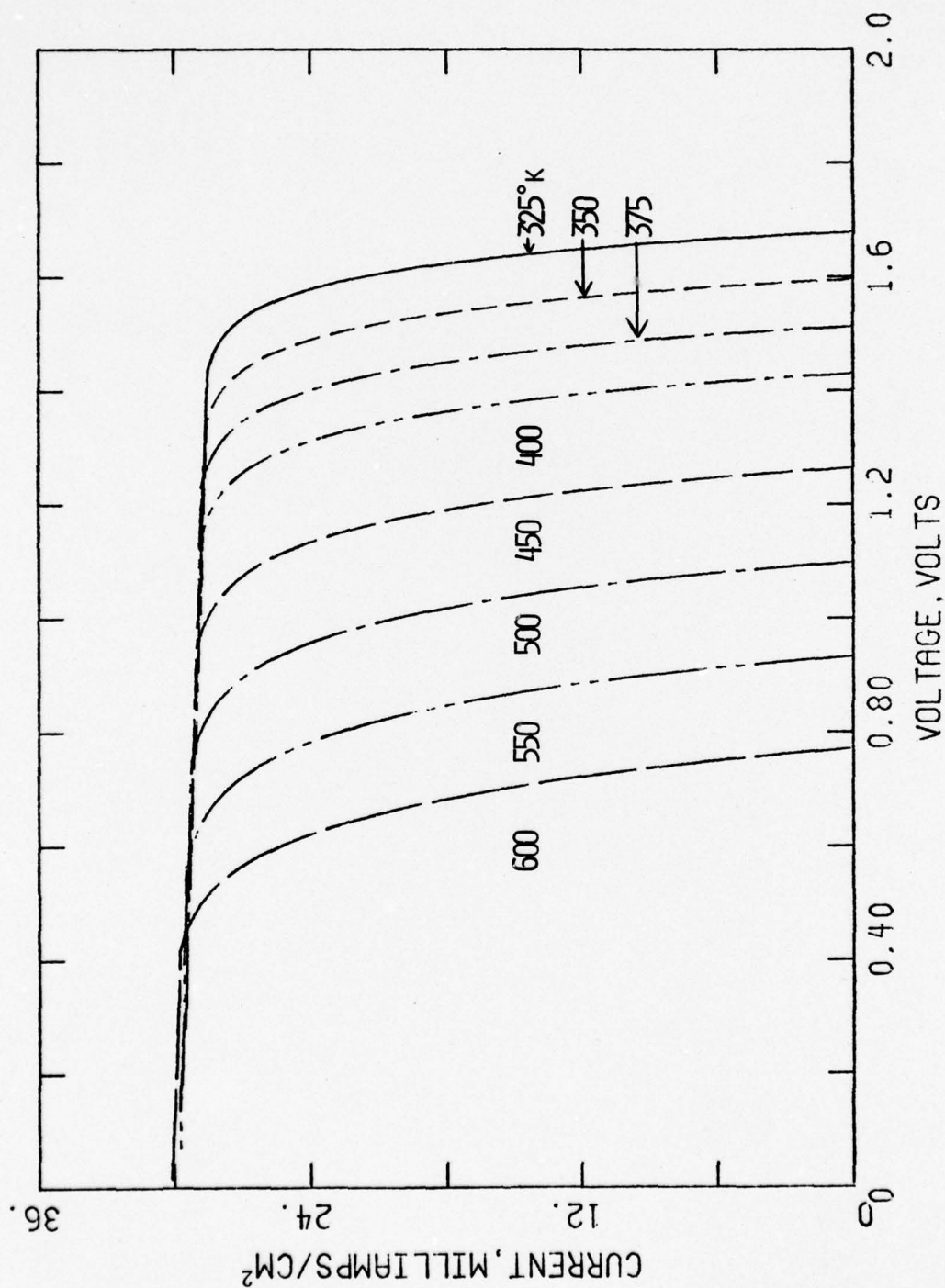
Figure 6.16. The cascade solar cell V-I curve with temperature a parameter for S = $10^6$ cm sec$^{-1}$.

176

The computer program calculates the maximum power from the V-I curve for each temperature, determines the AMO efficiency and plots efficiency vs. temperature given in Figure 6.17. In addition, Figure 6.17 also shows a plot of the efficiency for the top and bottom cells also calculated by the program, from the V-I curves of the individual cells. The cascade cell efficiency exhibits a temperature coefficient of 0.0733%/°C or 0.099 mw/°C, which is approximately 50% higher than for the PW cell and nearly double the value of GaAs experimental values. The comparison between the PW and cascade temperature characteristics is made in Table 6.2. The most important temperature coefficient is that listed in the last column - the normalized power output temperature coefficient. It shows that the PW cell and cascade cells are approximately equivalent with the cascade having a slight edge. On a similar basis it can be shown that the normalized power temperature coefficient is lower for the top cell and higher for the bottom cell compared to the cascade as a unit. This arises because the photovoltage of the top cell is less sensitive to temperature than that of the bottom cell due to the larger bandgap of the top cell.

Figure 6.18 shows the total spectral response of the cascade solar cell with temperature as a parameter. The total spectral response is the sum of the spectral responses of electrons and holes of both the top and bottom cells. The short wavelength response decreases with increasing temperature because surface recombination loss increases at the window-atmosphere interface. At the long wavelength edge the response increases with increasing temperature because of bandgap shrinkage.

The component parts of the spectral response curves of Figure 6.18 may also be plotted as shown in Figure 6.19. These curves show that the

177
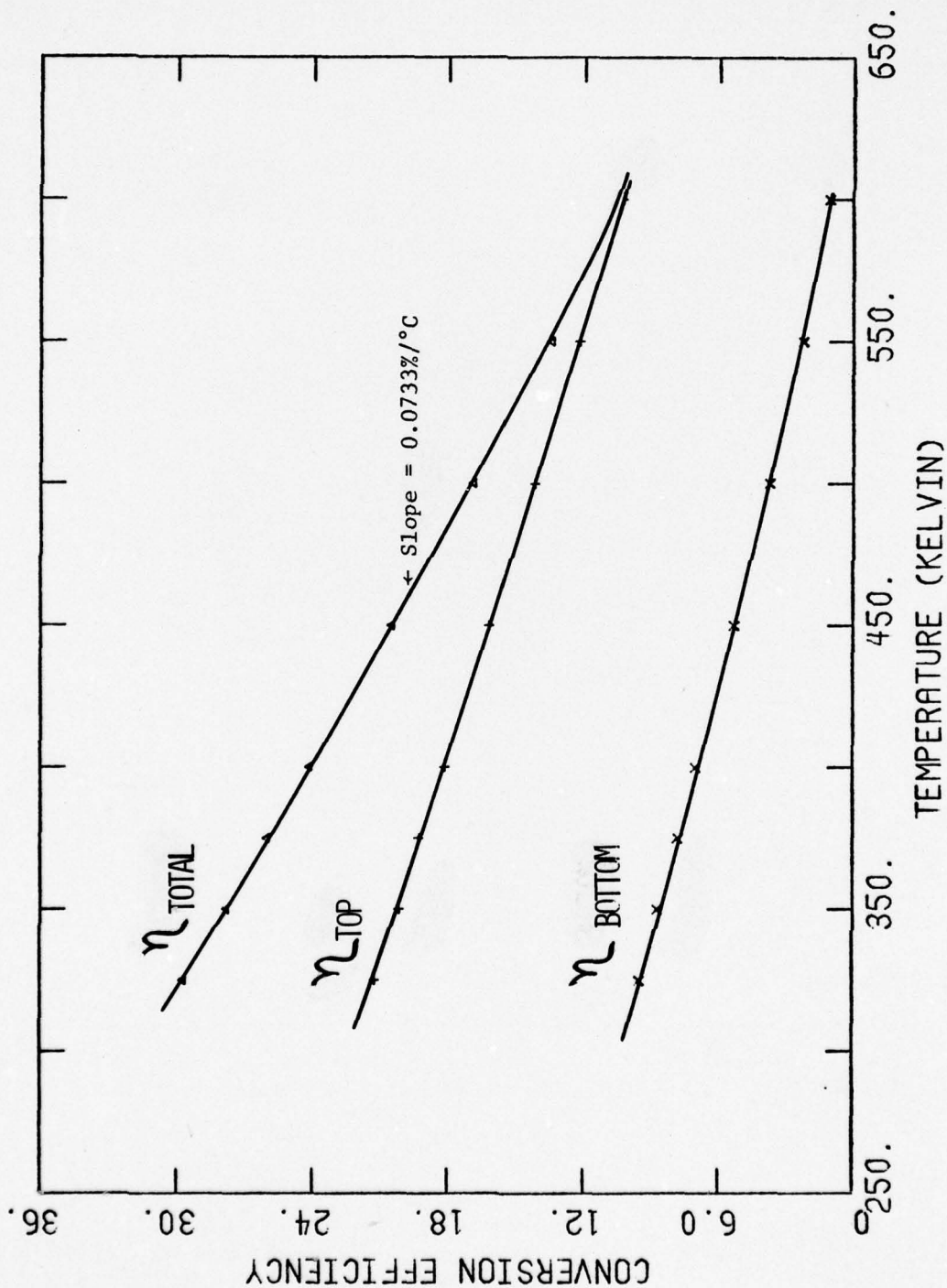
Figure 6.17. Conversion efficiency at AM0 of the top, bottom and the sum of the top and bottom cells as a function of temperature for $S = 10^6$ cm sec$^{-1}$.

178

Table 6.2. Comparison of PW and Cascade cell temperature characteristics at AMO and $10^6$ cm sec$^{-1}$ SRV.

| | $\eta$ | $P_m$ | $d\eta/dT$ | $dP_m/dT$ | $d(P_m/P_o)/dT$ |
|---|---|---|---|---|---|
| Potential Well | 21.5% | 29.1 mw/cm$^2$ | 0.0544%/°C | 0.074 mw/°C | 0.0025/°C |
| Cascade | 32.0 | 43.3 | 0.0733 | 0.099 | 0.0023 |

179
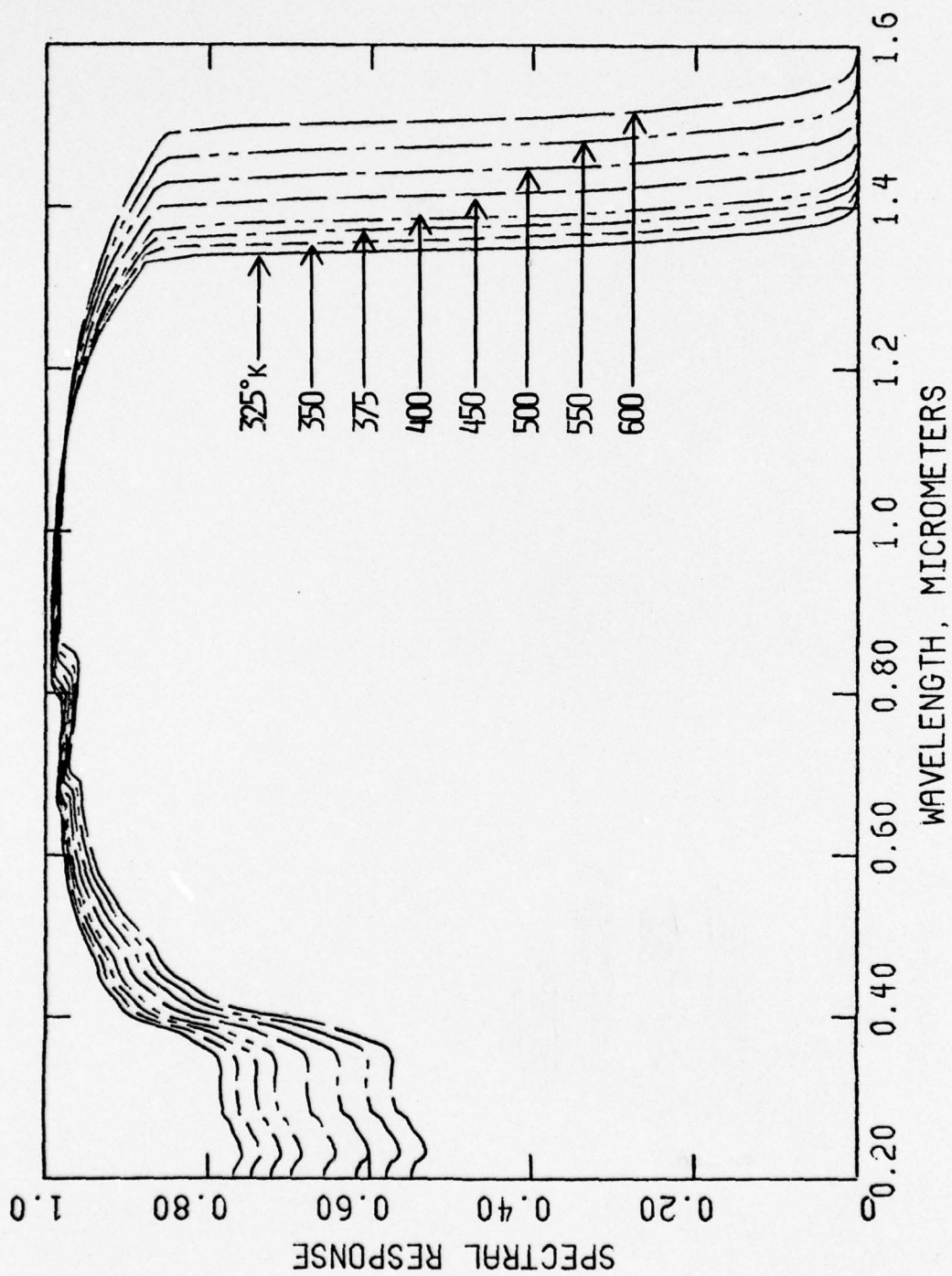
Figure 6.18. Spectral response of the two-cell, cascade solar cell with temperature a parameter for S = $10^6$ cm sec$^{-1}$.
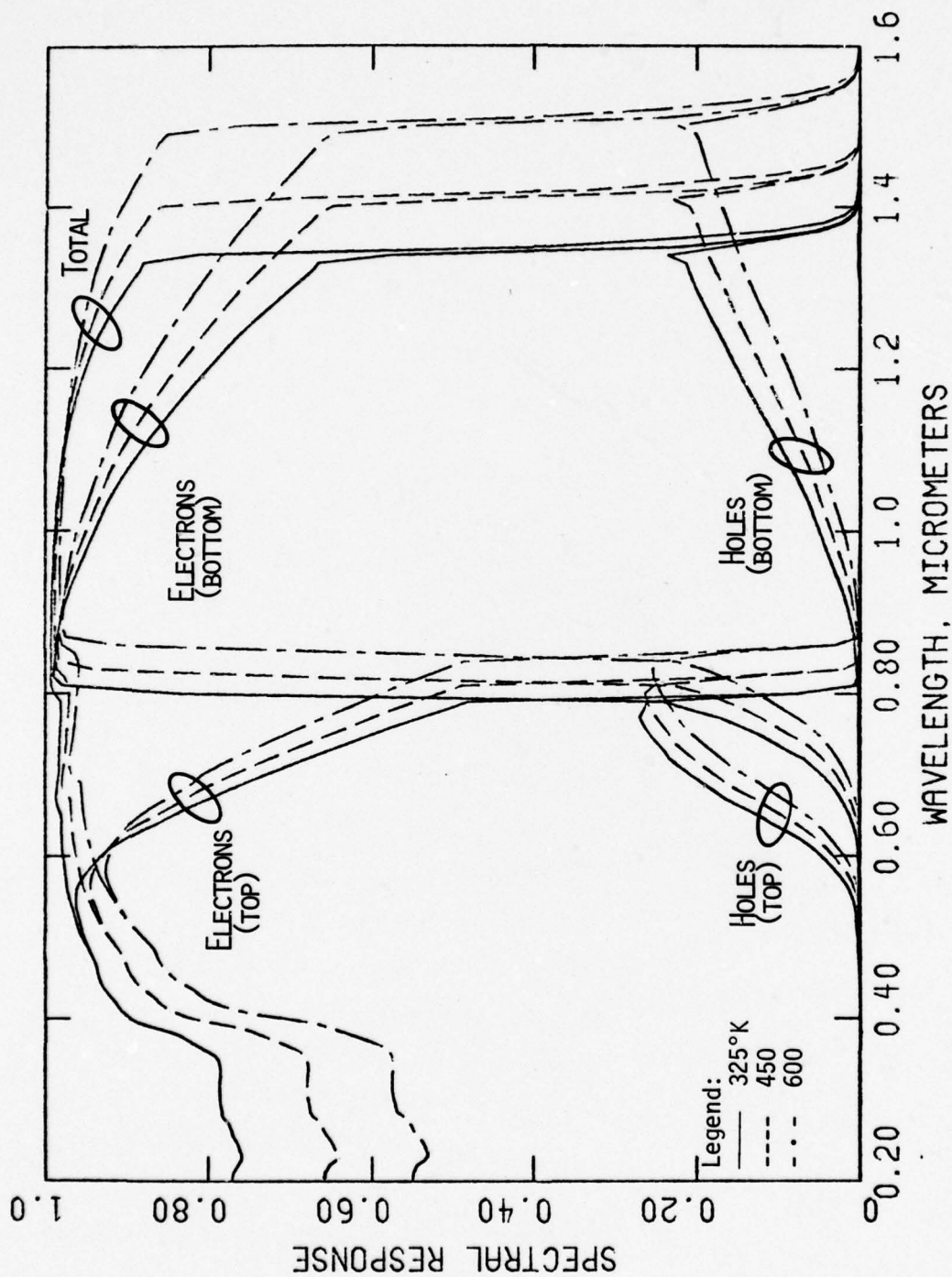
Figure 6.19. Spectral response of electrons, and holes for the top and bottom cells and the total of the cascade solar cell for $S = 10^6$ cm sec$^{-1}$.

181

electron response is substantially higher in both cells. This arises because the incident flux falls first on the p-region and then on the n-region for both top and bottom cells. Therefore, the total photon flux absorbed by each p-region of the homojunctions is substantially greater than in the corresponding n-regions.

Figure 6.20 shows the temperature behavior of the photovoltage at the maximum power point of the cascade, top and bottom cells. The normalized temperature coefficient of the top cell is smaller than either the cascade and bottom cells. This arises because the bandgap of the top cell is larger than the bottom cell.

The dark current increases with increasing temperature for both the top and bottom cells as shown in Figure 6.21. These calculations show that for the optimized configuration of Figure 6.15 the magnitude and temperature behavior of the dark current for the two cells are nearly equal, even though the bandgap of the top cell is substantially larger than the bottom cell. If the structure in Figure 6.15 were further optimized, the dark currents of the two cells would show a smaller differential.

## 6.4 Two-Junction Cascade Cell Structure - Voltage Opposing Configuration

The photovoltages are of opposite polarity in the voltage opposing configuration. This cascade cell configuration should be operated as a three-terminal device. If operated as a two-termination device, with the middle contact floating, the cascade cell efficiency is less than either cell operated as a conventional single junction solar cell.

182
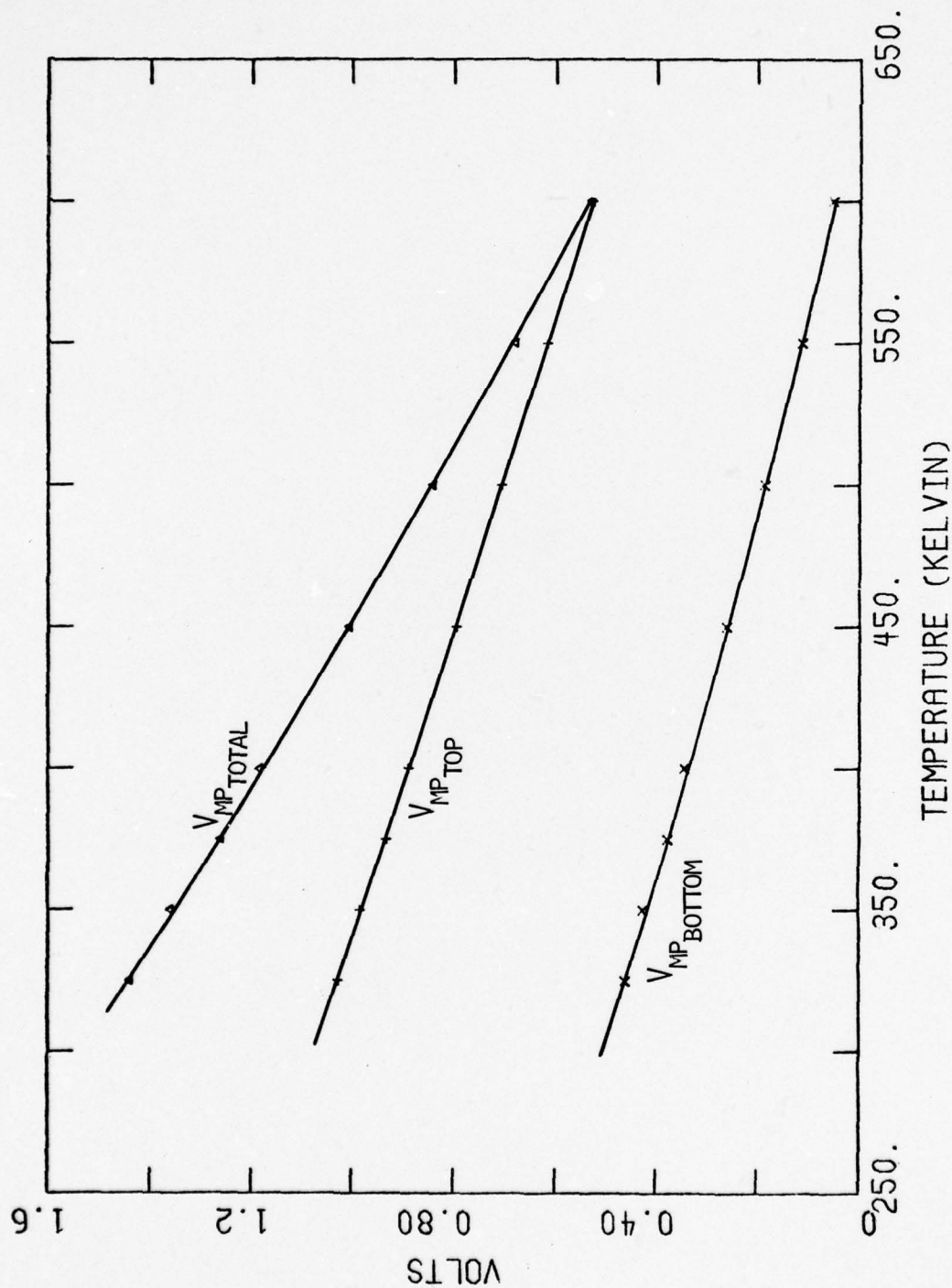
Figure 6.20. Voltage at the maximum power point of the top, bottom and the sum of the top and bottom cells as a function of temperature for S = 10⁶ cm sec⁻¹.

183
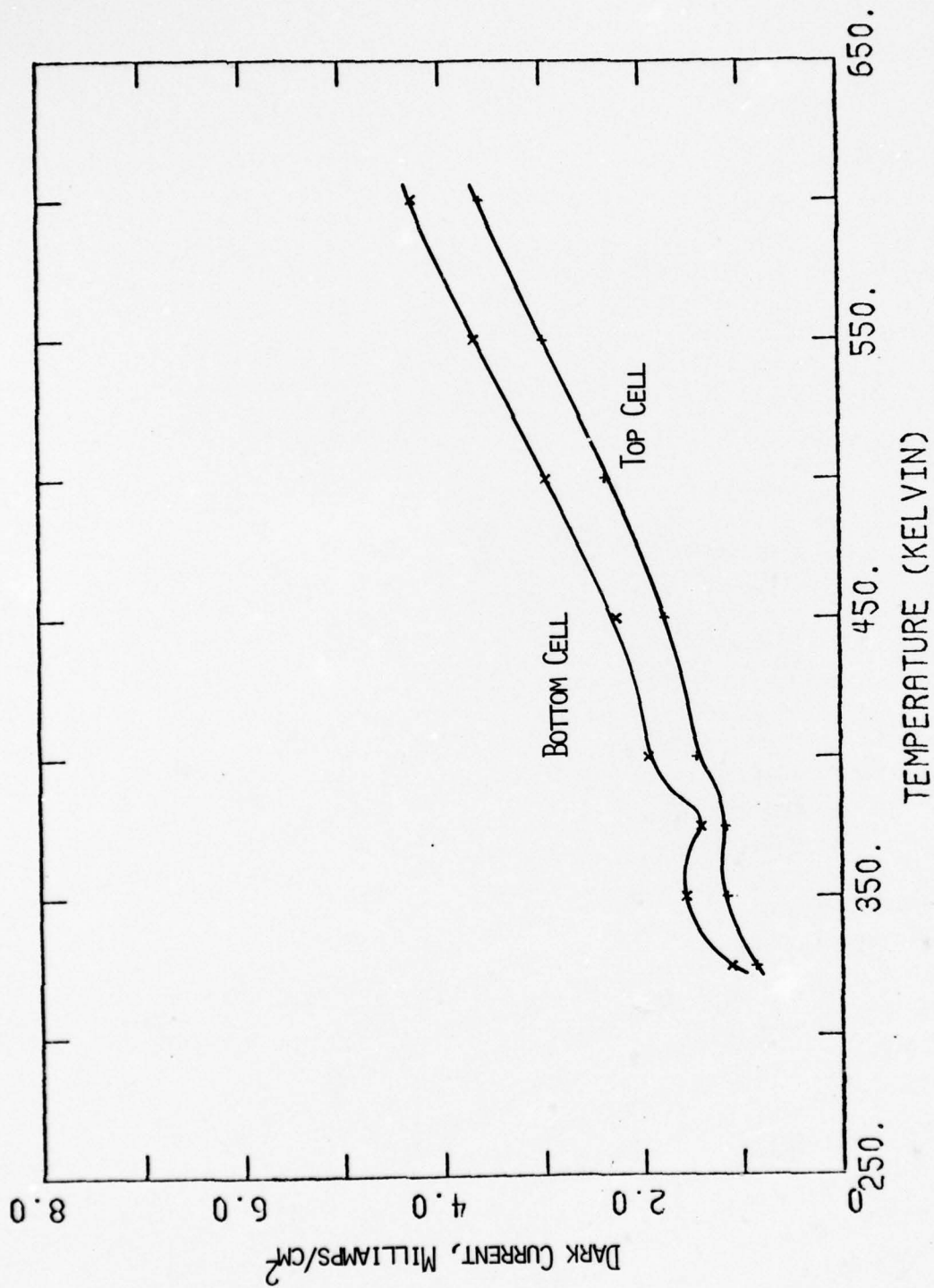
Figure 6.21. Logarithm of the total dark current of the top and bottom cells as a function of temperature for $S = 10^6$ cm sec$^{-1}$.

184

Neglecting contact problems for the center layer, the optimized cascade cell voltage opposing (CCVO) configuration will always exhibit an efficiency equal to or higher than the cascade cell voltage aiding (CCVA) configuration. This results because in the CCVA case equal photocurrents must flow through each cell and the voltage drop across the tunnel junction. Area lost in making contact to the center layer will reduce somewhat the advantage of the voltage opposing case.

The computer program written for the closed form analysis has been modularized so that it may be applied for single junction and up to n-junctions in a cascade solar cell. On each side of a junction, the program provides for up to three distinct layers. This allows for input structure and material parameters for each of three layers such as described in APPENDIX F for the PW cell and in APPENDIX G for cascade cells. Moreover, the modularization allows for the program to be applied to simple Si and III-V materials cells with or without the low-high junction (LHJ), to the PW cell and to cascade cells with voltage aiding or opposing.

Figure 6.22 shows the idealized CCVO structure which is to be optimized for maximum efficiency. It contains seven (7) distinct layers plus a GaAs substrate. The latter is optically and electronically inactive in a properly designed cascade structure. Regions 1, 2 and 3 serve the same functions as for the corresponding layers of the PW cell described in Section 5.0. Region 4 is graded to accelerate holes toward the bottom cell. Regions 5, 6 and 7 serve the same functions as described in Section 5.0 for the corresponding layers of the PW cell. The cell
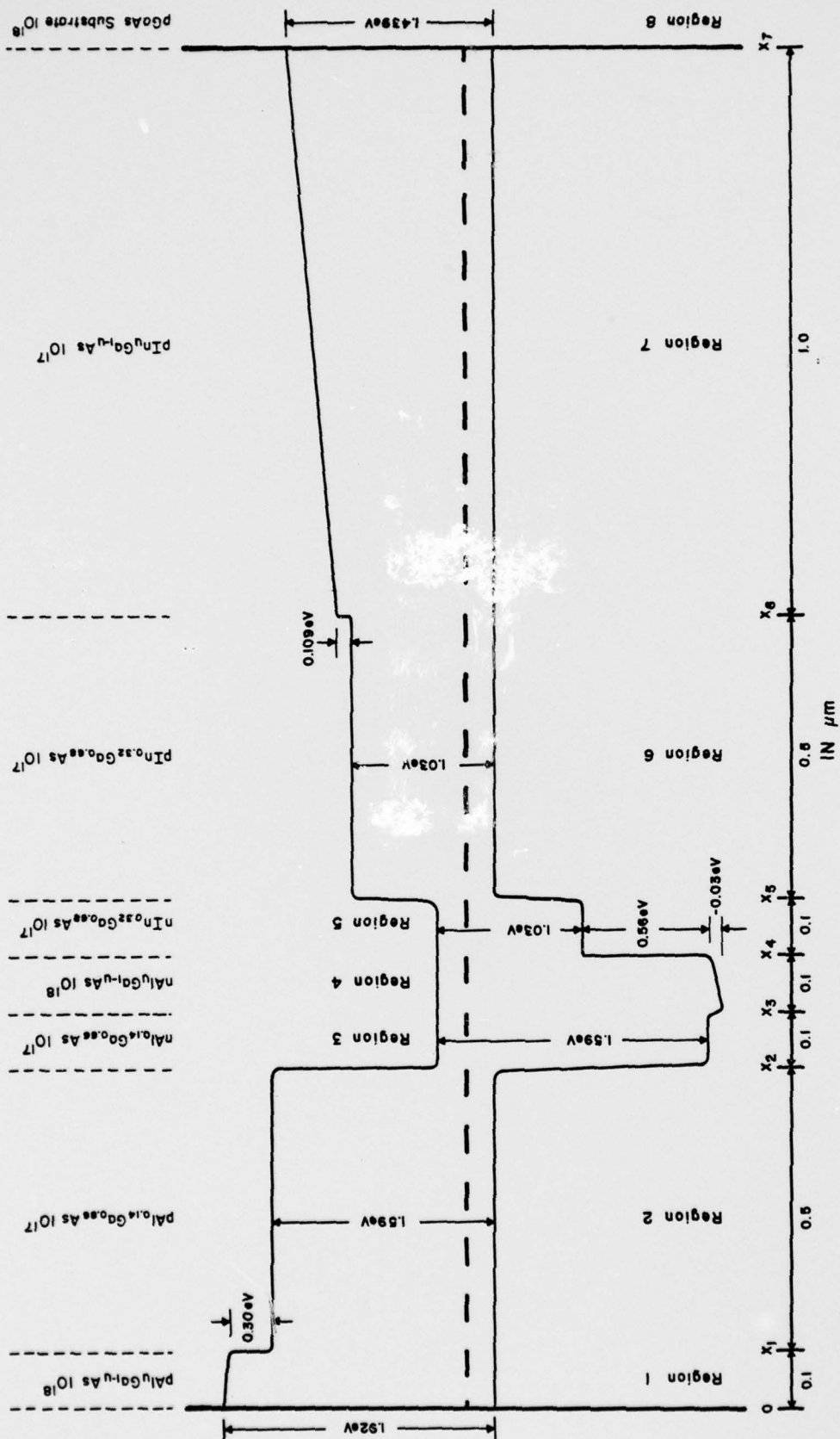
Figure 6.22. A cascade, idealized, 2-junction, voltage opposing solar cell structure.

design provides for the built-in electric field intensity at 290°K to be 3000 volts per cm in Regions 1, 4 and 7. The field in Region 1 accelerates electrons toward Region 2, while the field in Region 4 accelerates holes toward Region 5 and the field in Region 7 accelerates electrons towards Region 6.

The design optimization represents a preliminary effort. The band-gap at the surface was chosen to be 1.92 eV, while the top and bottom homojunction chosen are 1.590 and 1.030 eV, respectively. These bandgap values selected were only educated guesses and do not represent optimized values. Similarly the layer thickness of Regions 1, 3, 4 and 5 were chosen to be 0.1 μm. None of these thicknesses were optimized, but, only represent arbitrarily chosen values. Further optimization studies of thickness and bandgaps beyond that reported here will result in higher efficiency values. The bandgap of Region 4 was selected so that it is optically inactive. The materials of the top cell was chosen to be $Al_{0.14}Ga_{0.86}As$ and that of the bottom cell $In_{0.32}Ga_{0.68}As$ because of their high mobility values and reasonable lifetime values. Lattice misfit and the resultant recombination centers which may be introduced in this structure are not included in this model.

The design optimization described below is based on the band structure given in Figure 6.22 and the sequence is as follows:

1.  Bottom cell p-layer thickness
2.  Valence band edge discontinuity, $\Delta E_{v3}$, at $x_3$
3.  Top cell p-layer thickness

The cascade optimization is conducted on the basis that the sum of the efficiencies of the top and bottom cells is maximized.

### 6.5 Results and Discussion – Voltage Opposing Configuration

### 6.5.1 Bottom Cell

The optimization study commenced with the determination of the thickness of the p-type $In_{0.32}Ga_{0.68}As$ layer, $x_6-x_5$. Figure 6.23 shows the results of the cascade cell (sum of efficiencies of the top plus the bottom cells) efficiency calculation as a function of $x_6-x_5$. The surface recombination velocity (SRV) which is present at $x = 0$ is a parameter. The maximum efficiency occurs at approximately 2.0 μm for all three values of SRV. However, the efficiency is not a strong function of thickness over the range 1.5 to 4.0 μm. This arises because the diffusion length in $In_{0.32}Ga_{0.68}As$ is greater than 10 μm and the spectral response and dark current nearly compensate and there is little change in efficiency.

Figures 6.24(a), (b) and (c) show the total cascade spectral response for SRV values 0, $10^6$, $10^7$ cm sec$^{-1}$. The response was calculated over the wavelength range 0.2 to 1.2 μm. Each spectral response curve represents the sum of the electrons and holes of both the top and bottom cells. The p-type $In_{0.32}Ga_{0.68}As$ layer thickness is a parameter, using the following values: 0.5, 0.8, 1.1, 1.4, 1.7, 2.0 and 4.0 μm. The response increases in the spectral region $\lambda > 0.75$ μm with increasing $x_6-x_5$ because of increased photon absorption at longer wavelengths. This behavior is almost independent of the SRV. Even though the p-type $In_{0.32}Ga_{0.86}As$ layer thickness increases to 4.0 μm, the electron diffusion length in this region is greater than 10 μm and the bulk recombination increase is not a major factor. At the same time, however, carrier confinement in this region is monotonically

188
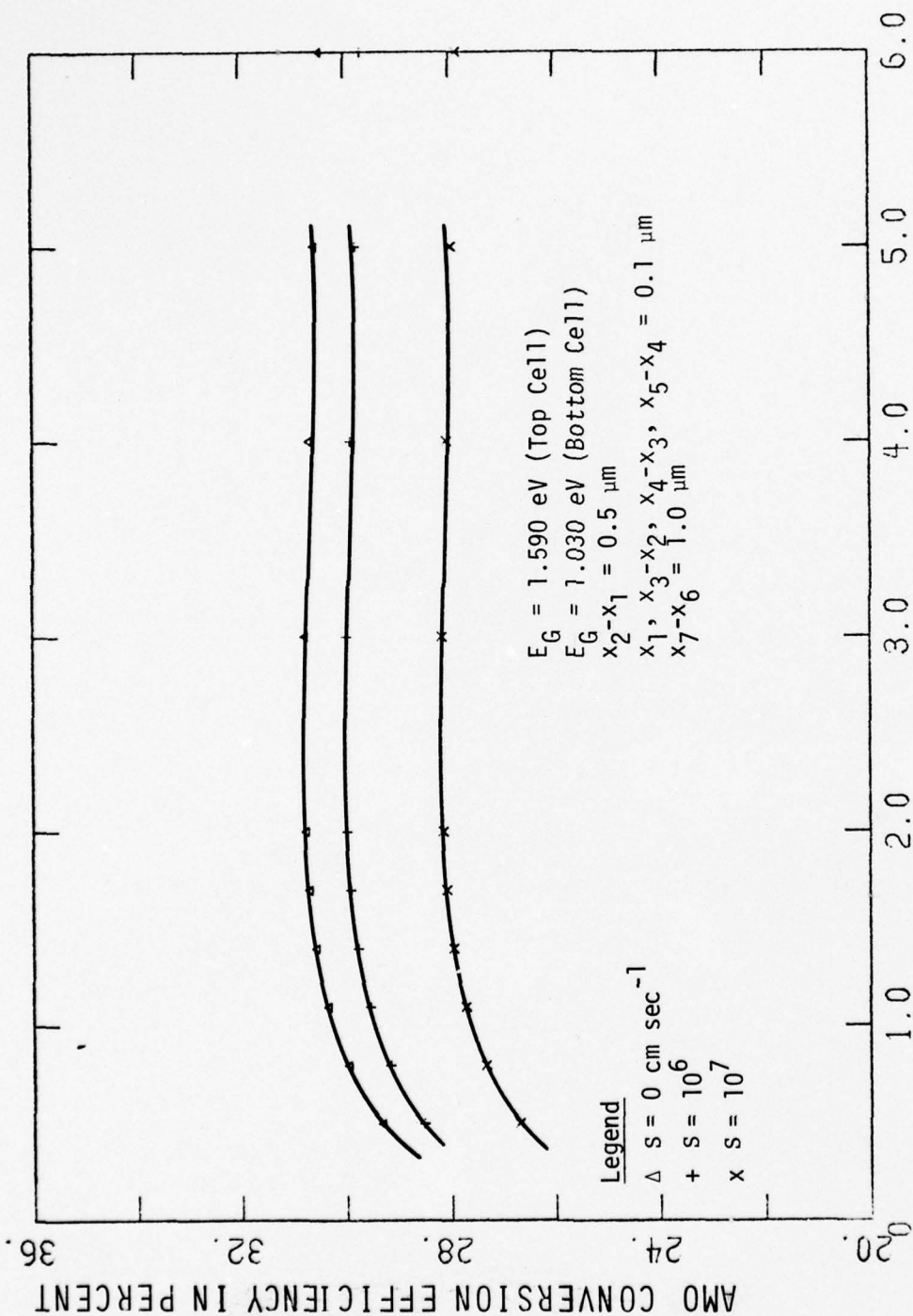
Figure 6.23. Conversion efficiency vs. bottom cell p-type thickness for the CCVO structure.

$E_G = 1.590$ eV (Top Cell)
$E_G = 1.030$ eV (Bottom Cell)
$x_2 - x_1 = 0.5$ $\mu$m
$x_1$, $x_3 - x_2$, $x_4 - x_3$, $x_5 - x_4 = 0.1$ $\mu$m
$x_7 - x_6 = 1.0$ $\mu$m

Legend
△ $s = 0$ cm sec$^{-1}$
+ $s = 10^6$
× $s = 10^7$

Bottom Cell p-type Region #6 Thickness, $x_6 - x_5$, in $\mu$m.

AM0 CONVERSION EFFICIENCY IN PERCENT
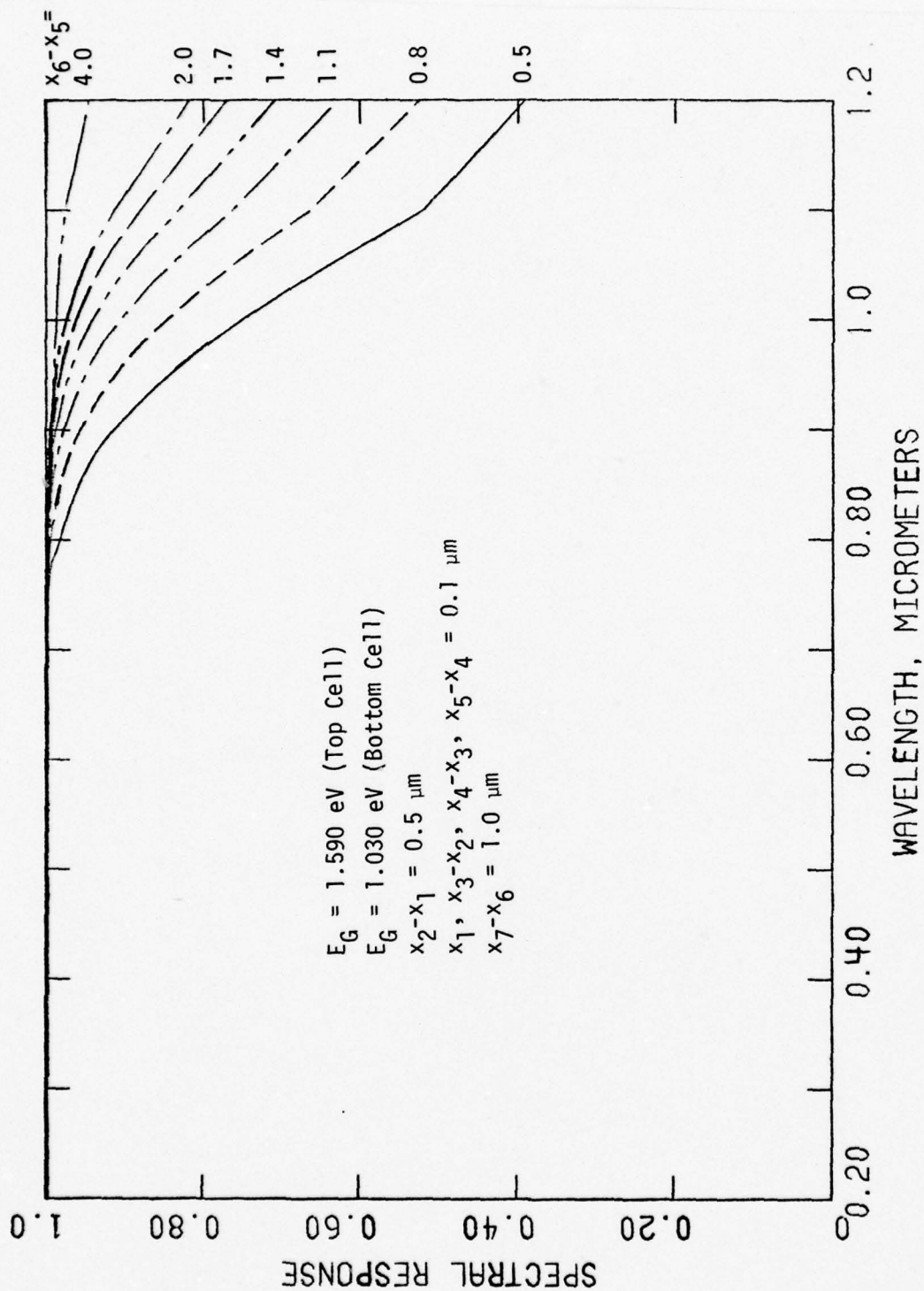
Figure 6.24(a). The total spectral response of the cascade structure with the thickness of the p-type $Ga_{0.68}In_{0.32}As$ layer a parameter for $S = 0$.
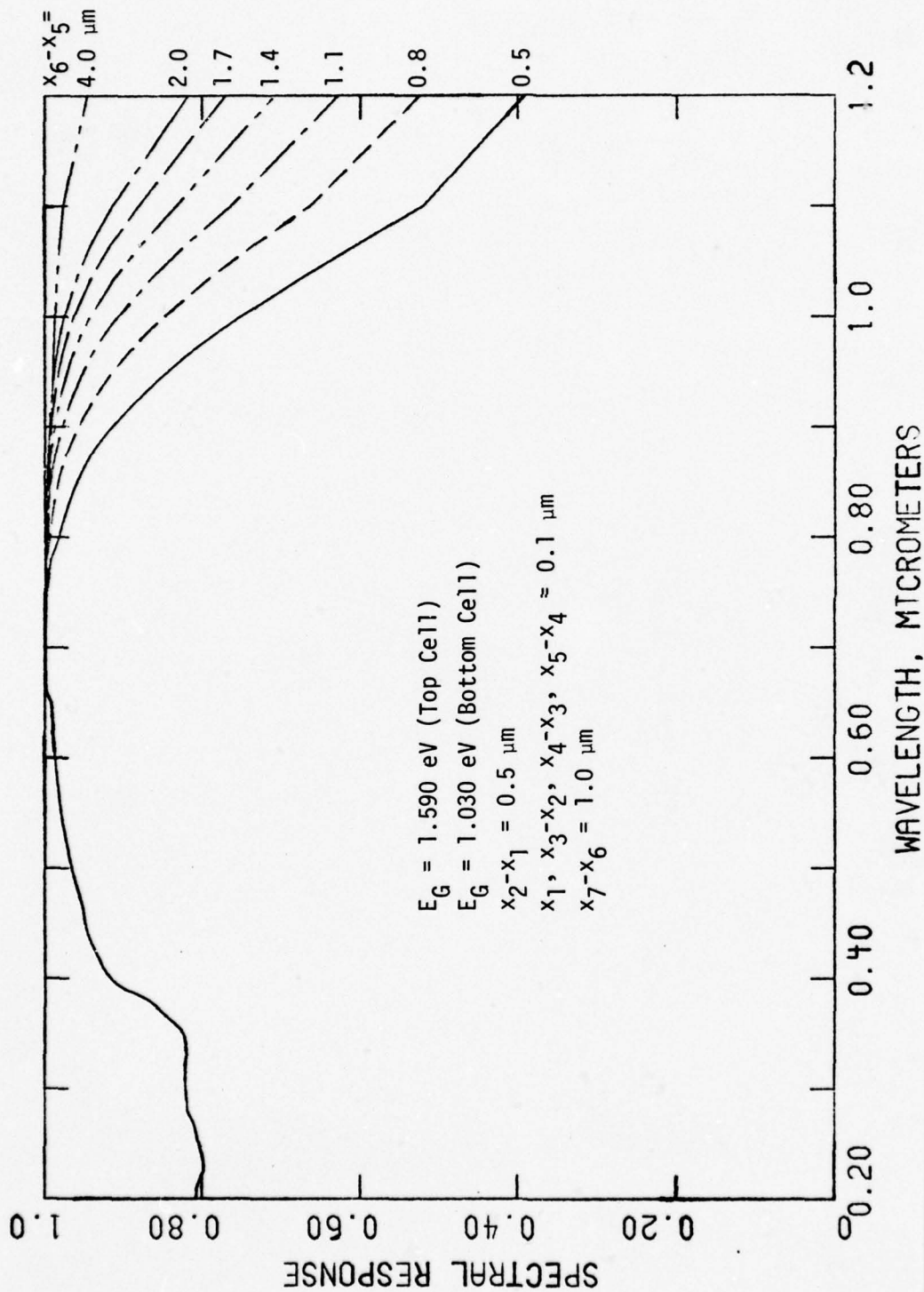
Figure 6.24(b). The total spectral response of the cascade (CCVO) structure with the thickness of the p-type $In_{0.32}Ga_{0.68}As$ layer a parameter for $S = 10^6$ cm sec$^{-1}$.

$E_G = 1.590$ eV (Top Cell)
$E_G = 1.030$ eV (Bottom Cell)
$x_2-x_1 = 0.5$ μm
$x_1$, $x_3-x_2$, $x_4-x_3$, $x_5-x_4 = 0.1$ μm
$x_7-x_6 = 1.0$ μm

$x_6-x_5 =$
4.0 μm
2.0
1.7
1.4
1.1
0.8
0.5

SPECTRAL RESPONSE

WAVELENGTH, MICROMETERS
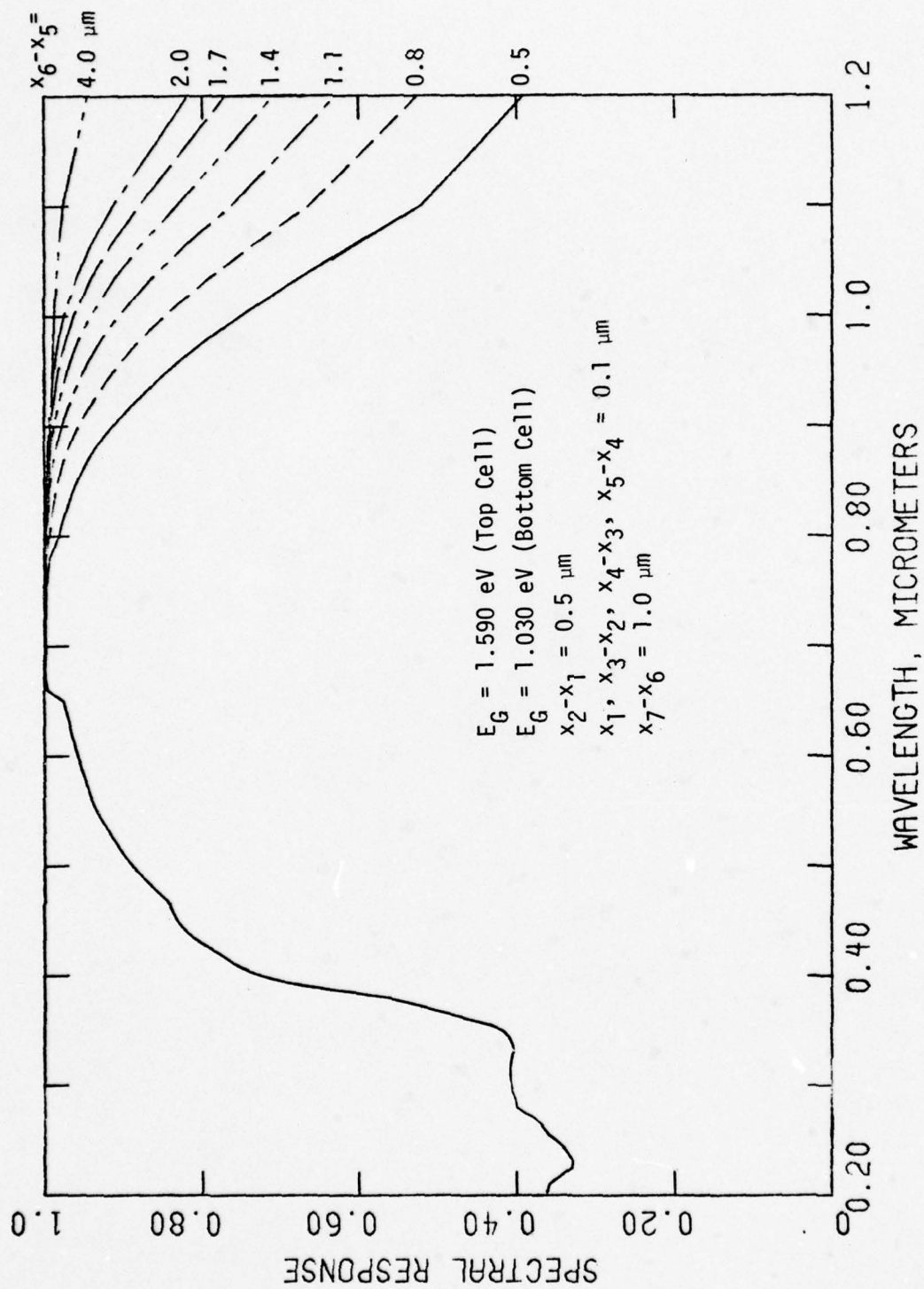
Figure 6.24(c). The total spectral response of the cascade (CCVO) structure with the thickness of the p-type $In_{0.32}Ga_{0.68}As$ layer a parameter for $s = 10^7$ cm sec$^{-1}$.

$E_G = 1.590$ eV (Top Cell)
$E_G = 1.030$ eV (Bottom Cell)
$x_2-x_1 = 0.5$ μm
$x_1$, $x_3-x_2$, $x_4-x_3$, $x_5-x_4 = 0.1$ μm
$x_7-x_6 = 1.0$ μm

decreasing with increasing $x_6$-$x_5$ resulting in an increase in the dark
current. This is shown in Figure 6.25 where the reciprocal of the electron
charge accumulation, $R_{n6}$, in Region 6 is shown to increase with increasing
$x_6$-$x_5$. Therefore, beyond $x_6$-$x_5$ = 2.0 μm the dark current begins to show
a significant increase and to more than overcome the increase in spectral
response. $R_{n6}$ increases by nearly an order of magnitude when $x_6$-$x_5$
increases from 0.8 to 4.0 μm and results in the dark current increasing
by the same factor. The electron dark current obtained is of the form

$$ J_{Dn6} = q \frac{D_{n6}}{L_{n6}} n_{p60} \left( e^{qV_2/kT} -1 \right) R_{n6} \qquad (6-1) $$

where $V_2$ is the photovoltage of the bottom cell, $R_{n6}$ is given in closed
form in Appendix G as a function of structure and material parameters
as well as temperature and where q, $D_{n6}$, $L_{n6}$ and $n_{p60}$ have the usual
meaning pertaining to Region 6.

For values of $x_6$-$x_5$ < 2.0 μm the incomplete absorption loss more than
compensates for the increased carrier confinement and increased collection
efficiency which results in a decrease in spectral response and efficiency.

In Figures 6.24(a), (b) and (c) the spectral response decreases with
increasing SRV in the range $\lambda$ < 0.65 because of increase surface losses. In
the spectral region 0.65 < $\lambda$ < 0.75 the spectral response is not sensitive
to SRV or to $x_6$-$x_5$.

In all subsequent calculations in this study, the optimized value for
$x_6$-$x_5$ = 2.0 μm is imposed on the structure in Figure 6.22.

193

$E_G$ = 1.590 eV (Top Cell)
$E_G$ = 1.030 eV (Bottom Cell)
$x_2 - x_1$ = 0.5 μm
$x_1$, $x_3 - x_2$, $x_4 - x_3$, $x_5 - x_4$ = 0.1 μm
$x_7 - x_6$ = 1.0 μm
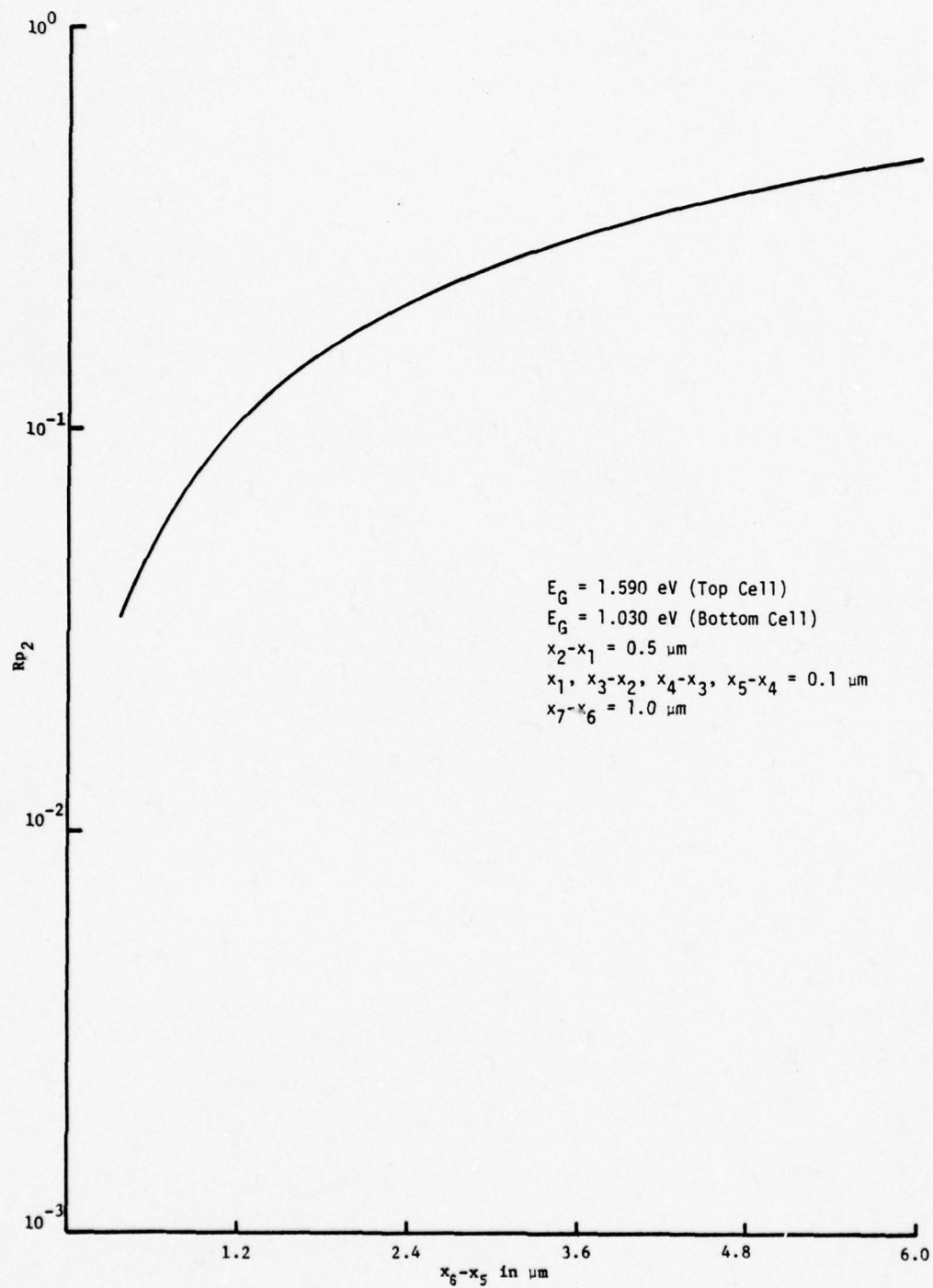
Figure 6.25.  The R-factor multiplying the electron component
at the saturation current in Region 6.

194

### 6.5.2  Top Cell

A study was conducted to determine the valence band barrier height, $\Delta E_{v3}$, at $x_3$ which results in sufficient hole charge confinement in Region 3 to significantly increase efficiency by reducing the hole component of dark current in the $Al_{0.14}Ga_{0.86}As$ homojunction.  Here the conversion efficiency was calculated for 8 values of $\Delta E_{v3}$ in the range 0 to 0.25 volts.  The calculated values are shown in Figure 6.26 with a curve drawn through the points.  It is seen that the efficiency increases from 30.7% at $\Delta E_{v3} = 0$ and asymptotically approaches 31.6% at $\Delta E_{v3} = -0.25$.  Further, it is seen that at -0.12 volts the efficiency is within 0.3% of the asymptotic value.  Therefore, the barrier height, in all subsequent work, was generally chosen at the 0.12 volt level.

The influence of $\Delta E_v$ on the $Al_{0.14}Ga_{0.68}As$ hole contribution to dark current in Region 3 is shown in Figure 6.27.  In Figure 6.27 the electron, hole and the sum of the electron plus hole saturation currents multiplied by the appropriate R- factors are plotted vs. $-\Delta E_{v3}$ for the $Al_{0.14}Ga_{0.68}As$ homojunction.  The electron contribution to dark current, which arises in Region 2, is independent of $\Delta E_{v3}$ and is represented by the horizontial line, $J_{Dn10}$.  In contrast, the hole contribution for $\Delta E_{v3} = 0$ is higher by approximately 30 times than the electron contribution.  The hole contribution is reduced by approximately 200 times between $\Delta E_{v3} = 0$ to $\Delta E_{v3} = -0.25$ volts.  The sum of the electron and hole contribution shows a reduction by approximately 30 times, approaching the horizontal line, representing the electron contribution, asymptotically.

Figure 6.28 shows the reciprocal of hole charge confinement factor, $R_{p3}$, vs. $E_{v3}$.  It shows a reduction of approximately 200 between $\Delta E_{v3} = 0$ to

195
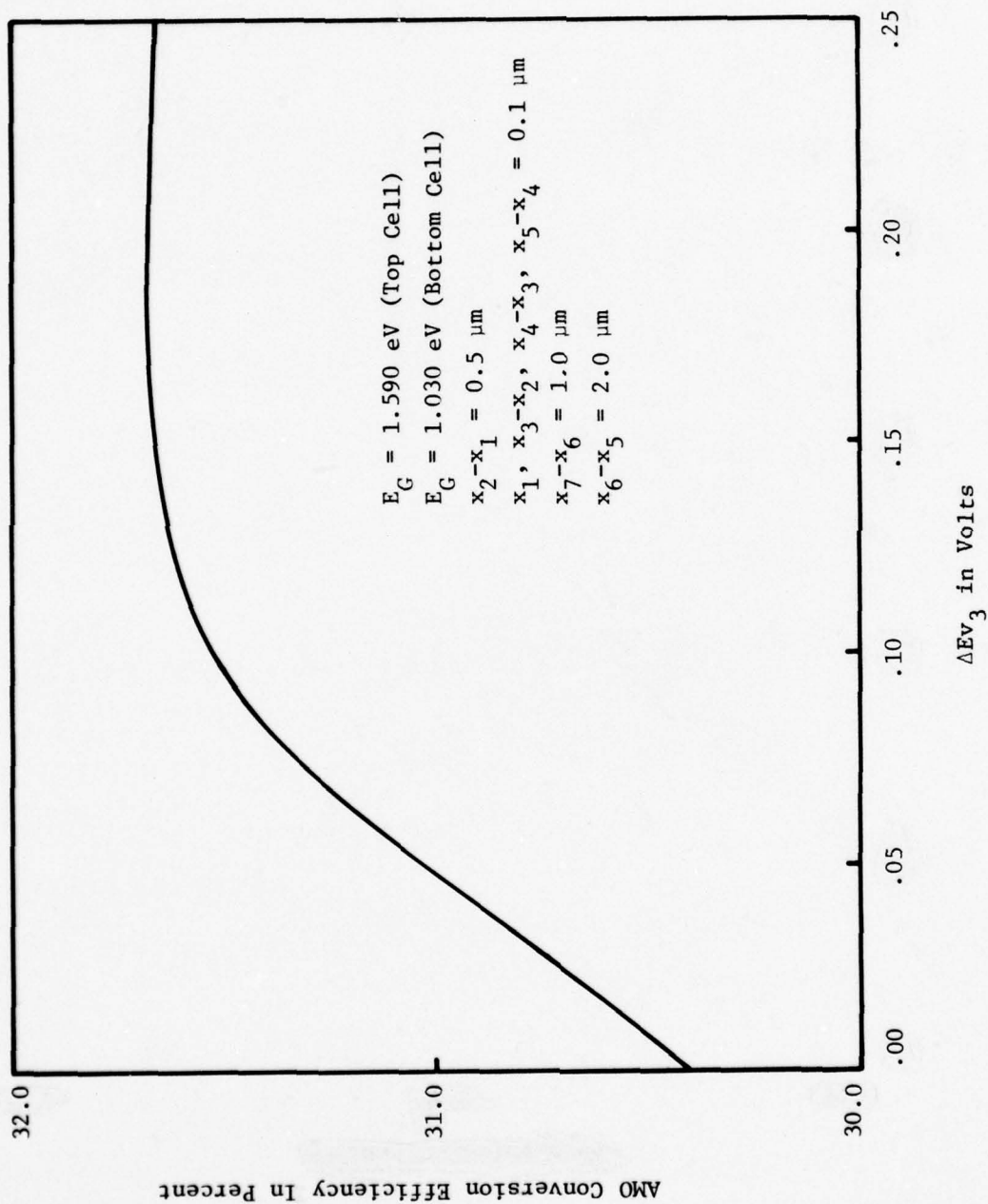
Figure 6.26. The 2-junction cascade (CCVO) conversion efficiency vs. $\Delta E_{v3}$ for $10^6$ cm sec$^{-1}$ recombination velocity.
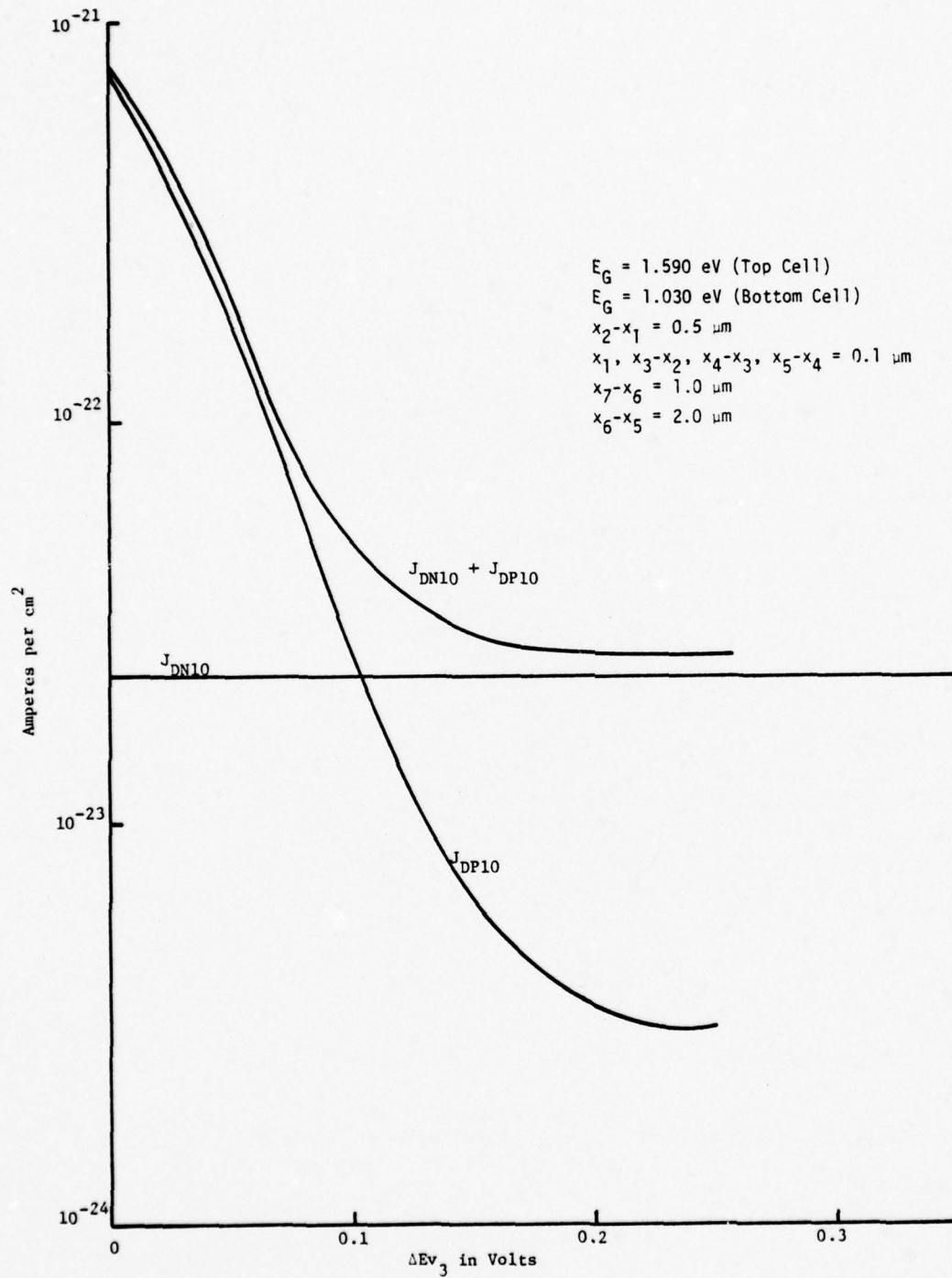
Figure 6.27. Electron, hole and the sum of electron and hole saturation values multiplied by the appropriate charge confinement R-factors vs. $\Delta E_{v3}$.

197
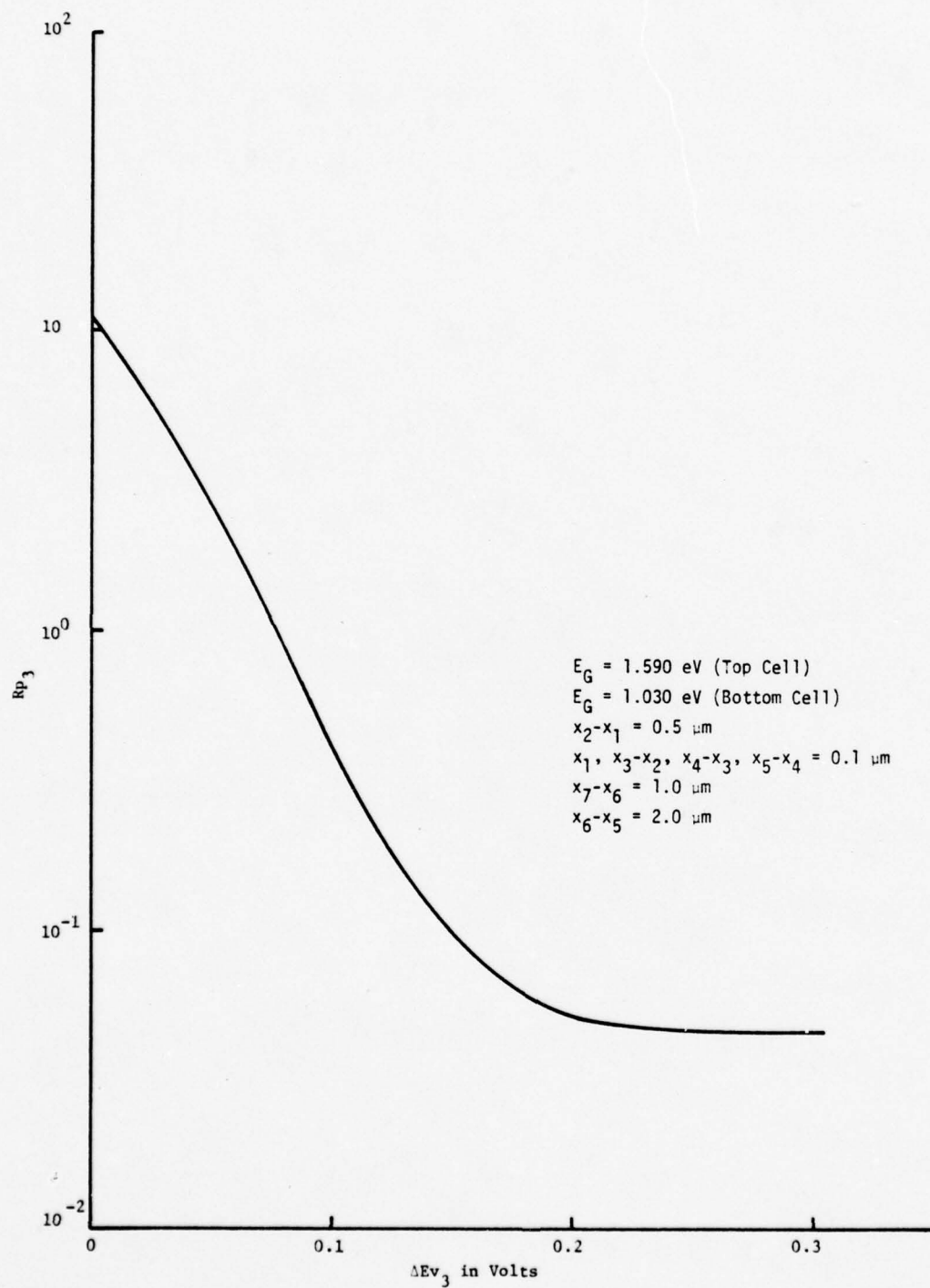
Figure 6.28. The hole charge confinement factor in Region 3 vs. $\Delta E_{v3}$.

-0.25 volts. It is seen to have the correct magnitude and shape to completely describe the hole dark current change in Region 3.

The optimum thickness of the p-type $Al_{0.14}Ga_{0.86}As$ was studied for three SRV values. The results are shown in Figure 6.29. The bottom cell efficiency, $\eta_2$, is independent of SRV because it is isolated from direct and indirect coupling phenomena. The top cell efficiency, $\eta_\tau$, of the CCVO is influenced by SRV and is represented by a curve for each SRV used. The maximum for $\eta_\tau$ occurs at approximately 1.4 to 1.5 μm where the efficiency curves are relatively flat with respect to $x_2-x_1$. In the range 1.4 to 1.5 μm for $x_2-x_1$, the efficiency is 29.7 and 32.4% for $10^7$ and 0 cm sec$^{-1}$ SRV, respectively.

Figure 6.30 shows the electron, hole and the sum of the electron and hole contributions to the short circuit current density of the top cell as a function of the p-type layer thickness. The hole contribution decreases with increasing $x_2-x_1$, while both the total and the electron contributions to short circuit current increase. This occurs because while the n-type thickness is held constant at 0.1 μm the p-type thickness increases. This results in increased photon absorption in the p-type and a decrease in absorption in the n-type. For $x_2-x_1 = 0.1$ μm the electron contribution to the short circuit current is less than 15 mA/cm$^2$ while the hole contribution is less than 5 mA/cm$^2$. $J_{scn1}$ increases sharply with increasing $x_2-x_1$, rising to 28 mA/cm$^2$ at approximately 2.0 μm.

Figure 6.31 shows the solar flux exiting Region 3, the top cell n-type layer decreasing sharply with increasing p-type layer thickness, $x_2-x_1$. This is a measure of the increased absorption occurring in Region 2.

199
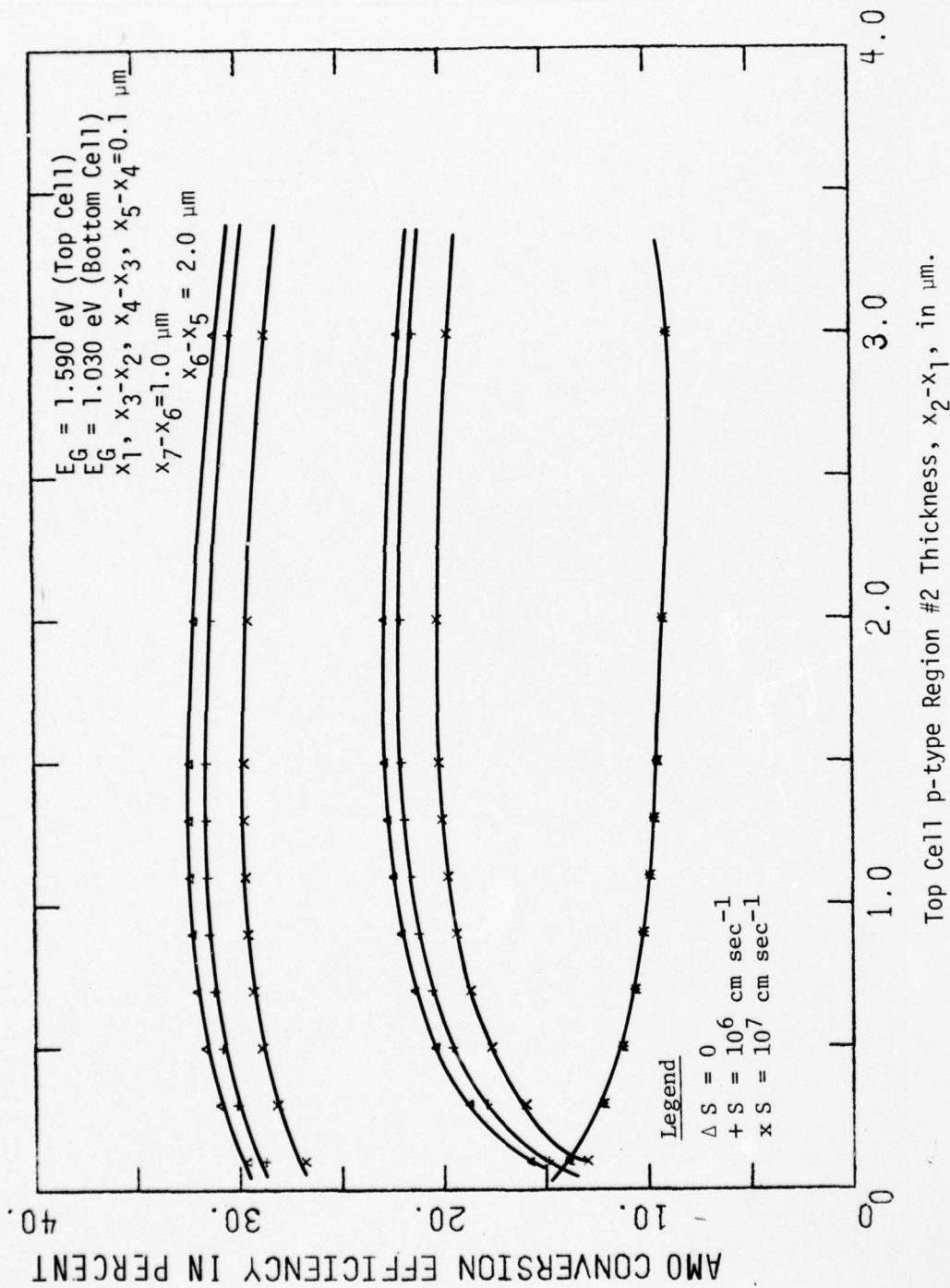
Figure 6.29. Conversion Efficiency vs. the thickness of the p- $Al_{0.14}Ga_{0.86}As$ region.

200
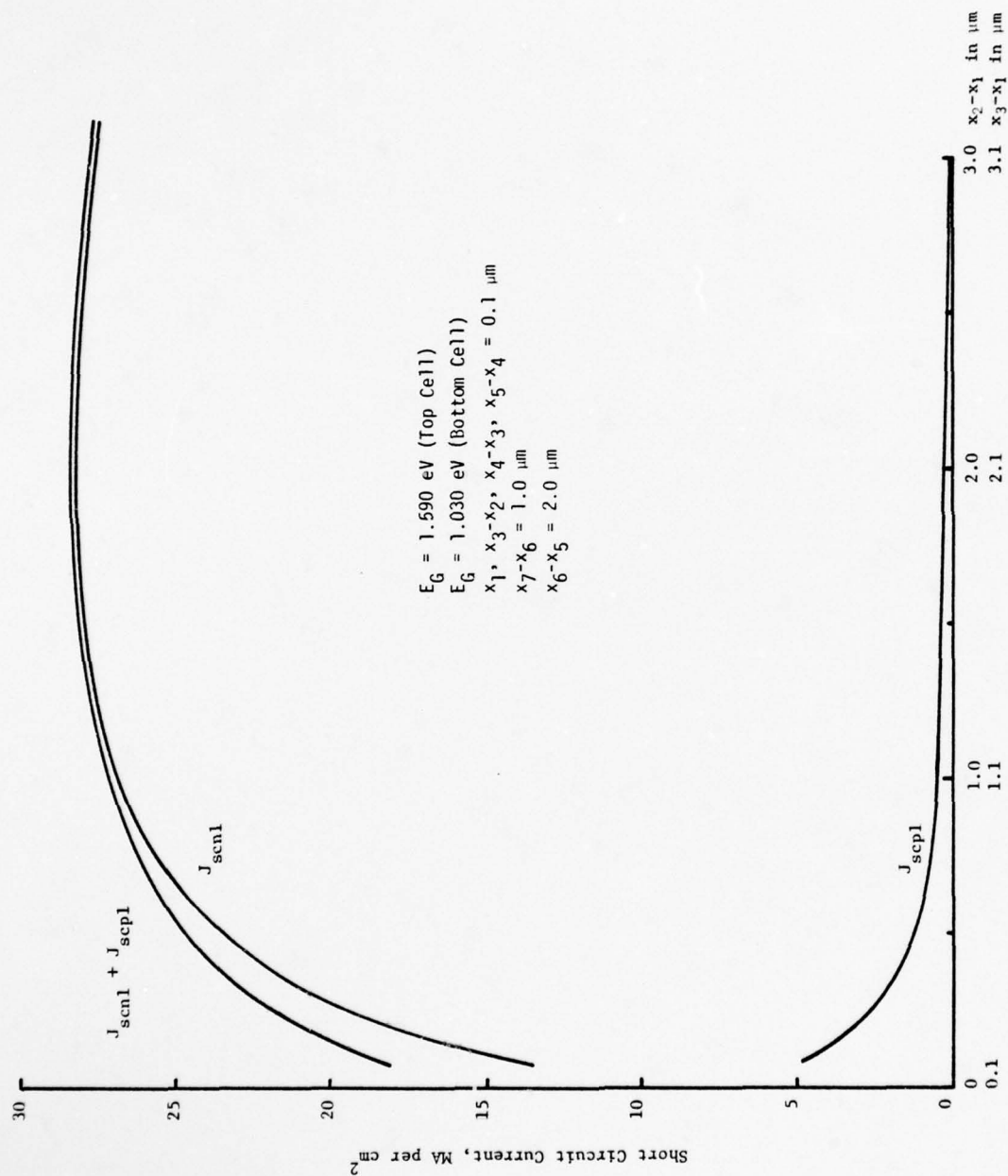
Figure 6.30. Short circuit currents top cell p-type thickness.
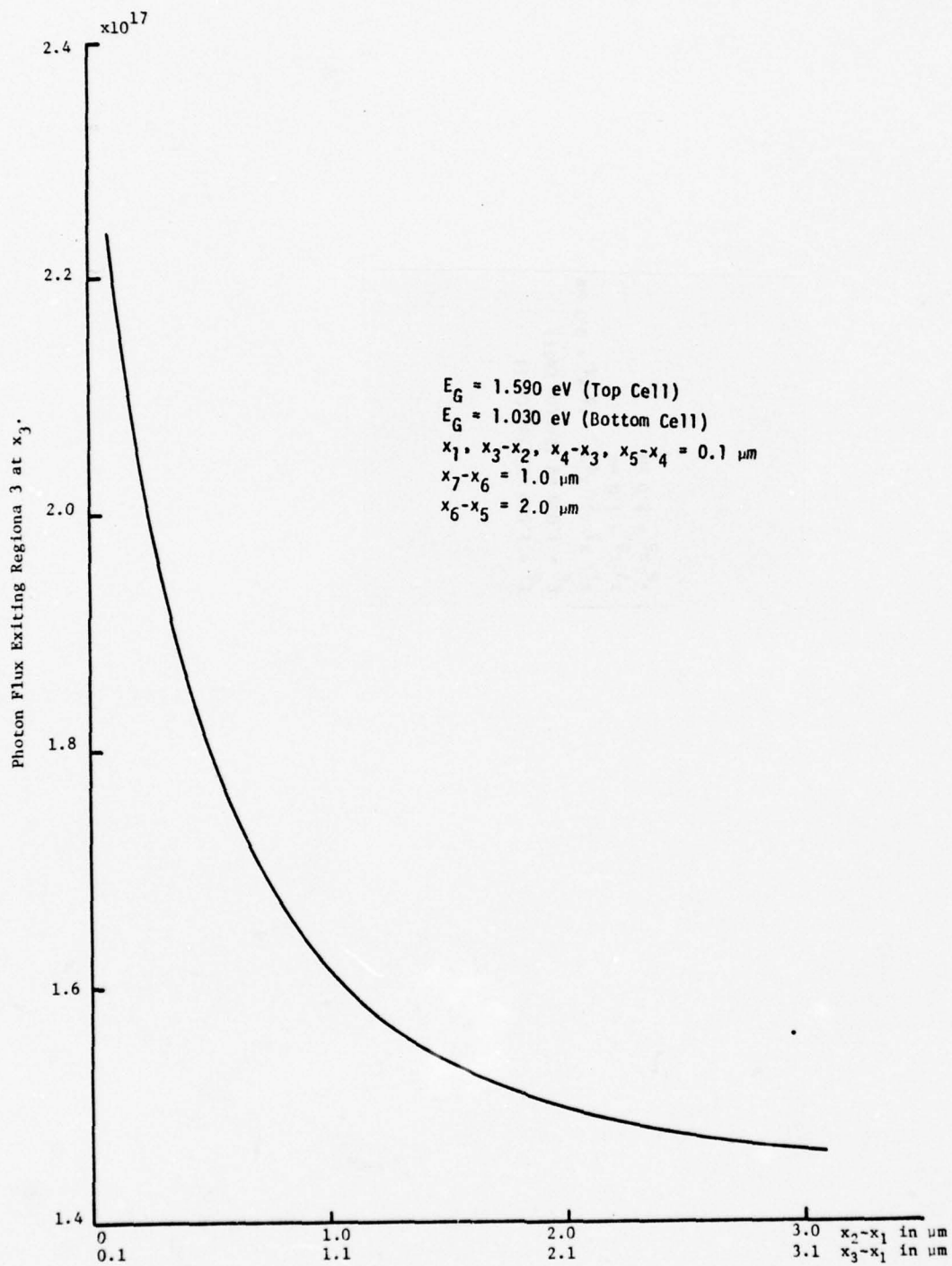
6.31. Photon Flux exiting Region #3 vs. $x_2 - x_1$.

The normalized spectral response for Region 1 plus Region 2 is defined by

$$Q_{N12} = \frac{J_{scn1}}{q[N_{ph}(0) - N_{ph}(x_2)]} \tag{6-2}$$

where $J_{scn1}$ is the electron contribution to short circuit current arising in Regions 1 plus Region2, $N_{ph}(0)$ is the photon flux entering Region 1, $N_{ph}(x_2)$ is the flux exiting Region 2, and q is the electronic charge. The normalized spectral response (NSR) for Regions 1 and 2 is shown in Figure 6.32 for 0, $10^6$ and $10^7$ cm sec$^{-1}$ SRV. The NSR decreases monotonically for zero SRV with increasing $x_2-x_1$, while it increases and peaks for $10^6$ cm sec$^{-1}$ up to 0.75 μm and for $10^7$ cm sec$^{-1}$ up to 1.3 μm. For non-zero values of SRV the NSR decreases. For zero SRV, increasing $x_2-x_1$ results in increased bulk recombination with a consequent reduction in NSR. For high SRV, NSR increases for small SRV because the increased absorption in Region 2 more than compensates for the surface losses. At $x_2-x_1$ values beyond the peak, NSR is reduced with increasing $x_2-x_1$ values because of increased bulk recombination.

Figure 6.33 shows the electron, hole, and the sum of the electron plus hole saturation currents with each component multiplied by its appropriate charge confinement factor vs. $x_2-x_1$. Since $x_3-x_2$, the n-type region of the top cell, is maintained constant, the hole contribution, $J_{Dp10}$, to dark current is independent of $x_2-x_1$ and is shown as a horizontal line. Decreasing $x_2-x_1$ results in increased electron charge confinement and, therefore, in decreasing dark current arising from electrons in Region 2. This is shown in Figure 6.33. The total of the electron and hole contributions is also shown and it is always greater than $J_{Dp10}$.

203
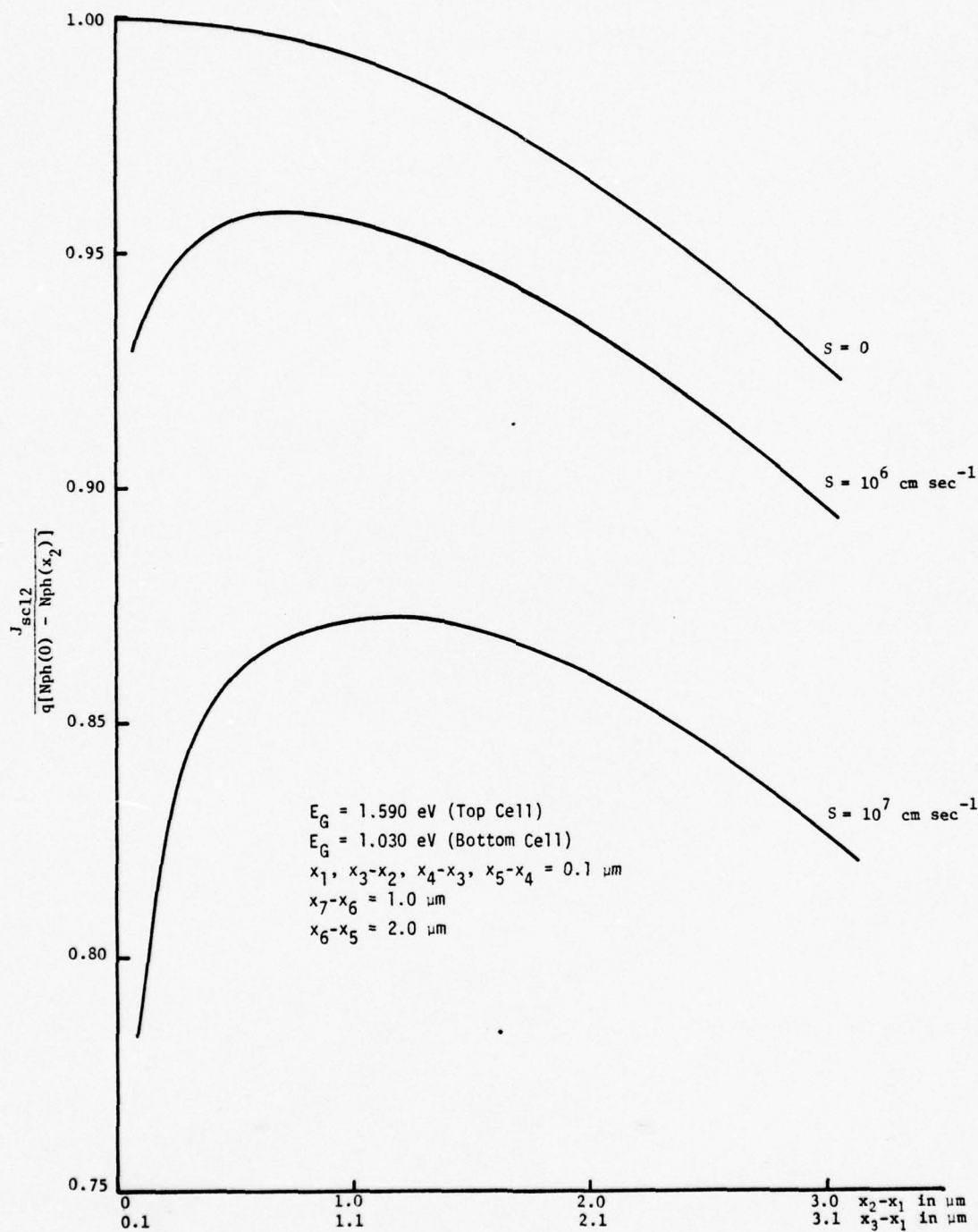
Figure 6.32. Normalized spectral response in Region 2 vs. $(x_2-x_1)$ with surface recombination velocity a parameter.
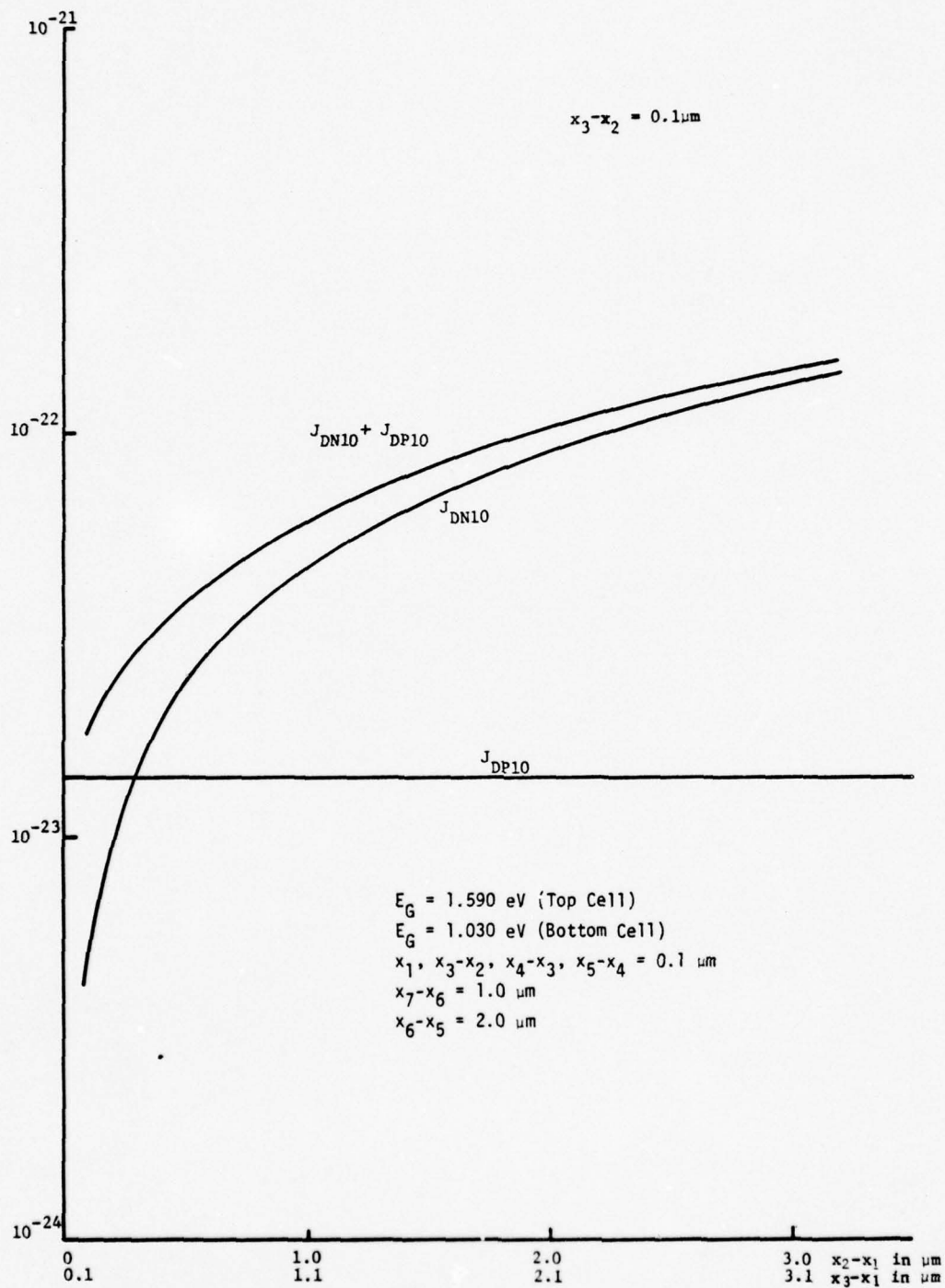
Figure 6.33.  Electron, hole and the sum of the electron and hole
saturation values multiplied by the appropriate
charge confinement R-factors vs. $x_2-x_1$.

205
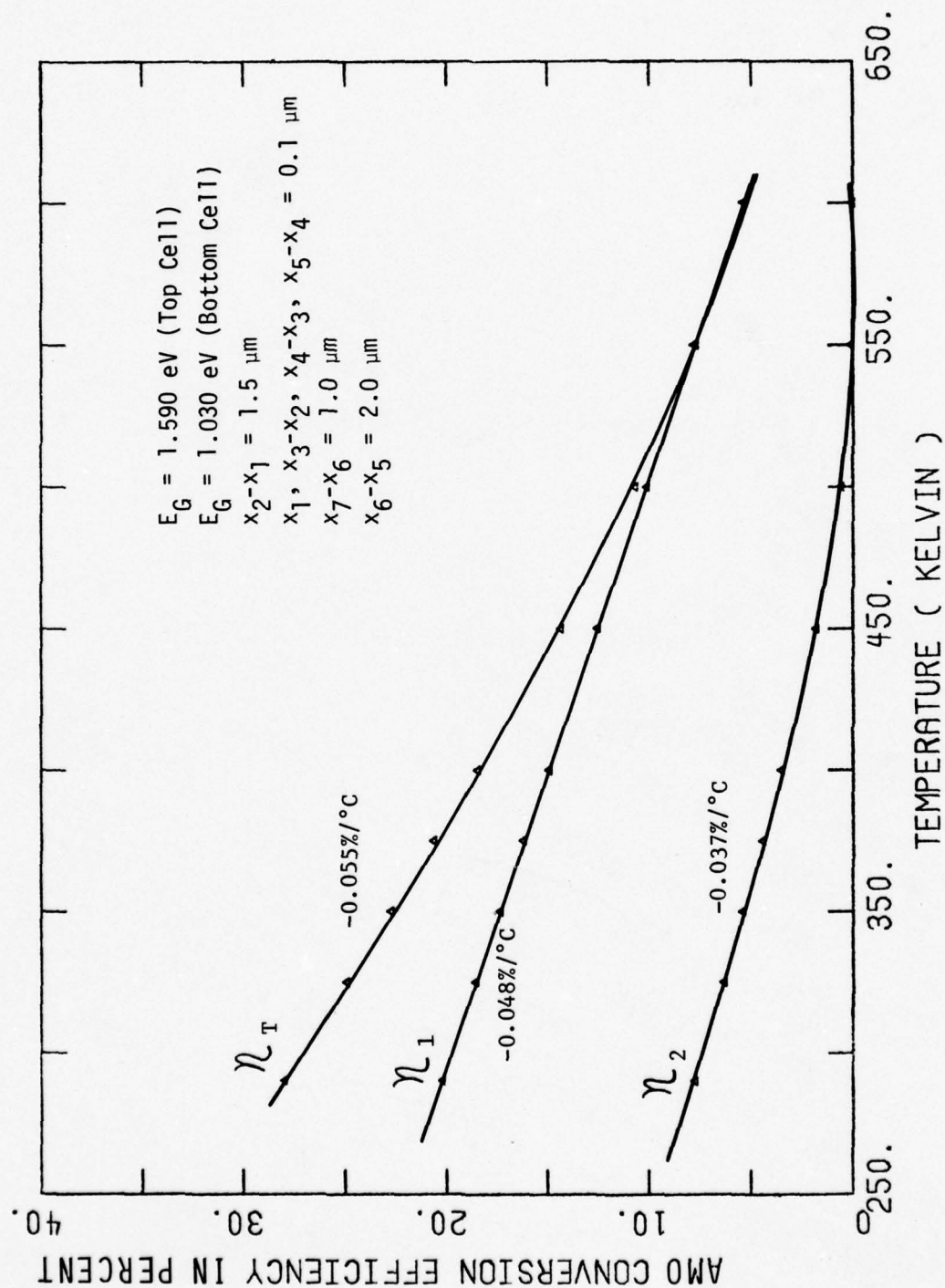
Figure 6.34(a). Efficiency vs. Temperature for the 2-junction cascade structure – voltages opposing, for S = 0.

In Figure 6.29 we have seen that the efficiency is maximum in the range 1.4 to 1.5 µm for $x_2-x_1$ and not at 2.0 µm as it is for the short circuit current, in Figure 6.30. This arises because at 1.4 to 1.5 µm the incomplete absorption loss is more than compensated by the reduced dark current arising from electron confinement in Region 2, and, therefore, the maximum efficiency occurs at 1.4 to 1.5 µm and not at 2.0 µm.

6.5.3 Temperature Studies

The optimization studies presented in Section 6.5.2 was conducted for 290°K. In this discussion the calculations with respect to temperature are presented.

In Figures 6.34(a), (b) and (c) the individual and the total AMO efficiency are shown as a function of temperature for surface recombination velocities of 0, $10^6$ and $10^7$ cm sec$^{-1}$, respectively. The efficiency of the bottom cell, $\eta_2$, is independent of SRV since there are no direct or indirect coupling phenomena. The conversion efficiency temperature coefficient for these curves show them to be relatively constant up to 450°K, and the slope is nearly independent of SRV. The total efficiency temperature coefficient lies in the range of GaAs and Si.

Due to the bandgap shrinkage with increasing temperature, the distribution of the absorbed photon flux through the cascade cell is a function of temperature. The curves in Figure 6.35 show the change in distribution. The sum of the photon flux absorbed in the top cell p-type layers, Regions 1 and 2, shows the largest increase with increasing temperature due to bandgap shrinkage. Regions 3, 4 and 5 show a slight decrease in photon absorption. The reason for this is not clear and more work is required to make any statements regarding this behavior. There is a small increase in photon absorption in Regions 6 and 7.

E$_G$ = 1.590 eV (Top Cell)
E$_G$ = 1.030 eV (Bottom Cell)

$x_2-x_1$ = 1.5 μm

$x_1$, $x_3-x_2$, $x_4-x_3$, $x_5-x_4$ = 0.1 μm

$x_7-x_6$ = 1.0 μm

$x_6-x_5$ = 2.0 μm

$\eta_T$

−0.088%/°C

$\eta_1$

−0.051%/°C

$\eta_2$

−0.037%/°C

TEMPERATURE ( KELVIN )

AM0 CONVERSION EFFICIENCY IN PRECENT
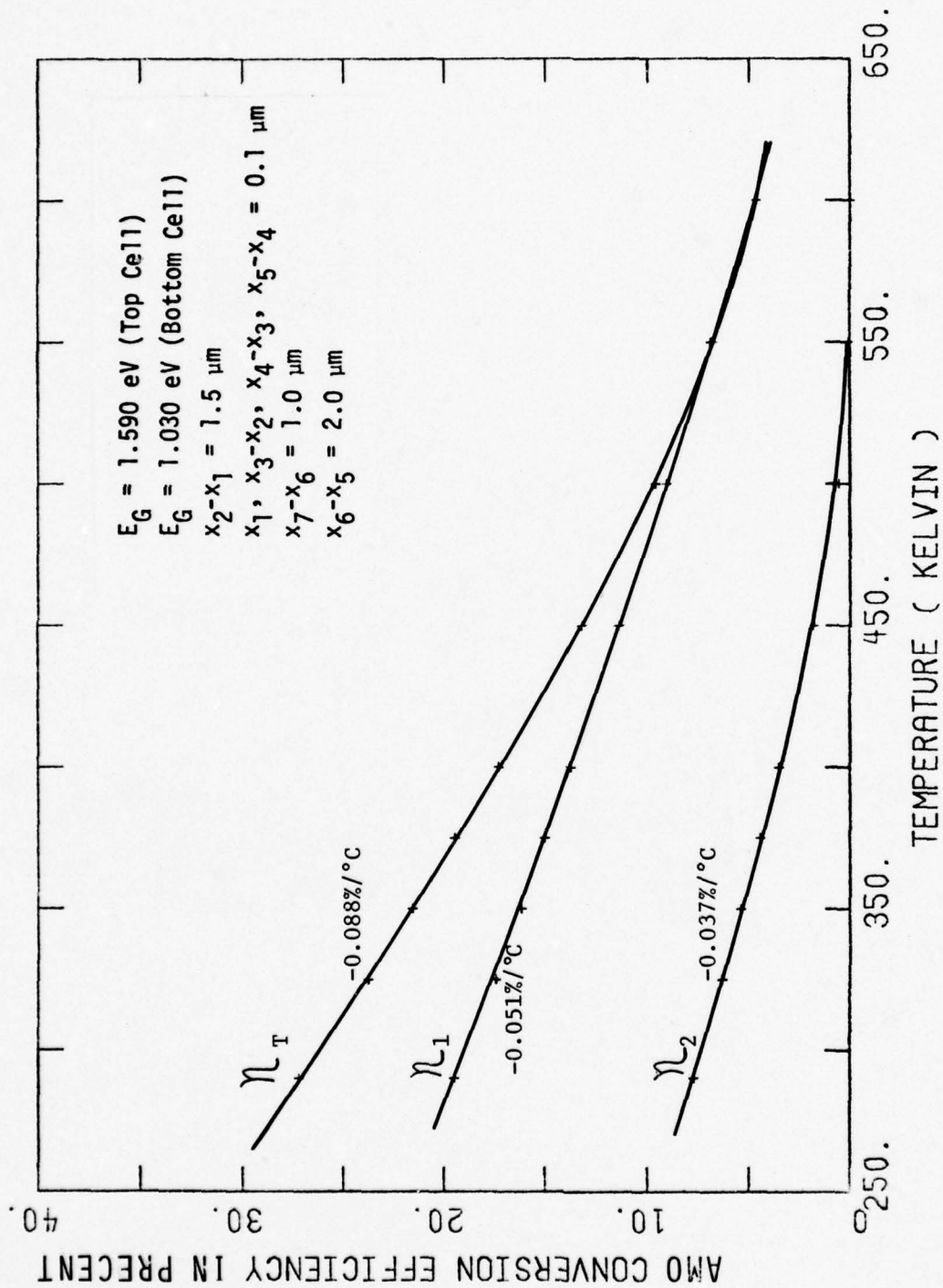
Figure 6.34(b). Efficiency vs. Temperature for the 2-junction cascade structure – voltages opposing, for S = 10$^6$ cm sec$^{-1}$.
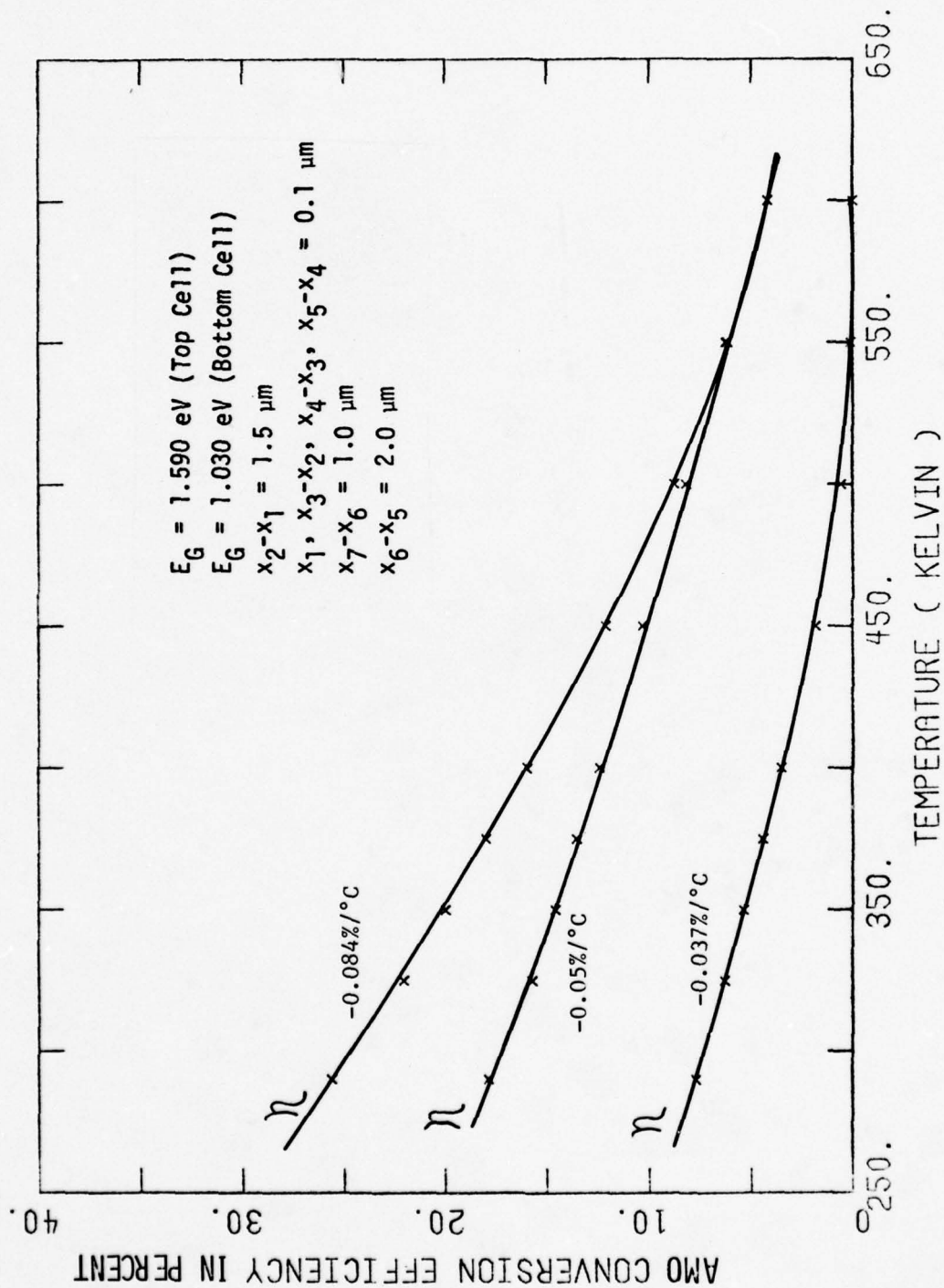
Figure 6.34(c). Efficiency vs. Temperature for the 2-junction cascade structure - voltage opposing, for $S = 10^7$ cm sec$^{-1}$.
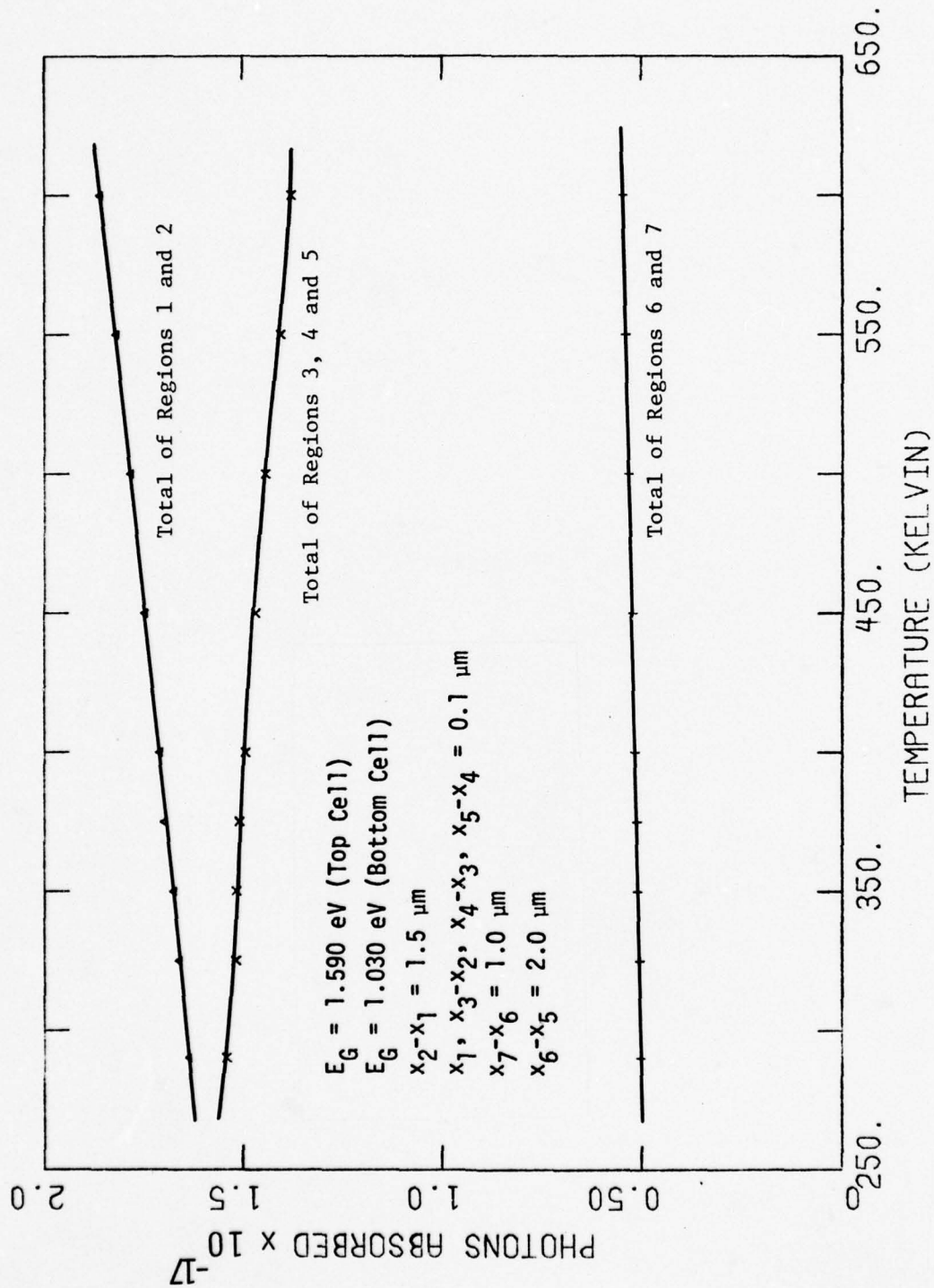
Figure 6.35. Photon absorption vs. temperature for the 2-junction cascade structure - voltages opposing.

## 6.6  Cascade Cell Fabrication -- Parameter Control

In this section percent changes in efficiency resulting from
an imposed ±10% change in various structural parameters of the
optimized CCVA structure (Figure 6.15) are calculated.  These para-
meters include the bandgap and the alloy composition of the bottom
junction, the p- or n-region thickness surrounding the homojunction
cells and the sum of the p-region thickness surrounding the homojunction
cells.  The curves in Figures 6.2, 6.3, 6.6, 6.9 and 6.12 have been
employed to determine the efficiency percent changes.  Table 6.3 lists
the parameters and the corresponding efficiency changes.  The efficiency
change is greatest for a ±10% change in the bandgap of the $In_xGa_{1-x}As$
alloy.  However, this represents as much as a 24% change in alloy com-
position.  LPE technology has been sufficiently developed for alloy
composition control to better than ±5%.  Therefore, the second listing
in efficiency to be less than 6% for a ±10% change in alloy composition
is a more reasonable production variance.  All efficiency changes are less
than 0.19% for impositions of ±10% changes on p- and n-region thicknesses.
It is also observed that in this optimized design, thickness control of the
active regions of each cell is reasonable to achieve high conversion
efficiency.

The surface layer window thickness is specified at 0.1 μm in Figure
6.15, but this thickness value should be viewed as a minimum rather than
an optimum value.  Its only purpose is to reduce surface recombination
losses because of the built-in field and the reduced flux absorbed in the
surface region due to its wider bandgap value at the surface.  This can
be accomplished by means of a thin layer and, in fact, a thicker AlGaAs

211

Table 6.3. Risk assessment relative to the fabrication
of the cascade structure shown in Figure 6.15
for $10^6$ cm$^{-1}$ surface recombination velocity.

| Parameter | Limits | | Efficiency | | Efficiency Percent Change | |
|---|---|---|---|---|---|---|
| | Low | High | Low | High | Low | High |
| Band Gap | 0.859 eV $u = 48\%$ | 1.049 eV $u \approx 33\%$ | 31.2% | ~28% | -2.5% | ~12.5% |
| Alloy Composition | $u = 35\%$ 1.00 eV | $u = 43\%$ 0.91 eV | 30.3% | 31.7% | -5.3 | 0.9% |
| $x_8-x_7$ $x_9-x_8$ | 0.95 0.94 | 1.16 1.15 | 32.07% | 32.07% | -0.03% | 0.03% |
| $x_9-x_7$ $x_8-x_7$ $x_9-x_8$ | 2.65 1.26 1.39 | 3.23 1.54 1.69 | 32.2% | 32.2% | -0.03% | 0.03% |
| $x_2-x_1$ $x_3-x_2$ | 0.63 0.73 | 0.77 0.87 | 32.2% | 32.2% | -0.03% | 0.03% |
| $x_3-x_1$ $x_3-x_2$ $x_2-x_1$ | 1.58 0.825 0.755 | 1.94 1.02 0.92 | 32.25% | 32.30% | -0.19% | 0.03% |

212

layer only absorbs more photons that would be otherwise absorbed in the $Al_{0.14}Ga_{0.86}As$ homojunction. This may reduce the efficiency slightly. A variation of $\pm 10\%$ in the surface layer thickness affects the efficiency less than 1%. In addition, the layers forming the tunnel diode portion of the cascade structure affect the conversion efficiency even less, because these layers are designed with materials for which the bandgap value is 1.62 eV. Therefore, they can neither aid or oppose the photo-electronic processes occurring in cell, provided free carrier absorption is small.

REFERENCES

6-1.  L. W. James, "III-V Compound Heterojunction Solar Cells", 1975 IEEE Electron Devices Meetings, Washington, D.C., December 1-3, 1975.

6-2.  T. Matsushuta and T. Mamine, "A New Class of Solar Cell with Multi-layer Structure", Technical Digest, 1975, Inter. ED Meeting, IEEE, New York, New York.

## 7.0 RISK ASSESSMENT AND CONCLUDING SUMMARY

In this study, an effort has been made to assess the state-of-the-art of III-V solar cells and to illuminate those areas offering the greatest potential for the development of high efficiency solar cells for military space applications. This has been accomplished through a review of the work of other investigators and through computer modeling and design optimization studies of existing as well as novel solar cell designs.

A tabulation of the more promising III-V solar cell configurations and materials combinations (discussed in Section 2.0 through 6.0 of this report) and a comparative summary of their major properties are shown in Table 7.1. Considerations of these and other factors previously discussed have resulted in the following overall assessment of III-V solar cells.

All III-V homojunction cells presently suffer surface recombination problems which seriously limit conversion efficiency values in actual structures. While some method for greatly reducing surface recombination velocity in III-V materials may ultimately be developed (native oxides, for example), it is felt that the chances of a breakthrough are too small to warrant major committments to III-V homojunction cell development.

The heterojunction configuration significantly reduces the front surface recombination problem and is an attractive alternative to the simple homojunction structure. It seems highly likely that active area efficiencies of 20% or more can be achieved in optimized[*] hetero-junction cells fabricated from materials carefully chosen to minimize

---

[*] Optimized layer thickness and doping levels and introduction of appropriate bandgap grading as discussed in Section 2.0.

214

Table 7.1. Summary of Solar Cell Properties

| Cell Configuration | Fabrication Technology | Special Problems | Relative Cost Unit Area[1] | Projected Efficiency at Maturity[2] | Temperature Coefficient (mw/°C) | Radiation Hardness (1 MeV e/cm$^2$)[3] | Years to Maturity[4] |
|---|---|---|---|---|---|---|---|
| **Homojunction** | | | | | | | |
| Si | Diff | --- | 0.1 | 17-19 | 0.09-0.1 | $10^{16}$ | --- |
| GaAs | Diff/EPI | Surface recombination | 1.0 | 15-17 | 0.05-0.06 | $10^{17}$ | 1-4 |
| AlAlAs | LPE | | 1.0-1.2 | 15-17 | 0.05-0.06 | $10^{17}$ | 2-5 |
| GaInAs | VPE/LPE | | 1.0-1.2 | 15-17 | 0.05-0.06 | $10^{17}$ | 3-6 |
| **Heterojunction/Graded/PW** | | | | | | | |
| GaAlAs-GaAs | LPE | Graded layer fabrication | 1.0-1.2 | 20-21 | 0.05-0.06 | $10^{17}$ | 2-5 |
| AlAs-GaAlAs | LPE | | 1.2-1.5 | 20-21 | 0.05-0.06 | $10^{17}$ | 3-6 |
| AlAsGaInAs | VPE/LPE | Lattice matching | 1.2-1.5 | 21-22 | 0.05-0.06 | $10^{17}$ | 3-6 |
| GaAsP-GaAs | VEP/LPE | | 1.0-1.2 | 19-20 | 0.05-0.06 | $10^{17}$ | 3-6 |
| **Shottky Barrier** | | | | | | | |
| GaAs | --- | Achieving large barrier heights | 1.0-1.2 | 10-12 | 0.05-0.06 | $\geq 10^{17}$ | 2-6 |
| GaAlAs | LPE | | 1.0-1.2 | 11-13 | 0.05-0.06 | $\geq 10^{17}$ | 2-6 |
| GaPAs | VEP/LPE | | 1.0-1.2 | 11-13 | 0.05-0.06 | $\geq 10^{17}$ | 2 6 |
| **MIS** | | | | | | | |
| GaAs | Oxidation | Insulation reproducibility | 1.0-1.2 | 15-17 | 0.05-0.06 | $10^{17}$ | 2-6 |
| InP | Oxidation | | 1.2-1.5 | 15-17 | 0.05-0.06 | $10^{17}$ | 2-6 |
| **Cascade (two jctn.)** | | | | | | | |
| Ternary or Quaternary | LPE/VPE | Lattice matching | 1.5-2.0 | 28-30[5] | 0.08-0.09 | $10^{17}$ | 5-10 |

[1] Present material costs--III-V costs will be reduced with increased production.
[2] AMO, 5% reflection, active area.
[3] For 50% power reduction
[4] Assumes concentrated effort.
[5] Reduced below calculated values in recognition of increased complexity of fabrication.

lattice mismatch recombination. At present, the AlAs-GaAs or GaAlAs-GaAs heterojunction is the most highly developed III-V solar cell; this cell is judged to be the leading candidate among single-junction III-V cells when evaluated in terms of its overall performance in the space environment and the technical risk associated with its fabrication in production quantities.

Schottky barrier cells, though relatively inexpensive and simple to fabricate, can be ruled out of the competition solely on the basis of extremely low projected efficiency values--lower even than present commercial silicon cells. MIS cells, on the other hand, are characterized by somewhat higher efficiencies than Schottky barrier cells but are more complex than simple Schottky barrier structures and are certainly more difficult to fabricate. Experimental efforts designed to refine MIS fabrication techniques and demonstrate theoretically predicted efficiencies are presently being funded by ERDA, and major Air Force support does not appear warranted.

The most promising avenue toward the realization of appreciably higher efficiency solar cells appears to be in the direction of multi-junction III-V structures. The two-junction, voltage-aiding cascade cell, described in detail in Section 6.0 of this report, is highly attractive from the standpoint of both theoretical efficiency and high temperature performance; also, it will very likely offer an improvement in radiation hardness over contemporary silicon cells. Although the particular materials system discussed in Section 6.0 is not lattice-matched, there are several alternative ternary and quaternary systems having essentially the same electrical properties and which avoid lattice mismatch between

216

the top and bottom cells.  We believe that a monolithic two-junction

cascade device of the type described can be fabricated via state-of-

the-art liquid-phase epitaxial (LPE) techniques, which have been used

successfully in fabricating multi-layer structures and which can be

adapted to a production process.

For improved high temperature performance and improved radiation

resistance of solar cells at efficiencies as good as or slightly better

than silicon cells, it appears that the III-V heterojunction offers

the highest probability of achieving these goals.  Over the long term,

however, it appears that the cascade type of solar cell in a monolithic,

lattice matched configuration offers the most promise for significant

increases in efficiency as well as good radiation hardness.

It is recommended that major Air Force solar cell programs be

directed toward the heterojunction and cascade types of solar cells;

smaller developmental efforts could focus on such areas as homojunction

III-V cells and MIS cells.

APPENDIX A.  SOLUTION OF SEMICONDUCTOR DEVICE EQUATIONS

The internal phenomena governing the operation of a solar cell are described in steady state by the following set of device equations:

$$J_n = \mu_n n \left[ qE - \frac{d\chi_c}{dx} + \frac{kT}{n} \frac{dn}{dx} - \frac{kT}{N_c} \frac{dN_c}{dp} \right] , \tag{A-1}$$

$$= q\mu_n n \frac{d\phi_n}{dx} , \tag{A-2}$$

$$J_p = \mu_p p \left[ qE - \frac{d\chi_c}{dx} - \frac{dE_g}{dx} - \frac{kT}{p} \frac{dp}{dx} + \frac{kT}{N_v} \frac{dN_v}{dx} \right] , \tag{A-3}$$

$$= q\mu_p p \frac{d\phi_p}{dx} , \tag{A-4}$$

$$0 = G_e - U + \frac{1}{q} \frac{dJ_n}{dx} , \tag{A-5}$$

$$0 = G_e - U - \frac{1}{q} \frac{dJ_p}{dx} , \tag{A-6}$$

$$\frac{d}{dx} (\varepsilon E) = q(p-n+N) \tag{A-7}$$

$$U = \frac{pn-n_i^2}{\tau_{po}(n+n_1) + \tau_{no}(p+p_1)} , \tag{A-8}$$

$$G_e = \int T \alpha N_p \exp \left( \int_0^x \alpha \, dx \right) d\lambda . \tag{A-9}$$

In this form, the equations are valid for graded bandgap materials as well as homogeneous materials.  In the special cases of constant bandgap ($E_g$) and constant electron affinity ($\chi_c$) the current density equations reduce to the more familiar form of

$$J_n = q \mu_n E + q D_n \frac{dn}{dx} , \tag{A-10}$$

219

$$J_p = q\mu_p pE - q D_p \frac{dp}{dx} \; . \tag{A-11}$$

Exact closed form solutions of the general set of device equations are impossible because of the nonlinear nature of the equations. To circumvent this difficulty two approaches are typically taken. One is to approximate the device equations for certain operating conditions to obtain a set of linear equations which can be solved in closed form. The other approach is to obtain exact numerical solutions of the complete set of device equations without any simplifying approximations. Both of these approaches have their place and when used together can be complementary and provide a complete understanding of device operations.

A-1 Approximate Solutions

In obtaining approximate, closed form solutions of the device equations, the approach is to divide a semiconductor into space charge regions occurring around junctions, surfaces and other interfaces and quasi-neutral regions which constitute the bulk of the device. In the space charge regions, operation is dominated by Poisson's equation and in the quasi-neutral regions only the transport and continuity equations are considered. The approximate boundary conditions appropriate to the space charge regions are well established and are not repeated here.

In the quasi-neutral regions, the current density equations can be written as

$$J_n = q\mu_n n E_n + q D_n \frac{dn}{dx} \; , \tag{A-12}$$

$$J_p = q\mu_p p E_p - q D_p \frac{dp}{dx} \; , \tag{A-13}$$

where

$$E_n = E - \frac{1}{q} \frac{d\chi_c}{dx} + \frac{kT}{q} \frac{1}{N_c} \frac{dN_c}{dx} \; , \tag{A-14}$$

220

$$E_p = E - \frac{1}{q} \frac{d\chi_c}{dx} - \frac{1}{q} \frac{dE_g}{dx} + \frac{kT}{q} \frac{1}{N_v} \frac{dN_v}{dx} \quad . \tag{A-15}$$

The terms $E_n$ and $E_p$ represent effective fields which act on electrons and holes and are equal to the electric field for constant band gap devices.

Combining the current density equation and continuity equation for electrons gives

$$\frac{d^2n}{dx^2} + \frac{1}{D_n} \frac{dn}{dx} \frac{dD_n}{dx} + \frac{\mu_n}{D_n} \left[ E_n \frac{dn}{dx} + n \frac{dE_n}{dx} \right] + \frac{n}{D_n} E_n \frac{d\mu_n}{dx}$$

$$- \frac{U}{D_n} + \frac{G_e}{D_n} = 0 \quad . \tag{A-16}$$

Further approximations are usually made by neglecting $dE_n/dx$ and approximating U as $(n-n_o)/\tau_n$ . If now $E_n$ is assumed to be a known function of position, a linear differential equation is obtained. Closed form solutions are still impossible unless any position dependence of $D_n$, $\mu_n$ and $E_n$ are neglected. The resulting linear equation for which closed form solutions can be obtained is

$$\frac{d^2n}{dx^2} + \frac{qE_n}{kT} \frac{dn}{dx} - \frac{n-n_o}{D_n \tau_n} + \frac{G_e}{D_n} = 0 \quad , \tag{A-17}$$

where $E_n$ is taken as a constant and $G_e$ is a known function of x. The closed form solutions of this equation are discussed in other sections of this report.

A-2  Exact Computer Solutions

The second general approach to the device equations is to treat the equations as a coupled set of non-linear equations which are to be solved numerically. The complete set of device equations can be written as a set of three non-linear, second order equations in three selected variables. The equations for a graded bandgap material are readily expressed in terms of the two quasi-Femi potentials $\phi_n$ and $\phi_p$ and the electrostatic

221

potential $\psi$ as

$$\frac{d^2\phi_n}{dx^2} + \frac{d\phi_n}{dx} \left[ \frac{1}{n}\frac{dn}{dx} + \frac{1}{\mu_n}\frac{d\mu_n}{dx} \right] - \frac{U}{\mu_n n} + \frac{G_e}{\mu_n n} = 0 \qquad (A-13)$$

$$\frac{d^2\phi_p}{dx^2} + \frac{d\phi_p}{dx} \left[ \frac{1}{p}\frac{dp}{dx} + \frac{1}{\mu_p}\frac{d\mu_p}{dx} \right] + \frac{U}{\mu_p p} - \frac{G_e}{\mu_p p} = 0 \qquad (A-19)$$

$$\frac{d^2\psi}{dx^2} + \frac{1}{\varepsilon}\frac{d\psi}{dx}\left(\frac{d\varepsilon}{dx}\right) + \frac{q}{\varepsilon}\ (p-n+N) = 0 \qquad (A-20)$$

To complete this set of equations only requires that n and p be expressed in terms of $\phi_n$, $\phi_p$, and $\psi$. This is readily done as

$$n = n_{io}\ \exp\left[\frac{q}{kT}\ (\ \psi - \phi_n + \theta_n\ )\right]\ , \qquad (A-21)$$

$$p = n_{io}\ \exp\left[\frac{q}{kT}\ (\ \phi_p - \psi + \theta_p)\right]\ , \qquad (A-22)$$

where

$$\theta_n = \frac{\chi_c}{q} - \psi_o + \frac{kT}{q}\ \ln\left(\frac{N_i}{n_{io}}\right) \qquad , \qquad (A-23)$$

$$\theta_p = \frac{1}{q}\ (\chi_c + E_g) + \psi_o + \frac{kT}{q}\ \ln\left(\frac{N_v}{n_{io}}\right)\ . \qquad (A-24)$$

In these $n_{io}$ is some convenient constant intrinsic carrier density and $\psi_o$ is some reference potential. Both $n_{io}$ and $\psi_o$ can be conveniently selected so that $\theta_n = 0$ and $\theta_p = 0$ at any desired composition.

The solution of Equations (A-18) through (A-24) can be obtained by any appropriate numerical techniques such as finite difference techniques. To obtain solutions, boundary conditions are required for the three variables

222

$\phi_n$, $\phi_p$ and $\psi$ at the terminals of the device.  These are easily obtained
if ohmic boundary conditions are assumed at the terminals.  In solar
cells, however, the front surface is typically a low surface recombination
boundary.  This can be taken into account in the solution of the device
equations.  Techniques used in solving the equations have been discussed
elsewhere [A1, A2] and will not be repeated here.

In any modeling of solar cells, the various device parameters such
as mobility, fields, etc. must be known.  Most of the device parameters
depend on doping density and in graded band gap devices also depend on
the material composition at any point within the device.  The modeling
of these device parameters is discussed in Appendix B.

REFERENCES

A1.  E. D. Graham and J. R. Hauser, "Effects of Base Doping and Width on
     the J-V Characteristics of the $n^+$-$n$-$p^+$ Structure", Solid-State Elec.,
     15, March 1972, pp. 303-310.

A2.  P. M. Dunbar and J. R. Hauser, "A Theoretical Analysis of the Current-
     Voltage Characteristics of Solar Cells", Annual Report on NASA Grant
     NGR 34-002-195, August 1975.

# APPENDIX B. MODELING OF DEVICE PARAMETERS[*]

## B-1  Introduction

The material parameter modeling discussed in the following sections makes possible the computer analysis of solar cells made of a spatially varying alloy of two compatible semiconductors.  Given the material properties of the two binary semiconductors, the computer program generates approximate parameters for the specified ternary composition. For example, solar cells made of the alloy, $Al_xGa_{1-x}As$, are analyzed by providing the material properties of AlAs and GaAs, along with the desired composition profile, i.e. the mole fraction of AlAs, x, vs. position.  Equations of both a theoretical and empirical nature have been used to obtain the alloy material parameters from the binary material parameters.  Whenever possible, these approximations have been checked against experimental results and adjusted to improve the agreement with available data.  The most important approximations are described in the following sections.

## B-2  Dielectric Constant vs. Composition

Given the dielectric constants, $\varepsilon_1$ and $\varepsilon_2$, for semiconductors 1 and 2, the following interpolation scheme is used to estimate the dielectric constant, $\varepsilon$, for an alloy that has mole fraction, C, of material 1, [B-1]:

$$\varepsilon = \frac{1+2\left[C\left(\frac{\varepsilon_1-1}{\varepsilon_1+2}\right) + (1-C)\left(\frac{\varepsilon_2-1}{\varepsilon_2+2}\right)\right]}{1-C\left(\frac{\varepsilon_1-1}{\varepsilon_1+2}\right)-(1-C)\left(\frac{\varepsilon_2-1}{\varepsilon_2+2}\right)} \tag{B-1}$$

---

224

B-3  Band Structure Parameters vs. Composition

Al$_x$Ga$_{1-x}$As and GaAs$_{1-x}$P$_x$ have both a direct and an indirect bandgap
which are important over various alloy compositions, and the solar cell
program permits the specification of two valleys, each with its own
composition dependent parameters such as band gap, effective mass and
mobility.  Assuming these two electron populations are at equilibrium
with each other, a single electron quasi-Fermi potential, $\phi_n$, can be used
in the device equations. Then an "effective" electron mobility and "effective"
electron mass can be defined such that a single current density equation
and a single carrier density equation is sufficient for this two conduction
band valley model.  The following sections describe the techniques used to
determine the resultant band structure parameters (such as electron and hole
mobilities) of an alloy, from the band structure parameters for each of the
two components.

Band Gap vs. Composition

Experimental studies have shown that the direct energy gap for III-V
alloys has an approximately quadratic dependence on composition such as [B-4].

$$E_{gd} = a\,C^2 + bC + E_{gd2} \tag{B-2}$$

where a and b are experimental values.  The same form was used to model the
indirect variation in GaAs$_{1-x}$P$_x$, while for Al$_x$Ga$_{1-x}$Ax, the indirect gap
was estimated by a linear variation with composition.  The bandgap is the
minimum of the direct or indirect bandgaps.

Effective Masses

The effective masses, m*, for holes and electrons were obtained by
interpolating between the effective masses, m$_1^*$ and m$_2^*$, of the alloy components

225

in the following manner [B-1]:

$$\frac{1}{m^*} = \frac{C}{m^*_1} + \frac{1-C}{m^*_2} .$$ (B-3)

For the direct and indirect conduction bands a single effective mass was obtained through use of the expression

$$n = N_c \exp \left(\frac{E_{Fn}-E_c}{kT}\right) = N_{cd} \exp \left(\frac{E_{Fn}-E_{cd}}{kT}\right) + N_{ci} \exp \left(\frac{E_{Fn}-E_{ci}}{kT}\right),$$ (B-4)

where $N_c$ is an effective density of states for the two valleys and $N_{cd}$ and $N_{ci}$ are the densities of states for the direct and indirect valleys respectively. From the above, a combined density of states effective mass can be defined for use in $N_c$ as

$$m^*_n = [m^{*\,3/2}_{cd} \exp \left(\frac{E_g-E_{gd}}{kT}\right) + m^{*\,3/2}_{ci} \exp \left(-\frac{E_g-E_{gi}}{kT}\right)]^{2/3}$$ (B-5)

where $E_{gd}$ is the direct energy gap, $E_{gi}$ is the indirect gap, $E_g$ is the actual gap (either $E_{gd}$ or $E_{gi}$) and $m^*_{cd}$ and $m^*_{ci}$ are the direct and indirect valley effective masses respectively.

### Hole Mobility

Mobility depends not only on alloy composition, but on the doping level as well. In order to calculate hole mobility for an arbitrary doping and composition, an empirical formula, $f_{p2}$, was constructed to approximate the doping dependence of hole mobility for one of the alloy components, to be referred to as material 2:

$$\mu_{p2} = f_{p2}(N)$$ (B-6)

where N = total impurity concentration. The form of $f_{p2}$ was taken to be

$$f_{p2}(N) = \frac{A_p}{(1+N/N_p)^\alpha} .$$ (B-7)

226

Now, because

$$\mu_p = \frac{q<\tau_p>}{m_p^*} = \mu_{p2} \frac{m_{p2}^*}{<\tau_{p2}>} \frac{<\tau_p>}{m_p^*} , \qquad (B-8)$$

it is apparent that if $<\tau_p>$ and $m_p^*$ can be specified as functions of composition, then a reasonable approximation to hole mobility for any doping level and composition can be made. In the III-V semiconductors, mobility is controlled primarily by a polar optical phonon scattering process[1] of the form [B-6]

$$<\tau> \frac{K}{m^* (\frac{1}{\varepsilon_h} - \frac{1}{\varepsilon_\ell})} , \qquad (B-9)$$

where K is a proportionality constant for all materials and $\varepsilon_h$ and $\varepsilon_\ell$ are the high and low frequency relative dielectric constants.

Combining Equations (B-8) and (B-9) then gives as an approximation to the mobility

$$\mu_p (N,C) = \frac{f_{p2}(N) \; m_{p2}^{*3/2} (\frac{1}{\varepsilon_{h2}} - \frac{1}{\varepsilon_{\ell2}})}{m_p^{*3/2} (\frac{1}{\varepsilon_h} - \frac{1}{\varepsilon_\ell})} . \qquad (B-10)$$

where $m_{p2}^*$, $\varepsilon_{\ell2}$, and $\varepsilon_{h2}$ are known parameters of material 2, and $\varepsilon_\ell$, $\varepsilon_h$, and $m_p^*$ are given as functions of composition by Equations (B-1) and (B-3).

### Electron Mobility

The modeling of electron mobility is more complex than hole mobility because of the indirect and direct bands. Treating the direct and indirect valleys independently, and using the same technique as described for hole mobility, a direct valley electron mobility, $\mu_d$, and an indirect valley electron mobility, $\mu_i$, can be determined approximately as:

---

[1]The validity of this assumption has been questioned for hole mobility in n-type indirect gap and p-type III-V semiconductors [B-5].

227

$$\mu_d(N,C) = \frac{f_{n2}(N) \; m^{*3/2}_{cd2} \left( \frac{1}{\varepsilon_{h2}} - \frac{1}{\varepsilon_{\ell2}} \right)}{m^{*3/2}_{cd} \left( \frac{1}{\varepsilon_h} - \frac{1}{\varepsilon_\ell} \right)} \qquad (B-11)$$

$$\mu_i(N,C) = \frac{f_{n1}(N) \; m^{*3/2}_{ci2} \left( \frac{1}{\varepsilon_{h1}} - \frac{1}{\varepsilon_{\ell1}} \right)}{m^{*3/2}_{ci} \left( \frac{1}{\varepsilon_h} - \frac{1}{\varepsilon_\ell} \right)} \qquad (B-12)$$

where $m^*_{cd2}$, $m^*_{ci1}$, $\varepsilon_{\ell2}$, $\varepsilon_{\ell1}$, $\varepsilon_{h2}$ and $\varepsilon_{h1}$ are known parameters of materials 1 and 2, $f_{n2}(N)$ is an empirical function relating electron mobility to doping for material 2, $f_{n1}(N)$ is an empirical function relating electron mobility to doping for material 1 and $\varepsilon_\ell$, $\varepsilon_h$, $m^*_{cd}$ and $m^*_{ci}$ are given by Equations (B-1) and (B-3). The functions $f_{n1}$ and $f_{n2}$ used the same functional form as Equation (B-7). An "effective" mobility for use in the current density equation can be found by weighing the direct and indirect mobilities by their respective electron populations, as

$$\mu_n(N,C) = \mu_d R_d + \mu_i (1-R_D) \qquad (B-13)$$

where $R_d$ is the fraction of electrons in the direct valley given by the expression

$$R_d = \frac{n_d}{n_d + n_i} = \frac{1}{1 + \left( \frac{m^*_{ci}}{m^*_{cd}} \right)^{3/2} \exp \left( \frac{E_{gd} - E_{gi}}{kT} \right)} \; . \qquad (B-14)$$

### Band Parameters, $\theta_n$ and $\theta_p$

In order to model the composition dependence of the band parameters, $\theta_n$ and $\theta_p$, some knowledge of the variation of electron affinity, $\chi_c$, and bandgap $E_g$, must be available. It has been found to be advantageous to select the potential reference, $\psi_o$, so that $\theta_n = \theta_p = 0$ when the mole fraction of material

228

1 is zero.  In other words, $\theta_n$ and $\theta_p$ are zero in regions of the solar cell consisting entirely of material 2.  Then

$$\psi_o = \frac{\chi_{c2}}{q} + \frac{kT}{q} \ln \left(\frac{N_{c2}}{n_{i2}}\right) \quad , \tag{B-15}$$

or equivalently,

$$\psi_o = \frac{\chi_{c2} + E_{g2}}{q} - \frac{kT}{q} \ln \left(\frac{N_{v2}}{n_{i2}}\right) . \tag{B-16}$$

Now, inserting Equation (B-15) into Equation (A-23), and Equation (B-16) into Equation (A-24) gives:

$$\theta_n = \frac{\chi_c - \chi_{c2}}{q} + \frac{kT}{q} \ln \left(\frac{N_{v2}}{n_{i2}}\right) \quad , \tag{B-17}$$

$$\theta_p = \frac{\chi_{c2} - \chi_c}{q} + \frac{E_{g2} - E}{q} + \frac{kT}{q} \ln \left(\frac{N_v}{N_{v2}}\right) . \tag{B-18}$$

Finally, in terms of effect mass:

$$\theta_n = \frac{\Delta\chi_c}{q} + \frac{3}{2} \frac{kT}{q} \ln \left(\frac{m_n^*}{m_{n2}^*}\right) \tag{B-19}$$

$$\theta_p = \frac{-(\Delta\chi_c + \Delta E_g)}{q} + \frac{3}{2} \frac{kT}{q} \ln \left(\frac{m_p^*}{m_{p2}^*}\right) \tag{B-20}$$

where $\Delta\chi_c = \chi_c - \chi_{c2}$ and $\Delta E_g = E_g - E_{g2}$.

Equations (B-19) and (B-20) are the forms used to compute the band parameters for an arbitrary alloy of two materials.

### Interface Recombination

At an abrupt interface between two semiconductors, lattice mismatch introduces trapping levels due to dangling bonds.  For a [100] interface, the density of dangling bonds is given by [B-7].

$$N_s = \frac{4(a_2^2 - a_1^2)}{a_2^2 a_1^2} \tag{B-21}$$

229

where $a_1$ and $a_2$ are the lattice constants of the two materials. If the composition change is gradual, rather than abrupt, the trapping levels have been assumed in this work to have a volume density that is proportional to the slope of the composition profile as

$$N_{RH} = N_{ST} \frac{dC}{dx} \, , \tag{B-22}$$

where $N_{ST}$ is the total density (per unit area) of dangling bonds in going from pure material 1 to pure material 2. These interface states have been incorporated into the Shockley-Read-Hall model by modification of the excess carrier lifetimes:

$$\frac{1}{\tau_{no}} = \frac{1}{\tau_{no}}\bigg|_{Bulk} + \frac{1}{N_{RH}C_R} \tag{B-23}$$

$$\frac{1}{\tau_{po}} = \frac{1}{\tau_{po}}\bigg|_{Bulk} + \frac{1}{N_{RH}C_R} \tag{B-24}$$

where $C_R$ is the capture coefficient. Ettenberg and Kressel [B-8] obtained a value of $8 \times 10^3$ cm/s for the interface recombination velocity at an abrupt $Al_{0.5}Ga_{0.5}As$ - GaAs heterojunction, indicating a value of $5.2 \times 10^{-9}$ cm$^3$/s for $C_R$. For the lack of further data, this value was used to determine the excess carrier lifetimes for holes and electrons in both $Al_xGa_{1-x}As$ and $GaAs_{1-x}P_x$ solar cells. The density of interface states is increased greatly, however, for the GaAs-GaP heterojunction because of the larger lattice mismatch. The bulk lifetimes, $\tau_{no}$ and $\tau_{po}$ were assigned values of 5.3 nsec and 8.5 nsec, respectively, as calculated from an estimate of the diffusion lengths as functions of doping [B-9].

230

## Optical Carrier Generation

The optical carrier generation rate was determined by the equation

$$G_e = \sum_\lambda T(\lambda)N(\lambda)\alpha[C(x),\lambda]\exp\{-\int_0^x \alpha[C(y),\lambda]dy\} \qquad (B-25)$$

where $T(\lambda)$ is the antireflection layer transmission coefficient, $N(\lambda)$ is the incident photon density per wavelength interval, $C(x)$ is the composition profile, and $\alpha[C(x),\lambda]$ is the absorption coefficient, which was taken to be the sum of two absorption coefficients, one pertaining to direct transitions and the other to indirect transitions. The direct absorption coefficient for a ternary semiconductor was approximated by shifting the $\alpha$ vs. E profile of GaAs by the amount of the difference between the direct band gaps of the alloy and GaAs. Similarly, the indirect portion of the $\alpha$ vs. E profile of the indirect binary material was approximated by shifting the indirect portion of the $\alpha$ vs. E profile of the indirect binary material (AlAs or GaP) by the amount of the difference between the indirect bandgaps of the alloy and its indirect binary component. This technique is similar to that used by Hutchby [B-10]. The resulting absorption coefficient is shown in Figure B.1 and B.2 for various compositions of $Al_{1-x}Ga_xAs$ and $GaP_{1-x}As_x$.
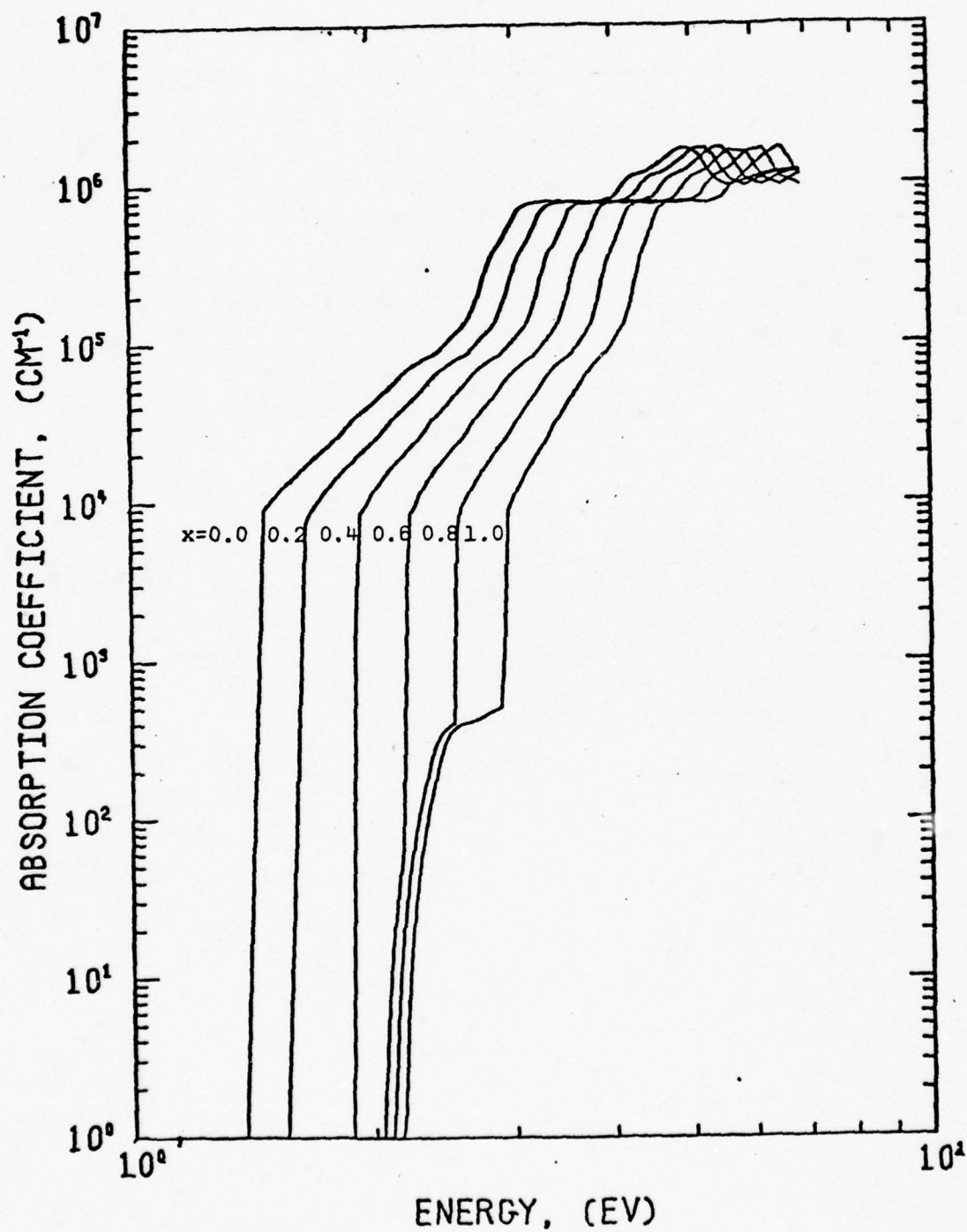
Figure B.1. Absorption coefficient versus energy for $Al_x Ga_{1-x} As$ with six values of x, mole fraction of AlAs.

232
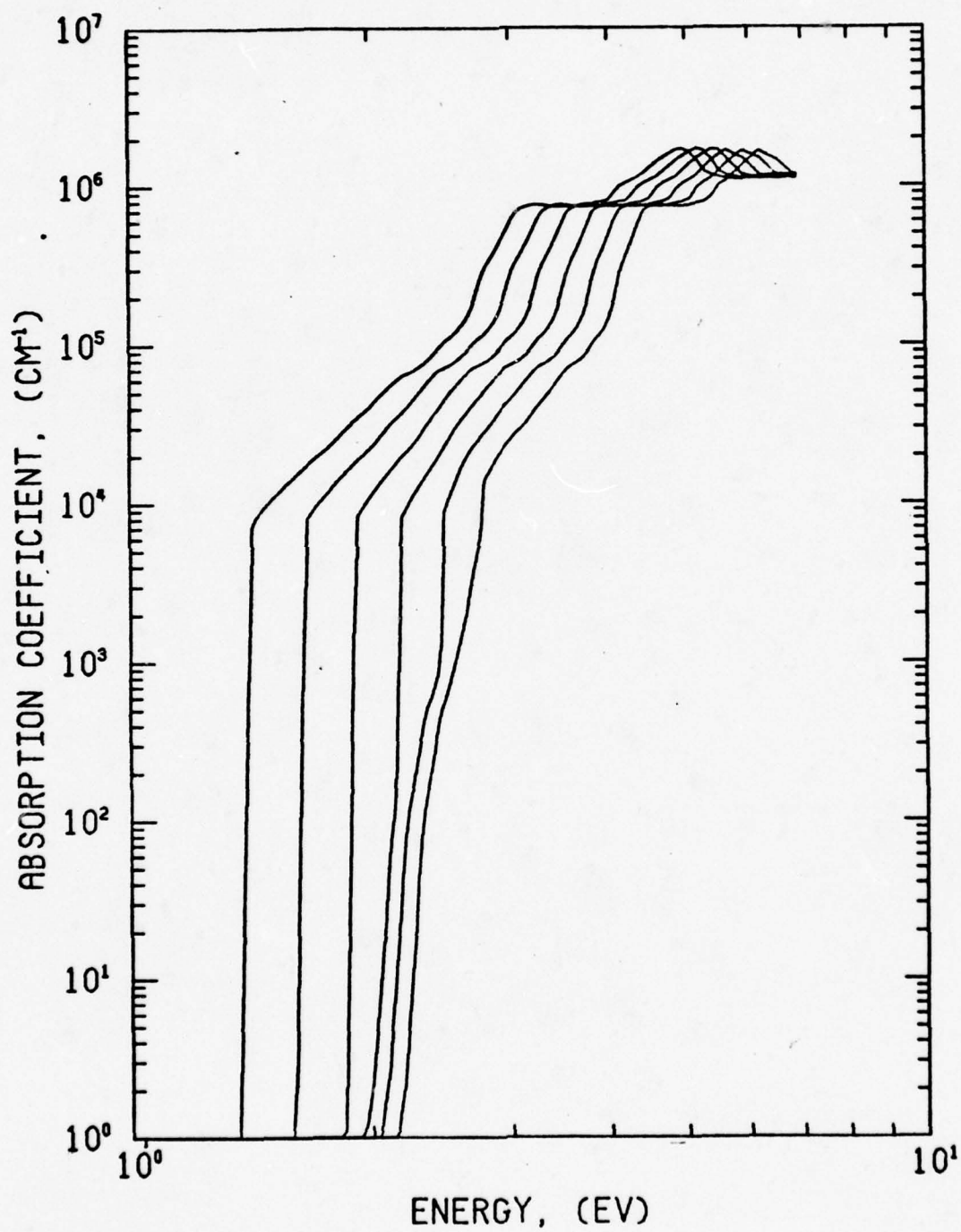
Figure B.2. Absorption coefficient versus energy for $GaP_{1-x}As_x$ with six values of x, mole fraction of GaAs.

233

REFERENCES

B1.  J. W. Harrison and J. R. Hauser, "Theoretical Calculations of
     Electron Mobility in Ternary III-V Compounds", Journal of Applied
     Physics, 47, January 1976, pp. 292-300.

B2.  J. E. Sutherland and J. R. Hauser, "Computer Analysis of Heterojunction
     and Graded Band Gap Solar Cells", 12th IEEE Photovoltaic Spec. Conf.,
     Baton Rouge, La., Nov. 15-18, 1976.

B3.  J. E. Sutherland and J. R. Hauser, "A Computer Analysis of Heterojunction
     and Graded Composition Solar Cells", accepted for publication in IEEE
     Trans. on Electron Dev.

B4.  A. G. Thompson and J. C. Woolley, "Energy-Gap Variation in Mixed III-V
     Alloys", Canadian J. of Phys., 45, February 1967, pp. 255-261.

B5.  J. D. Wiley and M. DiDomenico, Jr., "Lattice Mobility of Holes in
     III-V Compounds, "Physical Review B, 2, July 15, 1970, pp. 427-433.

B6.  E. M. Conwell, High Field Transport in Semiconductors, Academic Press,
     New York, 1967.

B7.  D. B. Holt, "Misfit Dislocations in Semiconductors", J. Phys. Chem.
     Solids, 27, June/July 1966, pp. 1053-1067.

B8.  M. Ettenberg and H. Kressel, "Interfacial recombination at (AlGa)As/GaAs
     heterojunction structures," J. of Appl. Phys., 47, April 1976, pp. 1538-1544.

B9.  B. Ellis and T. S. Moss, "Calculated Efficiencies of Practical GaAs and
     Si Solar Cells Including the Effect of Built-In Electric Fields", Solid
     State Electronics, 13, January 1970, pp. 1-24.

B10. J. A. Hutchby and R. L. Fudurich, "Theoretical Analysis of $AlGa_{1-x}As$-GaAs
     graded band gap solar cells", J. Appl. Phys., 47, July 1976,
     pp. 3140-3151.

234

APPENDIX C.   CURRENT COMPONENTS FOR SCHOTTKY BARRIER SOLAR CELLS

This appendix shows the relationships to material parameters and device dimension of each of the dark current density and photocurrent density components used in the device model for Schottky barrier solar cell calculations.

A.   Dark Current Components

The three dark current density components given in Eqn. (3-3) are:

$$1) \quad J_{SB} = A^{**}T^2 \, \exp\left(\frac{-\phi_B}{kT}\right)\left\{\exp\left(\frac{qV_a}{kT}\right) - 1\right\}$$

where

$$A^{**} = 120 \left(\frac{m_n^*}{m_o}\right) \text{amps/cm}^2 \, K^2$$

is the effective Richardson constant.  Here $m_n^*$ is the electron effective mass, $\phi_B$ is the barrier height energy, k is Boltzmann's constant (8.62 x $10^{-5}$ eV/K), T is absolute temperature, q is electron charge, and $V_a$ is applied voltage.

$$2) \quad J_R = \frac{q \, n_i^2 \, W_n \, \left\{\exp\left(\frac{qV_a}{kT}\right) - 1\right\}}{(\tau_{po}n_1 + \tau_{no}p_1) + (\tau_{po} + \tau_{no})n_i \, \exp\left(\frac{qV_a}{kT}\right)}$$

For a discussion of this model for recombination current see reference [3-21].

$$3) \quad J_{Diff} = J_s \left\{\exp\left(\frac{qV_a}{kT}\right) - 1\right\}$$

where

$$J_s = \frac{qD_p P_o}{L_p} \; \frac{\sinh\left(\frac{W}{L_p}\right) + \frac{SL_p}{D_p} \cosh\left(\frac{W}{L_p}\right)}{\cosh\left(\frac{W}{L_p}\right) + \frac{SL_p}{D_p} \sinh\left(\frac{W}{L_p}\right)}$$

and the terms are defined in the text.

B.  Photocurrent Components

The components of photocurrent density per unit optical band
width used in Eqn. (3-3) are given by:

$$1) \quad J_{DR}(\lambda) = \frac{qG_o(\lambda)}{\alpha(\lambda)} \left\{ 1 - \exp\left[-\alpha(\lambda)W_n\right] \right\}$$

where $G_o$ is the surface generation rate and $\alpha$ is the absorption coefficient.

$$2) \quad J_p(\lambda) = \frac{qG_o(\lambda)L_p \exp\left[-\alpha(\lambda)W_n\right]}{\left[\alpha(\lambda)L_p\right]^2 - 1} \left[\alpha(\lambda)L_p - F(\lambda)\right]$$

where

$$3) \quad F(\lambda) = \frac{\frac{SL_p}{D_p}\left\{\cosh\left(\frac{W}{L_p}\right) - \exp\left[-\alpha(\lambda)W\right]\right\} + \sinh\left(\frac{W}{L_p}\right) + \alpha(\lambda)L_p \exp\left[-\alpha(\lambda)W_n\right]}{\cosh\left(\frac{W}{L_p}\right) + \frac{SL_p}{D_p}\sinh\left(\frac{W}{L_p}\right)}$$

For a discussion of this equation see reference [3-1], p. 112 ff.

236

APPENDIX D.   ASSUMPTIONS USED IN THE CLOSED FORM ANALYSIS

The assumptions used in the derivation of the closed form equations and in the calculations are described below.

### D.1   Statistics

Nondegenerate semiconductor material will be assumed over the temperature range of interest.   Therefore, Boltzmann statistics will be considered applicable in all cases; i.e., the Fermi level is at least several kT below the conduction band edge in n-type and several kT above the valence band edge in p-type.

### D.2.   Recombination

The usual single trapping level model is assumed for recombination. While for III-V semiconductor compounds multiple recombination levels are not uncommon, the single level is useful, nevertheless, because it does include the general features of the multilevel model without the increased complexity of a multiple level model analysis.

The recombination rate for a single level recombination center located at energy $E_t$ and concentration $N_t$ is given by

$$r = \frac{\sigma_n \sigma_p v_{th}(pn - n_i^2)N_t}{\sigma_n\left[n + n_i e^{(E_t-E_i)/kT}\right] + \sigma_p\left[p + n_i e^{-(E_t-E_i)/kT}\right]} , \qquad (D\text{-}1)$$

where

$\sigma_n, \sigma_p$  :  electron and hole capture cross sections, respectively

$v_{th} = \left[\dfrac{3kT}{m^*}\right]^{1/2}$  :  carrier thermal velocity

$m^*$  :  effective mass

237

$E_i$  :  intrinsic Fermi energy level

$n_i$  :  intrinsic carrier concentration

$n, p$  :  electron and hole non-equilibrium concentration, respectively.

A simplifying assumption usually made is that

$$\sigma_n = \sigma_p = \sigma \tag{D-2}$$

reducing Eq. (D-1) to

$$r = \sigma v_{th} N_t \frac{pn - n_i^2}{n + p + 2n_i \cosh(E_t - E_i)/kT} \tag{D-3}$$

The recombination rate is a maximum when the recombination energy level, $E_t$, is at approximately the center of the forbidden bandgap, i.e.,

$$E_t = E_i , \tag{D-4}$$

for which

$$\cosh(E_t - E_i)/kT = 1 . \tag{D-5}$$

Thus, recombination centers located at mid bandgap are most effective in affecting recombination. Equation (D-3) also shows that increasing the concentration of recombination centers also increases the rate.

In solar cells irradiated up to several solar constants, the minority carrier concentrations are low compared to the majority carrier concentrations, i.e.,

$$n_p - n_{po} \ll p_{po} \tag{D-6}$$

and

$$p_n - p_{no} \ll n_{no} \tag{D-7}$$

where $n_{po}$, $p_{po}$, $p_{no}$, $n_{no}$ are the equilibrium values, and $n_p$ and $p_n$ are

238

the non-equilibrium values of electrons and holes. The low injection
level recombination rates are well established and given by

$$r_n = \frac{n_p - n_{po}}{\tau_n} \tag{D-8}$$

for electrons in p-type, and

$$r_p = \frac{p_n - p_{no}}{\tau_p} \tag{D-9}$$

for holes in n-type material, where $\tau_n$ and $\tau_p$ are the electron and hole
lifetimes, respectively.

In n-type solar cell semiconductors $n \approx n_{po}$ and $n \gg p \gg n_i$, and
if in Eq. (D-1) we set $E_t = E_i$, the result is the hole recombination given
by

$$r_p = \sigma_p v_{th} N_t (p - p_{no}) . \tag{D-10}$$

Comparing with Eq. (D-9) it is seen that

$$\tau_p = \frac{1}{\sigma_p v_{th} N_t} . \tag{D-11}$$

Similarly, the electron lifetime in p-type is given by

$$\tau_n = \frac{1}{\sigma_n v_{th} N_t} . \tag{D-12}$$

Therefore, we observe that electron and hole lifetimes are inversely pro-
portional to the recombination center concentration. This has been established
many times by experiment. Thus, Eqs. (D-8) and (D-9) will be employed as
the recombination rate in the integral-differential continuity equations.

239

D.3  Junction Recombination/Transport Processes

The junction current mechanisms have been studied extensively and
are too numerous to reference.  Shockley's ideal diffusion transport
model is one in which minority carriers are injected across the space
charge of a forward biased junction and the minority carrier flux is
not attenuated by depletion region recombination.  This results in the
smallest dark current and, therefore, the highest open circuit voltage
for a given short-circuit current.  The dark current is given by

$$I_D = q\left[n_{po}\left(\frac{D_n}{\tau_n}\right)^{1/2} + p_{no}\left(\frac{D_p}{\tau_p}\right)^{1/2}\right]\left(e^{qV/kT} - 1\right). \qquad (D-13)$$

The space charge recombination model includes a recombination process
in the space charge region which attenuates the minority carrier flux,
increases the dark current, reduces the open circuit voltage, and also
reduces the fill factor, $F_c$.  It is sometimes approximated by

$$I_{rg} = I_{rgo}\left[e^{qV/2kT} - 1\right] \qquad (D-14)$$

where

$$I_{rgo} = \frac{qn_iW}{\sqrt{\tau_p\tau_n}} \; ; \qquad (D-15)$$

W is the depletion width and $\tau_n$ and $\tau_p$ are the electron and hole life-
times in the space charge region.

D.4  Carrier Transport

The carrier mobilities are considered as being independent of
position through a layer.  Where necessary, average values are determined

240

in the analysis. However, the influence of active impurity concentration
on the average carrier mobilities (ionized impurity scattering) is
included at the point where the alloy composition changes from a direct
to an indirect transition material such as in $Al_xGa_{1-x}As$ and $GaP_xAs_{1-x}$.
When such an alloy is present, the layer may be separated into two
layers and solutions obtained in each layer. In those cases where the
calculation is improved significantly or pertinent design understanding
is enhanced, this has been done.

Changes in mobility are also reflected in the minority carrier
diffusion coefficient through the Einstein relationships,

$$D_n = \frac{kT}{q} \mu_n \tag{D-16}$$

$$D_p = \frac{kT}{q} \mu_p \tag{D-17}$$

for electrons and holes, respectively, where (kT/q) is the thermal voltage.

In all cases, the electric field values considered are less than
the critical field value, 3000 v/cm, so as to avoid the consideration
of hot electrons. Exceeding the critical field value results in a decrease
in minority carrier diffusion length and is, therefore, to be avoided in
solar cells.

D.5 Solar Cell V-I Curve Fill Factor

The power out put of a solar cell is determined experimentally by
obtaining the solar cell V-I curve and calculating the maximum power point.
The short-circuit current is obtained from the spectral collection
efficiency Q as

$$I_{sc} = \int_0^{\lambda_c} (1 - R)N_o Q d\lambda \tag{D-18}$$

where R is the reflectivity, $N_o$ the incident solar radiation photon flux

per unit wavelength, and $\lambda_c$ the cut-off wavelength of the material. The open circuit voltage is given by

$$V_{oc} = \frac{1}{\beta} \ln \frac{I_{sc}}{I_o} \qquad (D-19)$$

where $\beta$ and $I_o$ are defined in the dark current relationship

$$I = I_o(e^{\beta V}-1) \ . \qquad (D-20)$$

Maximum power is then determined from the equation

$$P_{max} = F_c \frac{I_{sc}}{\beta} \ln \frac{I_{sc}}{I_o} \ . \qquad (D-21)$$

The value of $F_c$ is sensitive to the dark current parameters, $I_o$ and $\beta$. $F_c$ may change significantly for cases of dark current arising from diffusion, space charge recombination or tunneling.

In the solutions to the integral-differential equations, the fill factor is not required to determine the maximum power. The maximum power point is obtained directly from the calculated solar cell V-I curve. The maximum power point is dependent on the dark current mechanism used in the boundary conditions, which is the equivalent of determining the appropriate fill factor.

D.6  Current Conventions

The current density equations for the one-dimensional case are

$$J_n = q\mu_n nE + qD_n \frac{dn}{dx} \qquad (D-22)$$

$$J_p = q\mu_p pE - qD_p \frac{dp}{dx} \qquad (D-23)$$

for electrons and holes, respectively, where

q:  electronic change,

$\mu_n$, $\mu_p$:  electron and hole mobility

242

E:  electric field,

n, p:  minority carrier concentrations,

$D_n$, $D_p$:  minority carrier diffusion coefficient.

The first terms in Eqs. (D-22) and (D-23) are the drift components to
the total current due to the drift field, E, whether externally applied
or built-in.  The second terms are the diffusion component contribution
to total current.

### D.7  Reflectivity

In the multiple layer structures discussed in Section 6.0, the
reflectivity is low at the interfaces and the absorption is strong
enough within the layers such that multiple reflections are not present.

While reflectivity data between III-V binaries and ternaries is
not generally available, there exists some data at vacuum-semiconductor
interfaces.  These data are shown in Tables D.1 through D.8.  With the
exception of AlAs and GaP, over the high solar photon flux region, the
data show that the reflectance at a vacuum interface is typically 0.35
± 0.10.  Therefore, the reflectance between most III-V binaries and
ternaries is generally less than 0.05 in this region of the solar spectrum.
Moreover because a cascade cell design dictates that direct transition
materials be used, except for the window material, the absorption is
typically very strong.  As a result of low reflectivity and strong absorp-
tion, multiple reflections in the cascade structure is expected to be
minimal.

### D.8  Drift Field

Aiding drift fields for minority carriers in solar cells has been
demonstrated to provide improvement in conversion efficiency.  In this

243

Table D.1.  REFLECTANCE $R$ OF ALUMINUM ANTIMONIDE
AS A FUNCTION OF WAVELENGTH $\lambda$*

| $\lambda$ (microns) | $R$ | $\lambda$ (microns) | $R$ | $\lambda$ (microns) | $R$ |
|---|---|---|---|---|---|
| 0.22 | 0.29 | 0.36 | 0.17 | 0.50 | 0.14 |
| 0.24 | 0.30 | 0.38 | 0.17 | 0.52 | 0.13 |
| 0.26 | 0.32 | 0.40 | 0.17 | 0.54 | 0.13 |
| 0.28 | 0.34 | 0.42 | 0.17 | 0.56 | 0.12 |
| 0.30 | 0.30 | 0.44 | 0.18 | 0.58 | 0.12 |
| 0.32 | 0.26 | 0.46 | 0.16 | | |
| 0.34 | 0.22 | 0.48 | 0.15 | | |

*T. E. Fischer, Phys. Ref., <u>139</u>, A1228 (1965).

Table D.2.  REFLECTANCE $R$ OF ALUMINUM ANTIMONIDE
AS A FUNCTION OF WAVELENGTH $\lambda$*

| $\lambda$ (microns) | $R$ | $\lambda$ (microns) | $R$ | $\lambda$ (microns) | $R$ |
|---|---|---|---|---|---|
| 15.0 | 0.255 | 29.0 | 0.058 | 31.8 | 0.580 |
| 16.0 | 0.252 | 29.2 | 0.027 | 31.9 | 0.558 |
| 17.0 | 0.250 | 29.4 | 0.095 | 32.0 | 0.541 |
| 18.0 | 0.247 | 29.6 | 0.610 | 32.1 | 0.522 |
| 19.0 | 0.245 | 29.8 | 0.754 | 32.2 | 0.517 |
| 19.5 | 0.243 | 30.0 | 0.850 | 32.3 | 0.492 |
| 20.0 | 0.242 | 30.1 | 0.877 | 32.5 | 0.473 |
| 21.0 | 0.238 | 30.2 | 0.888 | 32.7 | 0.454 |
| 21.5 | 0.237 | 30.3 | 0.895 | 33.0 | 0.436 |
| 22.0 | 0.236 | 30.4 | 0.899 | 33.5 | 0.412 |
| 22.5 | 0.234 | 30.5 | 0.902 | 34.0 | 0.392 |
| 23.0 | 0.232 | 30.6 | 0.903 | 34.5 | 0.378 |
| 23.5 | 0.229 | 30.7 | 0.904 | 35.0 | 0.368 |
| 24.0 | 0.226 | 30.8 | 0.906 | 35.5 | 0.359 |
| 24.5 | 0.222 | 30.9 | 0.906 | 36.0 | 0.353 |
| 25.0 | 0.217 | 31.0 | 0.906 | 36.5 | 0.344 |
| 25.5 | 0.212 | 31.1 | 0.904 | 37.0 | 0.338 |
| 26.0 | 0.205 | 31.2 | 0.901 | 37.5 | 0.331 |
| 26.5 | 0.196 | 31.3 | 0.878 | 38.0 | 0.326 |
| 27.0 | 0.187 | 31.4 | 0.808 | 38.5 | 0.320 |
| 27.5 | 0.172 | 31.5 | 0.731 | 39.0 | 0.318 |
| 28.0 | 0.153 | 31.6 | 0.664 | 40.0 | 0.317 |
| 28.5 | 0.120 | 31.7 | 0.609 | | |

*W. J. Turner and W. E. Reese, Phys. Rev., <u>127</u>, 126 (1962).

244

Table D.3.    REFLECTANCE $R$ OF GALLIUM PHOSPHIDE
AS A FUNCTION OF WAVELENGTH $\lambda$

| $\lambda$ (microns) | $R$ | Reference | $\lambda$ (microns) | $R$ | Reference | $\lambda$ (microns) | $R$ | Reference |
|---|---|---|---|---|---|---|---|---|
| 0.049 | 0.007 | [1-4] | 0.095 | 0.188 | [1-4] | 0.194 | 0.416 | [1-4] |
| 0.050 | 0.010 | | 0.103 | 0.216 | | 0.207 | 0.469 | |
| 0.052 | 0.013 | | 0.113 | 0.240 | | 0.229 | 0.580 | |
| 0.054 | 0.019 | | 0.124 | 0.273 | | 0.234 | 0.583 | |
| 0.056 | 0.020 | | 0.135 | 0.239 | | 0.239 | 0.568 | |
| 0.059 | 0.019 | | 0.139 | 0.246 | | 0.264 | 0.463 | |
| 0.063 | 0.015 | | 0.146 | 0.286 | | 0.288 | 0.402 | |
| 0.065 | 0.025 | | 0.157 | 0.385 | | 0.295 | 0.398 | |
| 0.069 | 0.045 | | 0.165 | 0.419 | | 0.302 | 0.398 | |
| 0.073 | 0.077 | | 0.177 | 0.455 | | 0.310 | 0.408 | |
| 0.077 | 0.108 | | 0.180 | 0.459 | | 0.318 | 0.428 | |
| 0.083 | 0.134 | | 0.188 | 0.422 | | 0.330 | 0.480 | |
| 0.089 | 0.161 | | 0.190 | 0.411 | | 0.335 | 0.491 | |
| 0.344 | 0.468 | | 19.44 | 0.195 | [5] | 27.14 | 0.924 | [5] |
| 0.354 | 0.435 | | 20.00 | 0.188 | | 27.19 | 0.903 | |
| 0.375 | 0.384 | | 20.43 | 0.183 | | 27.26 | 0.875 | |
| 0.413 | 0.331 | | 21.25 | 0.172 | | 27.33 | 0.846 | |
| 0.459 | 0.302 | | 22.34 | 0.144 | | 27.40 | 0.806 | |
| 0.517 | 0.280 | | 23.18 | 0.107 | | 27.46 | 0.771 | |
| 0.620 | 0.263 | | 23.87 | 0.069 | | 27.54 | 0.736 | |
| 0.689 | 0.257 | | 24.19 | 0.029 | | 27.64 | 0.700 | |
| 0.885 | 0.251 | | 24.66 | 0.016 | | 27.76 | 0.669 | |
| 1.240 | 0.247 | | 24.80 | 0.077 | | 27.89 | 0.646 | |
| 1.377 | 0.246 | | 24.86 | 0.269 | | 28.02 | 0.627 | |
| 2.066 | 0.244 | | 24.95 | 0.550 | | 28.49 | 0.467 | |
| 3.099 | 0.244 | | 25.00 | 0.669 | | 29.16 | 0.421 | |
| 6.198 | 0.243 | | 25.03 | 0.736 | | 30.00 | 0.385 | |
| 13.17 | 0.228 | [5] | 25.03 | 0.824 | | 31.30 | 0.352 | |
| 14.00 | 0.226 | | 25.22 | 0.906 | | 32.64 | 0.331 | |
| 14.88 | 0.222 | | 25.26 | 0.925 | | 33.95 | 0.321 | |
| 15.75 | 0.219 | | 25.39 | 0.957 | | 35.00 | 0.315 | |
| 16.00 | 0.220 | | 25.79 | 0.966 | | 35.44 | 0.313 | |
| 16.59 | 0.217 | | 26.22 | 0.971 | | 36.27 | 0.307 | |
| 17.40 | 0.210 | | 26.56 | 0.973 | | 37.39 | 0.302 | |
| 18.00 | 0.207 | | 26.80 | 0.966 | | 38.16 | 0.299 | |
| 18.55 | 0.202 | | 27.05 | 0.956 | | 38.95 | 0.299 | |

[1] H. R. Philipp and H. Ehrenreich, Phys. Rev. Letters, 8, 92 (1962)
[2] H. R. Philipp and H. Ehrenreich, Phys. Rev., 129, 1550 (1963).
[3] H. Ehrenreich, H.R. Philipp and J.C. Phillips, Phys. Rev. Letters, 8, 59 (1962).
[4] H. R. Philipp and H. Ehrenreich, Chapter 4 of this volume.
[5] D. A. Kleinman and W. G. Spitzer, Phys. Rev., 118, 110 (1960)

### Table D.4.   REFLECTANCE $R$ OF GALLIUM ARSENIDE AS A FUNCTION OF WAVELENGTH $\lambda$

| $\lambda$ (microns) | $R$ | Reference | $\lambda$ (microns) | $R$ | Reference | $\lambda$ (microns) | $R$ | Reference |
|---|---|---|---|---|---|---|---|---|
| 0.049 | 0.006 | [1-4] | 0.590 | 0.350 | [1-4] | 31.91 | 0.186 | [5] |
| 0.051 | 0.010 | | 0.653 | 0.335 | | 32.08 | 0.180 | |
| 0.054 | 0.013 | | 0.729 | 0.323 | | 32.25 | 0.173 | |
| 0.056 | 0.014 | | 0.827 | 0.314 | | 32.43 | 0.164 | |
| 0.058 | 0.015 | | 1.00 | 0.289 | [5] | 32.60 | 0.155 | |
| 0.059 | 0.015 | | 2.00 | 0.289 | | 32.78 | 0.144 | |
| 0.062 | 0.011 | | 3.00 | 0.289 | | 32.96 | 0.132 | |
| 0.065 | 0.014 | | 4.00 | 0.289 | | 33.14 | 0.117 | |
| 0.068 | 0.020 | | 5.00 | 0.289 | | 33.33 | 0.100 | |
| 0.073 | 0.032 | | 6.00 | 0.288 | | 33.52 | 0.080 | |
| 0.077 | 0.053 | | 7.00 | 0.288 | | 33.70 | 0.059 | |
| 0.083 | 0.077 | | 8.00 | 0.287 | | 33.89 | 0.046 | |
| 0.089 | 0.104 | | 9.00 | 0.288 | | 34.09 | 0.080 | |
| 0.096 | 0.131 | | 10.00 | 0.287 | | 34.28 | 0.255 | |
| 0.103 | 0.151 | | 11.00 | 0.287 | | 34.48 | 0.473 | |
| 0.115 | 0.175 | | 12.00 | 0.286 | | 34.68 | 0.617 | |
| 0.124 | 0.208 | | 13.00 | 0.266 | | 34.88 | 0.704 | |
| 0.138 | 0.265 | | 14.00 | 0.285 | | 35.08 | 0.756 | |
| 0.155 | 0.365 | | 15.00 | 0.284 | | 35.29 | 0.788 | |
| 0.177 | 0.443 | | 15.78 | 0.283 | | 35.50 | 0.806 | |
| 0.188 | 0.460 | | 16.66 | 0.283 | | 35.71 | 0.812 | |
| 0.197 | 0.419 | | 17.64 | 0.282 | | 35.92 | 0.804 | |
| 0.200 | 0.418 | | 18.75 | 0.280 | | 36.14 | 0.769 | |
| 0.207 | 0.438 | | 20.00 | 0.278 | | 36.36 | 0.699 | |
| 0.225 | 0.510 | | 21.42 | 0.276 | | 36.58 | 0.628 | |
| 0.248 | 0.605 | | 23.07 | 0.272 | | 36.81 | 0.576 | |
| 0.253 | 0.598 | | 25.00 | 0.266 | | 37.03 | 0.539 | |
| 0.276 | 0.494 | | 27.27 | 0.256 | | 37.26 | 0.510 | |
| 0.318 | 0.404 | | 30.00 | 0.230 | | 37.50 | 0.487 | |
| 0.326 | 0.402 | | 30.15 | 0.228 | | 37.73 | 0.469 | |
| 0.344 | 0.408 | | 30.30 | 0.225 | | 37.97 | 0.454 | |
| 0.365 | 0.425 | | 30.45 | 0.223 | | 38.21 | 0.442 | |
| 0.400 | 0.466 | | 30.61 | 0.220 | | 38.46 | 0.431 | |
| 0.409 | 0.465 | | 30.76 | 0.217 | | 38.71 | 0.422 | |
| 0.419 | 0.468 | | 30.92 | 0.214 | | 38.96 | 0.414 | |
| 0.425 | 0.484 | | 31.08 | 0.210 | | 39.21 | 0.407 | |
| 0.443 | 0.461 | | 31.25 | 0.206 | | 39.47 | 0.401 | |
| 0.459 | 0.436 | | 31.41 | 0.202 | | 39.73 | 0.395 | |
| 0.496 | 0.402 | | 31.57 | 0.197 | | 40.00 | 0.390 | |
| 0.539 | 0.373 | | 31.74 | 0.192 | | | | |

[1] H. R. Philipp and H. Ehrenreich, Phys. Rev. Letters, 8, 92 (1962).
[2] H. R. Philipp and H. Ehrenreich, Phys. Rev., 129, 1550 (1963).
[3] H. Ehrenreich, H.R. Philipp & J.C. Phillips, Phys. Rev. Letters, 8, 59 (1962).
[4] H. R. Philipp and H. Ehrenreich, Chapter 4, Semiconductors and Semimetals: edited by R.K. Willardson and A.C. Beer, Vol. 3, Academic Press, New York.
[5] B.Piriou and F. Cabannes, Compt. Rend., 255, 2932 (1962).

Table D.5. REFLECTANCE $R$ OF GALLIUM ANTIMONIDE
AS A FUNCTION OF WAVELENGTH $\lambda$*

| $\lambda$ (microns) | $R$ | $\lambda$ (microns) | $R$ | $\lambda$ (microns) | $R$ |
|---|---|---|---|---|---|
| 0.245 | 0.385 | 0.351 | 0.434 | 0.64 | 0.454 |
| 0.246 | 0.386 | 0.360 | 0.422 | 0.65 | 0.456 |
| 0.249 | 0.393 | 0.365 | 0.418 | 0.66 | 0.453 |
| 0.252 | 0.409 | 0.370 | 0.414 | 0.68 | 0.438 |
| 0.256 | 0.419 | 0.380 | 0.406 | 0.70 | 0.432 |
| 0.260 | 0.430 | 0.390 | 0.402 | 0.75 | 0.419 |
| 0.265 | 0.451 | 0.400 | 0.400 | 0.80 | 0.410 |
| 0.269 | 0.473 | 0.409 | 0.400 | 0.85 | 0.399 |
| 0.272 | 0.500 | 0.415 | 0.406 | 0.90 | 0.391 |
| 0.276 | 0.511 | 0.420 | 0.405 | 0.95 | 0.380 |
| 0.280 | 0.521 | 0.423 | 0.403 | 1.00 | 0.370 |
| 0.282 | 0.526 | 0.427 | 0.409 | 1.06 | 0.358 |
| 0.285 | 0.535 | 0.430 | 0.413 | 1.09 | 0.351 |
| 0.288 | 0.540 | 0.440 | 0.411 | 1.20 | 0.346 |
| 0.291 | 0.536 | 0.450 | 0.420 | 1.26 | 0.346 |
| 0.295 | 0.532 | 0.460 | 0.425 | 1.30 | 0.343 |
| 0.300 | 0.522 | 0.470 | 0.430 | 1.40 | 0.340 |
| 0.302 | 0.520 | 0.480 | 0.434 | 1.55 | 0.340 |
| 0.303 | 0.513 | 0.490 | 0.439 | 1.60 | 0.339 |
| 0.308 | 0.503 | 0.500 | 0.435 | 1.68 | 0.338 |
| 0.309 | 0.497 | 0.520 | 0.435 | 1.80 | 0.335 |
| 0.311 | 0.490 | 0.540 | 0.434 | 1.86 | 0.334 |
| 0.315 | 0.486 | 0.560 | 0.436 | 2.00 | 0.333 |
| 0.320 | 0.475 | 0.58 | 0.442 | 2.15 | 0.330 |
| 0.327 | 0.463 | 0.60 | 0.448 | 2.38 | 0.329 |
| 0.333 | 0.452 | 0.62 | 0.454 | | |
| 0.340 | 0.448 | 0.63 | 0.453 | | |

*M. Cardona, Z. Physik, 161, 99 (1960).

247

## Table D.6. REFLECTANCE $R$ OF INDIUM PHOSPHIDE AS A FUNCTION OF WAVELENGTH $\lambda$*

| $\lambda$ (microns) | $R$ | $\lambda$ (microns) | $R$ | $\lambda$ (microns) | $R$ |
|---|---|---|---|---|---|
| 0.059 | 0.091 | 0.133 | 0.316 | 0.194 | 0.417 |
| 0.060 | 0.087 | 0.135 | 0.320 | 0.197 | 0.410 |
| 0.062 | 0.083 | 0.136 | 0.325 | 0.200 | 0.408 |
| 0.064 | 0.080 | 0.138 | 0.330 | 0.203 | 0.415 |
| 0.065 | 0.075 | 0.139 | 0.336 | 0.207 | 0.429 |
| 0.067 | 0.072 | 0.141 | 0.343 | 0.210 | 0.442 |
| 0.069 | 0.069 | 0.144 | 0.359 | 0.214 | 0.452 |
| 0.071 | 0.068 | 0.146 | 0.366 | 0.217 | 0.465 |
| 0.075 | 0.075 | 0.148 | 0.370 | 0.221 | 0.477 |
| 0.077 | 0.094 | 0.149 | 0.376 | 0.225 | 0.490 |
| 0.079 | 0.111 | 0.151 | 0.380 | 0.229 | 0.504 |
| 0.083 | 0.132 | 0.153 | 0.385 | 0.234 | 0.517 |
| 0.085 | 0.162 | 0.155 | 0.390 | 0.238 | 0.528 |
| 0.089 | 0.178 | 0.157 | 0.395 | 0.243 | 0.544 |
| 0.093 | 0.194 | 0.159 | 0.407 | 0.248 | 0.553 |
| 0.095 | 0.205 | 0.161 | 0.409 | 0.253 | 0.538 |
| 0.099 | 0.210 | 0.163 | 0.414 | 0.258 | 0.524 |
| 0.103 | 0.218 | 0.165 | 0.419 | 0.264 | 0.491 |
| 0.108 | 0.232 | 0.167 | 0.423 | 0.269 | 0.450 |
| 0.113 | 0.246 | 0.170 | 0.428 | 0.275 | 0.404 |
| 0.118 | 0.266 | 0.172 | 0.430 | 0.282 | 0.380 |
| 0.124 | 0.298 | 0.175 | 2.432 | 0.288 | 0.364 |
| 0.125 | 0.300 | 0.177 | 0.433 | 0.295 | 0.352 |
| 0.126 | 0.301 | 0.180 | 0.432 | 0.302 | 0.343 |
| 0.128 | 0.303 | 0.182 | 0.431 | 0.310 | 0.339 |
| 0.129 | 0.305 | 0.185 | 0.429 | 0.318 | 0.336 |
| 0.130 | 0.309 | 0.188 | 0.427 | 0.326 | 0.338 |
| 0.132 | 0.311 | 0.191 | 0.422 | 0.335 | 0.343 |
| 0.344 | 0.351 | 0.477 | 0.336 | 0.729 | 0.290 |
| 0.354 | 0.361 | 0.496 | 0.329 | 0.775 | 0.286 |
| 0.375 | 0.406 | 0.517 | 0.322 | 0.826 | 0.285 |
| 0.387 | 0.424 | 0.539 | 0.316 | 0.885 | 0.282 |
| 0.399 | 0.416 | 0.563 | 0.310 | 0.953 | 0.273 |
| 0.413 | 0.394 | 0.590 | 0.307 | 1.033 | 0.269 |
| 0.427 | 0.375 | 0.620 | 0.304 | 1.126 | 0.265 |
| 0.443 | 0.356 | 0.652 | 0.301 | 1.240 | 0.263 |
| 0.459 | 0.346 | 0.689 | 0.295 | | |

*M. Cardona, J. Appl. Phys., 36, 2181 (1965; 32, 958 (1961).

Table D.7.   REFLECTANCE $R$ OF INDIUM ARSENIDE
AS A FUNCTION OF WAVELENGTH $\lambda$*

| $\lambda$ (microns) | $R$ | $\lambda$ (microns) | $R$ | $\lambda$ (microns) | $R$ |
|---|---|---|---|---|---|
| 0.049 | 0.010 | 0.153 | 0.384 | 0.443 | 0.435 |
| 0.052 | 0.012 | 0.172 | 0.432 | 0.451 | 0.437 |
| 0.054 | 0.013 | 0.180 | 0.435 | 0.459 | 0.435 |
| 0.056 | 0.014 | 0.188 | 0.421 | 0.468 | 0.430 |
| 0.059 | 0.015 | 0.195 | 0.433 | 0.477 | 0.433 |
| 0.062 | 0.015 | 0.211 | 0.395 | 0.496 | 0.443 |
| 0.064 | 0.014 | 0.225 | 0.435 | 0.517 | 0.430 |
| 0.067 | 0.013 | 0.248 | 0.501 | 0.563 | 0.396 |
| 0.070 | 0.009 | 0.259 | 0.550 | 0.620 | 0.373 |
| 0.077 | 0.020 | 0.264 | 0.559 | 0.689 | 0.355 |
| 0.082 | 0.034 | 0.269 | 0.550 | 0.775 | 0.341 |
| 0.089 | 0.060 | 0.282 | 0.502 | 0.885 | 0.330 |
| 0.095 | 0.108 | 0.310 | 0.391 | 1.033 | 0.321 |
| 0.103 | 0.166 | 0.335 | 0.354 | 1.240 | 0.314 |
| 0.108 | 0.200 | 0.344 | 0.349 | 1.377 | 0.311 |
| 0.112 | 0.219 | 0.354 | 0.350 | 2.066 | 0.305 |
| 0.123 | 0.260 | 0.387 | 0.360 | 3.099 | 0.302 |
| 0.136 | 0.310 | 0.413 | 0.393 | 6.198 | 0.300 |

[1]  H. R. Philipp and H. Ehrenreich, Phys. Rev. Letters, 8, 92 (1962).
[2]  H. R. Philipp and H. Ehrenreich, Phys. Rev., 129, 1550 (1963).
[3]  H. Ehrenreich, H. R. Philipp, and J. C. Phillips, Phys. Rev. Letters, 8, 59 (1962).
[4]  H. R. Philipp and H. Ehrenreich, Chapter 4, Semiconductors and Semimetals: Ed. R. K. Willardson and A. C. Beer, Vol. 3, Academic Press, New York.

Table D.8.   REFLECTANCE $R$ OF INDIUM ANTIMONIDE
AS A FUNCTION OF WAVELENGTH $\lambda$

| $\lambda$ (microns) | $R$ | Reference | $\lambda$ (microns) | $R$ | Reference | $\lambda$ (microns) | $R$ | Reference |
|---|---|---|---|---|---|---|---|---|
| 0.049 | 0.010 | [1] | 0.238 | 0.442 | [1] | 1.24 | 0.376 | [1] |
| 0.052 | 0.012 | | 0.243 | 0.436 | | 1.55 | 0.369 | |
| 0.054 | 0.013 | | 0.248 | 0.441 | | 2.07 | 0.364 | |
| 0.056 | 0.014 | | 0.282 | 0.530 | | 20.0 | 0.35 | [2] |
| 0.059 | 0.016 | | 0.302 | 0.579 | | 25.0 | 0.34 | |
| 0.062 | 0.016 | | 0.310 | 0.570 | | 30.0 | 0.31 | |
| 0.065 | 0.015 | | 0.344 | 0.466 | | 35.0 | 0.29 | |
| 0.069 | 0.012 | | 0.365 | 0.438 | | 40.0 | 0.25 | |
| 0.073 | 0.009 | | 0.413 | 0.398 | | 45.0 | 0.21 | |
| 0.080 | 0.007 | | 0.428 | 0.400 | | 50.0 | 0.19 | [3] |
| 0.083 | 0.009 | | 0.443 | 0.405 | | 50.3 | 0.18 | |
| 0.089 | 0.023 | | 0.477 | 0.425 | | 50.5 | 0.17 | |
| 0.095 | 0.053 | | 0.517 | 0.460 | | 50.8 | 0.15 | |
| 0.103 | 0.100 | | 0.539 | 0.458 | | 51.0 | 0.14 | |
| 0.113 | 0.160 | | 0.564 | 0.454 | | 51.3 | 0.12 | |
| 0.124 | 0.222 | | 0.590 | 0.448 | | 51.5 | 0.13 | |
| 0.138 | 0.274 | | 0.620 | 0.453 | | 51.8 | 0.17 | |
| 0.155 | 0.332 | | 0.656 | 0.479 | | 52.1 | 0.27 | |
| 0.163 | 0.348 | | 0.677 | 0.488 | | 52.4 | 0.42 | |
| 0.182 | 0.380 | | 0.689 | 0.480 | | 52.6 | 0.59 | |
| 0.207 | 0.430 | | 0.708 | 0.466 | | 52.9 | 0.70 | |
| 0.218 | 0.424 | | 0.775 | 0.430 | | 53.2 | 0.76 | |
| 0.221 | 0.429 | | 0.886 | 0.400 | | 53.5 | 0.79 | |
| 0.234 | 0.442 | | 1.03 | 0.385 | | 53.8 | 0.81 | |

[1] H. R. Philipp and H. Ehrenreich, Phys. Rev., 129, 1550 (1963).
[2] H. Yoshiriago and R. A. Oetjen, Phys. Rev., 101, 526 (1956).
[3] R. B. Sanderson, J. Phys. Chem. Solids, 26, 803 (1965).

study, drift fields are one of the major parameters studied to determine their effect on efficiency and other solar cell terminal properties. The integral-differential continuity equation has been derived and general solutions obtained with constant or average drift field. No attempt has been made to obtain a general solution with variable drift field. This decision has been reached because when the drift field exceeds 1500 V/cm in optimally designed cells, the improvement in efficiency is within 10% of the saturation level attained at 3000 V/cm in surface layers where surface recombination is high. Therefore, the most interesting cases for those solar cells with optimally designed structures and with drift fields in the range 1500 to 3000 V/cm.

In a practical endeavor to correlate device experimental results with theory, the use of an average, constant built-in field in micrometer thick layers is consistent with the other approximations, typically used in semiconductor analysis, for impurity concentration, minority carrier lifetime, mobility and mobility scattering processes, absorption coefficient, and the interpolation of the absorption coefficient for ternary alloys from the terminal binaries.

Exceeding 3000 V/cm, the critical field value, in many III-V compounds, results in a decrease in carrier velocity and a decrease in efficiency. Therefore, exceeding the critical field value is not of interest for solar cells.

251

REFERENCES

D-1. W. Shockley, <u>Electrons and Holes in Semiconductors</u>, D. Van Nostrand Co., Inc., Princeton, 1950.

D-2. R. N. Hall, "Electron-Hole Recombination in Germanium," Phys. Rev., <u>87</u>, 387 (1952).

D-3. W. Shockley and W. T. Read, "Statistics of the Recombination of Holes and Electrons," Phys. Rev., <u>87</u>, 835 (1952).

D-4. C. T. Sah, R. N. Noyce, and W. Shockley, "Carrier Generation and Recombination in p-n Junction and p-n Junction Characteristics," Proc. IRE, <u>45</u>, 1228 (1957).

D-5. A. G. Milnes and D. L. Feucht, <u>Heterojunctions and Metal-Semiconductor Junctions</u>, Academic Press, New York, 1972.

D-6. M. F. Lamorte, "Internal Power Dissipation in Gallium Arsenide Solar Cells," Advanced Energy Conversion, <u>3</u>, 551 (1963).

D-7. A. R. Riben and D. L. Feucht, "nGe-pGaAs Heterojunctions," Solid State Electron., <u>9</u>, 1055 (1966).

D-8. A. R. Riben and D. L. Feucht, Int. J. Electron, <u>20</u>, 583 (1966).

D-9. A. R. Riben and D. L. Feucht, "Evidence of Tunneling in Non-Degenerate Ge-GaAs Heterojunctions," IEEE Trans. Electron Devices, <u>ED-11</u>, 534 (1964).

D-10. R. H. Rediker, S. Stopek, and J. H. R. Ward, "Interface-Alloy Epitaxial Heterojunctions," Solid-State Electron., <u>7</u>, 621 (1964).

D-11. R. H. Rediker, S. Stopek, and E. D. Hinkley, "Electrical and Electro-optical Properties of Interface-Alloy Heterojunctions," Trans. AIME, <u>233</u>, 463 (1965).

D-12. U. Dolega, "Theory of the p-n Heterojunction Between Semiconductors with Different Crystal Lattices," Z. Naturforsch, <u>18</u>, 653 (1963).

D-13. J. P. Donnelly and A. G. Milnes, "The Epitaxial Growth of Ge on Si by Solution Growth Techniques," J. Electrochem. Soc., <u>113</u>, 297 (1966).

D-14. H. J. Hovel, <u>Semiconductors and Semimetals</u>, Vol. 11, Adademic Press, New York, 1975.

D-15. M. Wolf, "Drift Fields on Photovoltaic Solar Energy Converter Cells," Proc. IEEE, <u>51</u>, 674 (1963).

D-16. B. Ellis and T. S. Moss, "Calculated Efficiencies of Practical GaAs and Si Solar Cells Including the Effects of Built-in Electric Fields," Solid-State Electron., <u>13</u>, 1 (1970).

D-17. M. Konagai and K. Takahashi, "Theoretical Analysis of Graded-Band Gap Gallium-Aluminum Arsenide/Gallium Arsenide $pGa_{1-x}Al_xAs/pGaAs/nGaAs$ Solar Cells," Solid-State Electron., $\underline{19}$, 259 (1976).

D-18. J. B. Gunn, "Microwave Oscillation of Current in III-V Semiconductors," Solid-State Comm., $\underline{1}$, 88 (1963).

D-19. J. B. Gunn, "Instabilities of Current in III-V Semiconductors," IBM J. of Res. Dev., $\underline{8}$, 141 (1964).

D-20. H. Kroemer, "Theory of the Gunn Effect," Proc. IEEE, $\underline{52}$, 1736 (1964).

D-21. B. K. Ridley and T. B. Watkins, "The Possibility of Negative Resistance Effects in Semiconductors," Proc. Phys. Soc. (London), $\underline{78}$, 293 (1961).

D-22. C. Hilsum, "Transferred Electron Amplifiers and Oscillators," Proc. IRE, $\underline{50}$, 185 (1962).

APPENDIX E.  LAMBERT'S ABSORPTION LAW FOR POSITION-DEPENDENT ABSORPTION
COEFFICIENT

The absorption law for position-independent absorption coefficient
is well known and given by

$$N(x) = N_o e^{-\alpha x} \qquad \text{(E-1)}$$

where the incident flux is $N_o$ at x=0.  In graded bandgap materials
the absorption coefficient is position-dependent for a given wavelength.
This absorption law expression is derived below.

Consider monochromatic parallel beam of light characterized by wave-
length, $\lambda$, propogating in the x-direction and incident on an absorbing
material whose plane is perpendicular to the beam.  The material is assumed
to be uniform in composition and properties in the y-z directions and is
assumed to absorb, but not to scatter, light.  In Figure E.1, N is
denoted as the incident flux at x in units of $cm^{-2}$ $sec^{-1}$ $(\mu m)^{-1}$.  The absorbed
flux is proportional to the product

$$dN = -\alpha(x)Ndx \qquad \text{(E-2)}$$

so that the exiting flux is

$$N-\alpha(x)Ndx. \qquad \text{(E-3)}$$

From Eq. (E-2) we obtain the absorption law, after integrating, giving

$$N = N_o e^{-\int_0^x \alpha(x)dx}, \qquad \text{(E-4)}$$

for position-dependent absorption coefficient.  By setting $\alpha$ independent
of x, Eq. (E-1) is recovered.

254
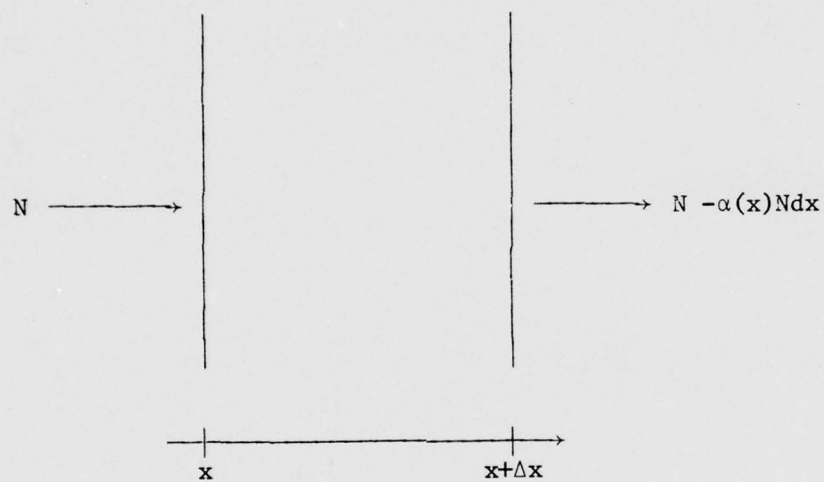
Figure E.1. Position-dependent absorption.

255

APPENDIX F. "POTENTIAL WELL" ANALYSIS

In this appendix an analytical solution is obtained for the PW cell.
The method employed in the analysis is to establish an integral form
of the steady-state continuity equation (See Section 4.0) for excess
minority carriers in each of the four regions. A general solution to each
of the continuity equations is obtained and the boundary conditions imposed.
The approximations employed were discussed in APPENDIX D. The current
relationship is then used to calculate cell performance.

The model used in the analysis is shown in Figure 5.1 and described in
Section 5.0. The electron current at the p-n junction, arising from Regions
1 and 2, is simultaneously dependent on the constants of integration of the
solutions in Regions 1 and 2. Similarly, the hole current is simultaneously
dependent on the constants of integration of the solutions in Regions 3 and
4. Therefore, the solutions to Regions 1 and 2 are discussed together and
similarly for Regions 3 and 4.

The assumptions made in the solution of the excess minority carrier
concentrations are as follows:

1. Each interface bounding a subregion, including the p-n junction,
is treated as a line boundary whose thickness is small compared to the sub-
region width and where the associated boundary condition(s) are considered
as a property of the interface [5-7, 5-27].

2. Shockley's diffusion mechanism is the dominant p-n junction carrier
transport and space charge recombination is small. This is a good
approximation in the PW cell because of the relatively low doping in each
of the GaAs subregions which form the p-n homojunction [5-40, 5-41].

3. For the one solar constant perturbation, the excited excess electron
and hole concentrations are small compared to the majority carrier concentrations

256

in their respective regions. Therefore, the recombination rate is assumed linearly proportional to the excess carrier concentration in each subregion [5-40].

4. Each photon of the solar spectrum may not excite more than one hole-electron pair.

5. The ternary alloy composition grading is such that the AlGaAs layers establish a constant built-in field.

6. In the graded layers the band gap grading is manifested through a slope of the minority carrier band edge. This arises because the majority carrier band edge position is dictated by the energy difference from the equilibrium Fermi level.

7. Uniform doping is assumed in each subregion.

8. The absorption coefficient in the graded layers is position dependent.

9. Minority carrier lifetime in AlGaAs is assumed to be the same as in GaAs for the same doping level [5-30].

10. A reflectivity of 5% is taken over the entire solar spectrum of interest.

11. The photovoltage generated across the graded layers and barriers are assumed small compared to that generated at the p-n junction and, therefore, neglected [5-28, 5-29].

12. Recombination at the AlGaAs-GaAs interfaces are assumed small [5-38].

13. The effective masses, hole and effective electron mobilities, density of states and absorption coefficient for AlGaAs are calculated by interpolation between the values of GaAs and AlAs.

14. An average mobility is assumed in the graded layers.

257

15.  The temperature effects in mobility, bandgap, and in the intrinsic concentration have been taken into consideration in the temperature behavior. However, the increase in lifetime with increasing temperature has been neglected, and the ambient temperature value used for all temperatures. Carrier mobility is assumed to be dominated by ionized impurity scattering and by polar optical photon scattering.

In the one-dimensional model used, the value of x increases from the surface into the cell.  The general case is solved for which the conduction band discontinuity, $\Delta E_{c1}$, and valence band discontinuities, $\Delta_{v3}$ and $\Delta E_{v4}$, are present as parameters in the solar cell V-I expression.  The interface boundary lines are denoted $x_1$, $x_2$, $x_3$, and $x_4$.

REGIONS 1 and 2: Electrons in the p-p regions

The inhomogeneous integral form of the steady-state continuity equation in the $Al_u Ga_{1-u} As$ graded bandgap layer is given by

$$0 = g_1 + D_{n1} \frac{d^2 n_1}{dx^2} + \mu_{n1} E_{10} \frac{dn_1}{dx} - \frac{n_1}{\tau_{n1}} , \tag{F-1}$$

where the generation term is

$$g_1 = \int_0^{\lambda_{c1}} \alpha_1 [1-R] N_o e^{-\int_0^x \alpha_1 dx'} d\lambda . \tag{F-2}$$

The symbols are defined in the List of Symbols.  The electric field, $E_{10}$, is constant and is established by an appropriate compositional grading. This results in a nearly linearly decreasing composition in this region. The field is given by

$$E_{10} = - \frac{E_{G0} - E_{G1} - \Delta E_{c1}}{x_1} \tag{F-3}$$

258

where $E_{G0}$ and $E_{G1}$ are the band gap values at the surface and in Region 2, respectively. The value of $E_{G0}$ used in the analysis is 1.739, which gives a value for x of 0.258. In the range of u from zero to 0.3 the electron mobility [5-41], diffusion coefficient, diffusion length [5-43] and lifetime [5-44] are not strong functions of the Al mole fraction. For our considerations here the electron effective mobility is calculated as a function of Al mole fraction in the graded larger and an average value taken for $\mu_{n1}$ and $D_{n1}$ in Eq. (F-1). The value of $\tau_{n1}$ is taken from GaAs data at the same doping concentration. The value for $\alpha_1$ in this region is interpolated between the GaAs and AlAs absorption curves, and the reflectance is taken to be 0.05 over the spectrum of interest.

The general solution to Eq. (1) is represented by

$$n_1(x) = c_{11}e^{\omega_{11}x} + x_{12}e^{\omega_{12}x} + \frac{1}{\omega_{12} - \omega_{11}} [G_{11}(x)e^{\omega_{11}x} + G_{12}(x)e^{\omega_{12}x}] \quad (F-4)$$

where $c_{11}$ and $c_{12}$ are constants of integration and where we define

$$G_{11}(x) = \frac{1}{D_{n1}} \int_0^{\lambda_{c1}} \int_0^x \alpha_1 N_{01}(x')e^{-\omega_{11}x'} \, dx'd\lambda, \quad (F-5)$$

$$G_{12}(x) = - \frac{1}{D_{n1}} \int_0^{\lambda_{c1}} \int_0^x \alpha_1 N_{01}(x')e^{-\omega_{12}x'} \, dx'd, \quad (F-6)$$

$$\omega_{11}, \omega_{12} = - \frac{\mu_{n1}E_{10}}{2D_{n1}} \pm \sqrt{\left(\frac{\mu_{n1}E_{10}}{2D_{n1}}\right)^2 + L_{n1}^{-2}}, \quad (F-7)$$

$$N_{01}(x) = (1-R)N_o e^{-\int_0^x \alpha_1 dx'}. \quad (F-8)$$

259

In Eq. (F-4) the first and second terms represent the homogeneous solution while the third represents the nonhomogeneous solution. The integration over x in $G_{11}$ and $G_{12}$ is a consequence of the position sensitive absorption coefficient due to the bandgap grading. Lambert's absorption law is also modified, as shown in Eq. (F-8), because the absorption is position sensitive and is represented by the integration of $\alpha_1$ over x. The value of $E_{G1}$ is given by

$$E_{G1} = E_{G2} + \Delta E_{c1} \tag{F-9}$$

where

$$\lambda_{c1} = \frac{1.2398}{E_{G1}} \tag{F-10}$$

and $E_{G2}$ is the GaAs bandgap value.

Both the homogeneous and nonhomogeneous solutions are functions of $E_{10}$ and $\Delta E_{c1}$. By setting $E_{10}$ and $\Delta E_{c1}$ to zero the general solution for constant bandgap, the zero field case may be recovered.

The integral form of the continuity equation in Region 2 is

$$0 = g_2 + D_{n2} \frac{d^2 n_2}{dx^2} - \frac{n_2}{\tau_{n2}} \tag{F-11}$$

where the generation term is given by

$$g_2 = \int_0^{\lambda_{c2}} \alpha_2 N_{01}(x_1) e^{-\alpha_2(x-x_1)} d\lambda. \tag{F-12}$$

This continuity equation is similar to that of Region 1 except that it is applicable to the region bounded by $x_1$ and $x_2$, a field is not present, the material constants apply to GaAs of constant bandgap, $\alpha_2$ is independent of position and the usual form of Lambert's absorption law applies.

260

The incident flux, $N_{01}(x_1)$, on Region 2 is dimished by the flux absorbed in Region 1 and given by

$$N_{01}(x_1) = (1-R)N_o e^{-\int_0^{x_1} \alpha_1 dx} . \qquad (F-13)$$

The general solution to Eq. (F-11) is

$$n_2(x) = C_{21} \cosh \frac{x-x_1}{L_{n2}} + C_{22} \sinh \frac{x-x_1}{L_{n2}} - C_{02}(x) \qquad (F-14)$$

where

$$C_{02}(x) = \int_0^{\lambda_{c2}} C_{23} e^{-\alpha_2(x-x_1)} d\lambda \qquad (F-15)$$

and

$$C_{23} = \frac{\alpha_2^2 L_{n2}^2 N_{01}(x_1)}{D_{n2}(\alpha_2^2 L_{n2}^2 - 1)} . \qquad (F-16)$$

The cut-off wavelength, $\lambda_{c2}$, is that of GaAs. The homogeneous solution is represented by the first and second term in Eq. (F-14) while the non-homogeneous solution is the third term.

In Regions 1 and 2 there are four boundary conditions that enable us to solve for the four constants of integration, $C_{11}$, $C_{12}$, $C_{21}$, and $C_{22}$. Due to the nature of the boundary conditions they are inter-related.

The boundary condition at $x = 0$ describes the electron current arising from surface recombination. Its direction is in the postive x direction. It is represented by the relationship

$$D_{n1} \frac{dn_1}{dx} \bigg|_0 + n_1(0)\mu_{n1}E_{10} = Sn_1(0) \qquad (F-17)$$

where the surface recombination velocity, S, is taken to be a positive quantity. The numerical value of $E_{10}$, for an aiding field, is negative

261

and represents the electron drift component whose direction opposes that of surface recombination current. For a nonvanishing value of S, the electron concentration gradient within several hundred angstroms of the surface is positive and represents the diffusion component of electron current into surface recombination states. When the built-in field, $E_{10}$, is sufficiently negative it reduces the surface recombination current to negligible values. Moreover, for indirect transition materials, $n_1(0)$ is smaller than for direct transition materials which also serves to reduce surface recombination current. From a substitution of the Einstein relationship

$$D = \frac{kT}{q} \mu,$$
(F-18)

into Eq. (F-17), it is observed that surface recombination current increases with increasing temperature. Phenomenologically this results because minority carrier diffusion increases with increasing temperature. In order for surface recombination current to vanish the relationship

$$E_{10} = - \frac{kT}{q} \frac{1}{n_1(0)} \frac{dn_1}{dx}\bigg|_0$$
(F-19)

must be satisfied. The value of $n_1$ required to satisfy Eq. (F-19) is 13% higher than $n_1(0)$ in a recombination layer thickness of $10^{-6}$ cm.

The second boundary condition to be satisfied is that the excess electron concentration at $x_1$ is described by Maxwell-Boltzmann statistics given by

$$n_1(x_1) = n_2(x_1)e^{-\Delta E_{c1}/kT}.$$
(F-20)

262

This relationship assumes non-degenerate materials and that the metallurgical heterojunction is very narrow compared to the thickness of either Region 1 or 2. The barrier energy, $\Delta E_{c1}$, is assumed to be a positive quantity as shown in Figure 5.1. In the case of a vanishing barrier then, of course, the continuity of charge is evident.

In the absence of heterojunction recombination, the electron current is continuous across the boundary at $x_1$. This gives the third boundary condition and is represented by

$$D_{n1} \frac{dn_1}{dx} \bigg|_{x_1} + n_1(x_1) \, n_1 E_{10} = D_{n2} \frac{dn_2}{dx} \bigg|_{x_1} . \tag{F-21}$$

Heterojunction recombination is not considered here because it has been shown to be small at the $Al_x Ga_{1-x} As$-GaAs interface [5-38]. This result is not surprising considering the small mismatch in lattice constant for $Al_x Ga_{1-x} As$ over a wide range of alloys compared to the GaAs lattice constant.

The fourth boundary condition relates to the non-equilibrium concentration at $x_2$. This boundary condition results in the only term that does not involve an integration over wavelength. In GaAs homojunctions the competing junction transport mechanisms are thermal diffusion and space charge recombination. Imposing thermal diffusion at $x_2$, the boundary condition becomes

$$n_2(x_2) = n_{2po} \, (e^{qV/kT} - 1) \tag{F-22}$$

where $n_{2po}$ is the equilibrium electron concentration. In the junction current equation we will show that the junction current which results is Shockley's ideal diffusion mechanism multiplied by a coefficient that describes charge confinement.

263

Having solved for the four constants of integration, the electron contribution to the terminal current may be obtained from

$$J_{n2} = qD_{n2} \left. \frac{dn_2}{dx} \right|_x \tag{F-23}$$

resulting in

$$J_{n2} = -J_{scn1} - J_{scn2} + J_{Jn2} , \tag{F-24}$$

where $J_{scn1}$ and $J_{scn2}$ are the contributions to the short-circuit current from Regions 1 and 2, respectively, and $J_{Jn2}$ is the contribution to dark current from electron injection across the p-n junction into Region 2. The quantities $J_{scn1}$, $J_{scn2}$ and $J_{Jn2}$ are positive quantities for all values of material and structural parameters. The presence of the negative signs indicates that the current component is in a direction opposite to the positive x-direction. The current components in Eq. (F-24) are represented by:

$$J_{scn1} = q \frac{N_{12}}{F_{12}} v_{21} \left( 1 - \frac{1}{R_n} \tanh \frac{x_2 - x_1}{L_{n2}} \right) \frac{e^{(\omega_{11} + \omega_{12})x_1}}{I_{01}} \int_0^{\lambda_{c1}} \int_0^{x_1} \alpha N_{01} (e^{-\omega_{11}x} - v_{s1} e^{-\omega_{12}x}) dx d\lambda$$

$$\tag{F-25}$$

$$J_{scn2} = q \int_0^{\lambda_{c1}} \alpha_2 D_{n2} C_{23} \left[ \left( R_n \cosh \frac{x_2 - x_1}{L_{n2}} - \sinh \frac{x_2 - x_1}{L_{n2}} \right) \left( \frac{v_{21}}{v_{\omega 1} e^{-\Delta E_{c1}/kT}} + \frac{1}{\alpha_2 L_{n2}} \right) \right.$$

$$\left. - \left( 1 + \frac{R_n}{\alpha_2 L_{n2}} \right) e^{-\alpha_2 (x_2 - x_1)} \right] d\lambda \tag{F-26}$$

$$J_{Jn2} = q \frac{D_{n2}}{L_{n2}} n_{2po} (e^{qV_2/kT} - 1) R_n \tag{F-27}$$

where

$$R_n = \frac{N_{12}}{F_{12}} \frac{v_{\omega 1} e^{-\Delta E_{c1}/kT}}{\cosh \frac{x_2 - x_1}{L_{n2}}}, \tag{F-28}$$

264

$$N_{12} = \frac{\cosh\frac{x_2-x_1}{L_{n2}}}{v_1 e^{-E_{c1}/kT}} \left[ v_{21} + v_{\omega 1} e^{-\Delta E_{c1}/kT} \cosh\frac{x_2-x_1}{L_{n2}} \right], \qquad \text{(F-29)}$$

$$I_1 = v_{21} + v_{\omega 1} e^{-\Delta E_{c1}/kT} \tanh\frac{x_2-x_1}{L_{n2}}, \qquad \text{(F-30)}$$

$$I_{01} = e^{\omega_{12}x_1} - v_{s1} e^{\omega_{11}x_1}, \qquad \text{(F-31)}$$

$$v_1 = \frac{D_{n1}\omega_{12} + \mu_{n1}E_{10}}{D_{n1}\omega_{11} + \mu_{n1}E_{10}}, \qquad \text{(F-32)}$$

$$v_{s1} = \frac{D_{n1}\omega_{12} + \mu_{n1}E_{10} - S}{D_{n1}\omega_{11} + \mu_{n1}E_{10} - S}, \qquad \text{(F-33)}$$

$$v_{21} = \frac{D_{n2}/L_{n2}}{D_{n1}\omega_{11} + \mu_{n1}E_{10}}, \qquad \text{(F-34)}$$

$$v_{\omega 1} = \frac{v_1 e^{\omega_{12}x_1} - v_{s1} e^{\omega_{11}x_1}}{I_{01}}, \qquad \text{(F-35)}$$

$$n_{2po} = \left(\frac{n_i^2}{N_{A2}}\right)_{GaAs}. \qquad \text{(F-36)}$$

We observe that the short-circuit contribution from Region 1, $J_{scn1}$, is characterized by an integration over x. This arises because of the band-gap grading and the position dependent absorption coefficient. An integration over x is not required for $J_{scn2}$ since Region 2 possesses a constant bandgap material and a position-independent absorption coefficient.

The form of the dark current, Eq. (F-27), is illuminating in that it predicts a higher or lower dark current represented by the more common expression of the diode equation

$$J = q \frac{D_{n2}}{L_{n2}} n_{2po} (e^{qV_2/kT} -1).$$ (F-37)

The multiplicative factor, $R_n$, in Eq. (F-27) predicts charge confinement in Region 1 and recombination of electrons in Region 1 and 2. In the absence of surface recombination, $R_n$ asymptotically approaches unity for increasing $(x_2-x_1)/L_{n2}>1$. For decreasing values of $(x_2-x_1)/L_{n2}$ and $\Delta E_{c1}>kT$ charge confinement occurs. $R_n$ is more sensitive to $\Delta E_{c1}$ than it is to $E_{10}$. We conclude that the barrier $\Delta E_{c1}$ is more effective in confining electrons to Region 2 when $\Delta E_{c1}>kT$.

In direct transition materials $(x_2-x_1)/L_{n2}$ may be made to take on values between $10^{-2}$ to $10^{-1}$ in order to affect a reduction in dark current without suffering incomplete absorption loss. This is particularly true in the PW solar cell where the p-type GaAs in lightly doped and for which mobility and lifetime attain their highest values. Moreover, the additional capability of fabricating a conduction band discontinuity $\Delta E_{c1}>>kT$ results in a more effective barrier in confining electrons to Region 2.

With increasing surface recombination velocity, $R_n$ may attain values greater than unity which indicates increased recombination. This gives a dark current higher than predicted by Eq. (F-37).

REGIONS 3 and 4: Holes in the n-n Regions

The solutions for Regions 3 and 4 are similar to those obtained in Regions 2 and 1, respectively. We briefly outline the analysis below.

266

The nonhomogeneous continuity equation, generation term, entering flux, general solution, and defined functions are:

$$0 = g_3 + D_{p3} \frac{d^2 P_3}{dx^2} - \frac{P_3}{D_{p3}} \qquad , \tag{F-38}$$

$$g_3 = \int_0^{\lambda_{c2}} \alpha_2 N_{02}(x_2) e^{-\alpha_3(x-x_2)} d\lambda \qquad , \tag{F-39}$$

$$N_{02}(x_2) = N_{01}(x_1) e^{-\alpha_2(x_2-x_1)} \qquad , \tag{F-40}$$

$$P_3(x) = C_{31} \cosh\frac{x-x_2}{L_{p3}} + C_{32} \sinh\frac{x-x_2}{L_{p3}} - c_{03}(x) \quad , \tag{F-41}$$

$$c_{03}(x) = \int_0^{\lambda_{c2}} C_{33} e^{-\alpha_3(x-x_2)} d\lambda \qquad , \tag{F-42}$$

$$C_{33} = \frac{\alpha_3 L_p^2 N_{02}(x_2)}{D_{p3}(\alpha_3^2 L_{p3}^2 - 1)} \qquad , \tag{F-43}$$

The cut-off frequency, $\lambda_{c2}$, corresponds to the GaAs bandgap energy.

The set of equations for Region 4 are summarized below:

$$0 = g_4 + D_{p4} \frac{d^2 P_4}{dx^2} - \mu_{p4} E_{40} \frac{d_{p4}}{dx} - \frac{P_4}{\tau_{P4}} \qquad , \tag{F-44}$$

$$g_4 = \int_0^{\lambda_{c3}} \alpha_4 N_{03}(x_3) e^{-\int_{x_3}^x \alpha_4 dx'} \qquad , \tag{F-45}$$

$$N_{03}(x_3) = N_{02}(x_2) e^{-\alpha_3(x_3-x_2)} \qquad , \tag{F-46}$$

$$P_4(x) = C_{41} e^{\omega_{41}(x-x_3)} + C_{42} e^{\omega_{42}(x-x_3)} +$$

267

$$+ \frac{1}{\omega_{42} - \omega_{41}} \left[ G_{41}(x) e^{\omega_{41}(x-x_3)} + G_{42}(x) e^{\omega_{42}(x-x_3)} \right] , \quad \text{(F-47)}$$

$$G_{41} = \frac{1}{D_{p4}} \int_0^{\lambda_{c3}} \int_{x_3}^{x} \alpha_4 N_{04}(x') e^{-\omega_{41}(x'-x_3)} dx' d\lambda , \quad \text{(F-48)}$$

$$G_{42}(x) = - \frac{1}{D_{p4}} \int_0^{\lambda_{c3}} \int_{x_3}^{x} \alpha_4 N_{04}(x') e^{-\omega_{42}(x'-x_3)} dx' d\lambda , \quad \text{(F-49)}$$

$$\omega_{41}, \omega_{42} = \frac{\mu_{p4} E_{40}}{2 D_{p4}} \pm \sqrt{\frac{\mu_{p4} E_{40}}{2 D_{p4}} + L_{p4}^{-2}} , \quad \text{(F-50)}$$

$$N_{04}(x) = N_{03}(x_3) e^{-\int_{x_3}^{x} \alpha_4 dx'} , \quad \text{(F-51)}$$

$$E_{G3} = E_{G2} + \Delta E_{v3} , \quad \text{(F-52)}$$

$$E_{40} = - \frac{E_{G4} - E_{G2} - \Delta E_{v3}}{x_4 - x_3} , \quad \text{(F-53)}$$

$$\lambda_{c3} = \frac{1.2398}{E_{G3}} . \quad \text{(F-54)}$$

The cut-off frequency $\lambda_{c3}$ is represented by the bandgap of the $Al_x Ga_{1-x}As$ at $x_3$.

Again, there are imposed four boundary conditions on the two general solutions from which we determine the four constants of integration. The boundary conditions are:

$$P_3(x_2) = P_{3n0}(e^{qV_2/kT} - 1), \quad \text{(F-55)}$$

$$P_3(x_3) = P_4(x_3) e^{\Delta E_{v3}/kT}, \quad \text{(F-56)}$$

$$D_{p3} \frac{dp_3}{dx}\bigg|_{x_3} = D_{p4} \frac{dp_4}{dx}\bigg|_{x_3} - P_4(x_3) \mu_{p4} E_{40}, \quad \text{(F-57)}$$

$$P_4(x_4) = P_{5n0} e^{\Delta E_{v4}/kT} . \quad \text{(F-58)}$$

The current is determined at $x_2$ from the relationship

$$J_{p2} = -qD_{p3} \left. \frac{dp_3}{dx} \right|_{x_2} \qquad \text{(F-59)}$$

resulting in an equation similar in form to Eq. (F-24) and given by

$$J_{p2} = -J_{scp3} - J_{scp4} + J_{Jp2} . \qquad \text{(F-60)}$$

The components $J_{scp3}$ and $J_{scp4}$ are contributions to short-circuit current from Regions 3 and 4, respectively, and $J_{Jp2}$ is the contribution to dark current from hole injection across the p-n junction into Region 3. The presence of the minus sign indicates current direction is in the negative x-direction while the plus sign indicates current direction in the positive x-direction.

The expressions for the current components of Eq. (F-60) are represented by:

$$J_{scp3} = q \int_0^{\lambda_{c2}} \alpha_3 D_{p3} C_{33} \left\{ 1 - \frac{R_p}{\alpha_3 L_{p3}} - \left[ \cosh \frac{x_3 - x_2}{L_{p3}} - R_p \sinh \frac{x_3 - x_2}{L_{p3}} \right. \right.$$

$$\left. \left. - \frac{1}{3^L p3} \left( R_p \cosh \frac{x_3 - x_2}{L_{p3}} - \sinh \frac{x_3 - x_2}{L_{p3}} \right) \right] e^{-\alpha_3 (x_3 - x_2)} \right\} d\lambda \qquad \text{(F-61)}$$

$$J_{scp4} = q \frac{D_{p3}}{L_{p3}} \frac{1 - v_{v4}}{I_{34}} \frac{e^{\Delta E_{v3}/kT}}{\sinh \frac{x_3 - x_2}{L_{p3}}} \frac{1/D_{p4}}{\omega_{41} - \omega_{42}} \int_0^{\lambda_{c3}} \int_{x_3}^{x_4} \alpha_4 N_{04}(x') \left[ e^{\omega_{41}(x_4 - x')} \right.$$

$$\left. - e^{\omega_{42}(x_4 - x')} \right] dx' d\lambda + q \frac{D_{p3}}{L_{p3}} p_{sno} \frac{1 - v_{v4}}{I_{34}} \frac{e^{(\Delta E_{v3} + \Delta E_{v4})/kT}}{\sinh \frac{x_3 - x_2}{L_{p3}}} \qquad \text{(F-62)}$$

$$J_{Jp2} = q \frac{D_{p3}}{L_{p3}} p_{3no} (e^{qV_2/kT} - 1) R_p . \qquad \text{(F-63)}$$

269

APPENDIX G:  TWO-JUNCTION CASCADE SOLAR CELL ANALYSIS

In APPENDIX F, "Potential Well Solar Cell Analysis", the details of the closed form analysis were presented.  The two-junction cascade analysis is discussed below; but, since the details are similar to the analysis presented for the PW cell, less detail is presented for the cascade cell.

The analysis is based on the band structures given in Figure 6.22 for the voltage opposing configuration.  The solution for the minority carrier distributions have been written into a computer program through Fortran IV and using an IBM 370-165 for numerical solution.  The analysis, while based on the CCVO configuration, has been generalized such that it can also be applied to Si, GaAs, window structures, PW, CCVA and other cascade structures up to n-junctions.  The PW analysis is a simplification of this analysis.

The appropriate continuity equation, Eqs. (4.10) through (4.13) is applied to each of the 10 regions in Figure 6.22.  The corresponding general solutions, Eqs. (4-14) and (4-19), are then subjected to the boundary conditions given in Table G.1.  The boundary conditions pertaining to excess minority carrier concentration and to minority carrier current density are listed in separate columns in Table G.1.

The electron current density, $J_{n2}$, of the top junction $(X = X_2)$ arising from the absorption of photons in Regions 1 and 2 is given as

$$J_{n2} = -J_{nsc1} - J_{nsc2} + J_{nJ2} \qquad (G-1)$$

where $J_{nsc1}$ and $J_{nsc2}$ are the contributions from Regions 1 and 2,

270

Table G.1. The list of boundary conditions imposed on the general solutions relating to the CCVO band structure given in Figure 6.22.

| Boundary | Excess Minority Carrier | Minority Carrier Current |
|---|---|---|
| $X = 0$ | None | $D_{n1} \left. \dfrac{dn_1}{dx} \right|_o + n_1(0)\mu_{n1}E_{10} = Sn_1(0)$ |
| $= X_1$ | $n_1(x_1) = n_2(x_1)e^{-\Delta E_{c1}/kT}$ | $D_{n1} \dfrac{dn_1}{dx} + n_1(x_1)\mu_{n1}E_{10} = D_{n2} \left. \dfrac{dn_2}{dx} \right|_{x_1}$ |
| $= X_2$ | $n_2(x_2) = n_{2p0}(e^{\beta_2^{1/2}} - 1)$  $p_3(x_2) = p_{3n0}(e^{\beta_2^{1/2}} - 1)$ | None |
| $= X_3$ | $p_3(x_3) = p_4(x_3)e^{-\Delta E_{v3}/kT}$ | $D_{p3} \left. \dfrac{dp_3}{dx} \right|_{x_3} = D_{p4} \left. \dfrac{dp_4}{dx} \right|_{x_3} -p_4(x_3)\mu_{p4}E_{40}$ |
| $= X_4$ | $p_4(x_4) = p_5(x_4)e^{-\Delta E_{v3}/kT}$ | $D_{p4} \left. \dfrac{dp_4}{dx} \right|_{x_4} - p_4(x_4)\mu_{p4}E_{40} = D_{p5} \left. \dfrac{dp_5}{dx} \right|_{x_4}$ |
| $= X_5$ | $p_5(x_5) = p_{5n0}(e^{\beta_5 V_5} - 1)$  $n_6(x_5) = n_{6p0}(e^{\beta_5 V_5} - 1)$ | None |
| $= X_6$ | $n_6(x_6) = n_7(x_6)e^{-\Delta E_{c6}/kT}$ | $D_{n6} \left. \dfrac{dn_6}{dx} \right|_{x_6} = D_{n7} \left. \dfrac{dn_7}{dx} \right|_{x_6} + n_7(x_6)\mu_{n7}E_{70}$ |

271
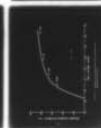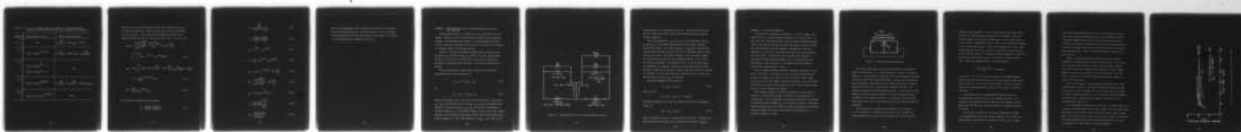
Table G.1.   The list of boundary conditions imposed on the general solutions relating to the CCVO band structures given in Figure 6.22 (Continued).

| Boundary | Excess Minority Carrier | Minority Carrier Current |
|---|---|---|
| X = 0 | None | $D_{n1} \left. \dfrac{dn_1}{dx} \right|_o + n_1(0)\mu_{n1}E_{10} = S n_1(0)$ |
| $= X_7$ | $n_7(x_7) = n_8(x_7)e^{-\Delta E_{c7}/kT}$ | $D_{n7} \left. \dfrac{dn_7}{dx} \right|_{x_7} + n_7(x_7)\mu_{n7}E_{70} = D_{n8} \left. \dfrac{dn_8}{dx} \right|_{x_7}$ |
| $= X_8$ | $n_8(x_8) = n_{8p0}(e^{\beta_8 V_8} - 1)$ <br> $p_9(x_8) = p_{9n0}(e^{\beta_8 V_8} - 1)$ | None |
| $= X_9$ | $p_9(x_9) = p_{10}(x_9)e^{+\Delta E_{v9}/kT}$ | $D_{p9} \left. \dfrac{dp_9}{dx} \right|_{x_9} = D_{p10} \dfrac{dp_{10}}{dx} - p_{10}(x_9)\mu_{p10}E_{100}$ |
| $= X_{10}$ | $p_{10}(x_{10}) = p_{11}(x_{10})e^{+\Delta E_{v10}/kT}$ | None |

272

respectively, to the electron short circuit current density and $J_{nJ2}$ is the electron contribution to dark current arising from the photovoltage of the top junction. The closed form relationships for each of the component currents in Eq. (G-1) are given in Eqs. (G-2), (G-3) and (G-4):

$$J_{nsc1} = q \frac{v_{21}\cosh \frac{x_2-x_1}{L_{n2}}}{v_{w1}e^{-\Delta_{e1}/kT}} \frac{e^{(w_{11}+CO_{12}x_1)}}{I_{01}} (R_n - \tanh \frac{x_2-x_1}{L_{n2}})$$

$$\times \int_o^{\lambda_{c2}} \int_o^{x_1} \alpha_1 N_{01} [e^{-w_{11}x} - v_{s1}e^{-w_{12}x}]dxd\lambda \; ; \qquad (G-2)$$

$$J_{nsc2} = qD_{n2} \int_o^{\lambda_{c2}} \alpha_2 C_{23} [(R_n \cosh \frac{x_2-x_1}{L_{n2}} - \sinh \frac{x_2-x_1}{L_{n2}})(\frac{v_{21}}{v_{w1}e^{-\Delta E_{c1}/kT}} + \frac{1}{\alpha_2 L_{n2}})$$

$$- (1 + \frac{1}{\alpha_2 L_{n2}})e^{-\alpha_2(x_2-x_1)}]d\lambda \; ; \qquad (G-3)$$

$$J_{n2} = q \frac{D_{n2}}{L_{n2}} n_{2po}(e^{\beta_2 V_2}-1)R_n \; . \qquad (G-4)$$

The constants are defined by the following:

$$v_{s1} \equiv \frac{D_{n1}w_{12} + \mu_{n1}E_{10}- S}{D_{n1}w_{11} + \mu_{n1}E_{10}- S}, \qquad (G-5)$$

$$v_{21} \equiv \frac{\dfrac{D_{n2}}{L_{n2}}}{D_{n1}w_{11} + \mu_{n1}E_{10}} , \qquad (G-6)$$

$$v_1 \equiv \frac{D_{n1}w_{12} + \mu_{n1}E_{10}}{D_{n1}w_{11} + \mu_{n1}E_{10}} , \qquad (G-7)$$

$$I_{01} \equiv e^{w_{12}x_1} - v_{s1}e^{w_{11}x_1} , \qquad (G-8)$$

$$v_{w1} \equiv \frac{1}{I_{01}} [v_1 e^{w_{12}x_1} - v_{s1}e^{w_{11}x_1}] , \qquad (G-9)$$

$$F_{12} \equiv v_{21} + v_{w1}2^{-\Delta E_{c1}/kT} \tanh \frac{x_2 - x_1}{L_{n2}} , \qquad (G-10)$$

$$N_{12} \equiv \frac{v_{21}\sinh\dfrac{x_2 - x_1}{L_{n2}}}{v_{w1}e^{-\Delta E_{c1}/kT}} + \cosh \frac{x_2 - x_1}{L_{n2}} \qquad (G-11)$$

$$N_{01} \equiv (1-r)N_o(\lambda)e^{-\int_o^x \alpha_1 dx'} \qquad (G-12)$$

$$R_n \equiv \frac{N_{12}}{F_{12}} \frac{v_{w1}e^{-\Delta E_{c1}/kT}}{\cosh \dfrac{x_2 - x_1}{L_{n2}}} \qquad (G-13)$$

$$C_{23} = \frac{\alpha_2 L_{n2}^2 (1-R)N_o}{D_{n2}(\alpha_2^2 L_{n2}^2 - 1)} \qquad (G-14)$$

274

These are corresponding current equations of holes for the top junction
and of electrons and holes for the bottom junction.  Due to the length
of these equations we will not present them in this report.  The results
of the calculations are presented in Section 6.0

APPENDIX H.   EQUIVALENT CIRCUIT FOR A VOLTAGE-OPPOSING CASCADE SOLAR
CELL STRUCTURE

The equivalent circuit of a cascade solar cell structure is not self-
evident.  Clearly, it must be derived from the solution to the continuity
equation.  An interesting characteristic of voltage-opposing structures
is that a fraction of the dark current of one p-n junction may be converted
to electrical energy in an adjacent junction.

Consider a two-junction pp/nnn/pp cascade structure where the load
resistance, $R_1$, and load voltage, $V_1$, relate to the first junction while
$R_2$ and $V_2$ to the second.  We assume that a drift field is present in
the middle n-type region which aids holes to flow forward the second p-n
junction.

The current solutions obtained from a solution of the continuity
equations for each of the junctions are

$$J_1 = J_{sc1} + \beta_2 \, J_{Dp2} - J_{D1} \qquad\qquad (H-1)$$

and

$$J_2 = -J_{sc2} - \beta_1 \, J_{Dp1} + J_{D2} \qquad\qquad (H-2)$$

where the subscripts refer to the first and second junctions, respectively:
$J_{sc1}$, $J_{sc2}$ are the short-circuit currents; $J_{D1}$, $J_{D2}$ are the component dark
currents - electrons and holes; $J_{Dp1}$, $J_{Dp2}$ are the hole contributions to
the dark currents; $\beta_1$, $\beta_2$ are the hole transport factors in the (nnn) regions.
From Eqs. (H-1) and (H-2) the equivalent circuit may be constructed and pre-
sented in Figure H.1.  The current generator, $\beta_2 \, J_{Dp2}$, in Eq. (H-2) is not
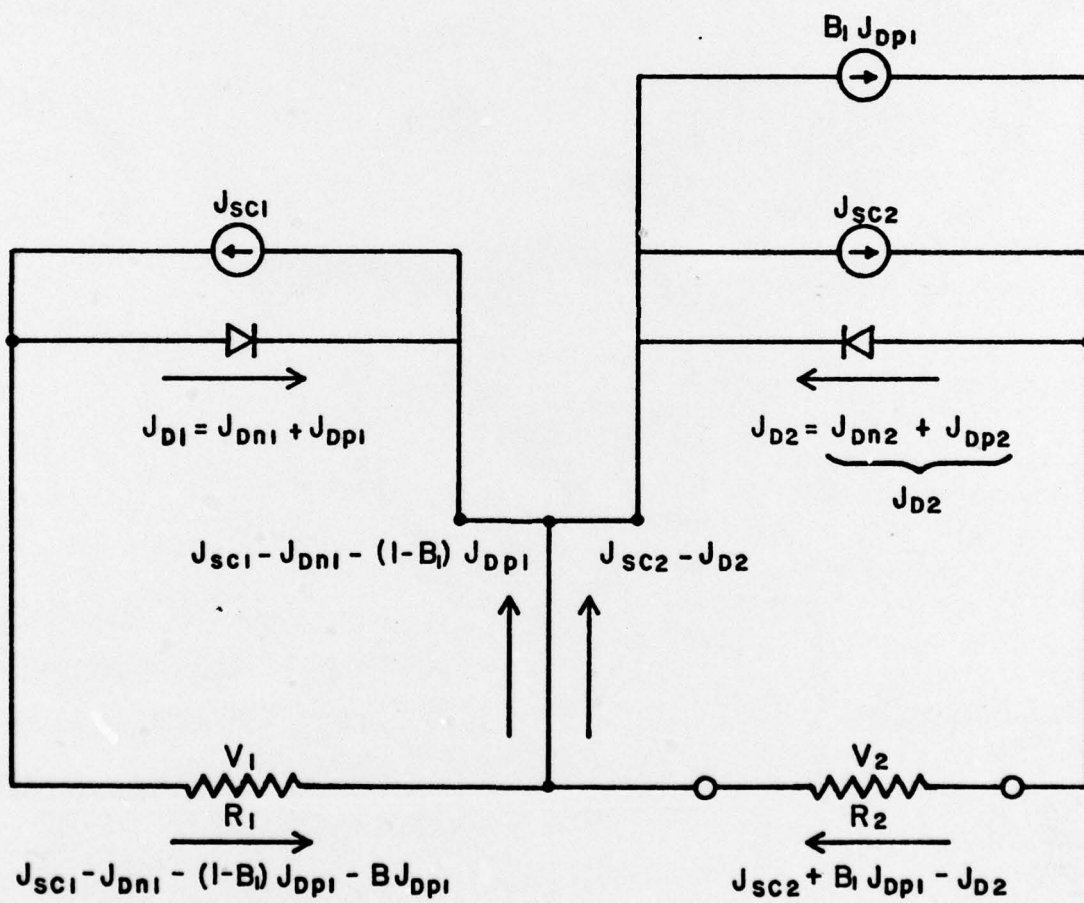
276

Figure H.1. Equivalent Circuit for 2-Junction Cascade Structure.

277

included because it is very small since $\beta_2 \ll 1$. This results because the built-in field in the middle n-type region accelerates holes toward the second p-n junction.

The current generators, $J_{sc1}$ and $J_{sc2}$, and the diode dark currents, $J_{D1}$ and $J_{D2}$, are the familiar quantities which are present in single junction solar cells. The current generator $\beta_1 J_{Dp1}$ arises from the hole contribution to the dark current of the first p-n junction which is transported to the second. This current component arises from holes flowing in the same direction as those holes produced by photons in the second and third n-type regions. The transport factor, $\beta_1$, can be nearly unity for appropriate cell designs. Therefore, an appreciable portion of this hole dark current may be converted to useful electrical energy by the second p-n junction. For the same reasons that $\beta_1$ may be unity, $\beta_2$ is much less than unity and the term $\beta_2 J_{Dp2}$ is neglected.

The power dissipated in the load $R_1$ is

$$P_1 = (J_{sc1} - J_{D1}) V_1 \qquad\qquad (H-3)$$

and in $R_2$ it is

$$P_2 = (J_{sc2} - J_{D2}) V_2 + \beta_1 J_{Dp1} V_2 .$$

The power dissipated in the load, $R_2$, without the dark current component, $\beta_1 J_{Dp1}$, is

$$P_{20} = (J_{sc2} - J_{D2}) V_2 \qquad\qquad (H-4)$$

which is identical in form to a single junction solar cell. Therefore, the power converted by the second cell is increased by the amount $\beta_1 J_{Dp1} V_2$.

278

APPENDIX J.  LOW VOLTAGE CONVERSION

The problem of converting low voltages (< 1 Vdc) to a higher, more useful level is a classical problem dating back to the early 1960's.  At that time, fuel cells and thermionic generators were promising new energy sources, and efficient voltage converters were urgently needed to exploit their characteristic low output voltages.  Consequently, there were numerous, concerted efforts to develop efficient, low voltage converters during the 1960's.  These efforts were only marginally successful. Converters for input voltages between 0.5 and 1 volts exhibited peak efficiencies of about 80 percent.  Efficiencies decreased sharply as voltages were reduced below 0.5 volts.

The low voltage conversion problem was somewhat circumvented in the mid- to late 1960's.  The solar cell, fuel cell, and thermionic energy sources, for example, were placed in series to obtain a higher output voltage and provide for a higher conversion efficiency.  The series source connections were generally more complex and less reliable than the single sources or sources connected in parallel.

Low voltage converters are basically configured as illustrated in Figure J.1.  The low input voltage is connected across the primary of a transformer.  As the transformer core approaches saturation, the switches are operated to apply the MMF ($V_{in}$) in the opposite direction.  Additional circuitry controls the state of the two switches, which must be alternately closed and opened, and provides other desired characteristics, e.g., a filtered, regulated dc output.
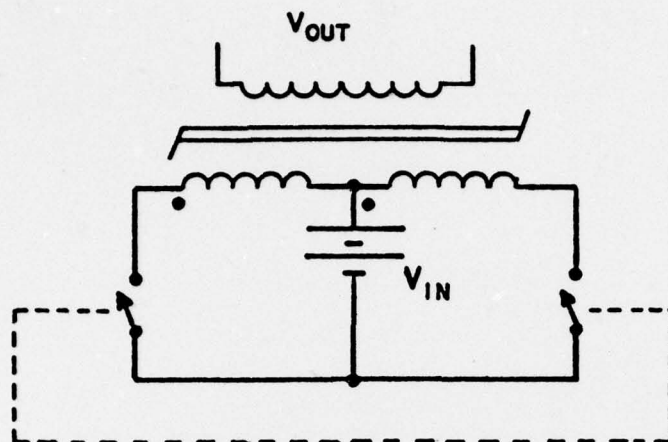
--

279

Figure J.1. Basic Converter Configuration.

For a given power input, the converter efficiency is determined by losses in the converter. ($\eta$ = Power out/Power in = (Power in - Losses)/ (Power in.). These consist of transformer core losses (hysteresis and eddy currents), copper losses, and switch losses. In practical converters for space applications, transistors are most suitable as switches. However, transistor switches have a characteristic threshold loss due to the voltage drop across the collector-emitter circuit. If the converter input voltage is low, this collector-emitter loss is very significant and is detrimental to the collecter efficiency. In contrast, core losses and copper losses vary with the converter output and are relatively small and manageable.

As an illustration, assume that the switches in the circuit of J.1 are transistors. At moderate current levels, e.g., 30-100A, the collector-emitter drop ($V_{ce}$ sat.) will typically be 50 mV for selected

germanium power transistors. (Low voltage converters must handle large currents if a significant power output is to be achieved.) Thus, the collector-emitter circuit loss is estimated to be $0.05 \, I_c$ watts where $I_c$ is the collector (transformer) current. Other typical transistor parameters are a dc current gain ($h_{FE}$) of 10 and a base-emitter drop of 0.5V. Thus, the base-emitter circuit has a loss ($0.5 \, I_c/h_{FE}$) equal to the collector-emitter, and the losses in a conducting switch are estimated as $(2)(0.05) \, I_c$. The converter input power is $V_{in} I_c$. With only the transistor switch losses considered, maximum efficiency can be estimated as

$$n = \frac{V_{in} - (2)(.05)}{V_{in}} \times 100 \text{ percent.}$$

If $V_{in}$ is 0.2, 0.4, or 0.6 volts, for example, the estimated maximum possible converter efficiencies are 50, 75, and 83 percent, respectively. Other losses, e.g., core, copper, switch control circuit, and regulator circuit, have been neglected and these will also reduce the converter efficiency.

A literature search of the NASA and DOD files has been made to determine the state-of-the-art in low voltage converters. It is noteworthy that references from the NASA search show numerous entries between 1962 and 1967, and a sharp curtailment of converter activities after 1967.

The literature confirms that the basic configuration of Figure J.1 is predominantly used in low voltage converters. The switches are special purpose, germanium power transistor with low $V_{ce}$ sat. values.

281

Design features characteristically include current feedback schemes to insure that conducting transistor switches were saturated ON, schemes to minimize excessive base currents which overdrive the conducting transistor, and schemes to eliminate extraneous losses associated with excessive transformer (and switch) currents when the power transformer approaches saturation. Converter operating frequencies tended to be 400 to 1000 Hz.

Figure J.2 shows some measured efficiencies from low voltage converters. The parameters are converter input voltages. The 1.6V and 1.2V curves are from a 150 watt, 28 volt, regulated output converter. The converter efficiency remained above 79 percent for input voltages between 1.2V and 1.6V over the 80 to 155 watt range [J-1]. The other curves in Figure J.2 are from two unregulated converters designed for lower input voltages [J-1].

The curves in Figure J.3 show measured efficiencies from a second regulated-output converter. The output voltages were regulated within $\pm$ 1 percent. For the 0.4V input case, the set point had to be changed to 24 VDC to maintain regulation. The 1.2 and 1.8V curves were obtained by operating from a laboratory power supply, and the others from a thermionic diode source [J-2].

It is interesting to note that the efficiency is a rather complicated function of the power output and the input voltage. For low voltage inputs, particularly, the efficiency tends to peak over a narrow range of output power. This reflects the fact that, for low input voltages, the efficiency is strongly dependent upon certain design considerations that can only be optimized over a small range of operating conditions.
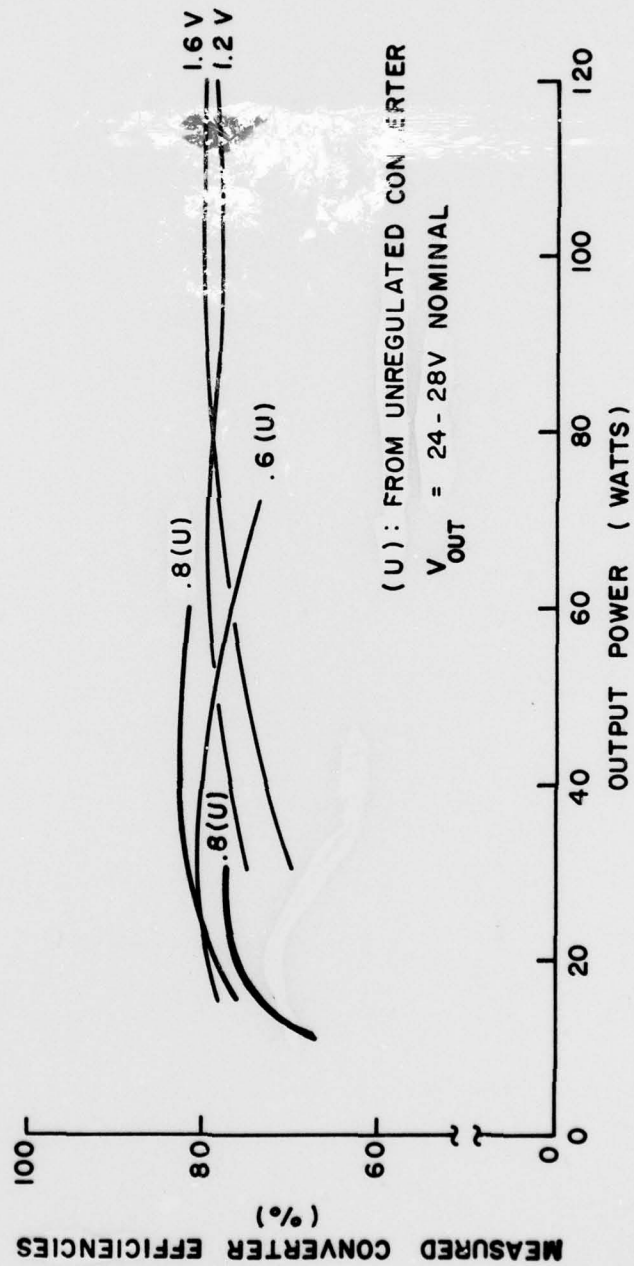
282

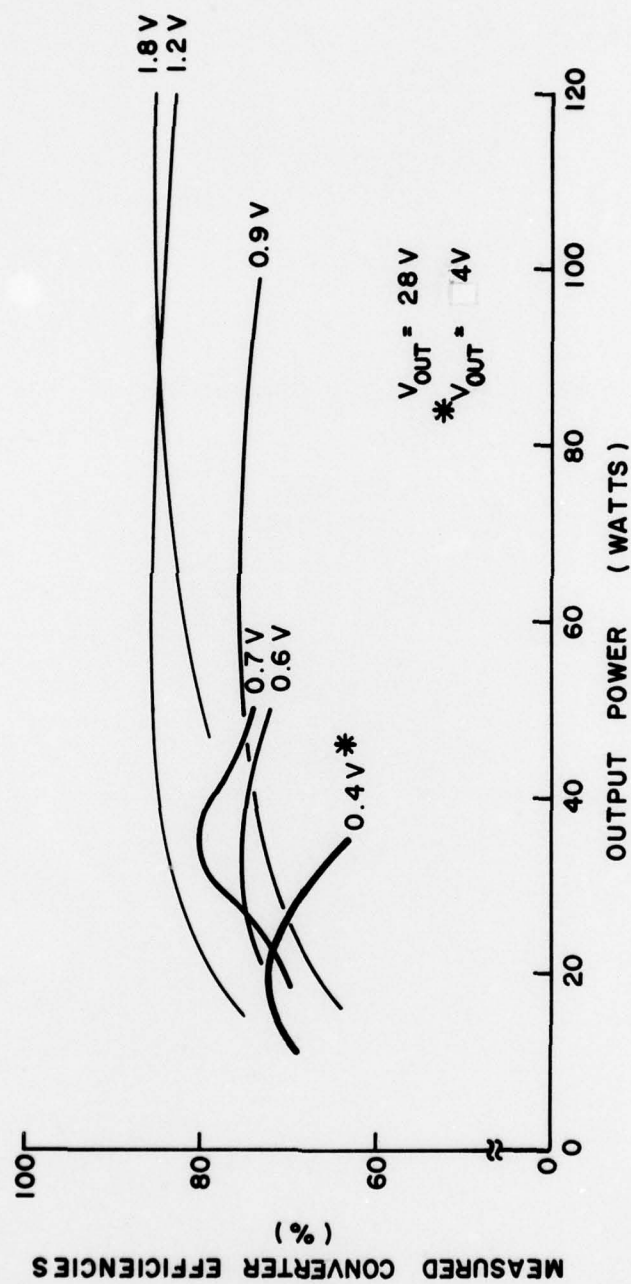Figure J.2. Some Measured Low-Voltage Converter Efficiencies

283

Figure J.3. Other Measured Converter Efficiencies

284

Figure J.4 shows efficiency data from an experimental low voltage converter as a function of input voltage. The input current was a constant average (over each cycle) of 20A. These data are especially interesting in that the efficiency is shown going to zero at about 0.23 volts. This implies that the transistor switches have a $V_{ce}$ sat. parameter of less than 0.23 volts, i.e., it is a very unusual transistor and is probably not readily available. This converter is an unregulated converter. It is basically configured similar to the configuration in Figure J.1 but with a unique, highly efficient innovation [J-3].

The data presented in Figures J.2, J.3, and J.4 are from the more efficient converters described in the literature reviewed.

## Conclusions

The data presented in this appendix confirm that the efficient conversion of low, dc voltages from less than one volt to a more useful level is a difficult problem. In the range of 0.5V to 1V input, efficiencies of 70-80 percent are obtained through careful design and selection of components. Below 0.5V inputs, the efficiency decreases.

REFERENCES

J-1. Lingle, J. T., Low Input Voltage Conversion, Proceedings of the 18th Annual Power Sources Conference, 1964.

J-2. Lingle, J. T., Energy Source -- Low Voltage/Conversion System, Proceedings of the 19th Annual Power Sources Conference, 1965.

J-3. Wilson, T. G., and Moore, E. T., Inverter for Use With Very Low Input Voltages, IEEE Transactions on Communications and Circuits, July, 1964.
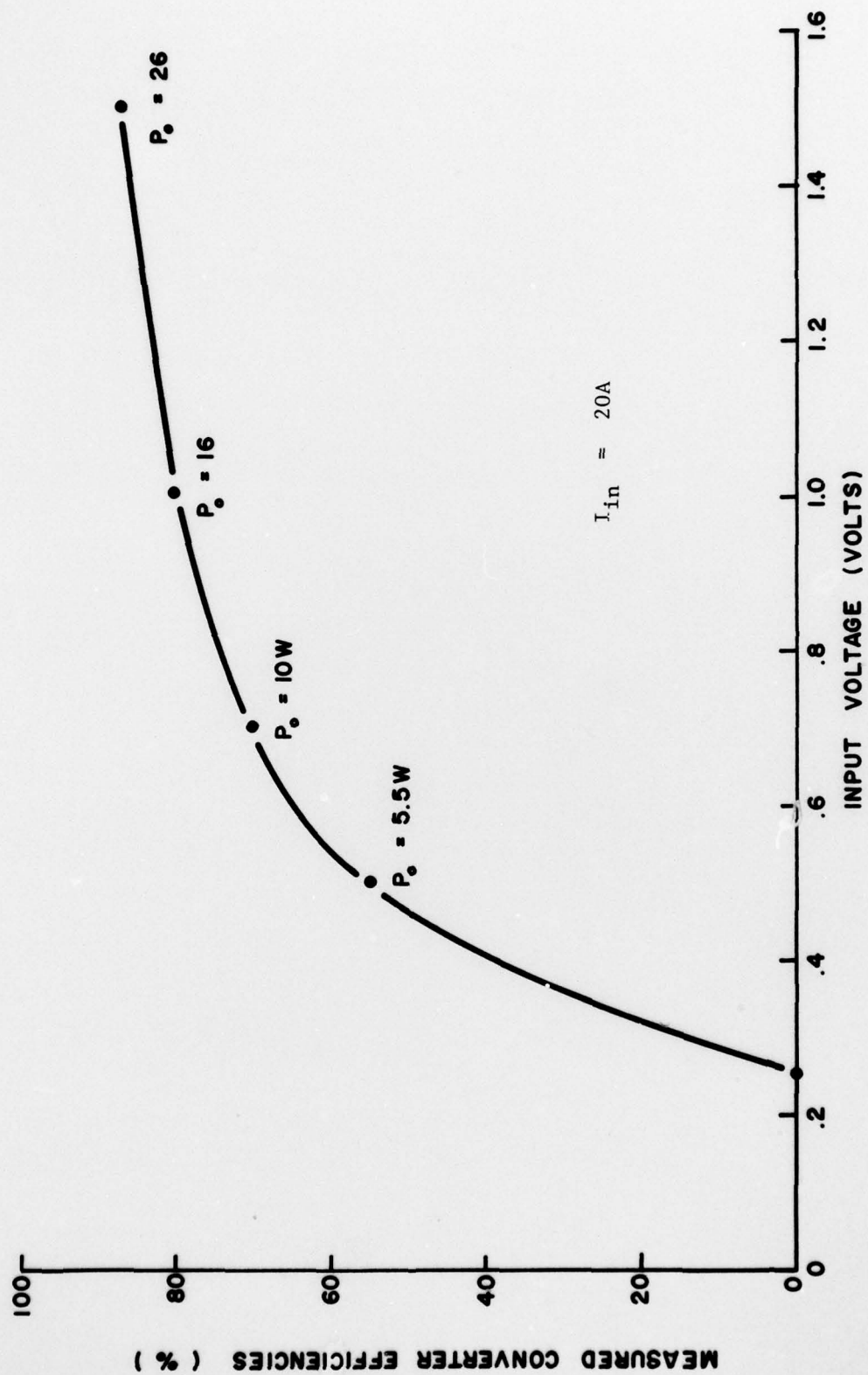
Figure J.4.  Measured Efficiencies Versus Input Voltage from an Experimental Converter